



New model systems with perpendicular magnetic anisotropy for spin transfer torque experiments

Matthias Gottwald

► To cite this version:

Matthias Gottwald. New model systems with perpendicular magnetic anisotropy for spin transfer torque experiments. Other [cond-mat.other]. Université Henri Poincaré - Nancy 1, 2011. English. NNT : 2011NAN10053 . tel-01746197

HAL Id: tel-01746197

<https://hal.univ-lorraine.fr/tel-01746197>

Submitted on 29 Mar 2018

HAL is a multi-disciplinary open access archive for the deposit and dissemination of scientific research documents, whether they are published or not. The documents may come from teaching and research institutions in France or abroad, or from public or private research centers.

L'archive ouverte pluridisciplinaire **HAL**, est destinée au dépôt et à la diffusion de documents scientifiques de niveau recherche, publiés ou non, émanant des établissements d'enseignement et de recherche français ou étrangers, des laboratoires publics ou privés.



AVERTISSEMENT

Ce document est le fruit d'un long travail approuvé par le jury de soutenance et mis à disposition de l'ensemble de la communauté universitaire élargie.

Il est soumis à la propriété intellectuelle de l'auteur. Ceci implique une obligation de citation et de référencement lors de l'utilisation de ce document.

D'autre part, toute contrefaçon, plagiat, reproduction illicite encourt une poursuite pénale.

Contact : ddoc-theses-contact@univ-lorraine.fr

LIENS

Code de la Propriété Intellectuelle. articles L 122. 4

Code de la Propriété Intellectuelle. articles L 335.2- L 335.10

http://www.cfcopies.com/V2/leg/leg_droi.php

<http://www.culture.gouv.fr/culture/infos-pratiques/droits/protection.htm>

Nouveaux systèmes modèles à aimantation perpendiculaire pour l'étude des effets de transfert de spin

Thèse

pour obtenir le titre de

Docteur de l'Université Henri Poincaré

Nancy-Université
en Physique

par Matthias GOTTWALD

Soutenue publiquement le 30 septembre 2011 devant le jury composé de :

Président :	Prof. M. Henkel	UHP Nancy
Rapporteurs :	Prof. M. Kläui	Universität Mainz
	Prof. T. Thomson	University of Manchester
Examineurs :	Prof. R. Stamps	University of Glasgow
	Prof. M. Aeschlimann	TU Kaiserslautern
Directeurs de thèse :	Prof. S. Mangin	UHP Nancy
	Prof. S. Andrieu	UHP Nancy

Table des matières

1	L'état de l'art	15
1	Basics of magnetism and spin transfer torque	17
1.1	Magnetic moment and magnetic interactions	17
1.1.1	Magnetic moment	17
1.1.2	Itinerant vs localized magnetism	18
1.1.2.1	Transition metals (TM)- model of itinerant magnetism	18
1.1.2.2	Magnetism of rare earth elements(RE) - model of localized electrons	19
1.1.3	Magnetic interactions	21
1.1.3.1	Zeeman energy	21
1.1.3.2	Exchange interaction	21
1.1.3.3	Dipolar energy and shape anisotropy	22
1.1.3.4	Magnetocrystalline anisotropy (MCA)	23
1.1.4	MCA of rare earth elements and MCA of transition metals . . .	24
1.1.5	Anisotropy of thin films	25
1.1.6	Magnetic domains and domain walls (DW)	26
1.2	Magnetoresistance	27
1.2.1	Anisotropic magnetoresistance (AMR)	28
1.2.2	Giant magnetoresistance (GMR)	28
1.2.3	Extraordinary Hall effect (EHE)	29
1.3	Magnetization reversal	30
1.3.1	Stoner Wohlfarth model	30
1.3.2	Magnetization reversal in thin films	31
1.3.2.1	Nucleation process	32
1.3.2.2	Propagation process	33
1.3.3	Domain wall propagation in a nanowires under field	35
1.3.4	Propagation of a DW in a nanowire without pinning sites . . .	35
1.3.5	Propagation of a DW in a nanowire considering pinning sites . .	36
1.3.5.1	DW pinning sites in nanowires	36
1.3.5.2	The depinning process in nanowires	37
1.3.6	Conclusion for the choice of a material as a model system . . .	38
1.4	Magnetization reversal induced by a spin-polarized current	38
1.4.1	Dynamic of a magnetic moment : LLGS equation	38
1.4.2	Current-induced magnetization reversal and steady states precession in nanopillars	40
1.4.3	Current-induced DW propagation	41

1.5	Materials for spin torque experiments	44
1.5.1	In-plane vs out-of-plane materials	44
1.5.2	Materials used for experiments on spin transfer torque switching in nanopillars	46
1.5.3	Materials used for experiments on spin current driven domain wall propagation	47
1.6	Outline for the following manuscript	47
2	Les alliages de $Co_{1-x}Tb_x$	51
2	CoTb-based alloys	53
2.1	Growth and Structure	53
2.1.1	Sample preparation by DC magnetron sputtering	53
2.1.2	Structural analysis by transmission electron microscopy (TEM)	54
2.2	Magnetic properties	57
2.2.1	Magnetic structure of rare earth(RE) - transition metal(TM) alloys	57
2.2.2	Magnetization of the CoTb system	59
2.2.3	Perpendicular anisotropy in CoTb alloys	60
2.2.4	Magnetism of CoTb alloys as a function of layer thickness	62
2.2.5	Further data	62
2.2.5.1	Soft-magnetic contribution to hysteresis loops	62
2.2.5.2	Effects of annealing	62
2.2.6	Models describing the origin of PMA in RE-TM alloys	64
2.2.7	Conclusion on the magnetic properties of CoTb alloys	66
2.3	Magnetization reversal in $Co_{1-x}Tb_x$ alloys and $Co_{1-x}Tb_x$ -based spin valves	67
2.3.1	Reversal process of CoTb films	67
2.3.1.1	Domain pattern of CoTb films during reversal	67
2.3.1.2	Barkhausen length l_B of the reversal process	69
2.3.1.3	Conclusion on the reversal process	70
2.3.2	Dipolar coupling in CoTb-based spin valves	70
2.3.2.1	Magnetometry results	71
2.3.2.2	Analysis by MFM imaging	74
2.3.2.3	Modelization of the dipolar field	75
2.3.2.4	Modification of the nucleation field	80
2.3.2.5	Conclusion	81
2.3.3	Conclusion on magnetization reversal in $Co_{1-x}Tb_x$ alloys and $Co_{1-x}Tb_x$ -based spin valves	81
2.4	Transport properties of CoTb alloys	83
2.4.1	Magnetoresistance of a $Co_{0.88}Tb_{0.12}$ layer	83
2.4.2	Magnetoresistance of CoTb-based spin valves	85
2.4.3	Temperature dependence of magnetoresistance	86
2.4.4	Angular dependence of magnetoresistance in CoTb alloys	89
2.4.5	Conclusion on the magnetoresistance of CoTb alloys	91
2.5	All-Optical magnetization switching in $Co_{1-x}Tb_x$ alloys	93
2.5.1	Mechanisms of all-optical magnetization switching	93
2.5.2	First results obtained for $Co_{1-x}Tb_x$ alloys	93
2.5.3	Conclusion and new perspectives	94

2.6	Conclusion and perspectives for CoTb alloys	96
3	Les super-réseaux $[Co/Ni](111)$ épitaxiés	99
3	Epitaxial $[Co/Ni](111)$ superlattices	101
3.1	Growth and structure of epitaxial $[Co/Ni]$ films	101
3.1.1	Growth of $[Co/Ni](111)$ superlattices	101
3.1.1.1	Al_2O_3 (11 $\bar{2}$ 0) substrate	101
3.1.1.2	Growth of V(110) on Al_2O_3 (11 $\bar{2}$ 0)	102
3.1.1.3	Growth of Au(111) on V(110)	103
3.1.1.4	Growth of $[Co/Ni](111)$ superlattices on Au(111) . . .	104
3.1.1.5	Conclusion on the growth of $[Co/Ni](111)$ superlattices by molecular beam epitaxy	104
3.1.2	Ex-situ analysis of the sample structure	105
3.1.2.1	Verification of the atomic stacking by transmission elec- tron microscopy (TEM)	105
3.1.2.2	Exact determination of lattice parameters	106
3.1.3	Conclusion on growth and structure of epitaxial $[Co/Ni]$ films .	111
3.2	Magnetic properties of epitaxial $[Co/Ni]$ superlattices	112
3.2.1	Part 1: Macroscopic magnetic properties	112
3.2.1.1	Hysteresis loops	112
3.2.1.2	Magnetization	112
3.2.1.3	Coercivity and saturation fields	113
3.2.1.4	Simple model explaining the perpendicular anisotropy of $[Co/Ni]$ superlattices	115
3.2.1.5	In-plane anisotropy of $[Co/Ni]$ superlattices	118
3.2.2	Part 2: Microscopic magnetic properties	120
3.2.2.1	Details on the experiment and the treatment of XMCD data	120
3.2.2.2	XAS results	122
3.2.2.3	Determination of the magnetic moment by XMCD . .	123
3.2.2.4	Conclusion on XMCD	127
3.2.3	Part 3: Dynamic magnetic properties	127
3.2.4	Conclusion on the magnetic properties of $[Co/Ni]$ superlattices .	130
3.3	Fully epitaxial spin valves based on $[Co/Ni](111)$ superlattices	131
3.3.1	Growth and magnetic properties	131
3.3.2	Spin-resolved photoemission	132
3.3.2.1	Basics of spin-resolved photoemission	134
3.3.2.2	Experimental results for $[Co/Ni]$ superlattices	137
3.3.3	Transport properties of $[Co/Ni]/Au/[Co/Ni]$ spin valves	140
3.3.4	Conclusion on $[Co/Ni]$ -based spin valve systems	142
3.4	Magnetization reversal of $[Co/Ni]$ nanowires	143
3.4.1	Magnetization reversal in patterned $[Co/Ni]$ layers	143
3.4.2	Propagation of domain walls in $[Co/Ni]$ nanowires	146
3.4.3	Conclusion on the DW propagation in $[Co/Ni]$ nanowires	147
3.5	Conclusions and perspectives for epitaxial $[Co/Ni]$ superlattices	150

4	Conclusion	151
4	Conclusion	153
	References	155

REMERCIEMENTS - ACKNOWLEDGMENTS

I'd like to thank M. Kläui, T. Thomson, M. Henkel, M. Aeschliman and R. Stamps for accepting to be part of my PhD jury and their remarks on the manuscript.

Ce travail a été réalisé à l'Institut Jean Lamour de Nancy. Je remercie Monsieur Jean-Marie Dubois, le directeur de l'Institut Jean Lamour de Nancy et Monsieur Michel Vergnat, le directeur du département de Physique de la Matière et des Matériaux, pour leur accueil.

Je suis arrivé à Nancy dans le cadre du Cursus Intégré Franco-Allemand en Physique le premier septembre 2006, en prévision de passer une année d'études en France pour améliorer mes connaissances de langue, pour me changer les idées, rencontrer de nouvelles personnes, apprendre la physique etc. Au cours de mes stages de Master j'ai eu la chance de rencontrer quelques membres de l'équipe Magnétisme qui m'ont donné envie de prolonger mon séjour en France et de faire une thèse dans cette équipe. Maintenant, en partant, je souhaite exprimer mes remerciements à tous ceux qui ont contribué à ces années de grand succès.

Tout d'abord je souhaite remercier mon directeur de thèse Stéphane Mangin pour ses idées, son enthousiasme, sa disponibilité, son soutien à tout moment, pour toutes les opportunités de rencontres autour des conférences, écoles et collaborations. Je le remercie pour la confiance qu'il a eue en moi et la grande liberté qu'il m'a accordée et dont j'ai profité ces quatre années durant lesquelles nous avons travaillé ensemble.

Je remercie aussi Stéphane Andrieu, qui a également dirigé cette thèse. Ça a toujours été un grand plaisir pour moi de travailler avec lui. Merci de m'avoir initié à l'élaboration des échantillons par MBE et à la photoémission. Je le remercie également pour sa disponibilité. De plus, ses extraordinaires qualités pédagogiques m'ont été d'une grande aide lors de nos discussions nombreuses.

Je remercie également Michel Hehn pour son encadrement et environ 500 échantillons faits avec sa pulvé. J'ai bien profité de sa disponibilité et son ouverture envers des nouvelles pistes de recherche. Il faut aussi dire que même avant ces dernières observations douteuses des neutrinos qui se propagent plus vite que la lumière, il est la preuve que la causalité n'est pas un principe fondamental : Moi : "Michel, j'aurais besoin d'un échantillon X pour faire une manip Y. Tu pourras lancer un dépôt ?" Michel : " Oui, j'ai mis l'échantillon dans ton casier ce matin." Moi : "OK ???".

Je remercie Thomas Hauet pour son engagement dans mon sujet de thèse, ses encouragements, les discussions, ses conseils, et les manip qu'il a faites pour accélérer le progrès de mes sujets de recherche. Un grand merci aussi à Christine Bellouard pour la formation sur les instruments en cryogénie et sa disponibilité pour des discussions autour de ces manip. Je remercie également François Montaigne pour des nombreuses lithographies faites dans le cadre de cette thèse, les discussions et l'aide avec les manip de photoémission à Soleil. Merci beaucoup à Daniel Lacour pour la formation et l'aide avec le MFM et les discussions, spécialement sur les effets du couplage dipolaire.

Je souhaite aussi exprimer mes remerciements à Stéphane Suire pour la préparation de quelques centaines de litres d'hélium liquide et ses interventions efficaces en cas de problèmes techniques. Je remercie Gwladys Lengaigne pour les lithographies optiques et la formation pour la salle blanche. Je remercie également Julien Cucchiara pour son aide sur les manip de transport et les discussions. Et je remercie Sylvie Robert pour l'analyse X de mes échantillons. Je souhaite aussi remercier Mathieu Da Silva pour

l'élaboration de quelques échantillons MBE. En plus je remercie Karine Dumesnil, Cathy Dufour (qui nous a quittés beaucoup trop tôt), Christian Senet(informatique), Cori Tiusan, Hamid M'Jahed, Alexandre Boucher (la scie à fil), Laurent Buvot (formation à la micro soudure), Danielle Pierre, Luc Moreau, Marc Alnot, Yuan Lu, Damien Engeldinger, Martine , Jean-Georges Mussot et François Mouginet, pour tout les petits coups de mains pendant ma thèse. Et je remercie aussi Valérie Madeline, Hélène Huon et Anne-Sophie Latreille pour leur aide avec tout ce qui concerne les ordres de mission, les bons de commande etc.

Et j'ai aussi eu le plaisir de travailler avec un grand nombre de personnes en dehors l'IJL :

Je remercie l'équipe de l'IEF à Paris, spécialement Dafiné Ravelosona et Nicolas Vernier, de m'avoir donné la possibilité de faire la microscopie Kerr avec un champ perpendiculaire et pour les discussions sur les nanofils. Vielen Dank an die AG Aeschli-mann der TU Kaiserslautern für die Erfolgreiche Zusammenarbeit beim "all-optical switching", besonders an Daniel Steil und Sabine Alebrand. Auch Danken möchte ich der AG Farle der Universität Duisburg für die TEM Aufnahmen der CoTb Proben. I'd like to thank Andrew Kent and Jean-Marc Beaujour for the FMR analysis of the $[Co/Ni]$ samples. And I'd like to thank P. Fischer for the XMCD imaging of the CoTb samples. Furthermore I'd like to thank Eric Fullerton and Andreas Berger for discussions. Je remercie les chercheurs de la ligne CASSIOPEE au synchrotron SOLEIL, François Bertrand, Patrick Lefevre et Amina Taleb, pour leur aide avec les expériences de photoémission. Je remercie également Etienne Snoeck pour les images TEM du système $[Co/Ni]$ et Lionel Calmels et Florian Gimbert pour leurs calculs ab-initio permettant de mieux comprendre nos résultats expérimentaux.

Mais je veux remercier également tous ceux qui m'ont soutenu par leur amitié :

Tout d'abord un grand merci à Amandine, ma collègue de bureau pendant deux ans, ce qui lui permettait toujours de savoir en premier quand une de mes manips ne marchait pas ;-). Merci pour tous les moments quand on a bien rigolé ensemble au bureau, pendant des conférences, l'école en Roumanie, les séances de piscine du samedi après-midi et les soirées. T'as placé la barre assez haut pour mes futurs collègues de bureau.

Je remercie aussi tous les autres chercheurs, (ex)doctorants, profs, (ex)post-doc et associés avec lesquels j'ai passé des moments sympas pendant ces années :

Thomas, François, Stéphane, Bea, Dan, Emilie, Hanna (les pauses café vont me manquer), Sylvain, Sandra, Fréd, Julien, Cédric, Emilie, Aurélie (je suis sûr un jour la physique des plasmas va voir un grand succès) , Guillaume, Christel, Kaname, Sébastien (n'oublies pas la 428),Clément, Rajani, Weiwei, Mathias, Mathieu et ceux que j'ai oublié de remercier.

Et finalement je salue ceux qui ont osé plonger avec moi dans des eaux troubles et profondes :

Ibrahim, Vivien (le MF1), Hervé, Olivier, Cédirc, Fabien, Nico, Martial, Alizée, Mathieu, Pierre, Grégoire, Noémie, Hélène, David, Florence, Maxime et Jimmy.

J'espère de pouvoir garder le contact avec vous tous !

Zuletzt möchte ich auch noch meinen Eltern für ihre Unterstützung danken.

Introduction

Le rôle du spin de l'électron pour les phénomènes de transport électriques est devenu un champ de fort intérêt pour la recherche fondamentale mais aussi pour le développement de nouveaux éléments électroniques. En effet, depuis la découverte de la magnétorésistance géante (GMR) à la fin des années 1980 par P. Grünberg [1] et A. Fert [2] une nouvelle thématique s'est développée : l'électronique de spin. L'idée de base de la GMR repose sur le fait que la résistance d'un système constitué de deux couches magnétiques séparées quelques nanomètres dépend de l'orientation relative des aimantations de ces deux couches. La raison est liée à la dépendance de la résistance électrique en fonction de l'orientation du spin dans un matériau comme décrit par Mott [3]. Cet effet de GMR repose observable par exemple dans des systèmes nommés vannes de spin, constitués de deux couches ferromagnétiques séparées par une couche métallique non magnétique, où les épaisseurs de couches sont de l'ordre du nanomètre. Rapidement après cette découverte, l'effet de GMR était utilisé par l'industrie dans le domaine des mémoires de données magnétiques. Ceci a été possible grâce à un développement rapide des techniques de nanostructuration de vannes de spin et de jonctions tunnel magnétiques permettant la production d'un nouveau type de tête de lecture pour des disques durs. Avec ces nouvelles possibilités la densité de stockage de données a pu être augmentée considérablement dans les années suivantes.

Un autre phénomène relié au spin, l'effet de transfert de spin, a été prédit théoriquement par L. Berger [4] et J. Slonczewski [5] en 1996. L'idée est qu'un courant électrique polarisé en spin est porteur d'un moment cinétique. Ce moment cinétique peut être transféré à l'aimantation d'un système magnétique et par conséquent exciter cette aimantation, la renverser ou permettre une précession permanente. Là aussi, cet effet peut être observé dans des vannes de spin et dans des jonctions tunnel magnétiques. Dans un tel système, une couche joue le rôle de polariseur en spin du courant, qui peut transférer du moment cinétique à la deuxième couche en appliquant un couple sur l'aimantation de cette deuxième couche. Depuis les premières preuves expérimentales de la précession d'aimantation [6] et du renversement de l'aimantation par le couple de transfert de spin [7], une large communauté scientifique a travaillé sur cette thématique. La forte densité de courant nécessaire pour ce genre de phénomènes a pu être diminuée de quelques $10^{12} A/m^2$ à quelques $10^{10} A/m^2$. De plus, l'industrie s'intéresse aux applications possibles comme les oscillateurs haute fréquence [8] ou les mémoires magnétiques à accès sélectif basées sur le transfert de spin [9] (STT-MRAM).

A part l'effet décrit en haut dans des structures vannes de spin, le transfert de spin peut aussi entraîner la propagation d'une paroi magnétique. Cela a aussi été prédit par L. Berger en 1984 [10]. Des densités de courant élevées, de l'ordre de $10^{12} A/m^2$, sont nécessaires pour l'observation d'un effet. Des nanofils d'une épaisseur d'une centaine de

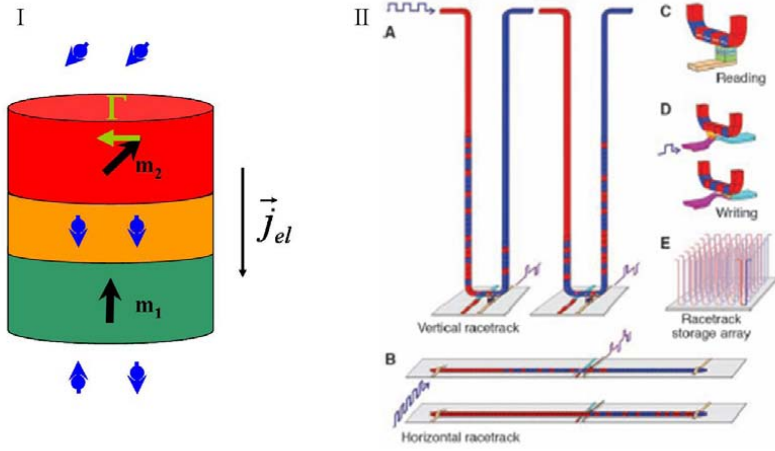


Fig. 1: Deux exemples pour la manipulation d'une aimantation avec un courant polarisé en spin : Dans I) nous voyons une vanne de spin où un courant électrique est polarisé en spin par les couches magnétiques. Dans cet exemple, le courant polarisé en spin applique un couple Γ sur l'aimantation de la couche en haut car la polarisation du courant et la direction de l'aimantation ne sont pas alignées. II) Concept du Magnetic Domain Wall Racetrack Memory suggéré par S. Parkin [11].

nanomètres ont pu être réalisés grâce au progrès des nanotechnologies. Ceci a permis une large étude expérimentale pour la propagation d'une paroi unique dans des tels fils. Des applications industrielles ont été proposées. La plus fameuse est probablement le principe du "Magnetic Domain Wall Racetrack Memory" suggéré par S. Parkin [11]. Dans ce concept, les données sont stockées sous forme d'une séquence de domaines dans un nanofil en forme de U. La séquence peut être déplacée dans les deux sens par la propagation de domaines sous l'effet d'un courant polarisé en spin.

Malgré le progrès technologique et un travail expérimental et théorique important, il y a encore des questions sur la compréhension des phénomènes liés au transfert de spin. Il est donc nécessaire d'avoir des "systèmes modèles" pour progresser dans la compréhension du phénomène. Nous entendons par "systèmes modèles" un système magnétique, pour lequel les paramètres intrinsèques pertinents pour le transfert de spin peuvent être modulés. Avec un tel système, des dépendences prédites théoriquement entre le transfert de spin et les propriétés magnétiques et la structure électronique pourraient être testées.

Dans cette thèse, l'aptitude de deux systèmes magnétiques à former des systèmes modèles était testée. Ces deux systèmes sont des super-réseaux $[Co/Ni]$ épitaxiés et des alliages amorphes de $Co_{1-x}Tb_x$. Le manuscrit est divisé en cinq chapitres :

1. Nous commençons avec l'état de l'art. Tout d'abord les bases du magnétisme et du transfert de spin sont présentées. Ensuite nous discutons les résultats expérimentaux principaux obtenus jusqu'à maintenant sur les phénomènes liés au transfert de spin. Enfin nous présentons les exigences requises pour un système modèle pour le transfert de spin.
2. Dans le deuxième chapitre nous présentons les méthodes expérimentales utilisées pour la préparation et l'analyse des échantillons.

3. Les résultats obtenus pour les alliages $Co_{1-x}Tb_x$ sont présentés dans le chapitre 3. La croissance, l'analyse de la structure, le magnétisme et les propriétés de transport de ces alliages sont décrits. De plus, le renversement de l'aimantation dans des couches minces de $Co_{1-x}Tb_x$ et des vannes de spin basées sur du $Co_{1-x}Tb_x$ est discuté. Finalement, nous montrons que ce matériau n'est pas seulement intéressant pour l'étude des effets de transfert de spin, mais aussi pour l'étude du renversement de l'aimantation avec des moyens optiques en utilisant un faisceau de laser polarisé circulairement. Ces derniers résultats sont tout à fait nouveaux.
4. Dans le quatrième chapitre nous nous focalisons sur les super-réseaux $[Co/Ni]$ élaborés par épitaxie par jets moléculaires. Une analyse détaillée de leur croissance et de leur structure est donnée. Les propriétés magnétiques sont discutées en mettant l'accent sur l'origine de l'anisotropie perpendiculaire dans ce système. Finalement un système de vanne de spin entièrement épitaxié et ses propriétés sont présentés.
5. Dans le dernier chapitre nous résumons les résultats obtenus et nous donnons une vue globale sur les perspectives de ce travail.

.

Introduction (English)

The role of the electron spin for electronic transport properties has become a field of high interest for fundamental research as well as for the development of new electronic devices since the discovery of the Giant Magneto Resistance (GMR) at the end of the 1980's by P. Grünberg [1] and A. Fert [2]. The basic idea of GMR is, that the resistance of a system consisting of two ferromagnetic layers which are closer to each other than a few nanometer depends on the relative orientation of their magnetizations. The reason is that the scattering probability of electrons in ferromagnetic materials is spin-dependent as described by Mott [3]. The GMR effect can be observed for example in spin valves, systems consisting of two ferromagnetic layers separated by a non-magnetic metallic spacer layer with layer thicknesses of the order of a few nanometer. The GMR effect was used soon after its discovery by magnetic data storage industry. This was made possible by a quick progress on nanofabrication and on thin film growth. This allowed the production of new types of high-performance read heads for hard discs. Due to these new devices the density of data storage on hard disk drives could be significantly increased in the following years.

A further spin-related phenomenon, the spin torque, was predicted by L. Berger [4] and J. Slonczewski [5] in 1996. The idea is that a current which is spin-polarized transports angular momentum. This angular momentum can be transferred to the magnetization of a system and hence excite its magnetization and reverse it or lead to steady state precessions of the magnetization. This effect can be observed in spin valve structures and magnetic tunnel junctions. In such a system one layer is supposed to act as a polarizer for an electric current, which can then transfer angular momentum by applying a torque on the magnetization of the other layer. Since the first experimental proofs for spin transfer driven magnetic precession by Tsoi in 1998 [6] and for spin transfer driven magnetization reversal by Myer in 1999 [7] a large community has been working on these phenomena. The necessary high current densities for spin transfer torque could be reduced from several $10^{12} A/m^2$ to the order of $10^{10} A/m^2$. Furthermore industry became interested in possible applications like current tunable high frequency oscillators by Kiselev 2003 [8] or spin transfer torque based random access memory by Huai 2004[9].

In addition to the above described effect in spin valve structures the transfer of angular momentum can also lead to propagation of magnetic domain walls. This was predicted again by L. Berger in 1984 [10]. High current densities of the order of $10^{12} A/m^2$ were necessary to observe this effect. The progress in nanotechnology made it possible to pattern wires with a width of the order of $100nm$. This allowed large studies on the current induced propagation of single domain walls in such nanowires. Industrial applications were proposed, the most famous is probably the so-called Magnetic Domain

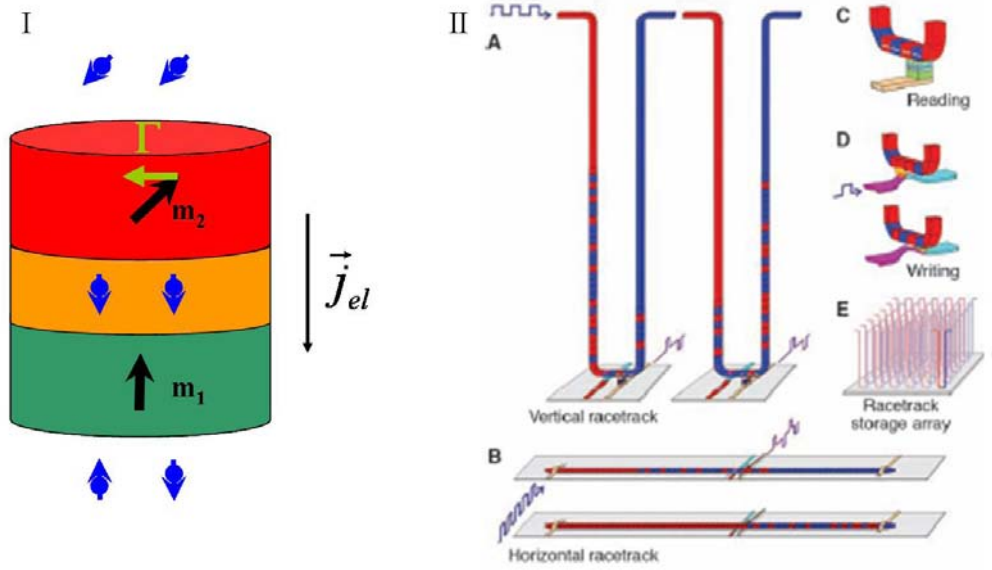


Figure 2: Two examples for the manipulation of a magnetization due to a spin-polarized current. I) shows a spin valve where an electric current is spin-polarized by the magnetic layers. In this example, the spin-polarized current applies a torque Γ on the upper magnetic layer as polarization and magnetization are not aligned. II) Concept of the Magnetic Domain Wall Racetrack Memory suggested by S. Parkin [11].

Wall Racetrack Memory suggested by S. Parkin [11]. In this concept the data is stored as domain sequence in a U-shaped nanowire. The sequences can be moved forward and backward to the read and write heads by current induced domain wall motion.

Despite the technological progress and large experimental and theoretical work, there are still some questions remaining for the understanding of the phenomena related to the transfer of angular momentum by a spin-polarized current. For further understanding it would be helpful to have experimental "model systems" for spin transfer torque related phenomena. Under a "model system" we understand a magnetic system, for which the essential intrinsic parameters related to spin transfer torque can be tuned. With such a system theoretically predicted dependencies between spin transfer torque and magnetic and electronic properties could be tested.

During this PhD thesis the suitability of two magnetic systems as model systems for spin transfer torque related phenomena was tested. These two systems are epitaxially grown $[Co/Ni](111)$ superlattices and sputtered amorphous $Co_{1-x}Tb_x$ alloys. The manuscript is divided in four chapters:

1. We begin with the state of the art. First of all the basics of magnetism and spin transfer torque are presented. We then review the main experimental results obtained up to now on spin transfer torque related phenomena. The requirements of a model system for spin transfer torque are discussed.
2. The obtained results for $Co_{1-x}Tb_x$ alloys are presented in chapter two. Growth, structure, magnetism and transport properties are shown. Furthermore the

magnetization reversal in simple $Co_{1-x}Tb_x$ films and $Co_{1-x}Tb_x$ -based spin valves is discussed. In addition we show that this material is not only interesting for spin transfer torque but also for all-optical switching, a technique allowing to reverse magnetization by using circular polarized light.

3. The third chapter focuses on the epitaxially grown $[Co/Ni](111)$ superlattices. A detailed analysis of growth and structure is given. Magnetic properties are discussed with a special interest on the origin of the perpendicular magnetic anisotropy in this system. Finally the development of a fully epitaxial spin valve system and its properties are presented.
4. In the last chapter we briefly resume the obtained results and give an overview about the steps, that should be considered next.

Résumé

Etat de l'art

Les effets de transfert de spin ont été étudiés pour plusieurs applications. Les premières expériences ont consisté à tenter de manipuler l'aimantation sous l'effet du transfert de spin, tout d'abord dans des nanopiliers [12], puis de déplacer des parois de domaines magnétiques dans des nanofils ([13] et [14]). L'efficacité du transfert de spin a pu être améliorée dans une étape suivante en utilisant des nouveaux matériaux avec une anisotropie perpendiculaire (voir par exemple [15] et [16]). Depuis l'effet de transfert de spin est fortement étudié dans ce type de matériaux. Pour les nanopiliers, des diagrammes de phase [17], la dépendance angulaire du renversement sous courant [18], le bruit télégraphique [19] et la dynamique du renversement [20] ont été mesurés. Un large travail expérimental a été fait sur le comportement stochastique du dépiégeage d'une paroi sous courant dans un nanofil (voir par exemple [21]) et sur la détermination de l'origine des couples adiabatique et non-adiabatique (voir par exemple [22]) et leurs influences sur la propagation d'une paroi sous courant.

Ce qui n'a pas été fait pour le moment est l'étude de phénomènes de transfert de spin dans des systèmes modèles pour lesquels les propriétés magnétiques peuvent être modifiées pour une large gamme de valeurs. Un tel travail devrait permettre de vérifier les relations établies entre les paramètres magnétiques et les effets de transfert de spin (voir par exemple [23] et [24]).

Pour faciliter l'étude du transfert de spin, le système doit posséder les propriétés suivantes :

1. Des configurations magnétiques bien définies (par exemple anisotropie magnétique perpendiculaire (AMP)) : un système avec un axe d'anisotropie unique fort n'a que deux configurations stables. Ceci facilite la compréhension des processus de renversement.
2. Une faible densité de courant nécessaire pour le retournement de l'aimantation (efficacité) : les premières expériences de transfert de spin dans des nanopiliers [12] nécessitaient des densités de courant de l'ordre de $10^{12} A/m^2$. Pour la propagation de parois, des valeurs autour de $10^{11} A/m^2$ ont été rapportées [25]. Ceci entraîne un chauffage par effet Joule important. Une forte augmentation de la température peut entraîner des modifications des propriétés magnétiques ou même détruire l'échantillon.
3. Des propriétés magnétiques homogènes (homogénéité) : des défauts structuraux jouent souvent un rôle important pour le renversement de l'aimantation. Pour les expériences sur la propagation de parois dans des nanofils, le potentiel de

piégeage d'un site artificiel dépend des défauts intrinsèques du matériau. Dans des nanopiliers, le piégeage d'une paroi a été étudié par exemple dans la référence [19]. La force et la distribution locale de ces défauts suivent des lois stochastiques. Pour un système modèle, il est important de contrôler ces distributions pour pouvoir obtenir des propriétés reproductibles.

4. Modulation reproductible des propriétés magnétiques : les phénomènes reliés au transfert de spin dépendent fortement des paramètres magnétiques comme l'aimantation à saturation M_S , la constante d'échange A et l'anisotropie magnéto-cristalline K_{MC} de l'échantillon. Ainsi, la possibilité de pouvoir faire varier ces paramètres serait un grand avantage pour l'étude de modèles de transfert de spin.

Le but de cette thèse est d'étudier des systèmes magnétiques et de déterminer si ces systèmes sont des candidats intéressants pour l'étude des phénomènes liés au transfert de spin. Deux systèmes possédant potentiellement une anisotropie perpendiculaire ont été choisis : des super-réseaux $[Co/Ni]$ élaborés par épitaxie par jets moléculaires et des alliages amorphes de $Co_{1-x}Tb_x$ élaborés par pulvérisation cathodique. Les raisons du choix des super-réseaux $[Co/Ni]$ sont les suivantes :

Il a déjà été montré que l'efficacité du transfert de spin est très élevée dans des multicouches de Co/Ni polycristallines et texturées dans la direction (111) élaborés par pulvérisation cathodique ([15] et [16]). De plus, l'aimantation perpendiculaire peut être modulée en modifiant les épaisseurs de Co et de Ni. En effet, il est établi, que l'anisotropie vient des interfaces Co/Ni [26]. Notre objectif est l'amélioration du contrôle de l'anisotropie grâce à un meilleur contrôle des interfaces Co/Ni en utilisant l'épitaxie par jets moléculaires. D'ailleurs, dans un système épitaxié, nous pouvons nous attendre à un paramètre d'amortissement de Gilbert α plus faible. La qualité structurale devrait aussi diminuer le taux de diffusion et conduire à une longueur de diffusion de spin plus élevée, et par conséquent à une polarisation en spin P plus élevée pour un courant traversant le système. Ces deux contributions devraient augmenter l'efficacité du transfert de spin.

Le choix des alliages amorphes de $Co_{1-x}Tb_x$ élaborés par pulvérisation cathodique est lié au fait que leur aimantation perpendiculaire et leur anisotropie peuvent être modulées facilement en faisant varier soit la composition x , soit la température T [27]. Il a été démontré que des alliages composés de terres rares et de métaux de transition peuvent polariser un courant en spin, même s'ils ne possèdent pas d'aimantation [28]. Un désavantage du système CoTb est que le paramètre d'amortissement α est en général assez élevé ([29]). Cependant, comme certains modèles prédisent une grande efficacité de transfert de spin pour des systèmes à faible aimantation, le matériau devrait être un bon choix pour vérifier ce type de théories.

Les alliages $Co_{1-x}Tb_x$

Les alliages de $Co_{1-x}Tb_x$ élaborés par pulvérisation cathodique sont amorphes. Pourtant, ils possèdent une anisotropie magnétique perpendiculaire (AMP). Il est possible de choisir une composition avec $x \in [0.08; 0.34]$ pour laquelle l'aimantation est perpendiculaire. De plus, il est aussi possible de modifier l'AMP et l'aimantation en variant la température pour un échantillon de composition x donnée. La possibilité de travailler avec des aimantations nets très faibles est d'un grand intérêt puisque plusieurs

modèles prédisent des singularités sur la dynamique de l'aimantation à aimantation nulle.

Le renversement de l'aimantation dans des couches de 20 nm de $Co_{1-x}Tb_x$ a été étudié. Pour des champs magnétiques appliqués perpendiculairement à la surface, il se passe en deux étapes : nucléation de quelques domaines magnétiques et croissance par propagation de parois. Le nombre limité de nucléations pour des champs autour du champ de propagation dans le matériau rend le système adapté aux expériences de propagation de parois uniques dans des nanofils. L'étude du renversement de l'aimantation dans des structures du type vanne de spin par magnétométrie et par microscopie à force magnétique (MFM) a montré que la propagation des parois peut être modifiée en utilisant les interactions dipolaires entre les aimantations des deux couches. Ceci ouvre une perspective intéressante pour le contrôle des sites de piégeage artificiels.

Plusieurs effets de magnétorésistance ont été étudiés pour les alliages de $Co_{1-x}Tb_x$. Un fort coefficient de l'effet Hall extraordinaire a été obtenu qui pourrait être très utile pour les expériences de propagation des parois dans des nanofils. En revanche, les vannes de spin basées sur des alliages de $Co_{1-x}Tb_x$ montrent un petit effet de magnétorésistance géante ($GMR \approx 0.015\%$). Ceci prouve qu'un courant polarisé en spin peut être injecté dans la couche non-magnétique servant comme espaceur entre les couches magnétiques. Il a pu être démontré que la GMR est liée à l'orientation relative des sous-réseaux de Co et de Tb, et qu'elle n'est pas dépendant de l'orientation des aimantations totales. Par conséquent il est aussi possible d'observer la GMR, quand une des deux couches est compensée, donc de produire des courants polarisés en spin avec des matériaux sans aimantation nette.

Les alliages de $Co_{1-x}Tb_x$ sont donc un système modèle pour des expériences sur le transfert de spin, car leurs propriétés magnétiques peuvent être modulées. Depuis, l'analyse du renversement de l'aimantation a montré que ces alliages sont adaptés aux expériences de propagation d'une paroi. Les mesures de transport ont prouvé que les alliages de $Co_{1-x}Tb_x$ peuvent polariser un courant en spin. Ces résultats sont encourageants pour des futures expériences sur le transfert de spin.

Des premières expériences avec des nanofils ont été réalisées. Pourtant, la propagation d'une paroi unique dans des nanofils n'a pas encore pu être observée. Des expériences de microscopie Kerr avec un microscope équipé d'un aimant suffisamment puissant sont en cours. Cette observation de paroi se déplaçant sous champ magnétique sera la prochaine étape et mènera aux expériences de propagation sous un courant polarisé dans le système $Co_{1-x}Tb_x$.

Finalement, il a été montré en collaboration avec le groupe de M. Aeschlimann à Kaiserslautern qu'il est possible de renverser l'aimantation de certains alliages de CoTb de façon réversible en utilisant un faisceau laser à polarisation circulaire (*all optical switching*). Ceci ouvre une nouvelle perspective pour ces matériaux. La gamme de compositions de $Co_{1-x}Tb_x$ permettant l'observation d'un effet purement optique amène à la supposition que le point de compensation du système ferrimagnétique joue un rôle important pour ce mécanisme toujours incompris. Des expériences qui combinent des mesures de transport avec le processus du *all optical switching* sont en cours. Ceci pourrait conduire à des nouvelles applications intéressantes qui utiliseraient la possibilité de manipuler l'aimantation grâce à la lumière polarisée.

Les super-réseaux $[Co/Ni]$ épitaxiés

L'élaboration des super-réseaux $[Co/Ni]$ par épitaxie par jets moléculaires sur des substrats de saphir orientés dans la direction $[11\bar{2}0]$ est bien comprise. Des oscillations de RHEED pendant la croissance des couches de Co et de Ni prouvent que la croissance est bidimensionnelle, c.à d. couche par couche. Ces oscillations permettent de contrôler les épaisseurs déposées avec une précision de l'ordre du dixième de monocouche atomique. La structure fcc supposée du super-réseau a pu être confirmée par des techniques d'électro-holographie. Les paramètres de maille ont été obtenus par diffraction X et confirmés par l'application de la théorie élastique. Ces connaissances très détaillées de la structure permettent de simuler des propriétés magnétiques et électriques du matériau en utilisant des modèles standard et de les comparer aux résultats expérimentaux.

Les propriétés magnétiques ont été analysées par plusieurs méthodes. Des mesures macroscopiques utilisant des méthodes de magnétométrie ont confirmé que l'AMP et l'aimantation des super-réseaux $[Co/Ni]$ peut être facilement modifiée en faisant varier l'épaisseur de Co dans une large gamme de valeurs. Un modèle phénoménologique simple, explique l'anisotropie du système comme une somme de contributions d'anisotropies venant des interfaces Co/Ni et du volume ainsi que de l'anisotropie de forme. Une compréhension plus détaillée de l'AMP a pu être obtenue par des expériences utilisant le dichroïsme magnétique circulaire (XMCD), qui apporte des résultats sur le magnétisme à l'échelle atomique. Une augmentation de la contribution orbitale a pu être observée aux interfaces Co/Ni . Les propriétés dynamiques ont été analysées par des mesures de résonance ferromagnétique. Nous avons confirmé le faible paramètre d'amortissement intrinsèque α d'environ 0.01, ce qui est nécessaire pour une forte efficacité du transfert de spin.

Dans une étape suivante nous avons montré qu'il est possible d'élaborer des vannes de spin complètement épitaxiées basées sur les super-réseaux de $[Co/Ni]$ en utilisant des espaceurs non-magnétiques d'Au. Les deux couches magnétiques ont pu être découplées, ce qui permettait d'avoir une couche dure et une couche douce. En outre, nous avons vérifié en faisant des mesures de photoémission résolue en spin, que les super-réseaux $[Co/Ni]$ pouvaient permettre d'injecter un courant polarisé en spin dans l'espaceur d'Au. Une polarisation en spin de 68% pour les électrons proches du niveau de Fermi a été obtenue, pour des empilements finissant avec une couche de Co. En plus, nous avons pu montrer que cette polarisation est maintenue si la dernière couche de Co est recouverte d'or. Des mesures de transport avec un courant parallèle à la surface de l'échantillon ont été effectuées. Un effet de GMR de 1.5% à température ambiante et qui augmente jusqu'à 3.5% pour une température de 30 K a été obtenu.

Dans la suite, il faudra structurer ces vannes de spin en forme de nanopilier pour les expériences de transfert de spin.

Par ailleurs, des nanofils basés sur les super-réseaux de $[Co/Ni]$ ont été fabriqués. La propagation de parois uniques a pu être démontrée dans ces fils. Des échantillons permettant l'injection de courant dans ces nanofils sont en cours de réalisation.

Conclusion

Le but de cette thèse était d'étudier l'aptitude de deux systèmes magnétiques à former des systèmes modèles pour l'étude des effets de transfert de spin. Ces deux systèmes sont des super-réseaux de $[Co/Ni]$ élaborés par épitaxie par jets moléculaires et les alliages de $Co_{1-x}Tb_x$. Ces deux matériaux possèdent une AMP variable dans une large gamme de valeurs. L'origine de cette anisotropie a été bien comprise pour les super-réseaux de $[Co/Ni]$. Le travail effectué sur le processus de renversement de l'aimantation dans les deux systèmes a montré qu'ils sont de bons candidats pour des expériences sur la propagation de parois dans des nanofils, car le renversement des couches se fait par propagation d'un petit nombre de parois nucléées. Une grande efficacité de transfert de spin est favorisée par un faible paramètre d'amortissement de Gilbert α et une forte capacité des matériaux de polariser un courant en spin. Les super-réseaux de $[Co/Ni]$ satisfont ces deux conditions. Le paramètre d'amortissement de Gilbert α intrinsèque est de l'ordre de 0.01. La forte capacité de polariser des courants en spin a été prouvée par la photoémission résolue en spin et l'existence d'un effet de GMR important. Pour les alliages $Co_{1-x}Tb_x$, un petit effet de GMR a été mesuré prouvant que des courants électriques peuvent être polarisés en spin par ce matériau. Le paramètre d'amortissement de Gilbert α n'a pas été mesuré. Dans la littérature, des valeurs importantes ($\alpha > 0.1$) sont rapportées surtout autour du point de compensation du moment cinétique pour des alliages terre-rare métal de transition [29]. En revanche, l'annihilation du moment cinétique devrait augmenter l'efficacité du transfert de spin. Pour l'instant, nous ne pouvons pas estimer l'efficacité du transfert de spin pour ce matériau. Cependant, des résultats encourageants pour la propagation d'une paroi sous courant dans le matériau similaire CoTbFe viennent d'être publiés [30].

Outre des expériences sur le transfert de spin, d'autres applications pour ces deux matériaux devraient être considérées. Pour les alliages de $Co_{1-x}Tb_x$, il s'agit du domaine de la manipulation réversible de l'aimantation, en utilisant un faisceau laser à polarisation circulaire (*all-optical switching*) comme décrit dans le manuscrit. Pour les super-réseaux de $[Co/Ni]$ un travail sur la modification de l'anisotropie en utilisant des champs électriques [31] a été commencé, car ils possèdent une anisotropie bien contrôlable.

Chapitre 1

L'état de l'art

Dans ce chapitre nous donnons une vue d'ensemble sur les interactions fondamentales liées au magnétisme. Nous présentons les modèles de base expliquant les effets de transfert de spin qui conduise au renversement d'une aimantation dans un nanopilier ou à la propagation d'une paroi dans un nanofil.

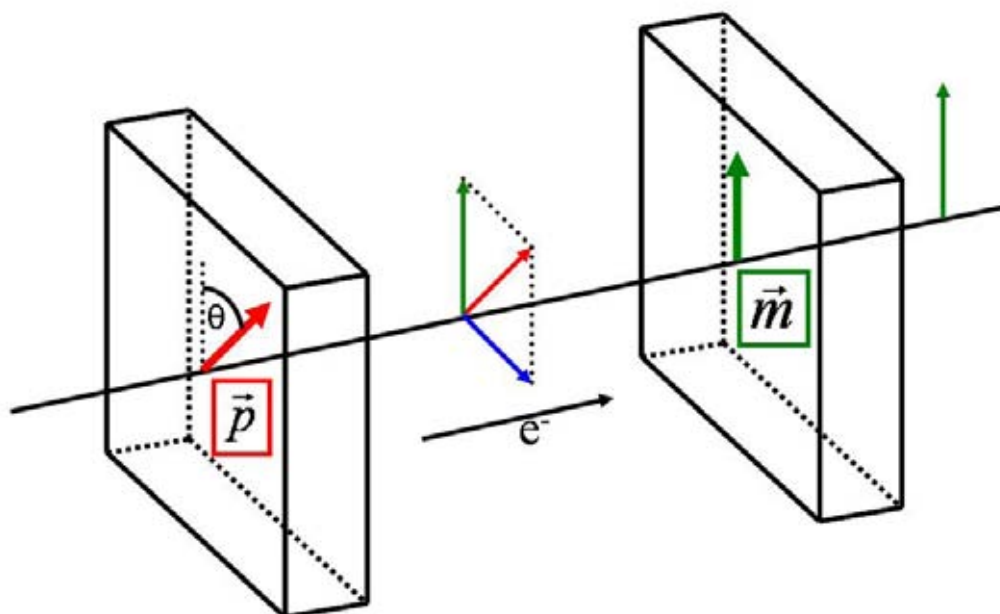


Fig. 1.1: Modèle de base pour le transfert de spin dans une structure vanne de spin : Le courant électrique est polarisé en spin quand il traverse une couche magnétique. Si la polarisation du courant et l'aimantation d'une couche traversée ne sont pas alignées, le courant peut appliquer un couple sur l'aimantation de cette couche : Le couple de transfert de spin.

Chapter 1

Basics of magnetism and spin transfer torque

This chapter has two goals: The first is one to give an overview about the basics of magnetism and to define the parameters used in the following chapters. Furthermore basic models of spin transfer torque related phenomena will be given. The second point is to give an overview on materials that were used for spin torque experiments in the past and to show the necessity of new materials, that can be used as model systems.

1.1 Magnetic moment and magnetic interactions

The following section gives a short overview about the origins of magnetic moments and magnetic interactions. More details and explications on this subject can be found in common text books about solid states physics and in other cited literature.

1.1.1 Magnetic moment

According to Bohr's atomic model, electrons circle on fixed orbits around the atomic nucleus. The electron rotates with a period $T = 2\pi r/v$ determined by the radius r of the circle and the electron velocity v . This corresponds to a current $I = -e/T = -ev/2\pi r$. Furthermore it is possible to introduce the angular momentum $\vec{l} = \vec{r} \times m_e \vec{v}$ (m_e is the electron mass, and e the elementary charge). Thus the magnetic momentum of this system is given by:

$$\vec{m}_l = I \cdot A \cdot \vec{n} = -\frac{e}{2} \vec{r} \times \vec{v} = -\frac{e}{2m_e} \vec{l} = \gamma \vec{l} \quad (1.1)$$

where \vec{n} is a normalized vector perpendicular to the surface $A = \pi r^2$ of the circle. $\gamma = -\frac{e}{2m_e}$ is called the gyromagnetic ratio.

In quantum mechanics, the angular momentum is described by a vector operator $\vec{\hat{l}}$. However only the eigenvalues of \hat{l}^2 and \hat{l}_z , with z the quantization axis, can be determined. The eigenvalues of \hat{l}^2 are $l(l+1)\hbar^2$ with $l < n$, l integer, where n represents the energy level of the electron. Those of \hat{l}_z are $m_z\hbar$ with $|m_z|$ and m_z integer. Consequently the magnetic momentum relying on the angular momentum of an electron is a vector operator, too, and it is given by:

$$\vec{m}_l = -g_l \frac{\hbar e}{2m_e} \vec{l} = -g_l \gamma \vec{l} = \gamma \vec{l} \quad (1.2)$$

with g_l , called the Landé factor, which equals to one in the case of an orbital momentum. Furthermore an intrinsic angular momentum for the electron must be introduced, the spin, as shown by experiments like the experiment of Stern and Gerlach. Its quantization rule says, that the projection of the spin on the z-axis can only take the values $\pm \frac{1}{2} \hbar$. The magnetic momentum induced by a spin is

$$\vec{m}_s = g_s \gamma \vec{s} \quad (1.3)$$

but in this case the Landé factor is $g_s = 2,002$. The fact, that $g - 2 \neq 0$, can be explained by quantum electrodynamics [32]. Both, spin and orbital momentum can be responsible for the magnetic momentum of an atom. For more details see [33].

1.1.2 Itinerant vs localized magnetism

Only atoms with partially filled orbitals may have a net moment since spin and orbital moments cancel in filled electron shells. Most atoms carry a magnetic moment when they are isolated. However in a solid the formation of interatomic bonds leads to compensation of the magnetic momenta in most cases. There are mainly two types of materials with nonvanishing magnetic moments: the transition metals (TM) and the rare earth elements (RE). In the following we are going to explain the origin of their magnetism.

1.1.2.1 Transition metals (TM)- model of itinerant magnetism

In TM systems the orbital moment usually vanishes due to the strong interaction of the 3d electrons with the magnetocrystalline field (1.1.3). This effect is called quenching [34]. Consequently the magnetization of these metals must be due to a disequilibrium of spin-up and spin-down populations. This disequilibrium was explained by Stoner's model based on the Pauli principle [35]. This principle prohibits the existence of two electrons in the same state. This implies for conducting electrons of a solid, that the wave functions of two electrons with the same spin have in average less overlap, than the wave functions of two electrons with opposite spin. Therefore the average Coulomb repulsion of two electrons with the same spin is smaller, than in the case of antiparallel spins.

Stoner introduces the potential energy I to describe the difference of repulsion between the parallel and the antiparallel spin state. We consider parabolic dispersion relations for the conduction electrons. In order to have a magnetic polarization, we assume that the up-spin population is increased by $\Delta N = n(\epsilon_F)(\delta\epsilon)^2$. $n(\epsilon_F)$ represents the density of states at the Fermi level, $\delta\epsilon$ the energy increase for these electrons compared to the Fermi level in a fictive nonmagnetic state. This imbalance between the two spin populations leads to an increase of the kinetic energy ΔE_C given by:

$$\Delta E_C = n(\epsilon_F)(\delta\epsilon)^2 \quad (1.4)$$

On the other hand the potential energy of the system due to the Coulomb interaction

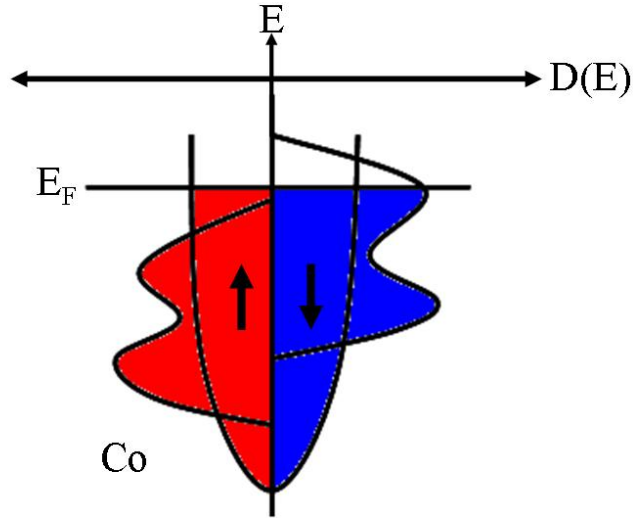


Figure 1.1: Schematic representation of the band structure of a magnetic 3d metal.

is lowered by ΔE_P , as there are more electrons with the same spin, compared to a nonmagnetic state:

$$\Delta E_P = I \left[\frac{n}{2} + n(\epsilon_F)\delta\epsilon \right] \left[\frac{n}{2} - n(\epsilon_F)\delta\epsilon \right] - I \left[\frac{n}{2} \right]^2 = -In^2(\epsilon_F)(\delta\epsilon)^2 \quad (1.5)$$

Consequently the total variation of the energy ΔE depends strongly on the electron density around the Fermi level.

$$\Delta E = n(\epsilon_F)(\delta\epsilon)^2[1 - In(\epsilon_F)] \quad (1.6)$$

This leads to the so-called Stoner criterion for ferromagnetism. A metal is magnetic if:

$$I \cdot n(\epsilon_F) > 1 \quad (1.7)$$

Thus, a high density of states around the Fermi level favors ferromagnetism.

1.1.2.2 Magnetism of rare earth elements(RE) - model of localized electrons

The magnetism of rare earth elements is due to their 4f electrons. These electrons are localized close to the atomic nucleus and do not participate in interatomic bonds. The total magnetic momentum of a rare earth atom is given by the sum of the moments of all 4f electrons of the atom. More precisely the total moment is the sum of all spin moments s plus all orbital moments l . The total moment of a RE atom can be calculated with the so-called Hund's rules:

1. Full electron shells do not contribute to the total angular moment J of the atom.

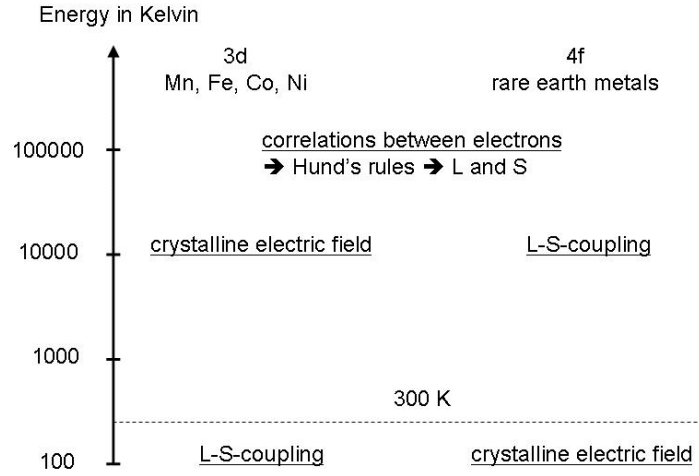


Figure 1.2: Order of magnitude of the different magnetic interactions [34]

2. The electrons occupy the free 4f orbitals in such a manner, that the sum of their spins S is maximum.
3. With respect to the first rule, the electrons occupy the orbitals in such a manner, that the sum of their orbital z-momenta L is maximum.
4. If the electron shell is less than half-filled, the total angular momentum is given by $J = |L - S|$, if the electron shell is more than half-filled, the total angular momentum is given by $J = |L + S|$

The remaining problem is to find the magnetic moment corresponding to J , i.e. the Landé factor (see also [33]). For pure spin moments it is approximately 2, for pure orbital moments it is equal to 1. Hence we require that:

$$g_j \vec{j} = \vec{l} + 2\vec{s} \quad (1.8)$$

This leads to g_j as a function of the eigenvalues of j^2 , l^2 and s^2 :

$$g_j = 1 + \frac{j(j+1) + s(s+1) - l(l+1)}{2j(j+1)} \quad (1.9)$$

Let's take the example of Terbium. The Tb^{3+} ion has the configuration $[Xe]4f^8$. Following Hund's first rule the angular momentum is due to the 4f electrons as it is the only nonfilled electron shell. Maximizing S as requested by the second rule leads to seven up electrons placed in the seven 4f orbitals. To place the eighth electron we follow Hund's third rule requesting $l=3$ for this electron in order to maximize L . With eight electrons the 4f shell is more than half-filled. Consequently we have $J = L + S = 3 + 3 = 6$. Another example would be the Gadolinium ion. Gd^{3+} has the configuration $[Xe]4f^7$. Hund's second rule claims to maximize S , leading to $L = 0$. The total angular momentum of Gd^{3+} is a pure spin moment. We find $J = S = \frac{7}{2}$.

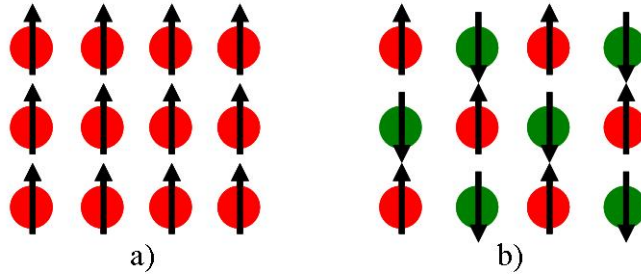


Figure 1.3: a) ferromagnetic order for $J > 0$ and antiferromagnetic order for $J < 0$

1.1.3 Magnetic interactions

Many effects in magnetism can be explained as the competition between the different magnetic configurations. In the following section we discuss the basic magnetic interactions.

1.1.3.1 Zeeman energy

The interaction between an external magnetic field \vec{H}_{ext} and a magnetic moment is described the so-called Zeeman energy E_Z given by:

$$E_Z = -\mu_0 \vec{m} \cdot \vec{H}_{ext} \quad (1.10)$$

For a sample with local magnetization $\vec{M}(r)$ we find:

$$E_Z = -\mu_0 \sum_i \vec{m}_i \vec{H}_{ext} = \mu_0 \int_V \vec{M}(\vec{r} \cdot \vec{H}_{ext}) dV \quad (1.11)$$

Consequently the Zeeman energy is minimum, when the magnetization is parallel to the applied field.

1.1.3.2 Exchange interaction

Magnetic order is due to the exchange interaction between spins. The origin of this interaction is due to the Coulomb interaction and the Pauli principle, which prohibits the existence of two electrons in the same state. The exchange interaction depends on the exchange constant J and the orientation of the spins \vec{S}_i . An important parameter which determines J is the distance between the two spins S_i and S_j at the positions \vec{r}_i and \vec{r}_j . We express then express the exchange energy between two moments as:

$$E_{ex} = -J(\vec{r}_i - \vec{r}_j) \vec{S}_i \cdot \vec{S}_j \quad (1.12)$$

The sign of J influences the different magnetic configurations: if $J > 0$ the minimum energy is obtained for a parallel arrangement of the two moments, $J < 0$ leads to an antiparallel arrangement of the two moments. In a solid the exchange interaction is a short-range interaction, basically limited to first neighbor moments. It will lead to a magnetic order like ferromagnetic order or antiferromagnetic order (see fig.(1.3)).

At finite temperature T magnetic moments are excited by an average energy of $k_B T$ with k_B the Boltzman constant. This excitation competes with the ordering due to the exchange interaction. At a certain critical temperature the magnetic long-range order is lost. For ferromagnetic order this critical temperature is called Curie temperature T_C , for antiferromagnetic order it is called Néel temperature T_N . For RE metals we find ordering temperatures smaller than 19 K for Nd and up to room temperature for Gd [36]. For transition metals the exchange interaction is stronger and consequently T_C is higher. We find $T_C = 1043$ K for Fe and $T_C = 1388$ K for Co.

1.1.3.3 Dipolar energy and shape anisotropy

The magnetic moments of a sample create a magnetic field, the dipolar field. Inside the sample this field points in the opposite direction of the magnetization \vec{M} and is therefore called demagnetizing field \vec{H}_d . The interaction of the magnetic moments with this demagnetizing field \vec{H}_d leads to the demagnetizing energy given by:

$$E_d = -\frac{1}{2}\mu_0 \int_V \vec{M}(\vec{r}) \cdot \vec{H}_d(\vec{r}) dV \quad (1.13)$$

The demagnetizing energy is always bigger or equal to zero. Consequently E_d orients the magnetic moments to directions, where $|\vec{H}_d|$ is minimum.

In general the calculation of the demagnetizing field \vec{H}_d is very difficult and can only be found by numerical methods. For uniform magnetizations, the relation between \vec{M} and \vec{H}_d is given by the so-called demagnetizing tensor $[N]$, which depends only on the shape of the sample:

$$\vec{H}_d = -[N]\vec{M} \quad (1.14)$$

The negative sign indicates that \vec{H}_d and \vec{M} are antiparallel. The determination of $[N]$ is in most cases not possible by analytical methods. Many sample shapes can be approximated by an ellipsoid of revolution (two axes a and c). In a coordinate system with axes parallel to the axes of the ellipsoid, the diagonal elements of N follow the relation

$$N_{xx} + N_{yy} + N_{zz} = 1 \quad (1.15)$$

The nondiagonal elements are zero. Consequently for a sphere ($a = c$) we get:

$$N_{xx} = N_{yy} = N_{zz} = \frac{1}{3} \quad (1.16)$$

If $a \neq c$ the calculation becomes more difficult. We define r as the ratio $r = c/a$. For $r > 1$ we find

$$N_{zz} = \frac{1}{r^2 - 1} \left[\frac{r}{\sqrt{r^2 - 1}} \operatorname{argcosh}(r) - 1 \right] \quad (1.17)$$

and for $r < 1$ it is

$$N_{zz} = \frac{1}{1 - r^2} \left[\frac{r}{\sqrt{r^2 - 1}} \operatorname{argcos}(r) \right] \quad (1.18)$$

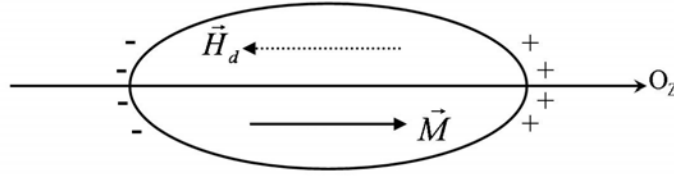


Figure 1.4: Ellipsoid uniformly magnetized along its z-axis. \vec{H}_d is the demagnetization field due to the existence of magnetic poles at the surface of the ellipsoid.

For $r > 1$ the preferential orientation of the magnetization is parallel to the z-axis. For $r < 1$ an orientation perpendicular to the z-axis minimizes the demagnetizing energy. Thin layers can be considered as an ellipsoid of revolution with r tending towards zero. In this case we find $N_{zz} = 1$ and $N_{xx} = N_{yy} = 0$. Therefore the interaction of the moments in a thin film with their demagnetizing fields favors an in-plane orientation of the moments. This can be expressed by:

$$E_d = -\frac{1}{2}\mu_0 M^2 \sin^2(\theta) V \quad (1.19)$$

where θ represents the angle between the sample surface and the magnetization and V the sample volume.

1.1.3.4 Magnetocrystalline anisotropy (MCA)

The magnetocrystalline anisotropy (MCA) refers to the dependence of the internal energy of a ferromagnetic material on the orientation of its magnetization relative to specific axes of the material. The MCA is related to the crystalline symmetry of a sample. Axes along which the magnetization is preferentially oriented are called easy axes. When the magnetization is preferentially orientated perpendicular to an axis, then this axis is called a hard axis.

In the case of a uniaxial crystal with volume V the MCA can be described phenomenologically by the following development:

$$\frac{E_{MCA}}{V} = K_1 \sin^2(\theta) + K_2 \sin^4(\theta) + \dots \quad (1.20)$$

The K_i represent the anisotropy constants and θ the angle between the magnetization and the axis of the crystal. For $K > 0$ we have an easy axis, for $K < 0$ the axis is a hard axis, magnetization has preferentially an orientation perpendicular to this axis.

As a second example, we treat the case of a cubic crystal symmetry. the cosines of the angles between the magnetization and the axes of the crystal are denominated by α_1 , α_2 and α_3 . The density of the anisotropy energy can be written as:

$$\frac{E_{MCA}}{V} = K_1(\alpha_2^2 \alpha_3^2 + \alpha_3^2 \alpha_1^2 + \alpha_1^2 \alpha_2^2) + K_2 \alpha_1^2 \alpha_2^2 \alpha_3^2 + \dots \quad (1.21)$$

The K_i represent the anisotropy constants. In fig(1.5) we show the example of a simple case when $K_2 = 0$ and K_1 is positive or negative. In the case of hexagonal symmetry the MCA is expressed by the angles θ and ϕ (see fig.(1.6)). For a volume V we can write:

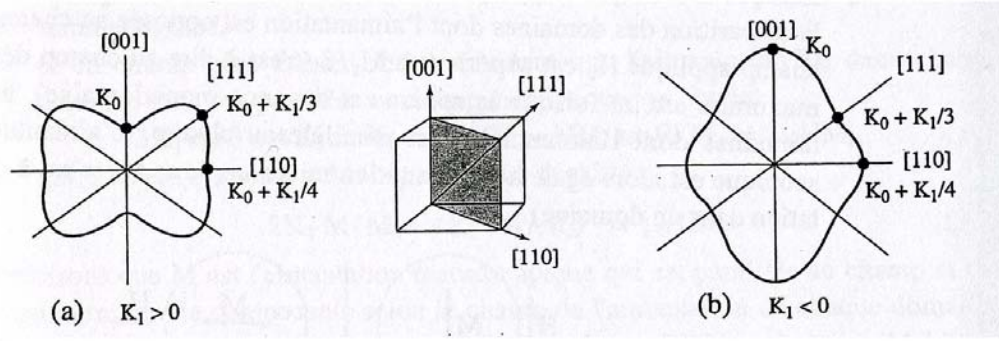


Figure 1.5: Cubic crystal: The energy is represented as a function of the magnetization direction in the plane (perpendicular to an axis with binary symmetry). This plane contains the three mayor symmetry axis. As the anisotropy is defined except to a constant term. K_0 is added to the anisotropy in order to facilitate the graphic presentation. [34]

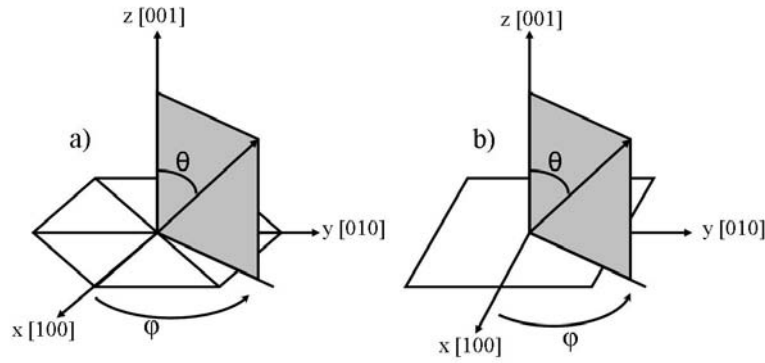


Figure 1.6: Definition of the angles θ and ϕ , for quadratic (a) and hexagonal (b) symmetry. [34]

$$\frac{E_{MCA}}{V} = K_1 \sin^2(\theta) + K_2 \sin^4(\theta) + K_3 \sin^6(\theta) + K_4 \sin^6(\theta) \cos(6\phi) \quad (1.22)$$

1.1.4 MCA of rare earth elements and MCA of transition metals

The MCA originates from the interaction of the orbital magnetic moment with the crystal lattice. The atoms forming the crystal exert electric fields on each other, called the crystalline electric field. this causes the loss of degeneration of the orbitals with the same angular momentum quantum number l , but different magnetic quantum number l_z . This is a so-called Stark effect. The spin contribution to the magnetic momentum is coupled to the orbital momentum via the L-S coupling and hence it is indirectly coupled to the lattice, too (see fig.(1.7)).

In bulk 3d metals like Co, Ni and Fe, the microscopic picture of the magnetocrystalline anisotropy is the following (see for example [37] or [38]): The atomic magnetic

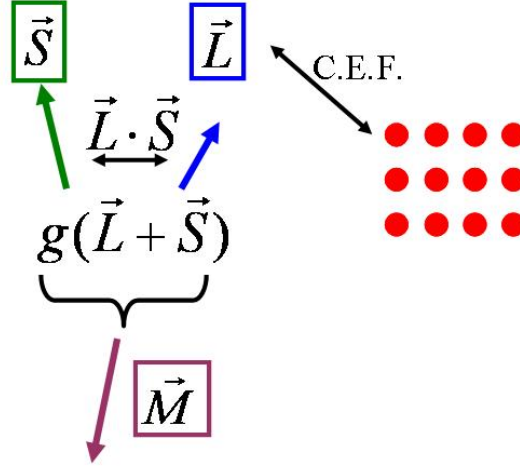


Figure 1.7: Sketch showing the interactions leading to magnetocrystalline anisotropy: crystalline electric field (C.E.F.) between lattice and orbital moment, and spin-orbit coupling between spin and orbital moment, the magnetic moment is the sum of a contribution from the orbital moment and from the spin moment

moment due the 3d bands has two sources, the orbital (m_{orb}) and the spin moment (m_{spin}). Both are coupled via the spin-orbit coupling. The orbital moment is coupled to the crystalline lattice via the crystalline electrical field (C.E.F.). Hence, the total moment consisting of spin and orbital contribution is coupled to the crystalline lattice. However, in general the strong lattice-orbit coupling leads to a vanishing orbital contribution to the magnetic moment of the electron called quenching. Consequently the relative orbital contribution m_{orb}/m_{spin} is found to be small (see for example results presented in [39]). The magnetization is mainly due to the spin. As the orbital moment vanishes, the indirect coupling of the spins to the lattice via the spin-orbit coupling also vanishes. Therefore transition metals have generally small magnetocrystalline anisotropies except hcp Co.

For rare earth elements the crystalline electric field is small compared to the transition metals (see fig.(1.2)). However, the spin-orbit coupling is in general strong. For materials containing elements like Tb with an important orbital moment we hence have strong anisotropies compared to 3d elements, when temperature is far below Curie temperature.

1.1.5 Anisotropy of thin films

In this work we are studying magnetic thin films and patterned thin films. The shape anisotropy tends to align the magnetic moments parallel to the plane. We have:

$$K_{shape} = -\frac{1}{2}\mu_0 M_S^2 \quad (1.23)$$

for a thin film with saturation magnetization M_S . The minus indicates, that this anisotropy favors an in-plane (IP) orientation of the magnetic moments. If we want to have an effective perpendicular magnetic anisotropy (PMA) one has to overcome this shape anisotropy. Further sources of anisotropy must exist, favoring an out-of-plane

(OOP) orientation and must be more important than the shape anisotropy. Such sources of anisotropy can be due to crystalline symmetry (K_u) and interfaces (K_S).

The idea of an interface contribution to magnetocrystalline anisotropy goes back to L. Néel [40]. For thin film multilayers, with thicknesses of the order of atomic monolayers, the special crystalline symmetry leading to the quenching effect is broken by the interfaces. Thus, one can expect an increase of the orbital momentum at the interface leading to a strong anisotropy. The symmetry breaking due to the interfaces distinguishes the direction perpendicular to the interface from all other directions. A possible consequence is, that the axis perpendicular to the interface becomes an easy axis of magnetization. This was observed for interfaces of magnetic layers with nonmagnetic layers (e.g. $[Co/Pd]$ multilayers [41]), as well as for interfaces of magnetic layers (e.g. $[Co/Ni]$ multilayers [26]). For a thin magnetic layer we have two interfaces (1) and (2) with the corresponding phenomenological interface anisotropies K_S^1 and K_S^2 . The interface contribution to the anisotropy energy for a layer of a thickness t can be expressed as:

$$\frac{E_{MCA,int}}{V} = \frac{K_S^1 + K_S^2}{t} \sin^2(\theta) \quad (1.24)$$

Taking into account these interface contributions, the bulk anisotropy K_u and the shape anisotropy, we can define an effective anisotropy K_{eff} :

$$K_{eff} = K_u + \frac{K_S^1 + K_S^2}{t} - \frac{1}{2} \mu_0 M_S^2 \quad (1.25)$$

The magnetic moments are perpendicular to the surface when $K_{eff} > 0$.

1.1.6 Magnetic domains and domain walls (DW)

Stable magnetic configurations correspond to a minimum of the total magnetic energy. The total magnetic energy is the sum of all four energy contributions mentioned above. For bulk material we observe the following competitions: The exchange interaction E_{ex} favors a uniform sample magnetization, whereas the dipolar interaction E_{dip} prefers an orientation of the moments, which minimizes the demagnetizing field. The Zeemann energy E_Z favors an alignment of the moments with the magnetic field, whereas the MCA E_{MCA} favors an alignment with special crystalline axes. In this section we are discussing the competition between E_{ex} and E_{dip} , which is the origin of the formation of magnetic domains. E_{ex} is a short-range interaction limited to few interatomic distances. E_{dip} is a long range interaction. The typical length scale where we pass from a regime governed by E_{ex} to a regime governed by E_{dip} is the so-called exchange length l_{ex} given by:

$$l_{ex} = \sqrt{\frac{A}{\mu_0 M_S^2}} \quad (1.26)$$

depending on the exchange constant A and the saturation magnetization M_S [34]. For samples with dimensions larger than l_{ex} it becomes energetically favorable to form domains compared to a magnetically uniform state. For a more realistic picture one has also to consider the energy contribution of the domain walls.

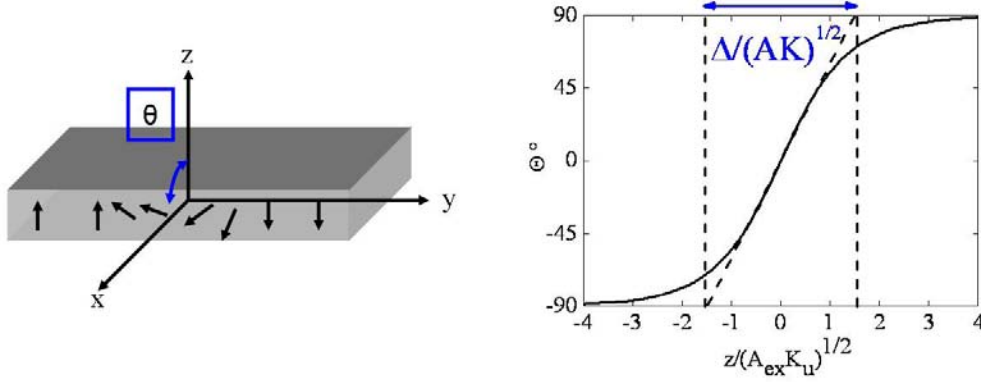


Figure 1.8: Bloch wall in a thin film with uniaxial perpendicular anisotropy K_u . The graph shows the rotation angle θ as a function of the normalized position z of the moment relative to the center of the domain wall. Δ corresponds to the usual definition of the domain wall width. (see [34])

Between two domains the orientation of the magnetization changes in a region called the domain wall (DW). Thickness and energy of this DW are determined by the competition between E_{ex} , E_{dip} and E_{MCA} . We are looking at the case of a thin film with uniaxial perpendicular anisotropy K_u and exchange constant A_{ex} . We suppose that the wall is a Bloch wall. θ represents the angle between the easy axis and the magnetic moments. We can then minimize the energy as a function of the domain wall configuration leading to:

$$\delta = \pi \sqrt{\frac{A_{ex}}{K_u}} \quad (1.27)$$

for the domain wall thickness δ , and

$$\gamma = 4\sqrt{A_{ex}K_u} \quad (1.28)$$

for the energy per DW surface σ . The definition of δ is the following: we take slope η of the angle θ as a function of the position z of the moment in the DW. Then, δ is defined as the distance between the two points of interception from the line with slope η with a line parallel to the z -axis at a distance of $\pm 90^\circ$ (see fig.(1.8)).

One can see, that the DW thickness can be tuned by varying the anisotropy K_u . This goes from a few atoms for highly anisotropic materials like $[Fe/Pt]$ -multilayers [42] to the order of $100nm$ for permalloy.

1.2 Magnetoresistance

Changing the magnetic configuration of a sample changes the electronic configuration of a sample, as the magnetization is directly linked to the spin and orbital momentum of the sample. Consequently one can expect the resistance of the sample to change. Such effects are called magnetoresistance. This section should give a brief overview of magnetoresistive effects, which were used in this PhD thesis, in order to analyze the

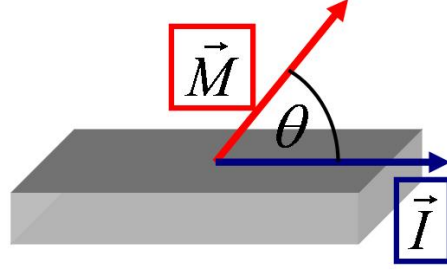


Figure 1.9: Current \vec{I} through a sample with magnetization \vec{M} . θ represents the angle between \vec{I} and \vec{M} .

magnetic configuration of a sample.

1.2.1 Anisotropic magnetoresistance (AMR)

One can see from experiments, that the resistivity ρ of magnetic materials depends on the angle between magnetization and the direction of the current (see fig(1.9)). This effect is called anisotropic magnetoresistance (AMR). The angular dependence of the resistance can be expressed by:

$$\rho(\theta) = \rho_{\parallel} + (\rho_{\perp} - \rho_{\parallel}) \cdot \sin^2(\theta) \quad (1.29)$$

with θ the angle between magnetization and current.

For further explications on AMR one should consider [43].

1.2.2 Giant magnetoresistance (GMR)

The effect of giant magnetoresistance was discovered in 1988 ([2] and [1]), and honored with the Nobel Prize in 2007. It can be observed in samples with nanometric length scales. These length scales are given, depending on the geometric configuration, by the electron mean free path or the spin diffusion length. A simple phenomenological approach is the following:

The resistivity of a magnetic layer differs for spins with a magnetic moment parallel to the magnetization r_{\uparrow} , from spins with a magnetic moment antiparallel to the magnetization r_{\downarrow} . In other words the resistivity is spin-dependent (see fig.(1.10)). Considering a configuration, where two magnetic layers are separated by a nonmagnetic conducting layer (a so-called spin valve), we discuss a parallel and an antiparallel orientation of the magnetic layers. Electrons with a spin parallel to the layer magnetization pass more easily through the trilayer(resistivity r_{\uparrow}), than spins, that are antiparallel to the magnetization (resistivity r_{\downarrow}). The total resistivity of this configuration is called r_P . In the case of antiparallel magnetic layers, the resistivity is the same for both spin directions. The total resistivity for the antiparallel configuration is called r_{AP} .

One can then define the GMR as:

$$GMR = \frac{r_{AP} - r_P}{r_P} = \frac{r_{\uparrow} - r_{\downarrow}}{4r_{\uparrow}r_{\downarrow}} \quad (1.30)$$

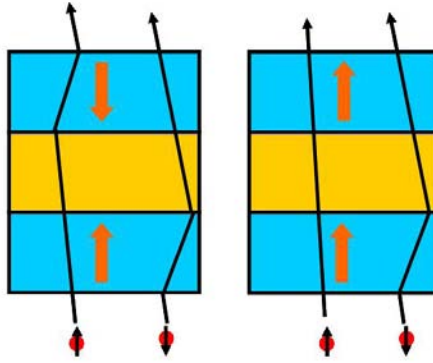


Figure 1.10: Scheme of the conduction mechanism in a ferromagnetic / nonmagnetic / ferromagnetic multilayer (spin valve). The antiparallel configuration of the magnetic layers is shown on the left, the parallel configuration is shown on the right hand side.

This description by a two current model, allows a phenomenological understanding of GMR. However more detailed understanding is necessary to describe GMR as a function of material parameters. The following model corresponds to a current perpendicular to the plane (CPP) configuration, where the injected current flows perpendicularly to the sample layers. It is explained in more detail in [44].

For CPP, one can make a quantitative analysis in terms of interface resistance $\rho_{\uparrow(\downarrow)} = 2[1 \mp \gamma]r_b^*$ and bulk resistivities $\rho_{\uparrow(\downarrow)} = 2[1 \mp \beta]r_F^*$. In addition we have to consider the resistivity of the nonmagnetic layer with $\rho_{\uparrow(\downarrow)} = 2\rho_N^*$. β describes the bulk contribution due to the asymmetry of spin-dependent scattering and γ the interface contribution. β is a material parameter, but can also contain contributions from scattering on impurities. γ is a parameter depending on the interface between the magnetic and nonmagnetic layer. The total spin depend scattering asymmetry is thus the sum of an interface and a bulk contribution. It is possible to chose materials for a spin valve where the spin dependent scattering asymmetry of the two layers is of opposite sign. In this case an inverse GMR can be observed. Inverse GMR means, that the resistance of the spin valve is higher for the parallel magnetic configuration, than for the antiparallel magnetic configuration (see also [44] and references in this paper).

GMR is also observed for a configuration where the current flows parallel to the layers of the spin valve, the so-called current in plane (CIP) GMR. The differences between the mechanisms of CIP GMR and CPP GMR are explained for example in [44].

1.2.3 Extraordinary Hall effect (EHE)

In materials with magnetic order, the Hall resistance is in general not a linear function of the applied field. We are going to discuss a sample configuration as presented in fig.(1.11). \vec{B} represents the magnetic flux through the sample due to applied fields and the sample magnetization. θ is the angle between magnetization \vec{M} and z-axis, ϕ is the angle between the magnetic flux \vec{B} and the z-axis.

We can than express the Hall resistivity ρ_{xy} as:

$$\rho_{xy} = R_0 \vec{B} \cdot \hat{e}_z + R_{EHE} \vec{M} \cdot \hat{e}_z = R_0 B \cos(\phi) + R_{EHE} M \cos(\theta) \quad (1.31)$$

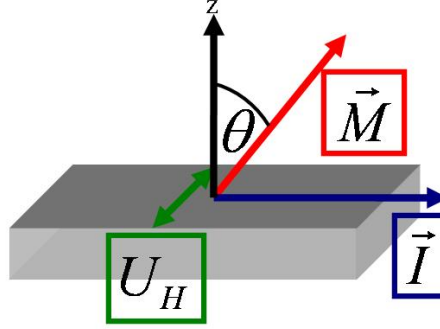


Figure 1.11: Geometric configuration for the measurement of the Hall voltage: θ is the angle between the magnetization \vec{M} and the z-axis.

where R_0 is the normal Hall coefficient and R_{EHE} is the extraordinary Hall coefficient. In most cases the EHE is much larger than the normal Hall effect. It arises from spin-dependent scattering of conduction electrons. Two contributions are discussed for R_{EHE} : skew scattering [45] and side-jump mechanisms [46]. The dependence of R_{EHE} on the electrical resistivity ρ can be expressed as:

$$R_{EHE} = a\rho + b\rho^2 \quad (1.32)$$

where a is attributed to the skew scattering and b to the side-jump mechanisms. The microscopic origin of EHE is still not completely understood. However it seems to be clear that a large spin-orbit coupling favors a strong EHE [47].

1.3 Magnetization reversal

Magnetization reversal is in general a very complex phenomenon as many different processes are of importance. These effects are continuous rotation of the magnetic moments, nucleation of domains and propagation of domain walls. Nucleation and propagation at finite temperature are thermally activated. Thus they have nondeterministic behavior and must be described by stochastic laws. In the following chapter we are going to start to explain reversal in a uniaxial macrospin model at zero temperature by Stoner and Wohlfarth [48]. We are then discussing nucleation and propagation processes in magnetic thin films. Furthermore we are concluding on material properties which allow to use a magnetic system as a simple model system for spin torque experiments.

1.3.1 Stoner Wohlfarth model

In this model we discuss magnetization reversal in a sample with a uniaxial anisotropy K_{eff} taking into account shape anisotropy and MCA. The Stoner Wohlfarth model is a macrospin model meaning, that the magnetic moments of the samples are always aligned in the same direction. Thus we can treat the problem as if we had one moment \vec{m} under an applied field \vec{H}_{app} . θ represents the angle between the magnetic moment and the axis z . ϕ represents the angle between the applied field and the z -axis. In this simple model the reversal is described by a competition between anisotropy energy E_A

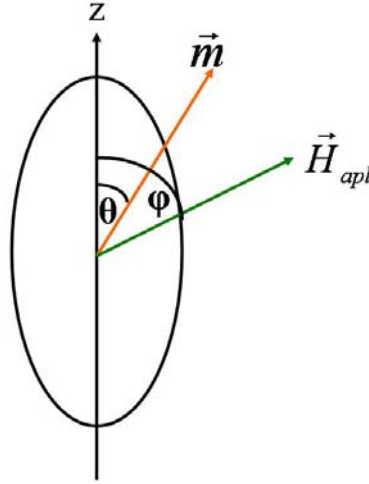


Figure 1.12: Ellipsoid with easy axis along the z-axis. θ represents the angle between the magnetic moment and the z-axis. ϕ represents the angle between the applied field and the z-axis.

and the Zeeman energy E_Z . We define:

$$H_K = \frac{2K_{eff}}{\mu_0 M_S} \quad (1.33)$$

In the case when the field is applied parallel to the easy z-axis, $\phi = 0$, the reversal happens instantaneously at a field given by:

$$\mu_0 H_C = \mu_0 H_K \quad (1.34)$$

which is in this case also equal to the coercive field and the saturation field. This switching is irreversible.

In the case when the field is applied perpendicularly to the easy z-axis, $\phi = 90^\circ$, the reversal happens by a continuous rotation of the field. The magnetization is saturated parallel to the field at an applied field H_S , given by:

$$\mu_0 H_S = \mu_0 H_K \quad (1.35)$$

One can see that for this model $H_S = H_C$. This model applies for samples that are too small to allow the nucleation and propagation of a domain-wall (e.g. [18]). For thin layers, with macroscopic surface the reversal is discussed in the following.

1.3.2 Magnetization reversal in thin films

In this section we are going to discuss the magnetization reversal in a thin film with PMA. The reversal happens in general in a nonuniform way. We are starting our discussion from a point, where the sample is saturated in a strong field. The field is then decreased until it reaches a strong value in the opposite direction. Two different modes of reversal can be imagined (see fig.(1.13)). One can imagine a sample, for which reversed domains can be nucleated at fields much lower than the fields necessary to move a DW. This case is called the propagation limited case. On the other hand, one

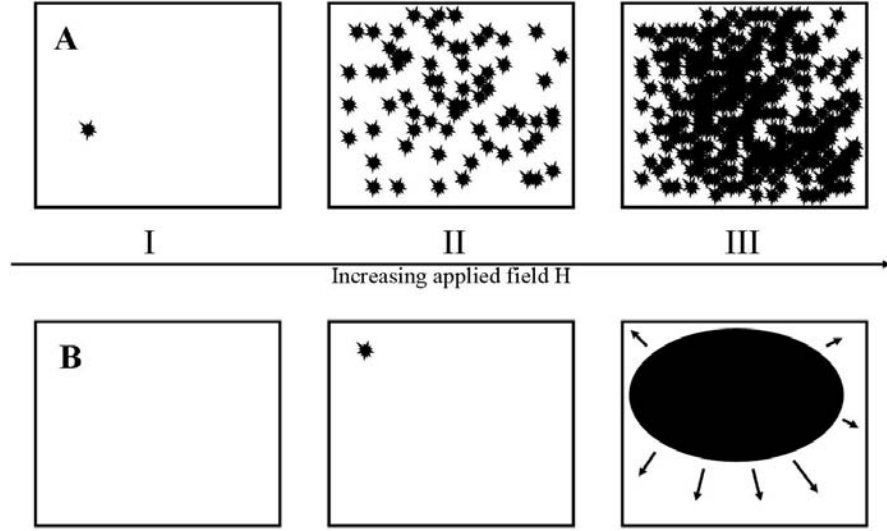


Figure 1.13: Schematic representation of the magnetization reversal process for two different types of samples A and B. The samples are saturated along their easy axis and a field is applied along the easy axis but antiparallel to the magnetization (I). This field is increased in the steps (II) and (III).

can also imagine a sample, where it is possible to move DWs at low fields, but where strong fields are needed to nucleate reversed domains. This is called the nucleation limited case. The observed behavior depends on the chosen material, as well as on parameters like film thickness, etc. For real samples the reversal behavior is usually a mixture of both phenomena.

1.3.2.1 Nucleation process

The nucleation of reversed domains is a thermally activated process. Nucleation happens most easily on structural defects and sample edges. As a simple model (following [49], who describes a Néel-Brown like process), we consider a sample with magnetization M_S at a temperature given by T . The energy barrier that must be overcome in order to nucleate a domain is E_n . The nucleation rate n due to thermal activation in an applied field $\mu_0 H$ is then given by [49]:

$$n = n_0 \exp - \left(\frac{E_n - 2\mu_0 M_S V_n H}{k_B T} \right) \quad (1.36)$$

This can be modified by introducing a nucleation field $H_n = E_n / 2\mu_0 M_S V_n$:

$$n = n_0 \exp \frac{2\mu_0 M_S V_n}{k_B T} (H - H_n) \quad (1.37)$$

Hence, the nucleation rate can be changed by:

- Sample quality: a very homogeneous sample has only few defects, leading to H_n close to H_K and low n_0 .

- Magnetization: a higher magnetization M_S leads to a higher Zeemann energy contribution, facilitating the nucleation process.
- Temperature: as the nucleation process is thermally activated, higher temperatures lead to higher nucleation rates.

A detailed description of the nucleation process in thin films with PMA considering more sophisticated models than the here described Néel-Brown picture can be found in [50].

1.3.2.2 Propagation process

Once a domain is nucleated it can grow by DW propagation. As for the nucleation process, thermal activation plays an important role for fields, which are smaller than the typical depinning fields for DWs in the sample. At low fields, a DW can be pinned by several defects along its length. Two competing energy contributions govern the shape of a DW: the pinning potentials of the defects, which favors a rough DW and the DW energy, which favors a short and thus a straight DW. Two characteristic length scales appear: The first one is ξ , the characteristic length scale between pinning defects, describing the roughness in a mechanical picture. The second one is the coherence length L_C , which corresponds to the length scale on which two pinning centers act as one. In other words, the DW can not be depinned independently from two pinning centers which are closer than L_C . At length scales L , with $L > L_C$ the wall can adjust itself elastically in order to reach the optimal local configuration [51]. In a mechanical picture this corresponds to the stiffness. [51] defines L_C as:

$$L_C = \left(\frac{\sigma^2 t^2 \xi}{f_{pin}^2 n_i^2} \right)^{1/3} \quad (1.38)$$

with f_{pin} the local pinning potential, t the sample thickness, σ the DW energy per surface and n_i the density of pinning defects. Consequently, not only the material parameters like anisotropy and magnetization are necessary to understand DW motion. Also the homogeneity plays an important role. In a very homogeneous sample we have nearly no intrinsic defects. The pinning will be only due to geometrical effects (see sec.(1.3.5.1)).

In a system with pinning sites for DWs in general three velocity regimes can be distinguished [53] if we consider the DW as a 1D object: First at low field a so-called creep regime, where the DW can only be moved by thermal excitations, at zero temperature the DW can not move. For very high fields we have the so-called flow regime, where we have a dissipative viscous flow motion with $v \propto H$. Between these two regimes we have the depinning regime. The transition between creep and depinning regime is smeared out at finite temperature. A graphical representation is given in fig.(1.15a). At high velocities DW can often not be considered any longer as 1D objects. The field at which the DW switches from 1D to a precessional regime is called the Walker field H_W . Above the Walker field the DW changes its structure during propagation. H_W depends in general on material parameters like magnetization, the Gilbert damping factor α , as well as on the geometrical configuration of the sample [54].

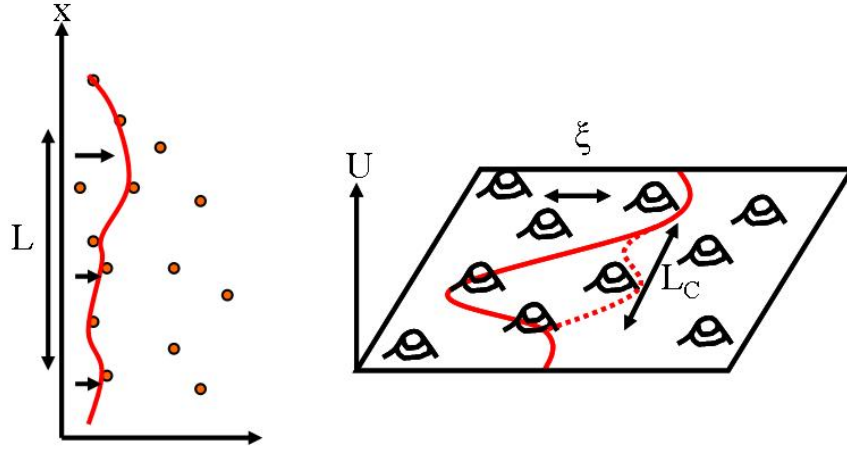


Figure 1.14: Scheme of a DW propagating in a rough energy landscape. ξ represents the characteristic distance between defects and L_C is the coherence length of the DW. (scheme taken from [52])

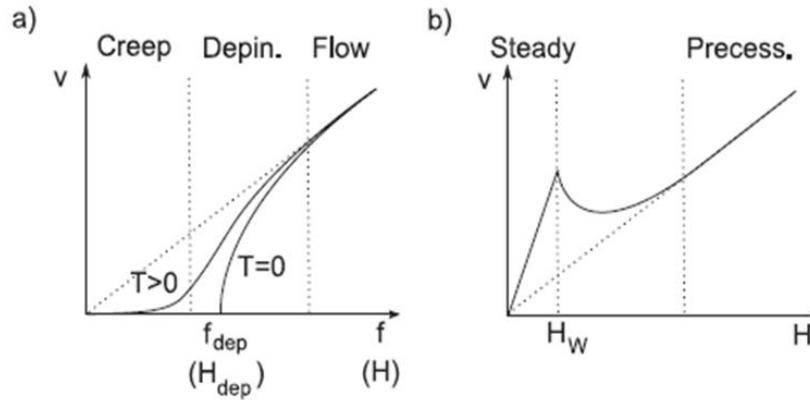


Figure 1.15: (a) Theoretical variation of the velocity, v , of a 1D interface (domain wall) in a 2D weakly disordered medium submitted to a driving force, f (magnetic field, H), at zero and finite temperature, T . The creep, depinning, and flow regimes are labeled. (b) Regimes of domain wall flow motion in an ideal ferromagnetic film without pinning. The steady and precessional linear flow regimes are separated by an intermediate regime which begins at the Walker field, H_W . from [53]

To conclude on DW motion in magnetic thin films: in small fields compared to the pinning fields H_{dep} the motion is strongly dependent on structural defects of the sample. This is the regime of the so-called DW creep (e.g. see [53]). Although for fields of the order of the pinning strength, the motion is still highly dependent on pinning sites. This regime is called the depinning regime and explained in detail for example by [49]. For fields much stronger than the typical pinning fields we observe the so-called flow regime. Here the velocity is linear with the field. The DW mobility, describing the proportionality of velocity and applied field is only determined by the material parameters DW width Δ , gyromagnetic ratio γ and the Gilbert damping factor α . In

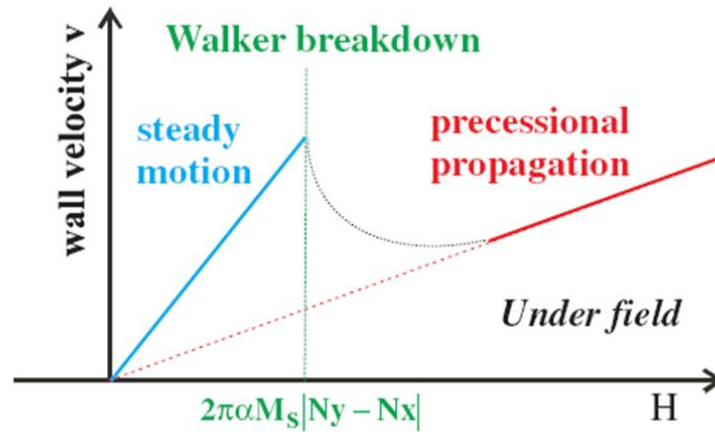


Figure 1.16: Sketch of a Bloch DW's velocity as a function of an external field. The dotted line in the transient nonlinear regime is a guide for the eyes. (taken from[55])

theory two linear regimes with different slopes are possible. One slope for $H < H_W$ and one for $H > H_W$. This is also explained in more detail for example by [53].

This section about the reversal process in magnetic thin films gives two important criteria for the choice of a good material in order to do experiments on current-induced DW motion. First of all for a good material in order to do propagation experiments must be close to the nucleation limited case in order to have propagation as the principal reversal mechanism. Second, to have a simple system with well-defined pinning sites, it is important to have a very homogeneous sample without intrinsic and statistically distributed defects.

1.3.3 Domain wall propagation in a nanowires under field

In this section we are going to discuss the propagation of a DW under field in a nanowire. Behaviors similar to the motion of DWs in thin films can be found.

1.3.4 Propagation of a DW in a nanowire without pinning sites

From micromagnetic simulations [55] equations describing the dynamics of a Bloch DW in an external field can be obtained. The used model neglects possible pinning sites of a real sample. In an experiment these equation would apply for the flow regime. As for thin films, two linear regimes can be distinguished, one for fields below the Walker breakdown field H_W by $v_{steady1}$, and one for fields $H > H_W$ by $v_{steady2}$. These two regimes are described by the two following equations [55]:

$$v_{steady1} = \frac{\gamma\Delta}{\alpha} H \quad (1.39)$$

$$v_{steady2} = \gamma\Delta \frac{\alpha}{1 + \alpha^2} H \quad (1.40)$$

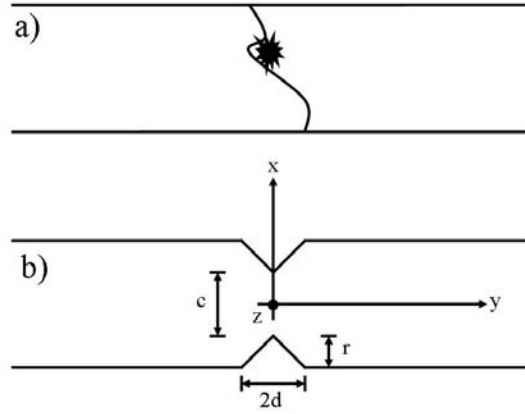


Figure 1.17: Pinning of a DW in a nanowire: a) pinning by an intrinsic defect of the wire, b) pinning by a geometrical pinning site. (taken from [52])

where Δ is the DW width, γ the gyromagnetic ratio and α the Gilbert damping factor. The result is graphically represented in fig.(1.16).

1.3.5 Propagation of a DW in a nanowire considering pinning sites

Pinning and depinning effects play an important role for the dynamics of a DW in a nanowire. In the following we are going to discuss pinning sites and then in a second part, the stochastic behavior of pinning and depinning events.

1.3.5.1 DW pinning sites in nanowires

Due to the geometrical confinement in a nanowire, we do not only have intrinsic pinning sites due to structural defects, but also geometrical pinning sites (see fig.(1.17)). The geometrical pinning is explained the following way: The total energy of a DW E_{DW} is given by:

$$E_{DW} = \sigma \cdot t \cdot l \quad (1.41)$$

where σ is the DW energy per surface, t the thickness of the magnetic layer and l the length of the DW. A DW can be pinned on a site where it is short. For real samples geometrical pinning comes for example from the roughness of the wire due to the lithography process, or it can be imposed by so-called notches (a constriction in the wire) or Hall crosses. The depinning from a geometrical pinning site under field is governed by a competition between the DW energy E_{DW} and the Zeeman energy E_Z .

$$E_{tot} = E_{DW} + E_Z \quad (1.42)$$

A small displacement of the DW leads to an increase of E_{DW} given by:

$$dE_{DW} = \sigma t \frac{\partial L}{\partial y} dy \quad (1.43)$$

But the Zeeman energy decreases E_Z :

$$dE_Z = -2\mu_0 M_S H t \frac{\partial S}{\partial y} dy \quad (1.44)$$

Considering a wire with magnetization M_S , thickness c at the center of the triangular constriction, r the depth of the constriction and $2d$ the length of the constriction one finds for the geometrical depinning field $H_{dep,geo}$:

$$\mu_0 H_{dep,geo} = \frac{\sigma}{2M_S(y + cd/(2r))} \quad (1.45)$$

Hence the pinning strength due to a geometric configuration can be tuned by varying the magnetic material parameters M_S and the DW energy per surface σ . In the case, where we have intrinsic pinning sites localized at a geometric pinning site, as it is often the case for real samples (see for example [56]), we find for the total pinning field:

$$H_{dep} = H_{dep,geo} + H_{dep,i} \quad (1.46)$$

Hence, the control of a geometric pinning sites, by tuning magnetic parameters is limited by the influence of intrinsic effects to pinning.

1.3.5.2 The depinning process in nanowires

As in the case of thin films, pinning and depinning is thermally activated in nanowires. The following can be found in more detail in [57]. The depinning probability per time unit p from a pinning site is given by:

$$p = \frac{1}{\tau} = f_0 \exp\left(-\frac{E(H)}{k_B T}\right) \quad (1.47)$$

where f_0 is the attempt frequency, τ the depinning time, and $E(H)$ is the energy barrier necessary to overcome for depinning as a function of the applied field H .

We can now calculate the probability $F(t)$, that the depinning time is less or equal to :

$$F(t) = 1 - \exp\left(-\frac{t}{\tau}\right) \quad (1.48)$$

This behavior corresponds to a Néel-Brown relaxation. However this is not forcefully the case for depinning. For large densities of pinning sites collective pinning and depinning phenomena must be expected. Consequently the depinning process can be better described by a Markov process (see fig.(1.18)). In the case of two alternative depinning processes the evolution of the system is represented by a vector $P(t)$ obeying the relation:

$$\frac{dP(t)}{dt} = \mathbf{M} \cdot P(t) \quad (1.49)$$

\mathbf{M} is a 3×3 matrix. Its matrix elements depend on the characteristic depinning times τ_{ij} , describing the relaxation time from a state i to a state j .

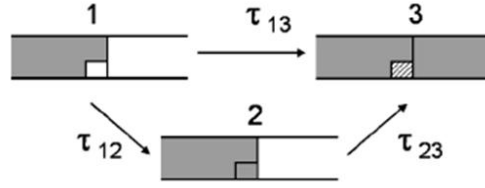


Figure 1.18: Scheme of the possible reversal states involved in the Markov process around the barrier. (taken from [57])

$$\mathbf{M} = \begin{bmatrix} -(\frac{1}{\tau_{13}} + \frac{1}{\tau_{12}}) & \frac{1}{\tau_{12}} & \frac{1}{\tau_{13}} \\ 0 & -\frac{1}{\tau_{23}} & -\frac{1}{\tau_{23}} \\ 0 & 0 & 0 \end{bmatrix}$$

1.3.6 Conclusion for the choice of a material as a model system

As seen in this section, the magnetization reversal process is highly influenced by structural defects. Nucleation and pinning of DWs happens essentially at such inhomogeneities. Stochastically distributed defects make the understanding of reversal processes as a function of magnetic material parameters like anisotropy and magnetization difficult. In order to have a good model system, a high homogeneity of the sample is necessary. This is specially true for DW propagation experiments in nanowires, with length of several tenth of μm . In nanopillars the homogeneity is less critical as the dimensions are of the order of $100 \times 100 nm^2$.

1.4 Magnetization reversal induced by a spin-polarized current

The effect of a spin-polarized current on a magnetic moment may be described as a torque. This is called spin transfer torque. It was predicted by L. Berger in 1984 [10] and shown in 1985 [14], that this effect can move a DW. Furthermore it was predicted again by L. Berger [4] and J. Slonczewski [5] in 1996 and shown by J. Katine in 2000 [12], that this effect can reverse the magnetization in a nanopillar.

In the following section we are first going to have a look at the equations describing the dynamics of a magnetic moment under field and spin-polarized current. Then we are discussing the spin torque effects for nanopillars and finally we discuss spin current induced DW motion in nanowires.

1.4.1 Dynamic of a magnetic moment: LLGS equation

The dynamics of a magnetic moment in a magnetic sample are influenced by several contributions, which can be expressed as field-like terms. These contributions are:

- an external applied field \vec{H}

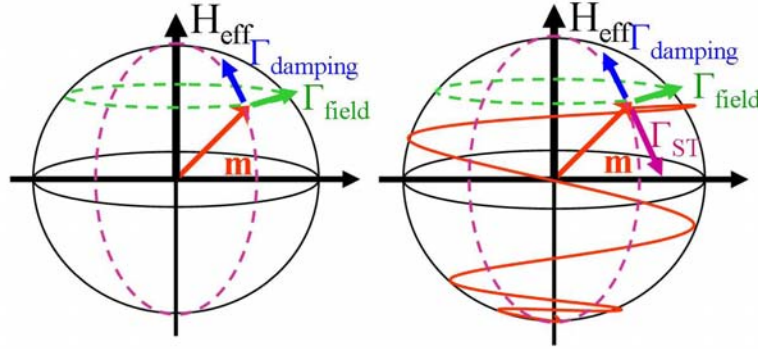


Figure 1.19: Dynamic of a magnetic moment in an effective field H_{eff} (left) and under the effect of a spin-polarized current (right).

- the dipolar field \vec{H}_d due to the sample magnetization
- the anisotropy field \vec{H}_K due to the MCA
- and the exchange field \vec{H}_{ex} due to the exchange interaction

The sum of all these field-like contributions is the so-called effective field H_{eff} given by:

$$\vec{H}_{eff} = -\frac{\partial E_{tot}}{\partial \vec{m}} = \vec{H} + \vec{H}_d + \vec{H}_K + \vec{H}_{ex} \quad (1.50)$$

Taking damping effects into account a moment \vec{m} in an effective field \vec{H}_{eff} follows:

$$\frac{\partial \vec{m}}{\partial t} = -\gamma_0 \times \vec{H}_{eff} \vec{m} + \alpha \gamma_0 (\vec{m} \times (\vec{m} \times \vec{H}_{eff})) \quad (1.51)$$

where α is the Gilbert damping constant and γ_0 the gyromagnetic ratio. This equation is called Landau-Lifschitz-Gilbert equation (LLG). The damping term in the equation describes the fact, that a moment relaxes to its equilibrium position, at a time scale $\tau \propto 1/\alpha$ once a precessional motion was excited. Thus, the LLG equation takes two torques into account: Γ_{eff} which makes the magnetization precess and Γ_{dam} bringing the moment back in its equilibrium position. When a spin-polarized current is flowing through the sample a third torque must be considered: the spin torque Γ_{ST} .

$$\frac{\partial \vec{m}}{\partial t} = -\gamma_0 \vec{H}_{eff} \times \vec{m} + \alpha \gamma_0 (\vec{m} \times (\vec{m} \times \vec{H}_{eff})) + \Gamma_{ST} \quad (1.52)$$

This is the so-called Landau-Lifschitz-Gilbert-Slonczewski equation (LLGS). The spin torque Γ_{ST} can be parallel or antiparallel to Γ_{dam} and hence either increase the damping or if antiparallel and big enough allow a steady precession or lead to a precessional reversal of the moment (see fig.(1.19)).

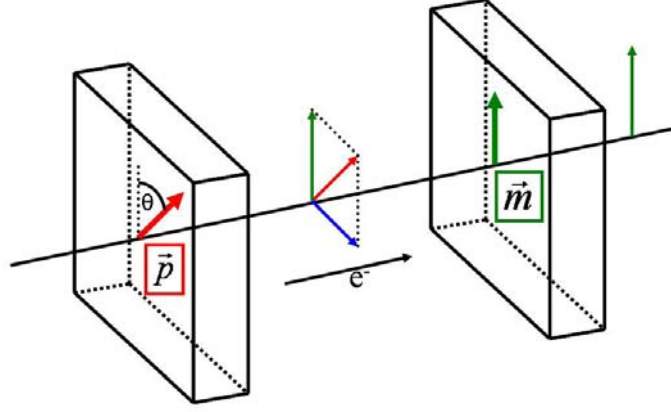


Figure 1.20: Phenomenological representation of the spin transfer effect in a three layer spin valve system.

1.4.2 Current-induced magnetization reversal and steady states precession in nanopillars

Nanopillars with a spin valve structure consist of two magnetic layers separated by a nonmagnetic metallic layer. The magnetic properties are generally chosen in a way, that one layer, the soft layer (SL), is much easier to reverse than the other layer, called the hard layer (HL) or reference layer. The current flows perpendicular to the layers. The idea is, that the current is spin-polarized when passing through the HL. This current then applies a torque on the magnetization of the SL depending on the relative orientation of current, polarization and magnetizations. This torque can lead either to magnetization reversal or to steady state precessions (e.g. [8]) (see fig.(1.20)). The dimensions of nanopillars are in general inferior to the exchange length l_{ex} (compare sec.(1.1.6)). Accordingly the application of a macrospin model is appropriate.

Such a model is developed for example by [58]. They find for the spin torque:

$$\frac{\Gamma_{ST}}{M_S} = -\beta I \eta(\Theta) \hat{e}_m \times (\hat{e}_m \times \hat{e}_p) \quad (1.53)$$

with

$$\beta = \frac{\hbar \gamma_0}{2\mu_0 M_S V e} \quad (1.54)$$

and

$$\eta(\Theta) = \frac{q_+}{A + B \cos(\Theta)} + \frac{q_-}{A - B \cos(\Theta)} \quad (1.55)$$

M_S is the magnetization of the SL and V its volume. The parameters q , A and B , are geometrical and material parameters. One can then express the LLGS equation in spherical coordinates by:

$$\frac{d\vec{m}}{dt} = \sin(\Theta) (\gamma_0 H_{eff} \hat{e}_\phi - [\alpha \gamma_0 H_{eff} + \beta I \eta(\Theta)] \hat{e}_\Theta) \quad (1.56)$$

In order to reverse the magnetization the spin torque must overcome the damping

torque. Thus reversal needs a critical minimum switching current I_{SW} to overcome the energy barrier U_K between two magnetic states of the SL. In a general form this is given by [15]

$$I_{SW} = \frac{4e\mu_0}{\hbar} \frac{1}{g(\theta)} \frac{\alpha}{P} M_S H_{eff} \quad (1.57)$$

with θ the angle between the two magnetizations, g a function describing geometry and band structure and H_{eff} the effective field.

In fig.(1.22) two geometrical configurations are described. One where the magnetization is perpendicular to the layers and one where the magnetization is in-plane. From [15] we take $I_{SW}^{P \rightarrow AP}$ for a switching from a parallel to an antiparallel configuration as:

$$I_{SW}^{P \rightarrow AP} = \frac{2e}{\hbar} \frac{2\alpha}{g(\theta)p} \left(U_K + \frac{1}{2} \mu_0 M_S^2 V \right) \quad (1.58)$$

for a magnetic in-plane configuration and

$$I_{SW}^{P \rightarrow AP} = \frac{2e}{\hbar} \frac{2\alpha}{g(\theta)p} U_K \quad (1.59)$$

for the perpendicular configuration. In both cases I_{SW} is directly proportional to the ratio α/p , with the Gilbert damping parameter α and the degree of spin polarization of the current p . $g(\theta)$ describes the angular dependence and U_K is the energy barrier that has to be overcome for reversal. The main difference between the two equations is, that in the perpendicular case, the switching current I_{SW} is directly proportional to the energy barrier U_K and in the in-plane case, we have to add a contribution due to the demagnetizing field to U_K .

A good criteria to estimate the spin torque efficiency ϵ_{ST} for magnetization reversal would be the coefficient $\epsilon_{ST} = U_K/I_{SW}$ of the energy barrier between the two states defining the thermal stability and the necessary minimum switching current (at reasonable time-scales). With this definition of efficiency, efficient materials are those with a small ratio α/p .

1.4.3 Current-induced DW propagation

The second big topic on spin transfer related phenomena is the propagation of DWs under spin-polarized current in the direction of the electron flow. Nowadays models describe two different mechanisms for the transfer of angular momentum from a current to a DW which are related to two different torques called the "adiabatic" and the "nonadiabatic" torque.

The spin of an electron in a magnetic wire is supposed to follow the magnetization of the wire. When passing a DW the spin has to change its orientation and thereby transfers angular momentum to the magnetization. Two mechanisms can be imagined for this reorientation. One can imagine, that the spin precesses around the local magnetization and consequently follows the local magnetization while passing through the DW. This is the so-called adiabatic process. Necessary condition is, that the dynamic of the electron precession is fast compared to the time the electron needs to pass through the DW. The used criterion is the ratio of the Lamour length λ_L to the thickness Δ of the DW. The Lamour length corresponds to the distance an electron

passes while one precession period in the local exchange field given by: $\lambda_L = \hbar v_F / A$. \hbar is the Planck-constant, A the exchange coupling and v_F the Fermi velocity. The adiabatic process is important when $\lambda_L / \Delta \ll 1$. The second mechanism is the relaxation of the spin in the direction of the local magnetization, the so-called spin flip. The typical length scale for this effect is the spin diffusion length λ_{sf} . We can conclude, that a high anisotropy leads to thin DWs, favoring the nonadiabatic torque. Low anisotropy leads to thick DWs favoring the adiabatic torque.

The spin torque Γ_{ST} on the local magnetization due to the adiabatic and nonadiabatic torque was calculated by [23].

$$\Gamma_{ST} = \frac{-b_J}{M_S^2} \vec{M} \times \left(\vec{M} \times \frac{\partial \vec{M}}{\partial y} \right) - \frac{c_J}{M_S} \vec{M} \times \frac{\partial \vec{M}}{\partial y} \quad (1.60)$$

b_J is the parameter describing the adiabatic torque and c_J describes the nonadiabatic torque. They were calculated as:

$$\begin{aligned} b_J &= \frac{P j_e \mu_B}{e M_S (1 + \beta^2)} \\ c_J &= \frac{P j_e \mu_B \beta}{e M_S (1 + \beta^2)} \end{aligned} \quad (1.61)$$

with j_e the electron current density, M_S the magnetization and β defined as

$$\beta \equiv \frac{\tau_{ex}}{\tau_{sf}} \quad (1.62)$$

which is called the nonadiabatic parameter. $\tau_{ex} = T_L / 2\pi$ with T_L , the Larmor period of the spin precession in the exchange field, and τ_{sf} the time constant of the spin flip process. As in the case of the nanopillars, a high spin polarization P increases the torque. Materials with important polarization P are expected to have higher efficiency for current induced DW motion as the angular momentum transfer from the current is higher.

Furthermore one can define u as:

$$u = \frac{J g P \mu_B}{2 e M_S} \quad (1.63)$$

which has the dimension of a velocity. Most authors claim, that it is only the nonadiabatic torque which can lead to a steady motion of a DW under current as proposed by [23].

The torque Γ_{ST} can lead to two different phenomena: first it can depin a DW from a pinning site. Second it can lead to a steady motion of a DW. In the following, we are going to discuss the case of steady motion. For this discussion we neglect pinning sites, we suppose that we are in the flow regime (see sec.(1.3.2.2)). Micromagnetic simulations done by [55] for a 180° Bloch wall lead to:

$$v_{steady} = \frac{\gamma \Delta}{\alpha} \left(H + \frac{\beta u}{\gamma \Delta} \right) \quad (1.64)$$

for velocities below the Walker breakdown and

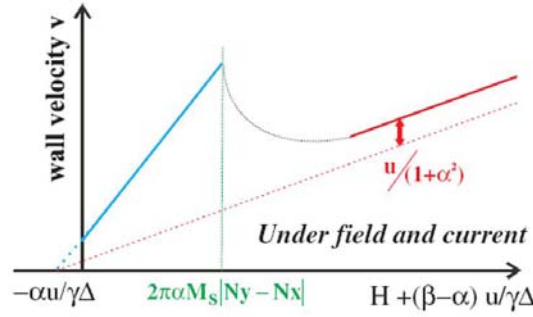


Figure 1.21: Micromagnetic simulation of DW propagation under field and current for a 180° Bloch wall. The cartoon indicates the two linear regimes of velocity, below and far above Walker breakdown. (from([55]))

$$\bar{v}_{steady} = \gamma \Delta \frac{\alpha}{1 + \alpha} \left[H + \frac{u}{\gamma \Delta} \left(\frac{1}{\alpha} + \beta \right) \right] \quad (1.65)$$

for velocities above the Walker breakdown. This behavior is represented in fig.(1.21).

For the choice of a good material for spin torque experiments it remains to define efficiency. In the case of current induced DW motion efficiency can be defined by comparison with the effect of an applied field. In the case of a steady DW motion this is:

$$\epsilon_{ST} = \frac{\beta u}{\gamma \Delta} \quad (1.66)$$

below the Walker breakdown and:

$$\epsilon_{ST} = \frac{u}{\gamma \Delta} \left(\frac{1}{\alpha} + \beta \right) \quad (1.67)$$

above the Walker breakdown. One can see, that for high efficiency small DWs, and consequently high anisotropy is helpful. Also a large nonadiabatic parameter β favors current-induced DW motion. Finally, as $u \propto 1/M$, a small magnetization increases the efficiency in this model. This is a quite interesting fact as the dependence between field and magnetization is that a field has a larger effect on a larger magnetization due to the Zeeman energy.

In ref.[52] a large study on the depinning of a DW has been done. It is proposed, that the spin current lowers the energy barrier, which must be overcome in order to depin the DW. The influence of the current on the depinning time τ is given by:

$$\ln \tau = \ln \tau_0 + \frac{E_{b,0} - \kappa_1 I}{k_B T(I)} \quad (1.68)$$

$E_{b,0}$ is the energy barrier without current, $T(I)$ is the temperature, which at the high current densities of spin torque experiments depends on I . κ_1 represents a phenomenological coefficient describing the spin torque efficiency. The decrease of the energy barrier by a current is equivalent to the decrease by a field H_I . One can then define a parameter ξ allowing to write the relation between H_I and the current density J as

$H_I = \xi J$. Furthermore it results that:

$$\xi = \frac{\kappa_1}{2M_S V_a} \quad (1.69)$$

where M_S is the magnetization and V_a the activation volume of the pinned DW. [52] concludes, that as V_a is directly related to the DW thickness, thin DWs favor current-induced depinning.

1.5 Materials for spin torque experiments

In the precedent section we discussed the relations between material parameters and spin torque phenomena which are established nowadays. In the following section we discuss the materials that have already been studied in spin torque experiments and specially focus on their magnetic parameters.

Several magnetic systems have been studied for spin torque experiments. These systems can be separated in two groups: systems with in-plane anisotropy and systems with perpendicular magnetic anisotropy (PMA). This classification is explained in the following. A separate discussion concerning materials for current induced magnetization reversal in nanopillars and for current induced domain wall propagation in nanowires comes afterward.

1.5.1 In-plane vs out-of-plane materials

First observations of spin torque phenomena were done on magnetic systems with an in-plane anisotropy. Often used materials were permalloy (Ni 81% Fe 19%) , and Co. As explained at the beginning of the chapter (see 1.1.3.3 and 1.1.3.4) a magnetic out-of-plane anisotropy can only be obtained in special materials. However there are reasons to work with magnetic systems possessing an out-of-plane anisotropy. One reason is that systems with a strong perpendicular anisotropy are model systems due to their symmetry. In first order the magnetic moments can only have the two configurations up or down (exceptions are for example moments in a DW). The second reason is due to the efficiency of spin transfer effects, which is higher in perpendicular systems.


In the case of a nanopillar the magnetization can be reversed by thermal activation. Therefore the system has to overcome an energy barrier U_K , depending on anisotropy and magnetization as described in fig.(1.22), between the two magnetic states. This reversal behavior can be described by the Néel-Brown model [59]. The time constant τ , for the thermal excitation is given by :

$$\tau = \tau_0 e^{\frac{U_K}{k_B T}} \quad (1.70)$$

As a consequence, for many applications and experiments a minimum energy barrier of $U_K = 45k_B T$ between the magnetic states of a nanopillar is required. This corresponds to a thermal activation time of more than 3 years (see table(1.1)). In perpendicular magnetized nanopillars the switching current is then directly proportional to the energy barrier separating the two stable magnetic states (compare to table (1.22) as shown by [15] and [17]. Usual volumes for the free layer of a nanopillar are of the order of $10^{-24} m^3$. The required effective anisotropy to reach $U_K = 45k_B T$ is then of the order of

U_K in $k_B T$	thermal stability
25	10^{-3} s
45	10^8 s (> 3 years)
68	10^{18} s ($>$ age of the universe)

Table 1.1: Thermal stability as a function of the energy barrier as calculated by [60].



Anisotropy	In-plane	Out-of-plane
$H_{eff}^{P \rightarrow AP}$	$H + H_{dip} + H_{K\parallel} + \frac{1}{2}M_s$	$H + H_{dip} + H_{K\perp} - M_s$
$U_K(H = H_{dip})$	$\frac{\mu_0 M_s V H_{K\parallel}}{2}$	$\frac{\mu_0 M_s V (H_{K\perp} - M_s)}{2}$
$I_{sw}(H = H_{dip})$	$\frac{2e}{\hbar} \frac{2\alpha}{g(\theta)p} \left(U_K + \frac{1}{2} \mu_0 M_s^2 V \right)$	$\frac{2e}{\hbar} \frac{2\alpha}{g(\theta)p} U_K$

Figure 1.22: Comparison between the effective magnetic field, the energy barrier between the two stable magnetic states and the switching current of spin valves with in-plane or out-of-plane anisotropy. The polarizer in red has a fixed magnetization whereas the free layer in green can be either parallel or antiparallel to the polarizer. taken from [61]

$10^5 J/m^3$. The shape anisotropy $1/2\mu_0 M_s^2$ for a Co film is of the order of $10^6 J/m^3$. The necessary current for switching can hence be about 10 times smaller for the out-of-plane geometry compared to the in-plane case.

In perpendicular magnetized nanowires the spin current induced DW propagation is expected to be more efficient compared to in-plane systems, because of an enhancement of the non adiabatic torque term β . In perpendicular magnetized materials the DW width is typically smaller than 10 nm due to the strong anisotropy, whereas the DW width is typically of the order of 10–100 nm for in-plane systems. Large DW correspond more to the adiabatic limit, meaning, that the DW is sufficiently large to allow the electron spin to follow the local magnetization direction, with transfer of spin momentum. In small DW the electron spin cannot follow the local magnetization and flips from the magnetization direction before the DW to the magnetization direction behind the DW. Thus small DWs represent the non adiabatic limit. The DW motion is essentially driven by the non adiabatic term. Consequently high anisotropy materials with small DWs, as are most of the perpendicular materials, are expected to have a high efficiency for spin current driven DW motion (see [56]).

In the following we are going to discuss the most common materials with PMA which are used nowadays for spin torque experiments.

Material	K_{eff} [kJ/m ³]	K_{MC} [kJ/m ³]	M_S [kA/m]	U_K [k _B ×300K]	I_{SW} [mA] (AP→P)	J_{SW} [10 ¹¹ A/m ²] (AP→P)	structure	reference
FePt-alloys	340	1080 +	1084	3×10 ⁴ +	40 (77K)	10 (77K)	L1 ₀ ordered alloy (tetragonal)	[60]
[CoFe/Pt] multilayer	5 +	155 +	500 +	100 +	45	10	(Poly crystalline structure with (111) texture in plane)	[61]
[Co/Pt] multilayer	475	586 +	425	60 +	5,5	6,4	Poly crystalline structure with (111) texture in plane	[62]
[Fe/Pt] multilayer	>3500 +	>5000	1100 +	60	1,6	1,1	L1 ₀ -structure (tetragonal)	[40]
[Co/Ni] multilayer	13 (OOP)+	266 +	660 +	45	0,12	0,7	Poly crystalline structure with (111) texture in plane	[17]
GdFe-alloy	un (OOP)	un	un	75	7,3 +	4,3	Sputtered, amorphous	[63]
Co	-42,6 (IP)+	un	1420	250 +	13	10	Sputtered on Si/Cu, no more details given	[12]
Ni ₈₁ Fe ₁₉	-13 (IP)	0	645	66	0,39	0,8	Sputtered Py, no more details given	[155]
Co ₇₄ Gd ₂₆	un (IP)	un	0-un.	un	2	2	Sputtered, amorphous	[156]
Co ₂ FeAl _{0,5} Si _{0,5}	-10 (IP)	un	960	36	2	1,2	Fully epitaxial growth (001) orientation	[157]
(Ga,Mn) As	-0,08 (IP)	un	32	52 (520)+	0,8	0,02	Fully epitaxial MTJ T _C =50K, T _{mes} = 30K	[154]

Figure 1.23: Overview of material parameters and switching currents in materials used for spin-torque experiments. Data was either taken from cited references or calculated from data given in the references (+). For the [Co/Pt] multilayers magnetic parameters were taken from [66] and for [Fe/Pt] from [67]. Listed are materials with magnetic moments perpendicular to the sample plane (OOP) and with an in-plane magnetization (IP). Unknown parameters are marked with the letters un.

1.5.2 Materials used for experiments on spin transfer torque switching in nanopillars

Only few groups in the world are able to pattern nanopillars with a contact geometry allowing spin torque experiments. Consequently the number of studied materials with PMA is quite small. First results on magnetization reversal in perpendicular magnetized nanopillars were published in 2006. Used materials were FePt alloys by [62], [CoFe/Pt] multilayers by [63] and [Co/Ni] multilayers by [15]. Results on [Co/Pt] multilayers were reported by [15] and later by [64] in 2009. Results on [Fe/Pt] multilayers were published in 2008 by [42]. Furthermore an RE-TM alloy with PMA, GdFe, was studied as a spin valve free layer by [65].

A table listing materials with PMA and in plane magnetization, which were used for spin torque experiments was obtained from literature 1.23. The parameters given by the table must be understood in the following way: not every author gives a complete set of material parameters characterizing the studied system. Moreover it is not specified if the patterning of the nanopillars might have changed the material parameters compared to full film samples. Some missing data could be calculated from other given parameters. This is marked with a +. For the [Co/Pt] multilayers magnetic parameters were taken from [66] and for [Fe/Pt] from [67]. Also the interpretation of

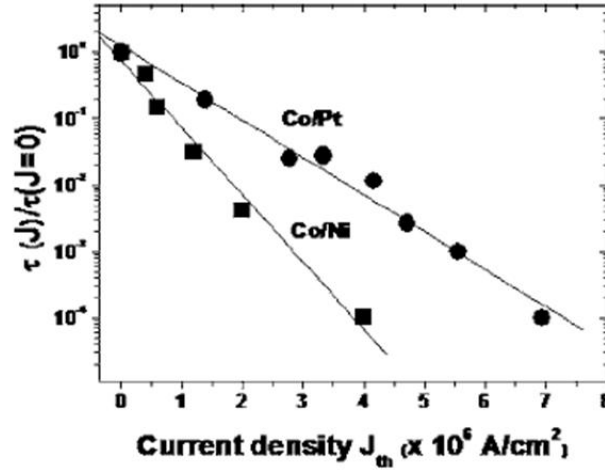


Figure 1.24: Normalized time of depinning as a function of the current density for $[Co/Ni]$ multilayers (squares) and $[Co/Pt]$ multilayers (circles). A DW is pinned in a Hall cross in the wire. Then a DC current I is applied and the depinning time $\tau(I)$ is measured. All taken from [16].

a relation between switching currents I_{SW} and energy barrier U_K must be done very carefully as information about the duration of switching current pulse is not given [20].

1.5.3 Materials used for experiments on spin current driven domain wall propagation

Current induced DW motion was first observed by [14] for thin permalloy films. Also for later studies on patterned nanowires mostly Py was studied. First studies on materials with PMA started in 2005 with $[Co/Pt]$ multilayers [56]. A comparison of threshold currents to depin a DW from a defect between $[Co/Pt]$ multilayers and $[Co/Ni]$ multilayers with PMA was done by [16]. As for current induced magnetization reversal in nanopillars it seems, that the efficiency of spin polarized currents is higher in the $[Co/Ni]$ system than in the $[Co/Pt]$ system (see fig.(1.24) and [15]). Typical critical current densities which are necessary to observe spin torque effects on DWs were of the order of 10^{11} A/m^2 for in plane materials and of the order of 10^{10} A/m^2 for materials with PMA.

Very low critical currents of the order of 10^9 A/m^2 were found for the GaMnAs system [68] with a magnetization close to 0 .

1.6 Outline for the following manuscript

Several materials have been studied in spin torque experiments. First experiments were specially focused on the question if spin torque effects can be used to manipulate the magnetic configurations of nanopillars [12] and to move domain walls in wires ([13] and [14]). In a further step the efficiency of spin transfer was optimized (e.g.[15] and [16]) by choosing special materials, like materials with perpendicular magnetic anisotropy

(e.g.[15] and [16]). Since this time, spin transfer has been studied exhaustively in these materials. For nanopillars phase diagrams [17], angle dependent reversal [18], telegraph noise [19] and reversal dynamics were measured [20]. For nanowires experimental large work has been done on the effect of spin-polarized current on the depinning statistics of trapped DWs (e.g. [21])and on the determination of the adiabatic and nonadiabatic torque term (e.g.[22]) and their influence on current induced propagation.

What has not been done for the moment is a study of spin transfer phenomena in model systems where the magnetic properties can be tuned in a large range. Such work would allow to check the theoretically established relations between parameters like anisotropy, magnetization, etc. and spin torque effects (see e.g. [23] and [24]).

For experimental model studies about spin transfer phenomena the following material properties are of advantage:

1. Well defined magnetic configurations (e.g. PMA): systems with a strong uniaxial easy axis have only two stable magnetic configurations when no field or current is applied. This facilitates the understanding of reversal processes.
2. Low current densities (efficiency): First spin torque experiments on nanopillars [12] required current densities of the order of $10^8 A/cm^2$. For DW propagation experiments the reported current densities are around $10^7 A/cm^2$ [25]. This leads to important Joule heating effects. A high temperature increase can change the structural sample properties by annealing effects or even destroy the sample. Besides, magnetic properties are dependent on temperature, consequently a sample temperature which is much higher than the ambient temperature must be considered for the analysis of experimental data.
3. Reproducible magnetic properties (homogeneity): Defects often play an important role for magnetization reversal (see section 1.3). For DW propagation in nanowires the pinning potential of artificial pinning sites depends on intrinsic defects of the material (see 1.46). In nanopillars a pinned DW was for example studied by [19]. Strength and local distribution of such defects follow stochastic laws. For an experimental model system it is important to control these distributions in order to get reproducible sample properties.
4. Reproducible tuning of magnetic properties (variability): as seen in section 1.4 spin transfer related phenomena depend strongly on material parameters like the magneto crystalline anisotropy constant K_{MC} , the exchange constant A and on the magnetization M of the sample. Thus the possibility of tuning these parameters would be a big advantage for studying models on spin transfer torque.

The aim of this PhD. thesis is to study magnetic systems for their suitability for spin torque experiments exploring basic models of material properties and spin transfer phenomena. Two systems with potentially a perpendicular magnetic anisotropy are chosen: $[Co/Ni]$ superlattices grown by molecular beam epitaxy and sputtered amorphous CoTb alloys.

The reasons for the choice of $[Co/Ni]$ superlattices grown by molecular beam epitaxy are the following:

It has already been shown that spin transfer is very effective in sputtered polycrystalline (111) textured Co/Ni multilayers ([15] and [16]). Furthermore perpendicular

anisotropy and magnetization can be tuned by varying the Co and Ni layer thicknesses. The anisotropy is known to come from the *Co/Ni* interfaces [26]. Our aim is to improve the control of the anisotropy by better controlling the *Co/Ni* interfaces using epitaxy. Besides, in an epitaxial system, where we have no grain boundaries as in a polycrystalline sample, we can expect to have a lower Gilbert damping parameter α . Less scattering on grain boundaries leads might also lead to larger electron spin mean free paths and thus to a higher effective spin polarization P of a current flowing through the system. Both, the lower α and the higher P would increase the efficiency of spin torque compared to the polycrystalline samples.

The choice of amorphous $Co_{1-x}Tb_x$ alloys prepared by sputtering is due to the fact, that their perpendicular anisotropy and magnetization can be easily tuned in large ranges by two ways: by changing the sample composition x and by changing the temperature T [27]. It has been demonstrated that rare earth transition metal alloys give rise to spin-polarized currents, even when their magnetization is close to zero [28]. A disadvantage of this system is, that the Gilbert damping parameter α is generally expected to be large ($\alpha > 0.1$) [29]. However, as some theoretical models predict high efficiency for systems with small magnetization, the system is a good choice to test such models.

The following script is split in three main chapters. First the experimental equipment used for sample preparation and analysis is briefly described. Then the results obtained for CoTb alloys are discussed. Finally the [*Co/Ni*] superlattices are described.

Chapitre 2

Les alliages de $Co_{1-x}Tb_x$

Dans ce chapitre nous présentons les résultats obtenus pour les alliages de $Co_{1-x}Tb_x$ élaborés par pulvérisation cathodique. Ce matériau est de structure amorphe. Les deux sous-réseaux de Co et de Tb sont couplés antiferromagnétiquement. L'aimantation possède une anisotropie perpendiculaire pour toutes les compositions x entre 0.08 et 0.34. La valeur de l'aimantation et de l'anisotropie peut être modifiée soit par x , soit en variant T .

La structure en domaines des alliages $Co_{1-x}Tb_x$ est analysée par différentes techniques de microscopie sensibles à l'aimantation. Il est démontré que l'alliage est adapté à des expériences sur la propagation d'un parois unique.

Enfin nous montrons des tout premier résultat sur le retournement de l'aimantation de CoTb grâce à une lumière polarisée : *all-optical switching*.

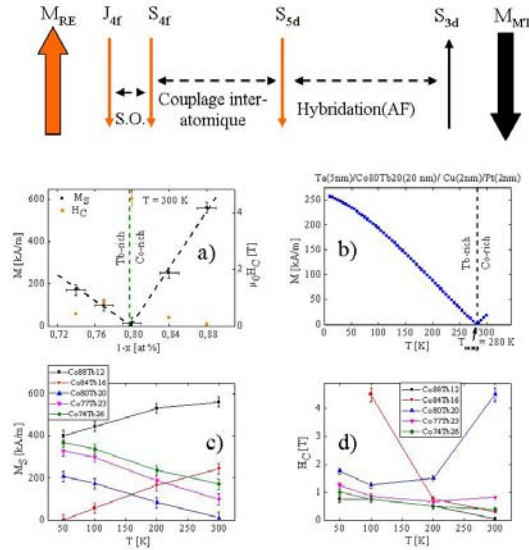


Fig. 2.1: Structure magnétique des alliages de $Co_{1-x}Tb_x$. Couplage antiferromagnétique entre les deux sous-réseaux de Co et de Tb. a)-d) aimantations en fonction de la concentration x et de la température T obtenue par magnétométrie.

Chapter 2

CoTb-based alloys

$Co_{1-x}Tb_x$ alloys were studied for their suitability for spin transfer torque experiments. They are known to have potentially a tunable perpendicular magnetic anisotropy and magnetization by tuning sample concentration and/or temperature. We begin this chapter with a description of growth and analysis of the sample structure. This section is followed by a description of the magnetic properties of $Co_{1-x}Tb_x$ alloys. In the following section dipolar coupling effects in CoTb based spin valve systems are studied by magnetometry and MFM microscopy. Thereafter the transport properties of $Co_{1-x}Tb_x$ alloys and spin valves are analyzed. At the end of the chapter some recent results about the so-called all-optical switching phenomenon in $Co_{1-x}Tb_x$ alloys are given and perspectives are discussed.

2.1 Growth and Structure

In the following section, we first describe the sample growth by DC sputtering. In the second part a structural analysis by TEM is shown.

2.1.1 Sample preparation by DC magnetron sputtering

The $Co_{1-x}Tb_x$ samples were grown by DC magnetron sputtering. Pure Co and Tb targets were used for a co-sputtering process. The relative atomic concentration of the two elements Co and Tb was controlled by the relative sputtering power.

The samples were in general deposited on silicon (100) substrates covered by a thin oxidized silicon layer. A plasma etching of the substrate is done in order to clean it. Deposition was done at ambient temperature. A 5nm thick Ta layer allows good adherence of the following metallic layers to the substrate and prevents from Si diffusion into the stack. The $Co_{1-x}Tb_x$ alloys were directly deposited on this Ta buffer. Finally a 2nm Cu and a 2nm Pt layer are deposited to protect the sample from oxidation. The whole sample stack is represented in fig.(2.1)

We defined a standard set of five samples with compositions around the magnetic compensation point (see sec.(2.2)), which was used as a reference for all studies with $x = 0.12; 0.16; 0.20; 0.23; 0.26$.

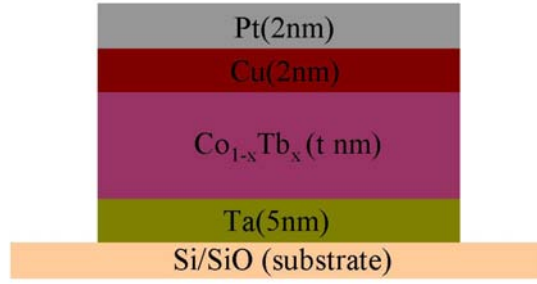


Figure 2.1: Sample stack for $Co_{1-x}Tb_x$ -alloys.

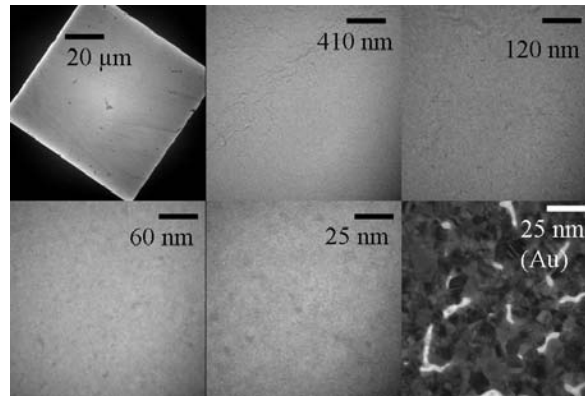


Figure 2.2: TEM images for a $Co_{74}Tb_{26}$ sample at different magnifications. The last image is the image of a polycrystalline reference Au layer.

2.1.2 Structural analysis by transmission electron microscopy (TEM)

Alloys of rare earth elements (RE) and transition metals (TM) are known to be amorphous when deposited by sputtering at room temperature ([27]).

A TEM analysis was done in order to check the structure of our samples. Therefore samples as described in sec.(2.1.1) were deposited on so-called TEM grids. These consist of a copper grid, with a $100 \times 100 \mu m$ mesh size. On this Cu grid there is a thin carbon membrane in order to have a continuous substrate. The metallic layers are deposited on this carbon membrane. Only the mesh, is transparent for the electrons, as the Cu absorbs the electrons. Such a quadratic mesh can be seen in the TEM image with the biggest field of view (see fig.(2.2)). In fig.(2.2) the TEM images taken for a $Co_{74}Tb_{26}$ sample are shown. A crystalline structure can not be observed in agreement with our supposition, that our samples are amorphous. Such a set of TEM images was taken for every sample composition. The images for the highest magnification are shown in fig.(2.3). They also do not show the signature of some crystalline structure.

The next step of our TEM analysis consists of doing electron diffraction. The diffraction images for the CoTb films as well as for a polycrystalline Au film are shown in fig.(2.4). Compared to the polycrystalline Au film, with well defined and sharp diffraction rings, the diffraction by CoTb films lead to a diffuse diffraction pattern.

One can measure the intensity as a function of the distance to the center for this

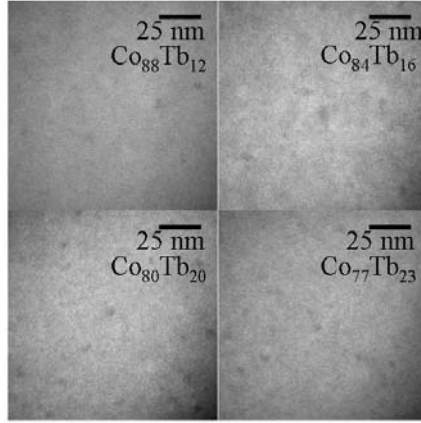


Figure 2.3: Further TEM images taken on CoTb samples with different compositions at high magnification.

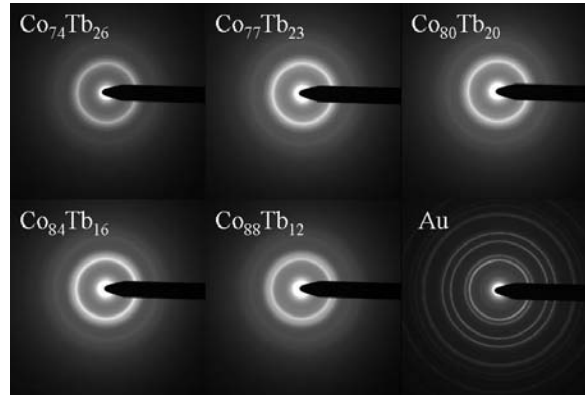


Figure 2.4: TEM diffraction images of CoTb films and of a Au reference layer.

image. As the lattice parameters of Au are known, this allows to determine the camera constant of the TEM. From the Au(111) diffraction ring one obtains that:

$$1/2.3556\text{\AA} = 91.5\text{pixel} \quad (2.1)$$

This allows to scale the diffraction-images of the CoTb-samples by:

$$1/\text{\AA} = 215.5\text{pixel} \quad (2.2)$$

The result of this analysis is represented in fig.(2.5). Sharp peaks, which are typical for crystalline structures can not be observed. One can see a large peak around $1/3.5\text{\AA}$. This is close to the nearest neighbor distance for Tb hcp crystals of 3.52\AA [69]. In literature (e.g. [70]) such diffraction patterns were interpreted as the result of an amorphous structure. We though conclude, that our samples have an amorphous structure.

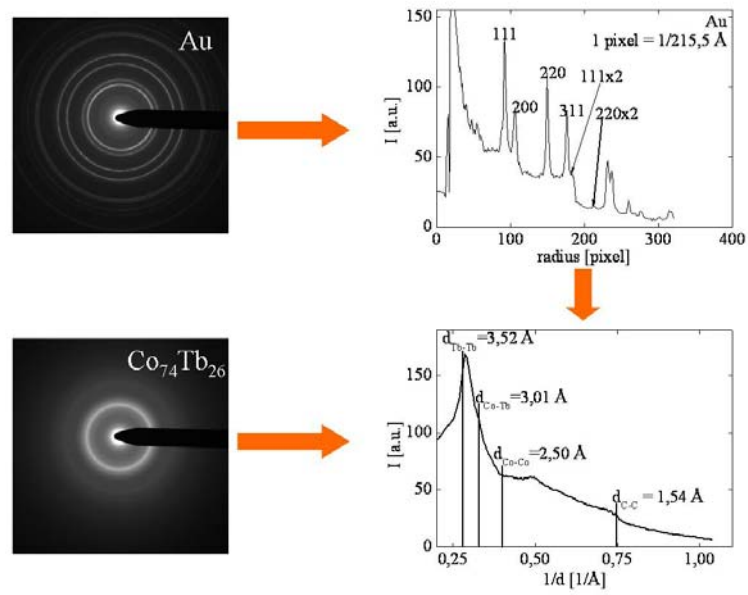


Figure 2.5: Analysis of the TEM diffraction image for the $Co_{74}Tb_{26}$ sample.

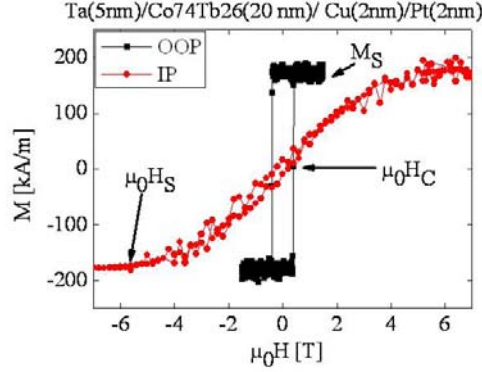


Figure 2.6: In-plane (IP)(SQUID) and out of plane (OOP) loop (VSM) for a $Co_{74}Tb_{26}$ sample. $\mu_0 H_C$ corresponds to the coercive field and $\mu_0 H_S$ to the IP saturation field ($M \approx 0.95 M_S$).

2.2 Magnetic properties

In this section we discuss the magnetic properties of $Co_{1-x}Tb_x$ alloys. Alloys of rare earth (RE) and transition metals (TM) have been studied for a long time and a detailed analysis of their properties has already been done by e.g. [27]. However we also exhaustively studied the magnetism of our CoTb alloys. The reason for this is, that the magnetic properties are very sensitive to the specific growth chamber (see [71] and references 1-5 of this paper). Furthermore, they depend strongly on small fluctuations of the sample composition as we are going to see in the following sections. The analysis of the magnetic properties was mainly done by measuring hysteresis loops with the field applied perpendicular (OOP) and parallel (IP) to the film plane. A typical example for an IP and an OOP loop for a sample are given in fig.(2.6). One can observe, that we have a square loop for the OOP case and a loop where the moment changes continuously with the applied field for the IP case. This is the typical signature of a sample with an effective perpendicular magnetic anisotropy (PMA) (see sec.(1.3)). The coercive field, as we are going to use it in the following, is the field, where the magnetization along the applied field is zero. The IP saturation field, is the field, where the magnetization is saturated to 95 % of the saturation magnetization.

A representation of the hysteresis loops measured at room temperature for five different sample compositions is shown in fig.(2.7).

For each composition IP and OOP hysteresis loops were also measured at different temperatures by SQUID magnetometry. An example for the development of the hysteresis loops with temperature is given in fig.(2.8).

The following results about magnetization and anisotropy, were obtained from those loops.

2.2.1 Magnetic structure of rare earth(RE) - transition metal(TM) alloys

The magnetism of CoTb alloys is due to the itinerant magnetism of the Co sublattice on the one hand, and on the other hand due to the localized 4f electrons of the Tb

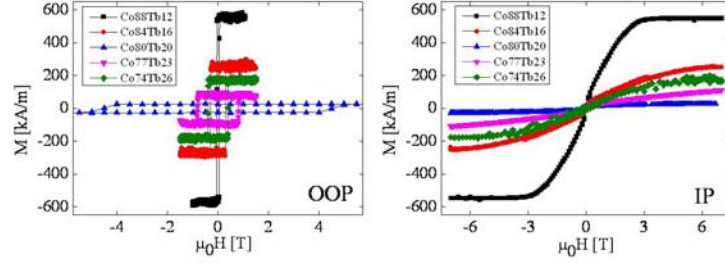


Figure 2.7: Hysteresis loops for $Co_{1-x}Tb_x$ alloys. The measurement was done by vibrating sample magnetometry (VSM) with a field perpendicular to the plane (OOP), and by a SQUID for the measurements with the field applied in the sample plane (IP).

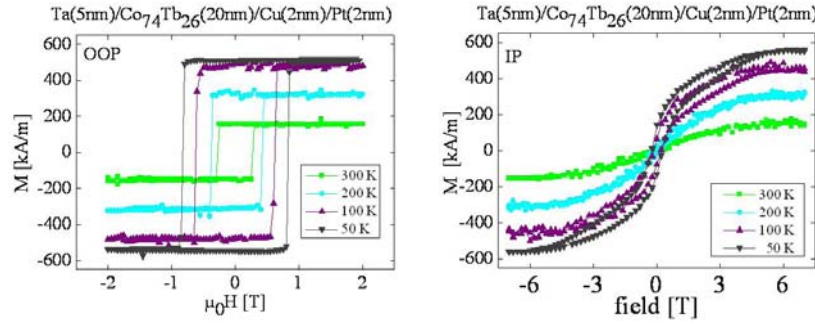


Figure 2.8: IP and OOP hysteresis loops of a $Co_{74}Tb_{26}$ alloy at different temperatures.

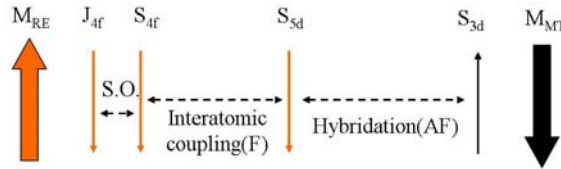


Figure 2.9: Schematic representation of the indirect exchange coupling between a RE and a TM (from [74]) in the case of an alloy.

atoms. The moments of the two sublattices are antiparallel. Thus, $Co_{1-x}Tb_x$ alloys are ferrimagnetic. The exchange constant between the Co moments is positive. Also the exchange constant between the Tb moments is positive [72]. The exchange constant between a Tb and a Co moment is negative. This last coupling between the RE and the TM happens on an indirect way via the conducting 5s electrons of the Tb atoms. This model from [73] is schematically represented in fig.(2.9).

The total magnetization M_{CoTb} of such an alloy is then described by the difference of the two sublattice contributions. This leads to

$$|M_{CoTb}(x_{vol}, T)| = |M_{Co}(T) \cdot (1 - x_{vol}) - M_{Tb}(T) \cdot x_{vol}| \quad (2.3)$$

with the temperature T , and x_{vol} the volumic sample composition. As the Curie temperature for Co is high compared to room temperature (1400K) we consider M_{Co}

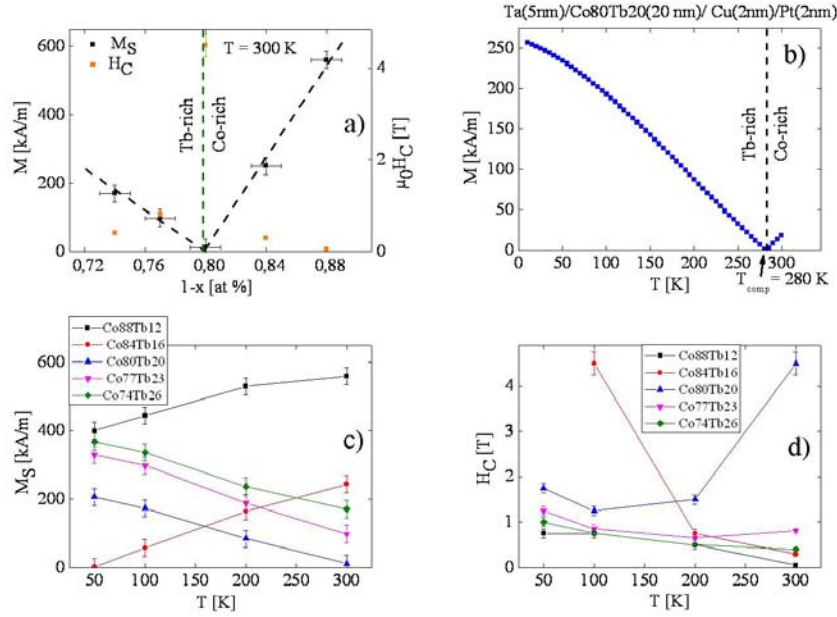


Figure 2.10: a) Saturation magnetization and coercivity as a function of the sample composition x at room temperature. b) Magnetization vs temperature for a $Co_{80}Tb_{20}$ sample. c) Magnetization vs temperature for different sample compositions. Lines are guides to the eye. d) Coercivity vs temperature for different sample compositions.

to be independent from T . However this is not the case for the Tb sublattice, which is very sensitive due to the low Curie temperature of Tb (237 K [75]). Consequently the compensation composition x_{comp} , where the netmagnetization M_{Co} is zero, is a function of temperature. This was extensively studied by [27].

2.2.2 Magnetization of the CoTb system

In fig.(2.10(a)) we see the magnetization of the CoTb alloys as a function of their composition $1-x$, with x between 12 and 26 atomic percent of Tb at room temperature. As the Co and Tb moments are antiparallel, they compensate each other for a certain compensation composition x_{comp} . In our case this is around 21 at. % of Tb. For Tb concentrations higher than 21 at. % the netmagnetization is parallel to the Tb sublattice at room temperature. The composition is then called a Tb-rich composition. For Tb concentrations lower than 21 at. % the netmagnetization is parallel to Co sublattice. The composition is then called a Co-rich composition. In fig.(2.10(a)) we see the magnetization of a $Co_{80}Tb_{20}$ alloy as a function of temperature. When we decrease the temperature starting from ambient temperature, the magnetization first decreases, until it reaches zero at 280K. This is the compensation temperature $T_{comp}(x)$ for $x = 20$. For $T < T_{comp}$ the magnetization increases with decreasing temperature, the sample is Tb-rich in this range. The determination of dM/dT is hence a good way to decide whether a sample is Co or Tb-rich. The results for $M(T)$ for five different sample compositions can be found in fig.(2.10(c)). There, two kinds of behavior are observed, too. For the Co-rich samples, the magnetization increases with increasing

temperature, whereas it decreases for Tb-rich samples.

We conclude, that with our CoTb alloys we can reach any magnetization between 0 and $600kA/m$ by choosing specific concentrations and temperatures.

A second remarkable property, that can be seen from the hysteresis loops, is the fact, that the coercivity field also changes in a large range, from $0.04T$ up to fields higher than the $7T$ maximum field of the used SQUID (see fig.(2.10a) and fig.(2.10d)). As explained in sec.(1.3) several interactions have to be considered to explain coercive fields. It is a competition between the Zeeman energy, working in favor of the reversal and the local anisotropy and exchange interactions, which work against the nucleation of a reversed domain. Once a reversed domain is nucleated the competition is between the Zeeman energy favoring the growth of this domain and local pinning fields, which block the propagation of its domain walls. Consequently coercivity diverges for small magnetizations as strong fields are needed in order to reach significant Zeeman energies.

This shows, that also the coercivity is tunable in a large range between $0.04T$ up to fields higher than $7T$, by choosing composition and temperature. However one has to be careful about these results when samples of nanometer dimensions are patterned as the nucleation and propagation field then strongly depend on geometry (see sec.(1.3)).

2.2.3 Perpendicular anisotropy in CoTb alloys

As explained in the section (1.4) magnetic anisotropy is an important material parameter for spin torque experiments. We determined the anisotropy of CoTb alloys by SQUID magnetometry. Therefore IP hysteresis loops were measured with fields up to $7T$. As we have seen in the section (1.3.1) the magnetic anisotropy can be determined if the anisotropy field H_A and the saturation magnetization M_S is known (see fig.(2.11 a,c and d)). The effective anisotropy K_{eff} can then be directly obtained with:

$$K_{eff} = \frac{1}{2}\mu_0 M_S H_A \quad (2.4)$$

and the uniaxial perpendicular anisotropy constant K_u as:

$$K_u = K_{eff} + \frac{1}{2}\mu_0 M_S^2 \quad (2.5)$$

The results for the anisotropy as a function of the sample composition x are represented in fig.(2.11b) and as a function of temperature in fig.(2.11e,f).

Missing points in the graphs for some samples indicate, that for fields up to $7T$ a saturation field could not be determined. Theoretically $H_A = H_S$, with H_S the IP saturation field. However for real samples this is not as easy. The reason is that for samples with small magnetic moments, as our CoTb samples, it is difficult to decide whether it is saturated or not. Furthermore the determination of the saturation magnetization can also cause problems for samples with small magnetization. This is due to the fact, that for CoTb alloys, we sometimes observe an unexpected contribution to the hysteresis loops at small fields (see sec.(2.2.5)). The incertitude for the determination of the anisotropy field H_A as well as for the saturation magnetization M_S leads to large incertitudes for the calculated anisotropy constants. The uniaxial anisotropy constant K_u increases with decreasing temperature. This is not surprising as the increase of magnetocrystalline anisotropy with decreasing temperature is described by several

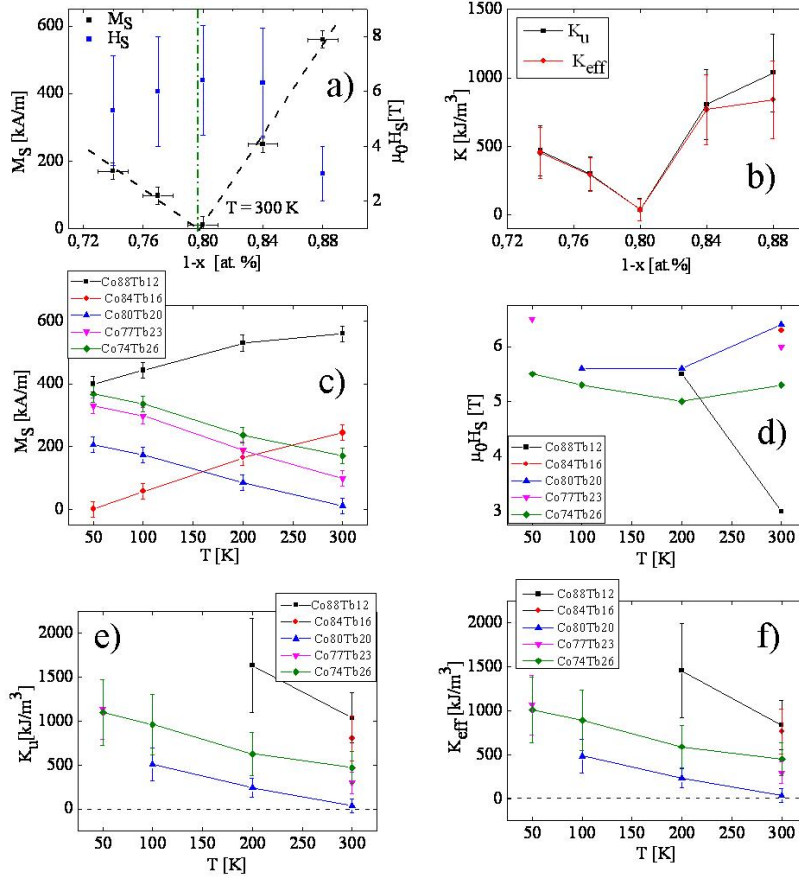


Figure 2.11: Results for $Co_{1-x}Tb_x$ alloys obtained from IP hysteresis loops. a) shows magnetization M_S and saturation field H_S as a function of the sample composition. b) represents the effective K_{eff} and the uniaxial K_u anisotropy of CoTb alloys as a function of their composition. c) shows the magnetization M_S and d) the saturation field H_S as a function of temperature. In e) we can see K_{eff} and in f) K_u as a function of temperature.

theoretical models e.g.[76].

However the explanation of the behavior of K_u as a function of the sample composition remains unclear. Similar behaviors of K_u as a function of composition for RE-Fe alloys can be found in [77], but also lack of a theoretical description. A short discussion about the usual models given in literature can be found at the end of this section.

At present we conclude, that we are not sure about how to control the uniaxial anisotropy constant K_u of our samples. One should probably try other techniques in order to measure the anisotropy as described by [78]. However under similar preparation conditions, samples with similar compositions have the same anisotropy. Furthermore we are able to tune the effective anisotropy of a sample by changing its temperature due to the change of the shape anisotropy with magnetization.

2.2.4 Magnetism of CoTb alloys as a function of layer thickness

The influence of the CoTb layer thickness t on magnetism was studied for a $Co_{88}Tb_{12}$ alloy. The results are represented in fig.(2.12). With increasing thickness the remanence and the coercivity decrease as we can see from fig.(2.12a and c). The thicker the sample, the more the dipolar field energy becomes important for a uniformly magnetized layer as:

$$E_d = \frac{1}{2}\mu_0\vec{H}_{dem} \cdot \vec{m} \quad (2.6)$$

with the magnetic moment $m = M_S \cdot V$ of the layer. Hence the nucleation of domains which are antiparallel to the originally saturated state becomes more easy with increasing thickness. For thick layers, which were saturated in a perpendicular field, such domains can even appear before the applied field is turned back to zero. This explains the decrease of remanence for layers thicker than 60 nm. An MFM image of the remanent state of a 120 nm thick $Co_{88}Tb_{12}$ alloy (fig.(2.12e)) shows these small ($0.5 - 1 \mu m$) antiparallel domains, with an orientation perpendicular to the surface.

From the IP magnetization loops fig.(2.12b) we obtain, that the IP saturation field H_S is constant as a function of thickness t between 20 and 120 nm. Only for the 10 nm thick sample a small increase of H_S can be observed, but this is not really significant as the error bars are large. We though conclude, that the PMA of CoTb alloys is independent of the layer thickness in a large range of thicknesses. This is an interesting point for spin torque switching in nanopillars, as this allows to tune the energy barrier U_K simply by varying the thickness of the layer (compare sec.(1.4.2)).

2.2.5 Further data

2.2.5.1 Soft-magnetic contribution to hysteresis loops

The CoTb alloys we grew, sometimes show a small soft-magnetic contribution to the loops (see fig.(2.13a)). The origin of this contribution remains unclear to us. For samples grown at the same time the effect has a similar amplitude. Measuring at different temperatures did not change the amplitude, too. We measured hysteresis loops of the substrates and of the substrates with deposited buffer layers. The measured signals showed only the expected diamagnetic or paramagnetic shapes. Thus it seems that the signal comes from the CoTb layers themselves. The EDX analysis, did not show any impurities like Fe, which could explain the magnetic signals of our layers. Furthermore we never observed any signal due to a soft-magnetic contribution measuring polar Kerr effect or transport properties. For the moment we have no explanation of this soft-magnetic contribution.

For the analysis of our magnetometry results we neglected the presence of this soft-magnetic contribution to the magnetization.

2.2.5.2 Effects of annealing

The magnetic properties of amorphous RE-TM alloys are known to be sensitive to annealing [79]. For nanofabrication we are using a lithography process during which

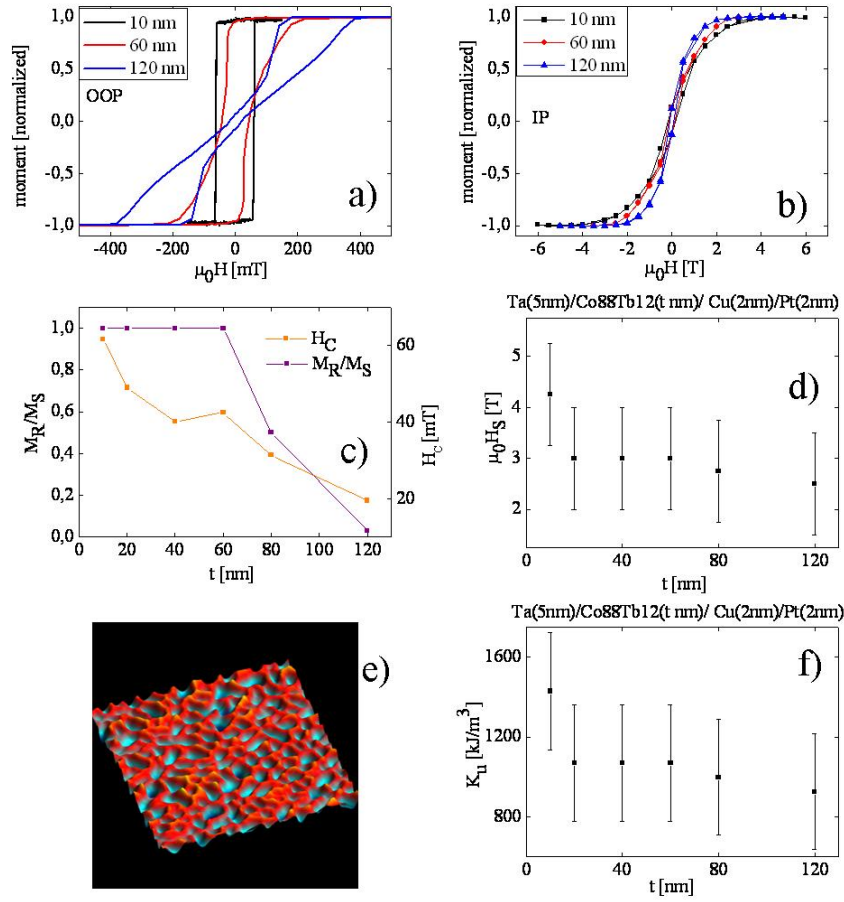


Figure 2.12: Magnetic properties of a $Co_{12}Tb_{88}$ alloy as a function of the layer thickness t . a) OOP hysteresis loops b) IP hysteresis loops c) remanence and coercivity as a function of thickness d) IP saturation field e) MFM (magnetic force microscopy) image of a $10 \times 10 \mu m$ large area of a 120 nm thick $Co_{12}Tb_{88}$ film f) uniaxial anisotropy constant K_u as a function of the layer thickness

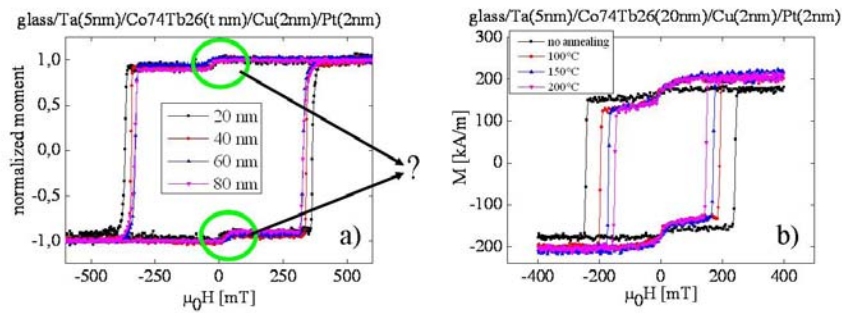


Figure 2.13: a) OOP hysteresis loops for $Co_{74}Tb_{26}$ samples of different thickness showing a soft magnetic contribution. b) OOP loops as a function of the annealing temperature. The annealing time was 2 hours for all experiments.

the sample is exposed to temperatures up to 180°C . Therefore we did some annealing experiments, in order to check if the PMA of our samples resists to heat. The samples were exposed to temperatures between 100 and 200°C . OOP loops were measured. The shape of the OOP loops remains quadratic even though the coercivity slightly decreases for all sample concentrations. Hence we conclude that the samples conserve a PMA when being annealed. An example of the development of the loops under annealing is given in fig.(2.13b). For very long annealing ($t > 10h$) at 200° the PMA was lost. This can be explained by a destruction of the order responsible for PMA due to crystallization [70]. We did not further investigate this phenomenon.

2.2.6 Models describing the origin of PMA in RE-TM alloys

In the literature the origin of anisotropy in RE-TM alloys was exhaustively discussed since the discovery of PMA in these samples by [80]. In spite of these discussions a final result was never obtained. The only thing that seems to be clear is, that despite the amorphous character of the RE-TM alloys, there must be some ordering effects in the samples. Furthermore as the anisotropy strongly depends on growth conditions, it seems that the nonisotropic ordering is related to sample growth [71]. However it is clear that this ordering can not be crystalline or polycrystalline as this would lead to typical diffraction peaks when doing diffraction experiments. In [81] it is experimentally shown that the PMA can be increased by increasing the substrate temperature during deposition. The given model (see also [82]) says that an order in the direction perpendicular to the surface appears as the arriving atoms during growth try to reach positions where their energy is minimum. A graphic representation of such a behavior is given in fig.(2.14). The idea is the following: the first RE and TM atoms that arrive on the surface of the sample take positions in a completely random way. On a short range of few atoms we have then regions which are rich in the RE and regions which are rich to the TM, simply due to their stochastic distribution. The following atoms also arrive in a completely random way. However RE and TM atoms do not adhere to RE-rich or TM-rich regions in the same way. Once arrived on the sample surface the RE and TM atoms can then reach energetically favorable regions due to thermal activation. This breaks the symmetry of the alloy structure in the direction perpendicular to the surface. Apart from the dependence of anisotropy on the substrate temperature during deposition this also explains why for samples with the same stoichiometric compositions the anisotropy can differ importantly. In this model the anisotropy depends on the ratio between the relaxation time, the atoms need to get to their energetically favorable positions by thermal excitation, and the time a deposited atom is covered by the following atoms. Consequently anisotropy is a function of the sample growth rate.

Another model related to growth, which is often cited (e.g. [83]), is the so-called stress induced anisotropy. Here PMA is due to strain of the RE-TM alloy with the substrate. We do not believe in this model, as we find PMA independent of thicknesses on a large range up to 120 nm . Such strain due to the substrate should relax with increasing layer thickness and hence the anisotropy should disappear.

A model as described by [82] only says, that the symmetry is broken in the direction perpendicular to the film plane. But it does not describe the anisotropic environment causing the moments to be preferentially oriented in a perpendicular way. In princi-

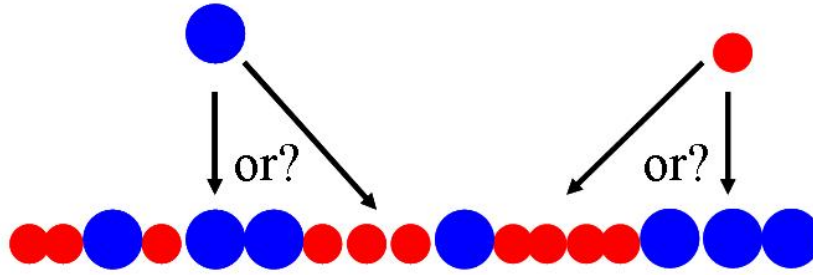


Figure 2.14: Representation of the growth-model given by [82].

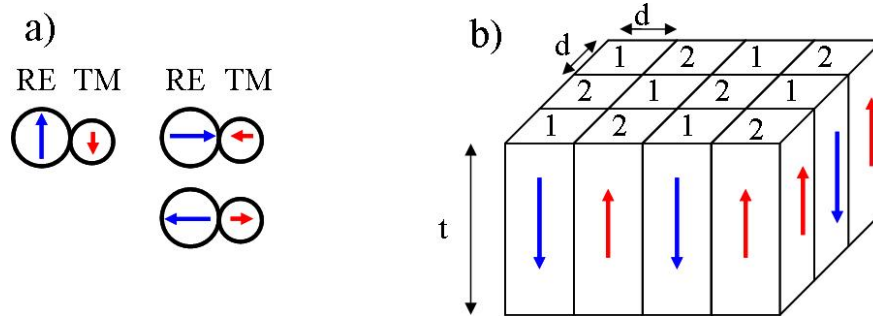


Figure 2.15: Models describing PMA due to dipolar interactions. a) shows a surface effect for antiparallel coupled moments [84]. b) shows a columnar structure of a thin film as it is considered by [71].

ple magnetic anisotropy can only have two different origins: either it is due to the magnetocrystalline field, or it is due to dipolar interactions.

We are starting our discussion with models based on dipolar interactions. First we discuss an effect due to the ordering of antiparallel magnetic dipoles at the surface [84]. This model considers that, if two magnetic moments are coupled antiferromagnetically, there exists an orientation which minimizes the dipolar interaction. This is schematically represented in fig.(2.15a). One can convince himself very easily, that in an atomic monolayer this favors a perpendicular arrangement of the magnetic moments. However for moments, which are not at the surface such a preferential orientation does not exist. Consequently described mechanism is a surface effect and thus anisotropy should disappear with increasing layer thickness, what is not the case.

A model considering dipolar interactions of columnar microstructures is given by [71]. They consider, that for samples close to magnetic compensation we have columns which are rich in either RE or TM moments. Such columns would be antiferromagnetically exchange-coupled. Similar to the above described phenomenon of out-of-plane anisotropy for antiparallel magnetic dipoles, dipolar interaction would lead to a perpendicular orientation of the magnetic moments, when the diameter d of the columns is small compared to the sample thickness t (see fig.(2.15b)). In the case of a ferrimagnet with the sublattices A and B, the sublattice magnetizations M_A and M_B , a composition difference Δx_A between the columns and a relative volume occupied by the columns of

and it is obtained that:

$$K_u = \frac{1}{4}\mu_0 v(1-v)(\Delta x_A)^2 \left(\frac{M_A}{x_A} + \frac{M_B}{x_B} \right)^2 \quad (2.7)$$

The microscopic parameters v and Δx_A are quite difficult to determine as the authors of [71] admit. An experimental proof of such a columnar growth has never been given. One can find sets of parameters for our CoTb alloys which allow to obtain values corresponding to the same order of magnitude as our experimental one. As an example, we took $\Delta x_A = 0.25$, $v = 0.4$, $M_{Tb} = 2100 kA/m$ and $M_{Co} = 1740 kA/m$. This leads to anisotropies K_u between $1.7 MJ/m^3$ for $x = 0.12$ and $0.5 MJ/m^3$ for $x = 0.26$ what is the same order of magnitude like our experimental values. However (besides the fact that there is no experimental proof for such columns), not explained by such models is the fact that the experimental anisotropies for RE-TM metals, where the RE has a L-contribution to the moment, like for Tb, Dy, Sm, can have much higher anisotropies as the Gd based alloys, which only have S-contributions [27].

To explain this, models, which are considering interactions of the magnetic moment with its environmental electronic structure are needed. Two models are mostly cited: bond-orientational anisotropy and pair-ordering effects. The idea of the bond-orientational anisotropy model is, that the interatomic distances in the in-plane direction slightly differ from the out-of-plane distances. Experimental proof of such so-called bond-orientational anisotropy is given by [85] and [86] for CoTbFe alloys. The pair ordering effects means that the number of nearest neighbor pairs for TM-TM, RE-RE and RE-TM, differ for the IP and the OOP direction [87]. Experiments can be found e.g. in [88] for TbFe alloys. Special studies on CoTb were not found in literature.

We conclude, that the origin of PMA in RE-TM alloys is still unclear in literature.

2.2.7 Conclusion on the magnetic properties of CoTb alloys

We have shown, that the magnetic parameters like magnetization and PMA of CoTb alloys can be tuned in a wide range. An explanation to the origin of PMA in our CoTb alloys was not obtained. It seems to be clear, that the anisotropy of RE-TM alloys depends strongly on growth conditions. From a practical point of view, we are able to grow samples reproducibly enough, in order to get similar results for samples with the same compositions grown at different moments during the last three years. Consequently CoTb alloys are a model system in the sense, that we are able to control magnetization and anisotropy of this system by changing composition and temperature.

2.3 Magnetization reversal in $Co_{1-x}Tb_x$ alloys and $Co_{1-x}Tb_x$ -based spin valves

In this section we study the magnetization reversal in thin films of $Co_{1-x}Tb_x$ alloys and in $Co_{1-x}Tb_x$ -based spin valves. The first point is the understanding of the domain pattern at different points of the reversal process for $Co_{1-x}Tb_x$ (20nm) films. This is a crucial point for the geometric design of samples for domain wall propagation experiments. In a second step we studied the effects of dipolar coupling on reversal for $Co_{1-x}Tb_x$ -based spin valves. Such effects might represent a possibility for controlling the propagation of a domain wall in nanodevices.

2.3.1 Reversal process of CoTb films

2.3.1.1 Domain pattern of CoTb films during reversal

The reversal process of a 20 nm thick $Co_{88}Tb_{12}$ layer is studied. The hysteresis loop for such a layer is represented in the center of fig.(2.16). The field sweep rate was $1mT/s$. The sweep rate of $1mT/s$ was chosen, as this is a typical value for our standard transport measurements. We start our discussion for a sample that is saturated in a strong perpendicular field. The sample shows a 100% remanence. At a certain critical field, here around 46 mT, the perpendicular moment drops very sharply with increasing field until it reaches a small value in the direction antiparallel to the original saturation. The distance between the nucleation field and the coercive field is about 2 mT. To saturate the sample in the direction antiparallel to the original orientation, the field has to be further increased by about 20 mT. The domain structure of the remanence of different points of the reversal process was imaged by Kerr microscopy, by magnetic force microscopy (MFM) and by circular magnetic dichroism (XMCD)¹. As we see from the loop, the magnetic moment does not change if the field is set back to zero during the reversal process. Hence we suppose, that the domain structure of the remanent state is the same as the domain structure, when the field is applied. A first series of images was taken by Kerr microscopy after applying a field sufficiently high to nucleate reversed domains (see fig.(2.16)a-c). The images show a $2 \times 3mm$ zone of the sample. About 25 nucleated domains can be observed corresponding to a density of approximately 5 nucleation points per mm^2 . 2 nucleation points appear only on one of the three images, further three appear on two of the three images, all other points are the same for all three images. Thus we conclude that the nucleation points correspond to structural defects, where magnetization can be reversed very easily compared to the rest of the sample. When the field is further increased those few nucleated domains grow by domain wall propagation. This can be seen in fig.(2.16e). The structure is very dendritic, what can be explained by a high number of pinning and depinning events during DW propagation. Close to saturation the residual non reversed domains have the shape of wires. The development of these wire-shaped domains with increasing field was imaged by XMCD at the Co edge (see fig.(2.17)). We observe, that the width of the residual domains shrinks down to a size of 100-200 nm before they disappear. A

¹For a description of these techniques see e.g. [89] for Kerr microscopy, [90] for MFM and [91] for XMCD

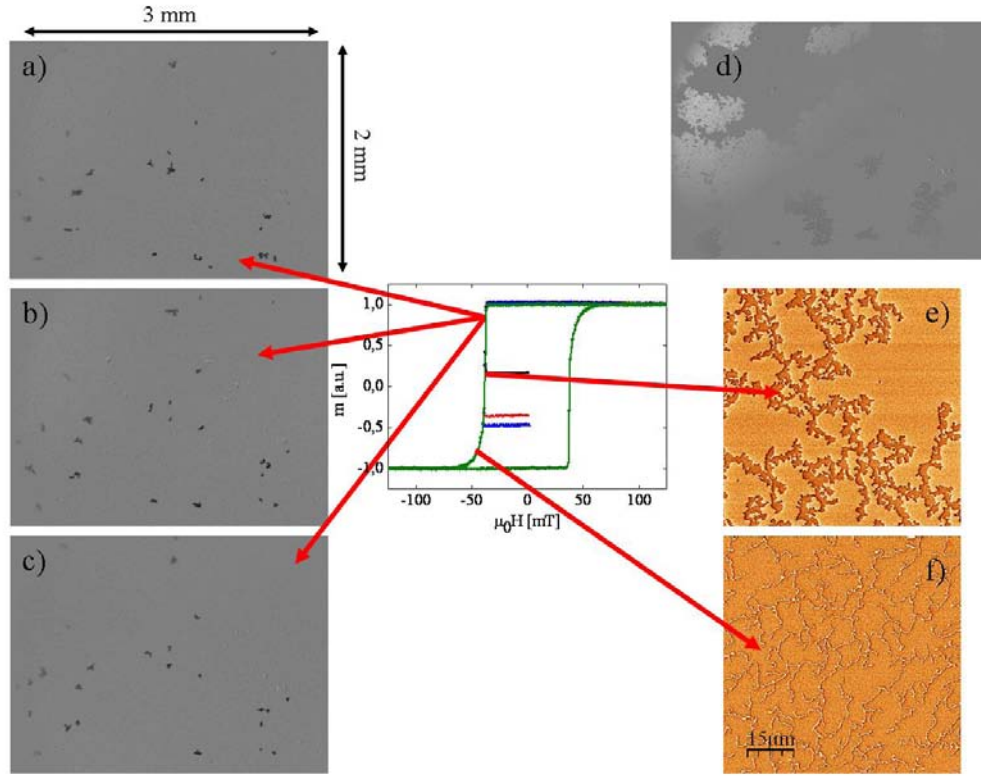


Figure 2.16: Reversal of a $Co_{88}Tb_{12}(20nm)$ layer from a saturated state under a field applied perpendicular to the sample surface. In the center: hysteresis loop obtained by VSM. a), b) and c): Nucleation process imaged by Kerr microscopy for different loops. d) Kerr microscopy image of the domain structure of the following experiment: small domains are nucleated by 2 second long pulses of 45 mT. Then a pulse of 40 mT is applied during 120 seconds. The Kerr contrast is inverted when crossing an imaginary line diagonal from the upper right to the lower left of the image due to an artifact of the microscope. e) MFM image of the domain pattern during reversal (approximately 1/3 of the magnetization reversed, the reversed zone is dark). f) MFM image of the domain pattern during reversal (approximately 85% of the magnetization reversed, not reversed domains bright)

last point is the link between propagation and nucleation fields: we first nucleate small reversed domains as shown in fig.(2.16)a-c) with a 2 second pulse of 45 mT. We apply a field of 40 mT during 120 seconds. The image fig.(2.16d) shows the resulting pattern, showing a growth of the nucleated domains compared to fig.(2.16a-c). For a field of 44 mT no nucleation was observed even when applying pulses up to 1000 seconds. Thus reversal is limited by the nucleation process in $Co_{1-x}Tb_x$ alloys.

We conclude, that for field sweep rates of the order of 1 mT, the reversal happens in two steps: first the nucleation of about 5 reversed domains per mm^2 , then growth of these domains by DW propagation. For other sweep rates the domain structure might differ, we did not study this. The problem of the sweep rate dependency of the domain pattern during reversal is discussed for example by [49] or [92].

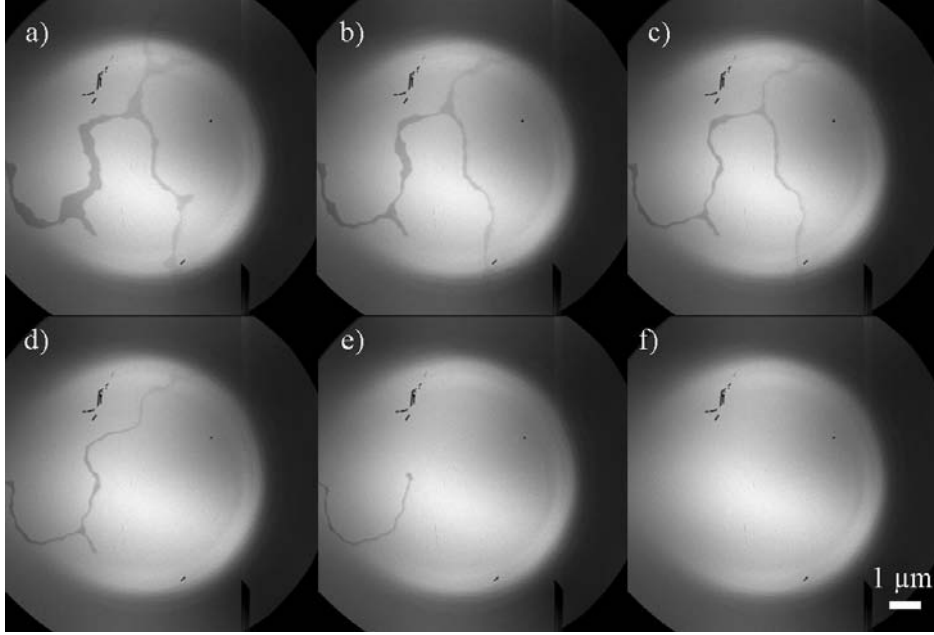


Figure 2.17: XMCD images of the domain pattern of $Co_{88}Tb_{12}$ (20nm) film during the reversal process. The field increases from a) to f).

2.3.1.2 Barkhausen length l_B of the reversal process

The dendritic structure of the domain pattern during reversal is explained as due to a large number of stochastic pinning and depinning events during the propagation process of the domain wall. The average reversed volume between two pinning events is called the Barkhausen volume V_B [93]. A relation between V_B , the field sweep rate dH/dt and the coercive field H_C of thin films can be found in [49]:

$$\mu_0 H_C = \mu_0 H_P + \frac{k_B T}{2V_B M_S} \ln \left[\frac{2V_B M_S}{k_B T} \mu_0 \frac{dH}{dt} \tau_s \ln(2) \right] \quad (2.8)$$

H_P is a constant term describing the strength of the average pinning sites, τ_s is the so-called characteristic switching time of the volume V_B . We measured the coercivity of a $Co_{86}Tb_{14}$ (20nm) and a $Co_{74}Tb_{26}$ (20nm) layer as a function of the field sweep rate dH/dt by VSM at room temperature (fig.(2.18)). The measurement shows the expected logarithmic behavior of the coercivity as a function of the field sweep rate. A linear fit leads to:

$$\frac{k_B T}{2V_B M_S} = (1.3 \pm 0.1)mT \quad (2.9)$$

for $Co_{86}Tb_{14}$ and to

$$\frac{k_B T}{2V_B M_S} = (8.6 \pm 1)mT \quad (2.10)$$

for $Co_{74}Tb_{26}$. With $M_S(Co_{86}Tb_{14}) = 450kA/m$ and $M_S(Co_{74}Tb_{26}) = 150kA/m$ this leads to Barkhausen volumes of $V_B = 3.2 \cdot 10^{-24}m^3$ for $Co_{86}Tb_{14}$ and $V_B = 1.5 \cdot 10^{-24}m^3$ for $Co_{74}Tb_{26}$. We can now determine the Barkhausen length l_B corresponding to the average distance overcome by a DW between two pinning events as:

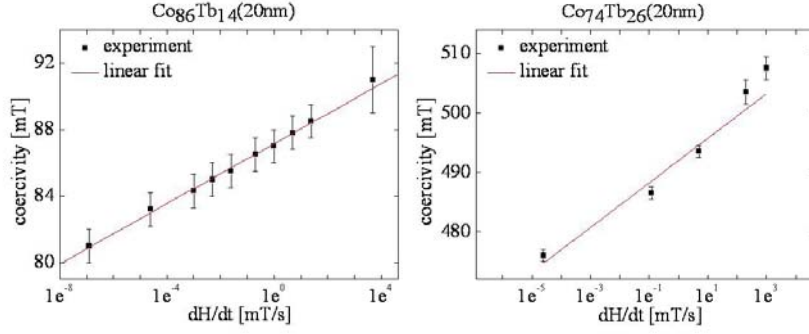


Figure 2.18: Field dependence of the coercivity of a $Co_{86}Tb_{14}(20nm)$ and a $Co_{74}Tb_{26}(20nm)$ layer as a function of the field sweep rate dH/dt measured by VSM at room temperature.

$$l_B = \sqrt{\frac{V_B}{h}} \quad (2.11)$$

where h is the sample thickness, which is of 20 nm in our case. We find $l_B = (12.6 \pm 2)nm$ for $M_S(Co_{86}Tb_{14})$ and $l_B = (8.7 \pm 1.5)nm$ for $M_S(Co_{74}Tb_{26})$ as the typical distance between pinning sites. However it is clear that such kind of model can only be used as long as the applied fields are smaller than the typical pinning fields of the sample.

2.3.1.3 Conclusion on the reversal process

We found, that the reversal process in $Co_{1-x}Tb_x$ thin films happens in two steps: it starts with the nucleation of few reversed domains (about 5 per mm^2) and is followed by the growth of these domains by DW propagation. Pinning and depinning events are quite frequent (about every 10 nm). For the use of $Co_{1-x}Tb_x$ for domain wall propagation experiments in nanowires this has the following consequences:

On the one hand the low density of nucleation points for fields allowing DW propagation is an advantage as nucleation in the wire is very unlikely. On the other hand the stabilization of a DW in the wire is supposed to be difficult. For fields, that are high enough to nucleate a DW, this DW can propagate through the hole wire. A solution to this would be the use of extremely large nucleation pads compared to the wire size, in order to have a reasonable probability to have a nucleation point in the pad with a nucleation field which is not too high compared to the propagation field. Furthermore intrinsic pinning sites seem to play an important role for DW propagation as the determination of the Barkhausen length of the order of 10 nm indicates. This might lead to a complicated analysis of the propagation process in the wire.

2.3.2 Dipolar coupling in CoTb-based spin valves

A crucial point of domain wall propagation experiments is the control of artificial pinning sites. A short explanation of pinning and depinning is given in the introduction of this manuscript sec.(1.3.5). A further idea for an artificial pinning site is presented in fig.(2.19). Instead of a single magnetic layer, a wire with spin valve structure is used.

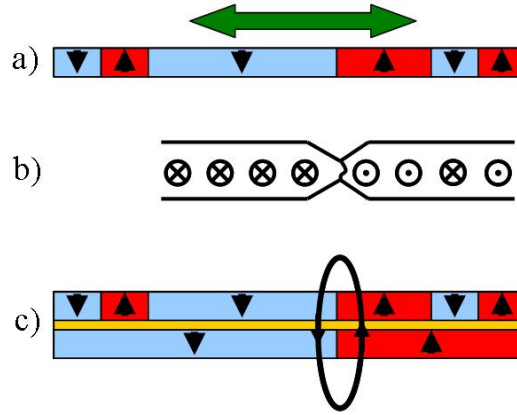


Figure 2.19: a) Sketch of propagating domain walls in a nanowire. b) A constriction as artificial pinning site. c) spin valve structure, where a DW in the hard layer (below) serves as pinning site for a DW in the soft layer (above) due to its dipolar field.

One can imagine, that a DW in the hard layer (HL) might block the propagation of a DW in the soft layer (SL) due to its dipolar field as recently shown by [94].

In literature several dipolar coupling effects in spin valve structures were already studied. It was shown that repetitive cycling of SL minor loops can lead to demagnetization of the HL [95]. Other authors showed, that the shape of the minor loop can be modified due to dipolar interactions between domains in the HL and the SL [96]. Furthermore magnetic domain replication was observed by several authors e.g. [97]. Finally coupling effects for spin valves, where the HL consists of a patterned nanodot array, were shown to be able to modify the propagation of domain-walls during magnetization reversal [98].

In this section we present a study on the dipolar coupling effects for in a full film spin valve structure based on CoTb alloys, which is meant to be a basic analysis for a later work on described wires. First studies were done by VSM. In a second step, the microscopic magnetic structure of the films is analyzed by MFM. Finally we try to compare MFM images and magnetometry results using a simple model of the dipolar coupling effects.

2.3.2.1 Magnetometry results

For the following experiment a sample stack was grown described in fig.(2.20a): the usual 5nm Ta seed layer on the Si substrate, then the magnetic hard layer $Co_{74}Tb_{26}$ with a thickness of 20nm, 3.5nm of Cu as nonmagnetic spacer layer, the 20nm thick magnetic soft layer $Co_{88}Tb_{12}$, and finally 2nm of Cu and 2nm of Pt to prevent the sample from oxidation. We analyzed the sample in every step starting from a sample with virgin magnetic state. This virgin state could not be re-established once the sample was exposed to magnetic fields. The sample was therefore cut in different pieces named A, B, ..., what allowed to start from equivalent magnetic states. In order to be able to compare the critical fields for different hysteresis loops all measurements were done using a field sweep rate of 1 mT/s.

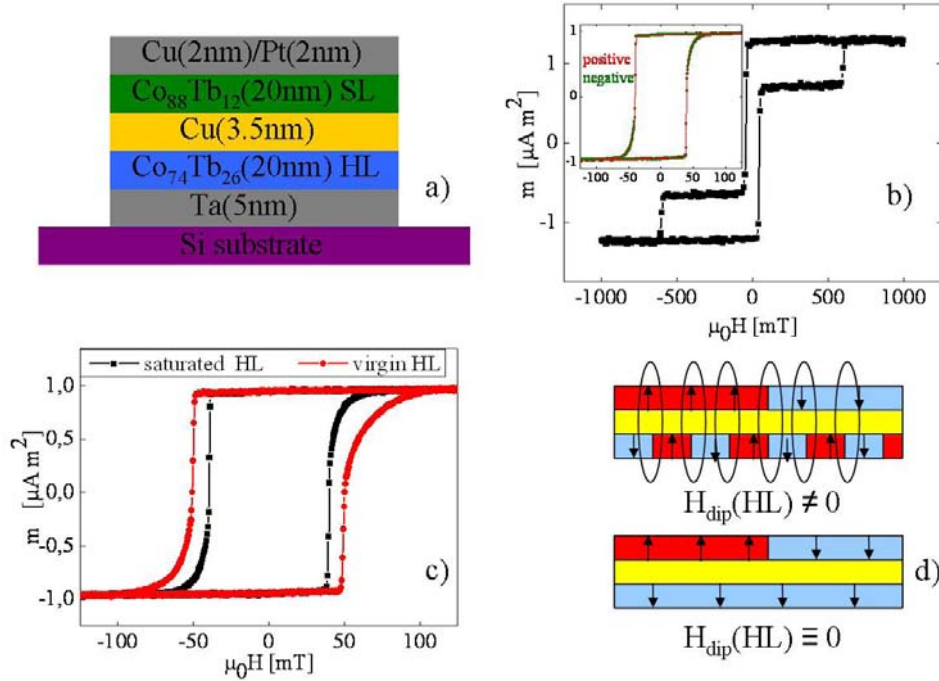


Figure 2.20: CoTb-based spin valve: a) sample stack: hard layer (HL) with $Co_{74}Tb_{26}$ composition separated from soft layer (SL) with $Co_{88}Tb_{12}$ composition by a 3.5 nm Cu layer. b) major hysteresis loop of the described spin valve, in the inset: minor loops with HL saturated to positive maximum value (red) and negative maximum value (green). c) minor hysteresis loops with saturated (black) and virgin (red) hysteresis loop. d) sketches of the domain structure during reversal of the SL when HL is saturated and when HL is in its virgin state.

In fig.(2.20b) one can see a major hysteresis loop of the spin valve. The reversal fields for HL and SL differ for a factor of 10. This should allow to manipulate the magnetization of the SL without changing the magnetic structure of the HL. The magnetization of the HL is $150kA/m$, the SL magnetization is $550kA/m$. In the inset of fig.(2.20b) the superposition of the SL minor loops for the two antiparallel perpendicular saturation states of the HL is shown. The two minor loops are identical, thus we conclude that the SL and the HL are decoupled, when the HL is saturated.

However, when the HL is in its virgin state, effects due to dipolar coupling appear. A first proof is the comparison between the SL minor loops for a saturated HL with the minor loop when the HL is in its virgin state. From fig.(2.20c) we see, that the coercive and the nucleation field are about 12 mT higher for the virgin HL, than for the saturated HL. In addition the necessary field in order to saturate the SL is increased for about 25 mT. Such effects can not be reached, when the HL is demagnetized in an decreasing AC field once it was saturated. The increase of nucleation coercive and saturation-field of the SL must though be due to small domains of the HL virgin state.

In fig.(2.21a) one can see the domain pattern of the spin valve with the HL in its virgin state during the reversal of the SL. The SL domains correspond to the large structure of several μm , the HL domains correspond to the small sub- μm structure in

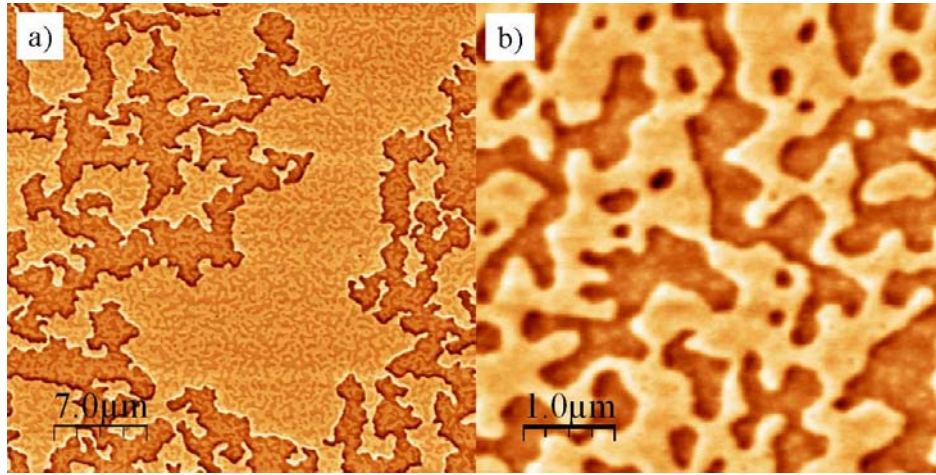


Figure 2.21: a) MFM image of the spin valve during the reversal of the SL magnetization, with the HL in its virgin state. b) MFM image of the HL, with a saturated SL.

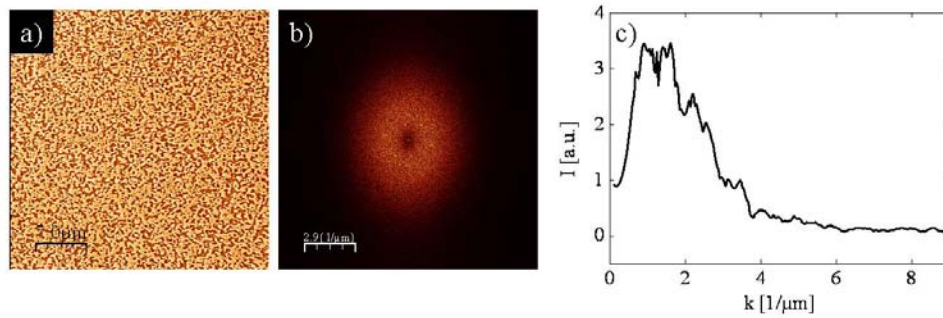


Figure 2.22: a) MFM image of the domain structure of the virgin state of the HL b) Fourier transformation of the HL domain structure. c) Profile of the Fourier-transformed HL domain structure.

the background. An image with high magnification of the HL structure for the case when the SL is saturated is shown in fig.(2.21b). It seems that the domain structure of the HL consists mainly of a large domain which surrounds small domains of a size of the order of a μm . A good approximation of the distribution of the typical domain sizes can be found by doing a Fourier transformation of the HL structure. This is represented in fig.(2.22). We see a maximum of the k -value, describing the inverse wavelength, between 1 and 2 $1/\mu m$. This corresponds to a typical domain size of 0.5 to 1 μm .

In the following we are now going to increase the saturation of the HL in the direction of the big domain for a piece of the sample (A). This direction is defined to be the negative saturation direction. The saturation is defined as the ratio $m_{HL}/m_{HL}(sat)$, where m_{HL} is the magnetic moment of the HL and $m_{HL}(sat)$ the magnetic moment of the HL when it is saturated. In the virgin state the sample has a saturation of about $-20 \pm 5\%$. This can be explained by the existence of a small magnetic field acting on the sample during the sputtering process. In fig.(2.23a) one can see the development of the minor loops with increasing HL saturation in the direction of the large HL domain. Coercivity, nucleation field and saturation field decrease with increasing HL saturation. We define as an "up" reversal a reversal from a state where the SL is

saturated antiparallel to the partial saturation of the HL in its virgin state, to a state where the SL is parallel to the partial saturation of the HL in its virgin state. The inverse case is called a "down" reversal (see inset fig.(2.23b)). The coercivity of the down reversal is found to be slightly higher (1-2 mT) than the coercivity of the up reversal. In fig.(2.23c) one can see a superposition of the up and the down reversal process for a HL saturation of -80% . It seems that for an up-type reversal higher a higher field is needed to saturate the SL. We thus have some kind of antiferromagnetic coupling between the layers. The difference of the up and down reversal is plotted in fig.(2.23d) after normalization to the saturation moment. From the minor loops at different percentages of HL saturation we can then obtain fig.(2.23e) by doing the same analysis. In order to quantify this asymmetry, the normalized difference between up and down reversal was integrated. The integrated asymmetry shows a maximum around -60% HL saturation.

We now take another sample piece (B) and measure its minor loops as a function of the HL saturation, but this time, the HL is saturated in the direction antiparallel to the direction of the big HL domain, which is defined as the positive direction. As the HL has a saturation of -20% in its virgin state, we change the sign of the saturation at some point. The asymmetry of the SL loop is analyzed as in the previous case. One can see, that we also observe a change of the sign of the asymmetry fig. (2.24b). The asymmetry reaches a maximum for a HL saturation between 60 and 80%. However, the amplitude of this maximum seems to be smaller than in the case, where the HL is saturated in the opposite direction. As we used normalized values we can now fit the results for piece A and B together (see fig.(2.24)).

2.3.2.2 Analysis by MFM imaging

For a detailed understanding of this asymmetry due to dipolar coupling, a microscopic picture of the domain structure is necessary. Hence a study by MFM was done. In fig.(2.25) we see the magnetic structure of the HL for different states of saturation. It seems, that the saturation process happens by elimination of domains. A Fourier transformation of the domain structure is done (fig.(2.25d)). A change of the distribution of the domain sizes is not observed. This confirms, that saturation is mainly an elimination process of domains, and does not affect the domain size.

To continue the MFM based study, we imaged the domain structure of the spin valve for an "up" and for a "down" reversal for identical HL saturation (fig.(2.26)). The saturation of the HL is in the direction of the partial saturation of the virgin state. The MFM images for "up" and for "down" reversal show a clear difference concerning the correlation of the domain structures in SL and HL: it seems, that in the case of the "down" reversal (fig.(2.26a)) a similar density of small HL domains can be found in the reversed and in the not reversed zones of the SL. But in the case of the "up" reversal (fig.(2.26b)) only very few HL domains can be found in the reversed part. We hence conclude that the pinning potential of the HL domain pattern is asymmetric with respect to the DW propagation direction and that is due to the small residual domains of the HL.

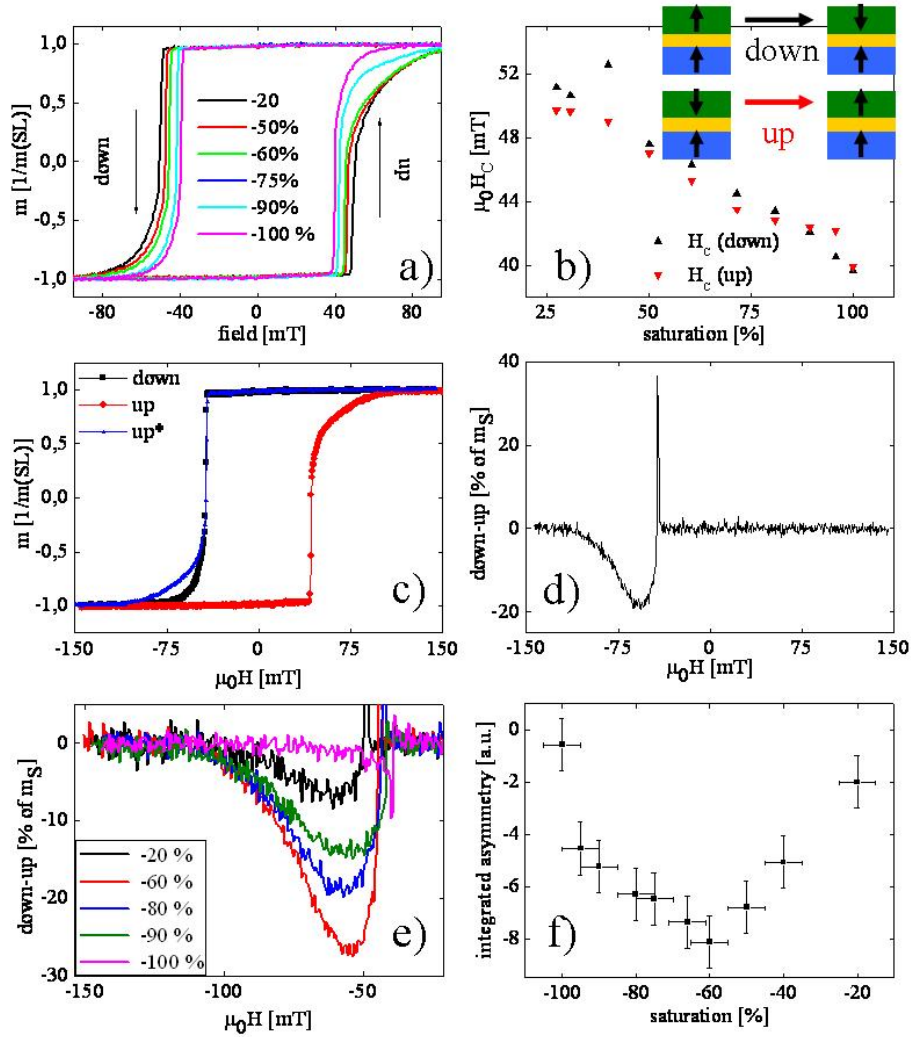


Figure 2.23: Minor-loops: a) minor loops of the SL as a function of saturation of the HL b) coercive fields of the minor loops c) comparison of the up and the down reversal normalized to the saturation moment d) normalized difference between down and up reversal e) normalized difference between down and up reversal as a function of HL saturation f) integrated difference between down and up reversal as a function of HL saturation.

2.3.2.3 Modelization of the dipolar field

In the following we now try to modelize the dipolar field emitted by the HL as a function of position in the SL in order to check the role of the small HL domains. Therefore we use a simple model considering semi-infinite domains as described by [99]. In the case of a single DW in a sample with thickness h , the DW width w , and a saturation magnetization M_S (see fig.(2.27a)), the dipolar stray field H_z perpendicular to the sample surface is given by:

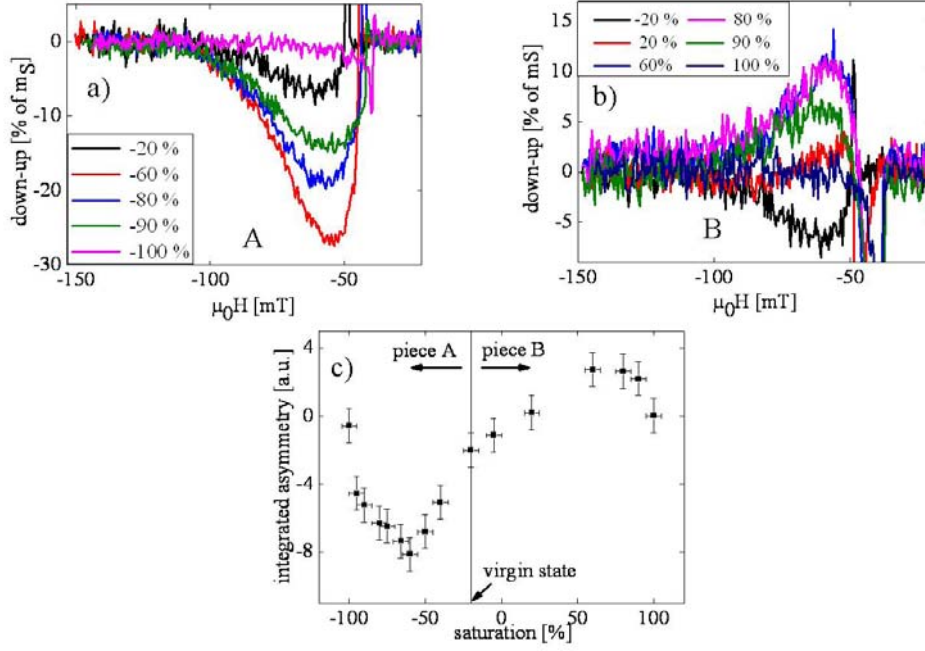


Figure 2.24: Asymmetry of the SL minor loops as a function of the HL saturation. a) Saturation of the HL of a piece A in the direction of the partial HL saturation in its virgin state. b) Saturation of the HL of a piece B in the direction antiparallel to the partial HL saturation in its virgin state. c) Integrated normalized asymmetry as a function of HL saturation for two different sample pieces A and B.

$$H_z = -4M_S \tan^{-1} \left(\frac{xh}{(z+w)(z+w+h) + x^2} \right) \quad (2.12)$$

where x corresponds to the horizontal distance to the center of the DW, and z to the vertical distance to the sample surface. The domain wall width w can be calculated using:

$$w = \pi \sqrt{\frac{A}{K_u}} \quad (2.13)$$

with the exchange stiffness A and the anisotropy K_u . We use $K_u(Co_{74}Tb_{26}) = 500 \text{ kJ/m}^3$ as measured by magnetometry (see sec.(2.2.3)). For A, we do not have any experimental results thus we calculated an approximative value using data from literature. [100] gives the exchange constant J between Co, Fe and Tb for CoTbFe alloys:

- $J_{Co-Co} = (2.4 - 2.5 \cdot x_{Tb}) \cdot 10^{-21} J$ for $Co_{74}Tb_{26}$ we then have $J_{Co-Co} = 1.75 \cdot 10^{-21} J$
- $J_{Co-Tb} = -2.4 \cdot 10^{-22} J$
- $J_{Tb-Tb} = 0.2 \cdot 10^{-22} J$

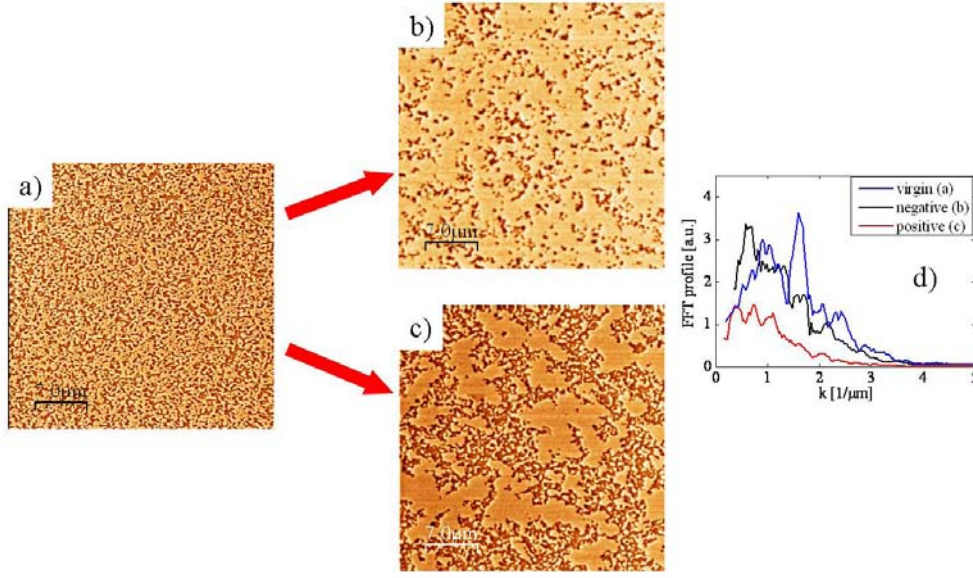


Figure 2.25: Analysis of the HL domain structure for increasing saturation: a) virgin state of the HL b) HL partially saturated in the direction parallel to the partial saturation of the virgin state (negative) c) HL partially saturated antiparallel to the partial saturation of the virgin state (positive, contrast inverted compared to other images). d) Fourier transformation of the HL domain pattern.

We now use an expression given by [101] to calculate the exchange stiffness A of Gd_xCo_{1-x} alloys and adapt it to Tb_xCo_{1-x} :

$$A = \frac{n_{11}J_{Tb-Tb}\bar{S}_1^2(1-x)^2}{a_{11}} + \frac{(n_{12} + n_{21})|J_{Tb-Co}|\bar{S}_1\bar{S}_2x(1-x)}{a_{12}} + \frac{n_{22}J_{Co-Co}\bar{S}_2^2x^2}{a_{22}} \quad (2.14)$$

Thereby the number of pairs per volume unit is taken as $n_{11} = n_{12} = n_{21} = n_{22} = 2$. The interatomic distance are $a_{11} = 3.5\text{\AA}$, $a_{12} = 3.0\text{\AA}$ and $a_{22} = 2.5\text{\AA}$. The missing parameter is the total angular momentum S_{Tb} and S_{Co} . [100] gives $S_{Tb} = 5.05$ and

$$S_{Co} = 0.775 - 0.848[x_{Tb}/(1 - x_{Tb})]^{1.5} \quad (2.15)$$

leading to $S_{Co}(Co_{74}Tb_{26}) = 0.60$. Combining these values leads to $A(Co_{74}Tb_{26}) \approx 6.2 \cdot 10^{-12} \text{ J/m}$. We hence can expect a DW thickness of about 10 nm.

We though calculate the dipolar field created by a single DW using the following parameters in equation(2.12):

- $w = 10\text{nm}$
- $h = 20\text{nm}$, our film thickness
- $M_S = 150\text{kA/m}$, the saturation magnetization of a $Co_{74}Tb_{26}$ film
- $3.5\text{nm} < z < 23.5\text{nm}$ the range of z -values for the SL of the spin valve.

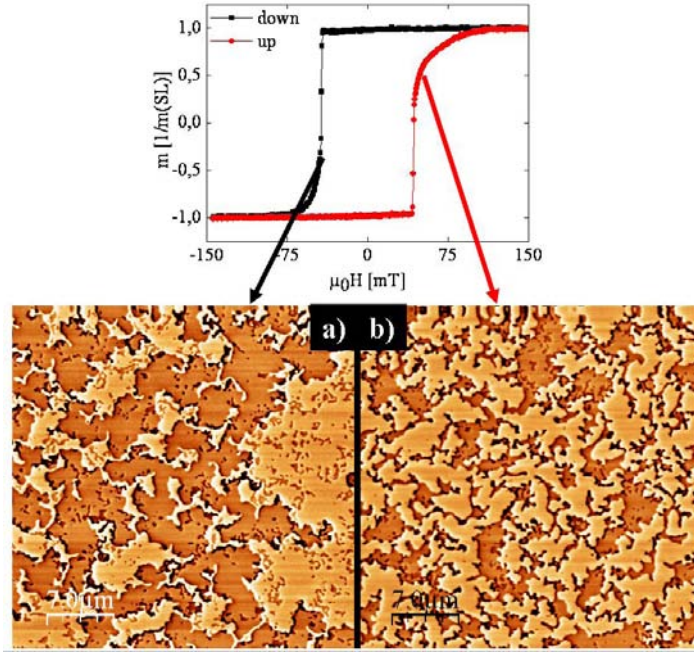


Figure 2.26: MFM images of a CoTb spin valve with partially saturated HL to about 60% in the direction parallel to the partial saturation of the virgin state (negative): a) SL saturated to -20% by VSM, "down" reversal. The reversed zone of the SL is brown, the not reversed zone is yellow. The reversed domains cover about 64% of the image. b) SL saturated $+20\%$ by VSM, "up" reversal. The reversed zone of the SL is yellow, the not reversed zone is brown. The reversed domains cover about 57% of the image.

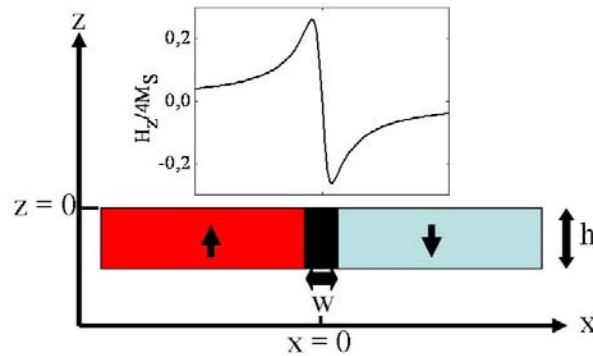


Figure 2.27: Modelization of the dipolar stray field of a DW between two semi-infinite domains. h: sample thickness, w: DW width

In order to keep the calculations simple, we consider $z = 13.5nm$, what corresponds to the center of the SL. To justify this simplification we calculated the dipolar field of a DW for $z = 3.5nm$, the bottom of the SL, $z = 13.5nm$ the SL center and $z = 23.5nm$ the top of the SL, and compared it to the average value of the three results. As we see from fig.(2.28) $z = 13.5nm$ seems to be a good approximation to the average dipolar field inside the SL. The amplitude of the dipolar field is normalized by $4M_S$. With a

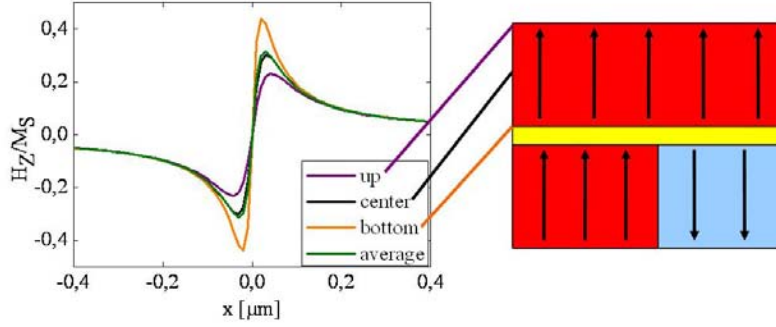


Figure 2.28: Dipolar field emitted by a DW in the HL at different levels inside the SL.

magnetization of $M_S = 150kA/m$, we have:

$$4\mu_0 M_S = 0.75T \quad (2.16)$$

what means, that the dipolar fields due to the HL are at least of the same order of magnitude as the coercivity of the SL.

The dipolar field of a single domain is modeled by adding the dipolar field of two above described domain walls. From the MFM images we know that the HL domains have diameters between 0.1 and $2 \mu m$. We hence decided to use a distance of $0.5 \mu m$ for our calculations. The result for the dipolar field H_Z of such a single domain antiparallel to its environment is plotted in fig.(2.29a). One can see, that the amplitude of the dipolar field is higher in the direction of the small domain, than the dipolar field in the direction of the rest of the sample. The ratio a of the maxima A_{up} and A_{down} is:

$$a = \frac{A_{up}}{A_{down}} = \frac{0.265}{0.345} = 0.77 \quad (2.17)$$

When the number of small domains is high, as in the case of the virgin state of the HL, this asymmetry disappears and we find for the ratio a of the maxima:

$$a = \frac{0.30}{0.30} = 1.0 \quad (2.18)$$

as we can see in fig.(2.29b), meaning that the amplitude of the dipolar field is equal in up and down direction. It seems from the MFM images, that while saturating the HL, clusters, where the original domain structure is conserved, remain. We modeled these clusters using our simple model considering semi-infinite domains. As one can see from fig.(2.30) the asymmetry of the dipolar field is the strongest at the borders of the clusters. The model hence confirms, that clusters consisting of view small domains are an important source of asymmetry as we expected from the MFM images. The missing argument is to find a correlation between the number of small clusters from MFM images as a function of the HL saturation and the asymmetry as a function of the HL saturation as shown in fig.(2.24).

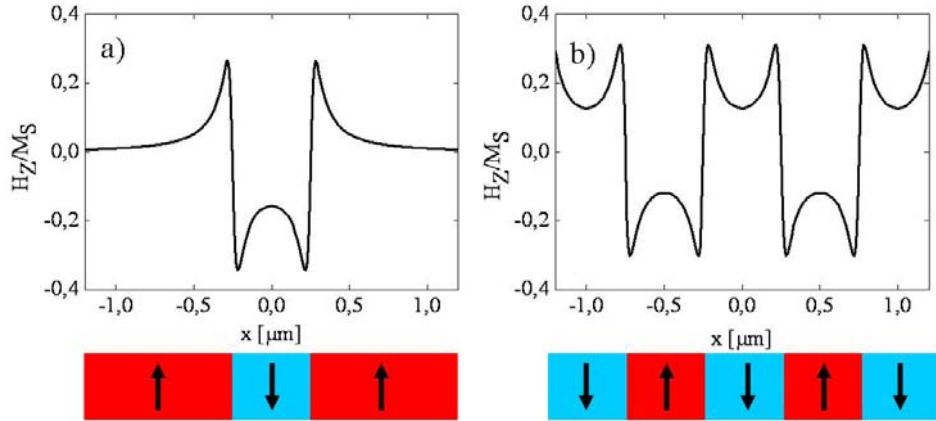


Figure 2.29: a) Dipolar field emitted by a single domain of the size of 0.5 nm antiparallel to its environment as a function of distance to the center of the domain. Dipolar field emitted by an infinity of domains of the size of 0.5 nm as a function of distance to the center of an arbitrarily chosen domain.

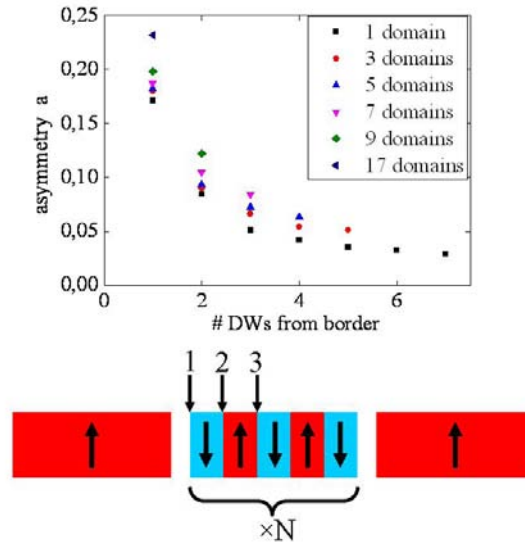


Figure 2.30: Asymmetry as a function of the cluster size.

2.3.2.4 Modification of the nucleation field

In the previous section we explained, that the coercivity and the saturation field of the SL can be modified due to the dipolar-field emitted by domain walls in the HL. From the minor loops one can also see (fig.(2.23)), that the nucleation field is decreasing with increasing HL saturation.

This is in some way surprising, as one could expect, that the dipolar field due to the HL domains locally increases the nucleation probability. In literature such effects were clearly observed and described as an imprinting effect of the HL structure in the

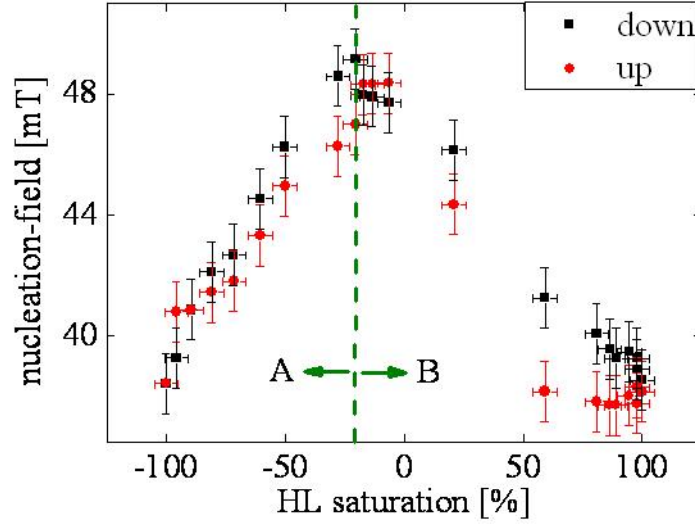


Figure 2.31: Nucleation field of the SL as a function of the HL saturation. A HL saturation of about -20% corresponds to the virgin state of the HL.

SL [96]. It seems, that a decrease of the nucleation field with increasing HL saturation has not been published yet. We do not have any explanation for this behavior for the moment. The difficulty is, that the nucleation points are quite rare, and thus it is very unlikely to observe them by MFM or XMCD, in arbitrarily chosen regions of the sample, as the fields of view are small. A solution would be to bring alignment marks by optical lithography on the sample. One could then observe the position of the nucleation-points by Kerr microscopy in a large field of view, and then find these points again under the reduced field of view of the MFM, with the help of these marks.

2.3.2.5 Conclusion

We showed in this study of dipolar coupling effects in CoTb-based spin valves due to domain walls in the HL can influence the propagation of domain walls in the SL in a significant way. These effects lead to a modification of the shape of the SL minor loop. An asymmetry of the minor loops with the signature of an antiferromagnetic coupling between HL and SL appears. This asymmetry is explained with a simple model considering semi-infinite domains.

2.3.3 Conclusion on magnetization reversal in $Co_{1-x}Tb_x$ alloys and $Co_{1-x}Tb_x$ -based spin valves

In $Co_{1-x}Tb_x$ alloys the reversal in perpendicularly applied field happens by the nucleation of few reversed domains, which then grow by domain wall propagation. This limitation of nucleation events makes them a good material to observe domain wall propagation in nanowires. Furthermore it could be shown, that the domain wall propagation in the soft layer of a spin valve can be tuned using the dipolar field of domain

walls in the hard layer. One can imagine to tune the pinning potential of pinning sites in a nanowire using a spin valve structure with an adapted domain pattern in the HL. In addition this dipolar pinning effect could be tuned by varying the temperature due to the ferrimagnetic character of the $Co_{1-x}Tb_x$ alloys.

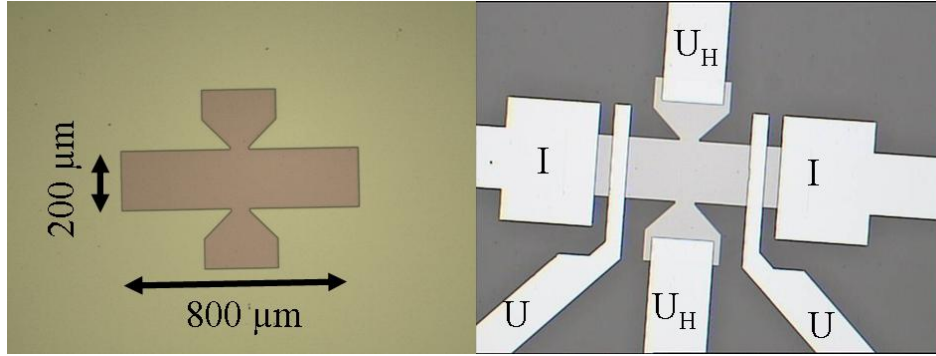


Figure 2.32: Used geometry for the analysis of transport properties. Sample patterned by optical lithography. On the left side we see the magnetic part, on the right side we see the magnetic part with the deposited gold contacts. Current is injected via the contacts marked with an I, voltage is measured on the contacts with U, and Hall voltage is measured on U_H (Hall cross).

2.4 Transport properties of CoTb alloys

As explained in sec.(1.2) magnetoresistive effects can be used to analyze the magnetic state of a nano-structured sample. Therefore we studied the magnetoresistance of our CoTb alloys using samples patterned by optical lithography². The results, discussed in this section, were obtained for samples with a geometrical configuration as presented in fig.(2.32). However, the magnetometry results which are given were obtained on full film samples.

2.4.1 Magnetoresistance of a $Co_{88}Tb_{12}$ layer

A $MgO(3nm)/Co_{88}Tb_{12}(20nm)/MgO(3nm)$ layer was deposited on a silicon substrate. The MgO buffer and capping has the advantage, compared to the Ta, Cu and Pt layers, that it is an isolator. Consequently there is no electrical short circuit to the CoTb layer. The four-point resistance of the sample was 162Ω . The distance between the two contacts for the voltage measurement is $400\mu m$, the film thickness is 20 nm, and the width of the sample is $200\mu m$. This leads to a resistivity of $\rho_{CoTb} = 162\mu\Omega cm$, which is the typical order of magnitude for amorphous RE-TM alloys [102]. The magnetoresistance signal of the Hall voltage and of the longitudinal resistance vs. field were measured by a four-probe measurement. The field was applied perpendicular to the surface (OOP) and parallel to the surface and the electrical current (IP). The results are represented in fig.(2.33).

The Hall signal is explained to be due to a large extraordinary Hall effect (EHE)(see sec.(1.2.3)). We find a maximum Hall resistivity of $\rho_H = 1.35\mu\Omega cm$. This value is of the same order of magnitude as found by [103]. From $\rho_H = \mu_0 M_S R_S$ we can deduce a spontaneous Hall coefficient of $R_S = 1.95\Omega m/T$. This value seems to be very large compared to the normal Hall coefficient, which seems to be too small to be measured. In literature [104] it is explained, that the EHE is large for amorphous systems, due to the large scattering caused by the atomic disorder. The reversal of the Hall resistance is

²Lithography was done by the platform for nano and micro structuration of the IJL "CC-MiNaLor".

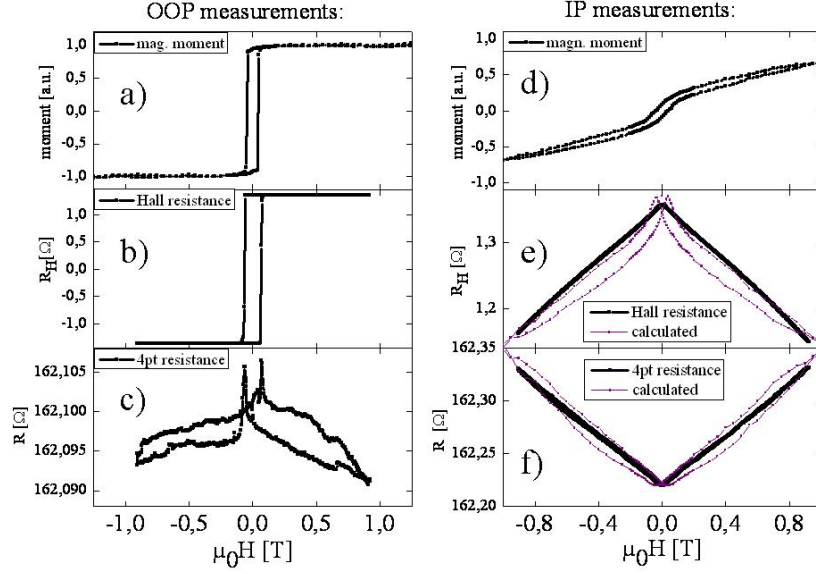


Figure 2.33: Transport measurements for a $MgO(3nm)/Co_{88}Tb_{12}(20nm)/MgO(3nm)$ layer. The field is applied perpendicular to the surface for the results (b-c) and parallel to the surface and the current for the results (e-f). a) and d) correspond to VSM results for full films. In e) and f) the resistance was calculated using equations (2.19) and (2.20), the VSM result, and the experimentally found amplitudes of the magnetoresistive effects.

sharp for the OOP measurement compared to the magnetization reversal of the full film. This is due to very local character of the Hall voltage, which is determined only by the part of the sample inside the Hall cross. For the IP measurement the Hall resistance changes continuously with the applied field. This can be explained by a continuous rotation of the moments inside the Hall cross, as the simulated data shows. This data was obtained in the following way:

The Hall signal is only sensitive to the z-component of the magnetization. For an IP measurement, considering the reversal as a coherent rotation of the moments, we have :

$$R_{Hall}(H) = R_{Hall}(H = 0) \cdot \cos \left[\arcsin \left| \frac{m_{IP}}{m_S} \right| \right] \quad (2.19)$$

with m_S the saturation moment and m_{IP} the in-plane moment measured by magnetometry. The obtained values are plotted with the experimental EHE-data in fig.(2.33e). The difference between calculated and experimental values might be due to a reversal, which is not coherent for the whole macroscopic sample measured by magnetometry. We conclude, that the large observed EHE and its local character make it a good tool to study DW propagation in CoTb-based nanowires.

The results for the resistance as a function of field (see fig.(2.33b,e)) can be explained as AMR effect (see sec.(1.2.1). Similar to the EHE one can calculate the AMR supposing the reversal to be a coherent rotation, when the field is applied in-plane. We find:

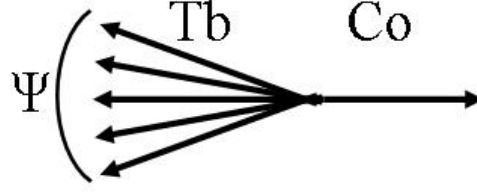


Figure 2.34: Sperrimagnetic order of CoTb alloys. The orientation of the Tb moments is distributed inside a cone with angle Φ . [106]

$$R(H) = R(H = 0) + A \cdot \left[\sin \left| \frac{m_{IP}}{m_S} \right| \right]^2 \quad (2.20)$$

with A , the maximum amplitude of the resistance change due to AMR, and $R(H = 0)$ the resistance of the sample when no field is applied. Such a behavior fits to our experimental data using $R(H = 0) = 162.225\Omega$ and $A = 0,28\Omega$. This leads to a maximum AMR of 0,17%. Similar AMR was found for TbFe alloys by [105].

For the resistance measurements, where the field is applied OOP, we observe two peaks of the resistance around the reversal fields observed by magnetometry and Hall measurement. In literature [105] this is explained as an AMR contribution of the DWs which appear during reversal. The signal to noise ratio is not very large for this measurement, however we think that a decrease of the resistance with field can be observed. It is expected, that the Tb moments are not aligned perfectly parallel to each other at zero field (see for example [106] or [74]). Their orientations are distributed inside a cone with the opening angle Φ (see fig.(2.34)). This angle shrinks when a strong perpendicular field is applied. Consequently the part of the magnetization, which is perpendicular to the IP current increases slightly and the resistance decreases due to AMR.

We conclude that the magnetization reversal in CoTb alloys gives rise to resistance changes due to AMR. However these are small and hence not very effective to study reversal processes.

2.4.2 Magnetoresistance of CoTb-based spin valves

CoTb-based spin valves with different compositions were grown on silicon substrates. Their structure was $Ta(5nm)/Co_{1-x}Tb_x(20nm)/Cu(3.5nm)/Co_{1-y}Tb_y(20nm)/Cu(2nm)/Pt(2nm)$. We used the same pattern (fig.(2.32)) as for the transport measurements with the single CoTb layer. Different combinations of sample compositions were studied. The idea was to have spin valves with both layers rich in Co ($x = 80$ and $y = 88$), both layers rich in Tb ($x = 77$ and $y = 74$) and a spin valve with one layer rich in Tb and one layer rich in Co ($x = 74$ and $y = 88$). The hysteresis loops obtained from magnetometry are shown in fig.(2.35a-c). We observe a reversal of the sign of the EHE, when passing from the Co-rich to the Tb-rich alloys as observed by [103]. The EHE in pure RE metals is known to be negative, the EHE of pure TM elements except Ni is known to be positive. However it is still unclear if the EHE in amorphous RE-TM alloys is due

to the TM sublattice, the RE sublattice or if the EHE is the sum of both. More details and bibliography on this subject can be found e.g. in [47]. Anyway, all of these three models explain, the reversal of sign of the EHE at the compensation point.

A quantitative analysis of the EHE in the spin valves is not possible, as we do not know how IP current flow is distributed between the different layers. It seems that the contribution to the Hall resistance of the layer, which is richer in Co is more important than the contribution of the layer which is richer in Tb. This can be explained by an increase of the normal resistivity of CoTb alloys with increasing Tb-content [103]. When a layer is more resistive than another, less current flows through it and consequently the Hall signal is smaller, compared to a layer with same Hall coefficients but lower resistivity.

Finally also resistance was measured as a function of field fig.(2.35g-i). A GMR signal with an amplitude of $0.018 \pm 0.004\%$ can be observed for all three spin valves. Furthermore a reversal of the sign of GMR is observed for the spinvalve consisting of a Tb-rich and a Co-rich layer fig.(2.35i). The reversal of the sign of GMR for spin valves with a RE-rich and a TM-rich layer was already observed for example for CoFeGd alloys [107] and for CoFeTb and CoFeGd alloys by [108]. In the cited literature the GMR is explained as only dependent on the TM sublattice. Consequently the resistance is minimum, when the TM sublattices are parallel, and it is maximum when the TM sublattices are antiparallel. For a spin valve with a Co-rich and a Tb-rich layer the Co sublattices are antiparallel when the netmoments are parallel, the resistance is maximum. When the netmoments are antiparallel, the Co sublattices are parallel and the resistance is minimum. When both layers are RE-rich, both Co sublattices are antiparallel to the netmoments. Hence the sign of the GMR is as usual in this case: a high resistance for antiparallel netmoments and a low resistance for parallel netmoments.

In [107] it is said, that the amplitude of GMR for RE-TM alloys is expected to be small compared to pure TM layers because of spin-orbit scattering due to the RE-element. However, the amplitude of the observed GMR is still small compared to the values up to 1% CIP GMR observed by [108]. This can be explained by shunting due to our metallic buffer and capping layers. Furthermore we used a thicker Cu spacer (3.5 nm compared to down to 1.4 nm used by [108]) in order to avoid exchange coupling.

The important result of this experiment is, that a current can be spin-polarized by CoTb alloys, and that the sign of this polarization can be changed relatively to the netmoment orientation, by crossing the compensation point between RE-rich and TM-rich alloys.

2.4.3 Temperature dependence of magnetoresistance

In sec.(2.2) we showed that magnetization and anisotropy of CoTb alloys can be tuned in wide ranges by changing the temperature. In this section we are going to study the influence of temperature on the transport properties of our samples. First we measured resistance and Hall resistance of a $Ta(5nm)/Co_{88}Tb_{12}(20nm)/Cu(2nm)/Pt(2nm)$ sample as a function of temperature (see fig.(2.36)). We can calculate a change of resistivity with temperature of:

$$\frac{\partial \rho}{\partial T} = 8.7 \frac{n\Omega cm}{K} \quad (2.21)$$

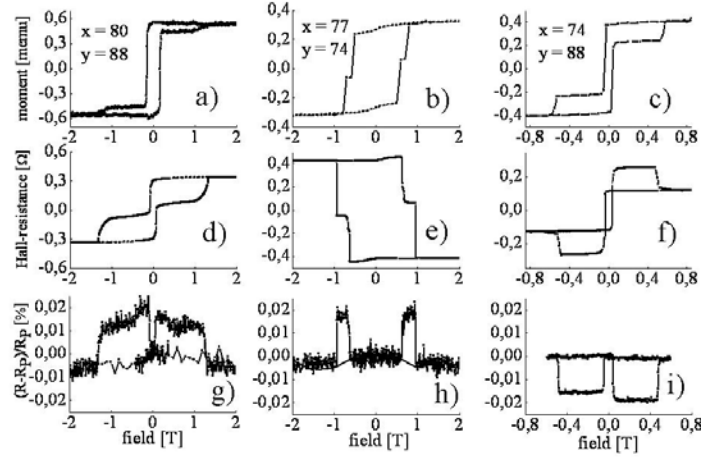


Figure 2.35: Transport properties of $Ta(5nm)/Co_{1-x}Tb_x(20nm)/Cu(3.5nm)/Co_{1-y}Tb_y(20nm)/Cu(2nm)/Pt(2nm)$. a-c) magnetometry hysteresis loops. d-f) hysteresis loops of the Hall resistance. g-i) hysteresis loops of GMR

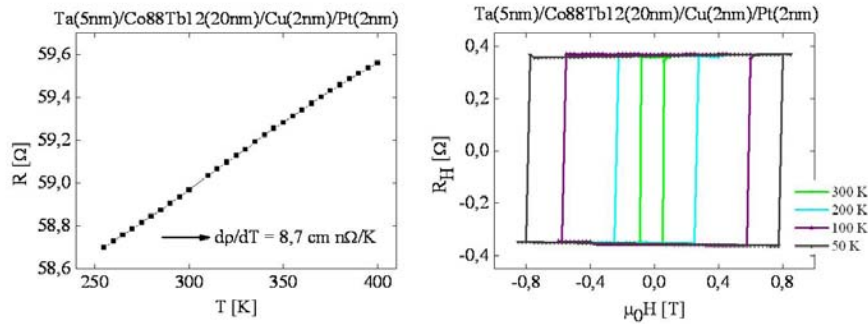


Figure 2.36: Temperature dependence of the resistance and the Hall-resistance of a $Ta(5nm)/Co_{88}Tb_{12}(20nm)/Cu(2nm)/Pt(2nm)$ sample.

and a resistivity of about $86\mu\Omega cm$. The relative change of the resistivity is about $\frac{\partial\rho/\partial T}{\rho} = 10^{-4}/K$. Models describing the resistivity of amorphous metals have been developed for example by [109]. Experimentally, both increase and decrease of resistivity with temperature has been observed for amorphous metals [110]. We decided not to work on this problem for our samples and to limit ourself to the use of the results for further interpretation of data.

The Hall resistivity of the $Co_{88}Tb_{12}$ sample is also found to be independent of temperature (see fig.(2.36)) whereas we know that the magnetization of this sample decreases with decreasing temperature (see sec. 2.2.1). As we have no microscopic explanation to the EHE of our CoTb alloys (see sec. 2.4.1) we do not further discuss this, too.

Finally, the Hall resistance and the GMR of spin valves was analyzed at temperatures

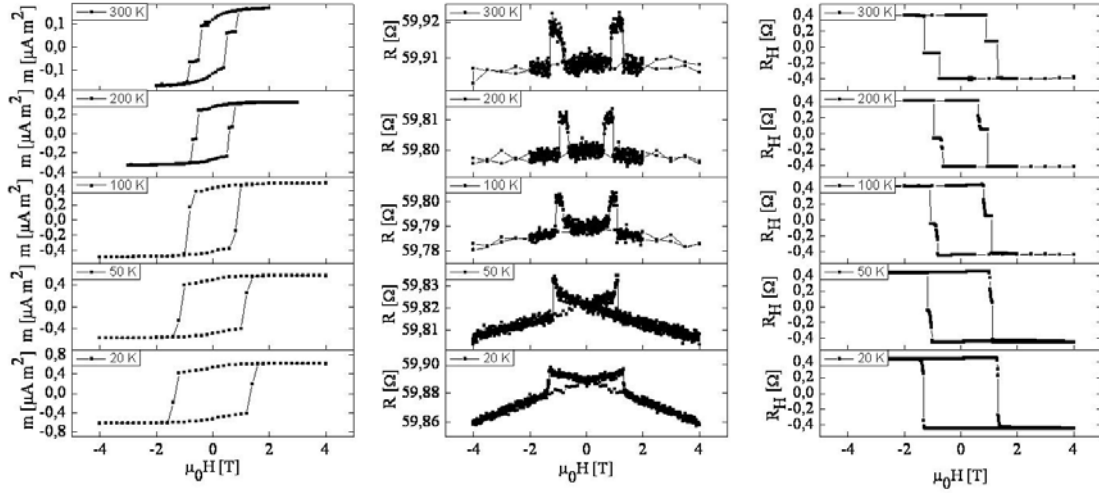


Figure 2.37: Temperature dependence of the magnetoresistance of a $Co_{77}Tb_{23}/Cu/Co_{74}Tb_{26}$ spin valve.

between 50 and 300 K. In fig.(2.37) the results for a spin valve with both layers rich in Tb is represented. As both layers are Tb-dominant, the magnetization of both layers increases with decreasing temperature. For temperatures below 100K the coercivities of both layers are very close and an independent reversal is no longer observed. One can see, that the Hall resistance is independent of temperature between 20 and 300 K as expected from the previous measurement of a single CoTb layer. The GMR seems to be independent from temperature between 100 and 300K, too. For lower temperatures the antiparallel configuration of the magnetic layers was not observed. In addition one can observe a linear variation of resistance with field, which increases when the temperature decreases. Its origin remains unclear to us. Similar signals have been interpreted as magnon contribution to the resistance in literature [111]. However, the magnon contribution is expected to decrease with decreasing temperature. Coercivities of both layers are very close and an independent reversal is no longer observed. One can see, that the Hall resistance is independent of temperature between 20 and 300 K as expected from the previous measurement of a single CoTb layer.

For a second spin valve both layers are Co-dominant at room temperature. However one of the layers has a compensation point at around $T_{comp} = 235K$ (see fig. (2.38g)). Consequently the Hall signal of this $Co_{80}Tb_{20}$ layer changes its sign when passing from the Co-dominant to the Tb-dominant regime (see fig. (2.38b and e)). Furthermore the GMR signal also changes its sign (see fig. (2.38c and f)). We then measured the GMR of the spin valve when the $Co_{80}Tb_{20}$ layer is compensated. First the temperature was set to 250 K (above T_{comp}), then a field of 9T was applied and the sample was cooled down to 235 K at zero field. As the $Co_{80}Tb_{20}$ layer has no netmagnetization at this temperature only a minor loop of the $Co_{88}Tb_{12}$ layer can be observed. Amplitude and sign of the GMR correspond to what is expected, when Co moments of $Co_{80}Tb_{20}$ are aligned in a positive field. For the extraordinary Hall coefficient of $Co_{80}Tb_{20}$ we find $R_H \rightarrow +\infty$. In a second step the temperature was set to 200 K (lower than T_{comp}) and a field of 9T was applied before heating up the sample to 235 K at zero field. The minor

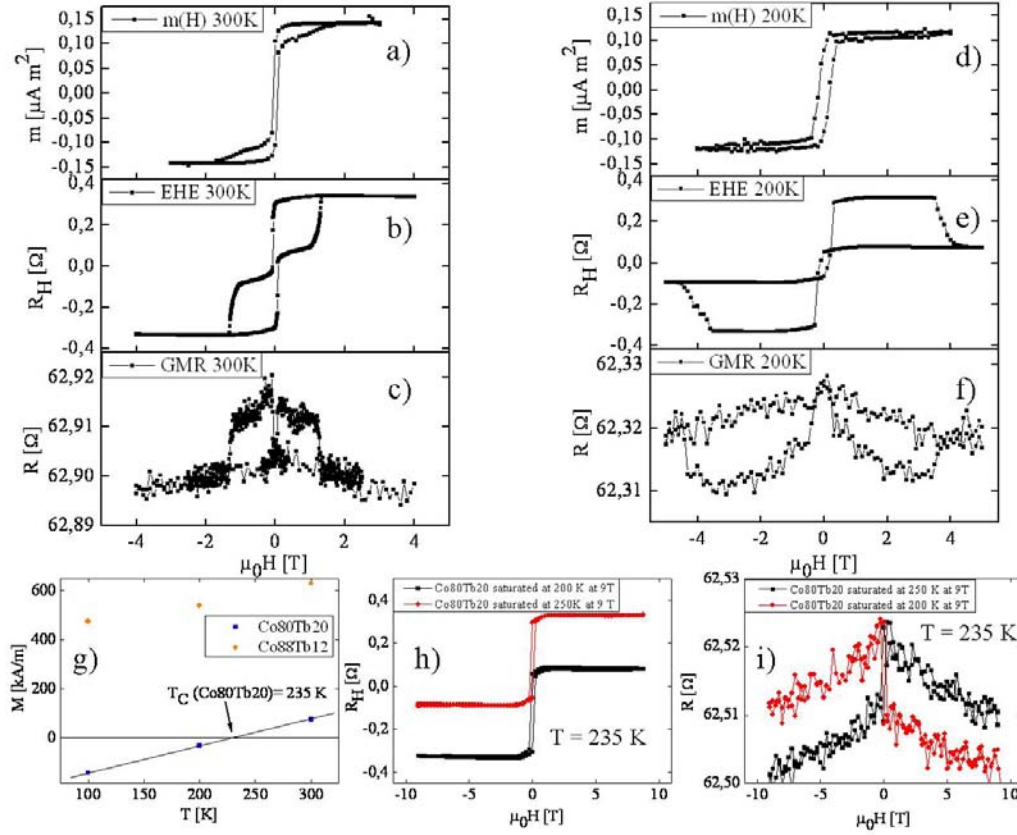


Figure 2.38: Magnetoresistance of a spin-valve at the compensation point of one of the layers. Used spin valve: $Co_{80}Tb_{20}/Cu/Co_{88}Tb_{12}$

loop of the magneto resistance corresponds now to what is expected, when Tb-moments of $Co_{80}Tb_{20}$ are aligned in a positive field. For the extraordinary Hall coefficient of $Co_{80}Tb_{20}$ we find $R_H \rightarrow -\infty$.

We make the following conclusions for the magnetoresistance of CoTb alloys as a function of temperature: First, the amplitude of magnetoresistive effects like the EHE and the GMR is independent of temperature. And second, the sign of the magnetoresistive effects changes, when passing a compensation temperature. The change of the sign can be well understood, as the magnetoresistance depends on the orientation of the Co and the Tb sublattice. However we leave the independence of the amplitude of magnetoresistive effects unexplained.

2.4.4 Angular dependence of magnetoresistance in CoTb alloys

We finished our investigation on magnetoresistance of CoTb alloys by analyzing the angular dependence of the magnetoresistive effects. Loops were measured with the field applied perpendicular to the sample surface (0° with the easy axis), at 30° , 60° and in-plane (90°). The maximum applied field was limited to $0.9T$ due to the used experimental set-up.

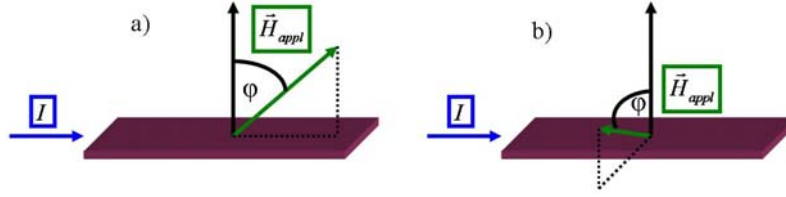


Figure 2.39: Different configurations for resistance measurements. a) Rotation of the applied field from perpendicular to the current at 0° , to parallel to the current at 90° . b) Applied field rotating in a plane perpendicular to the current.

We start with the magnetometry results of a $MgO(3nm)/Co_{88}Tb_{12}(20nm)/MgO(3nm)$ film. The measurement was done by VSM, which measures the moment of the sample which is aligned with the applied field. The coercivity increases, when the angle between easy axis and applied field increases, as it is expected for reversal by DW propagation (see sec.(2.3.1)). Except for the case, when the field is applied along the easy axis, the sample can not be saturated in the direction of the applied field (see fig.(2.40a)). The Hall resistance is proportional to the component of the magnetic moment, which is perpendicular to the sample surface. Consequently its amplitude is maximum at zero field and it decreases with increasing field as the magnetic moment is more and more along the axis of the applied field (see fig.(2.40b)). Finally we measured the resistance vs. field at different angles. For this measurement two different rotation directions were chosen. One case, where the applied field is rotated from perpendicular to the current at 0° , to parallel to the current at 90° (see fig.(2.39a)). And one case, where the applied field is rotated in a plane perpendicular to the current (see fig.(2.39b)). The resistance measurement of fig.(2.40c) corresponds to configuration fig.(2.39a) and (see fig.(2.40d)) corresponds to fig.(2.39b). Consequently, we can see an AMR signal appear, when increasing the angle between easy axis and field for fig.(2.40c). The small signal appearing in fig.(2.40d) which has the shape of an AMR signal, but a very small amplitude, can be explained by a small misalignment of the sample, and also have AMR as origin. Furthermore we can observe for both configurations similar peaks of the resistance around the coercive field. These peaks correspond to the AMR of the DWs, which appear during reversal.

The angular dependence of the magnetoresistance of a $Co_{74}Tb_{26}/Cu/Co_{88}Tb_{12}$ spin valve is represented in fig.(2.41).

As for the single layer saturation along the applied field is not obtained when the field is not applied in the directions of the easy axis (see fig.(2.41a)). We observe, as in the case of the single layer, a maximum of the Hall resistance amplitudes at zero field. However as one layer is Co-dominant and one layer is Tb-dominant, the EHE of the layers has not the same sign. The more the magnetic moments are misaligned with the easy axis by the applied field, the smaller the amplitude of the EHE becomes, as the EHE signal is only proportional to the part of the magnetization, which is perpendicular to the surface (see fig.(2.41b)). The resistance change due to GMR, when magnetization is reversed, shrinks slightly, when increasing the angle between applied field and easy axis (see fig.(2.41c)). This can be explained by the fact, that the maximum angle between both magnetizations is smaller than π when the applied field

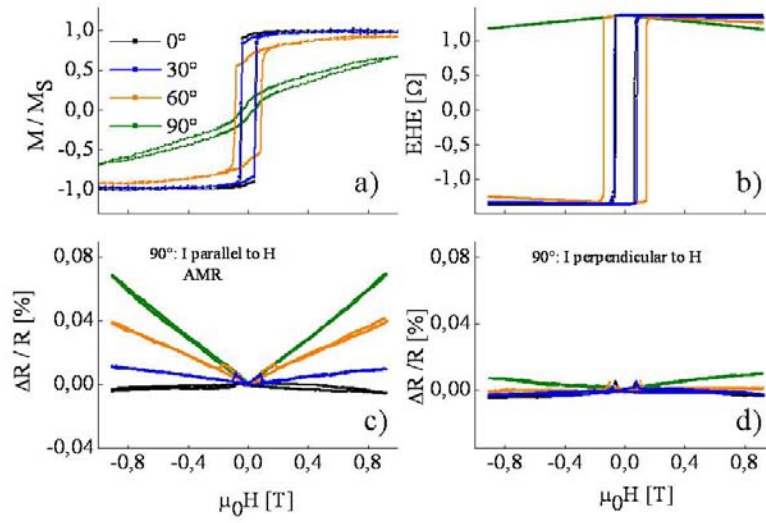


Figure 2.40: Results of magnetometry and transport measurements for a $MgO(3nm)/Co_{88}Tb_{12}(20nm)/MgO(3nm)$ film. Angle ϕ between normal to the surface and the surface varied between 0° and 90° (0° means measurement of an OOP loop). a) hysteresis loops by VSM. b) Hall resistance vs applied field. c) Resistance vs applied field, field rotating from perpendicular to the current at 0° , to parallel to the current at 90° . d) Resistance vs applied field, field rotating in a plane perpendicular to the current.

is misaligned with the easy axis. The small nearly linear increase of resistance with increasing field for large angles between applied field and easy axis, can be explained by the AMR contribution, that appears in this configuration.

2.4.5 Conclusion on the magnetoresistance of CoTb alloys

Extraordinary Hall effect, anisotropic magnetoresistance and for spin valves, giant magnetoresistance were observed. The EHE signal is large and allows to precisely analyze the z-component of the magnetization inside a Hall cross. Furthermore, as its sign changes when crossing the compensation point it is a good tool to detect the crossing of such a critical point. The presence of DWs in the sample can be detected due to AMR. However this signal is very small and a practical use will be difficult. GMR is also very small, but nevertheless, its existence proves that an electric current gets spin-polarized when passing through a CoTb layer, what is essential for spin torque experiments.

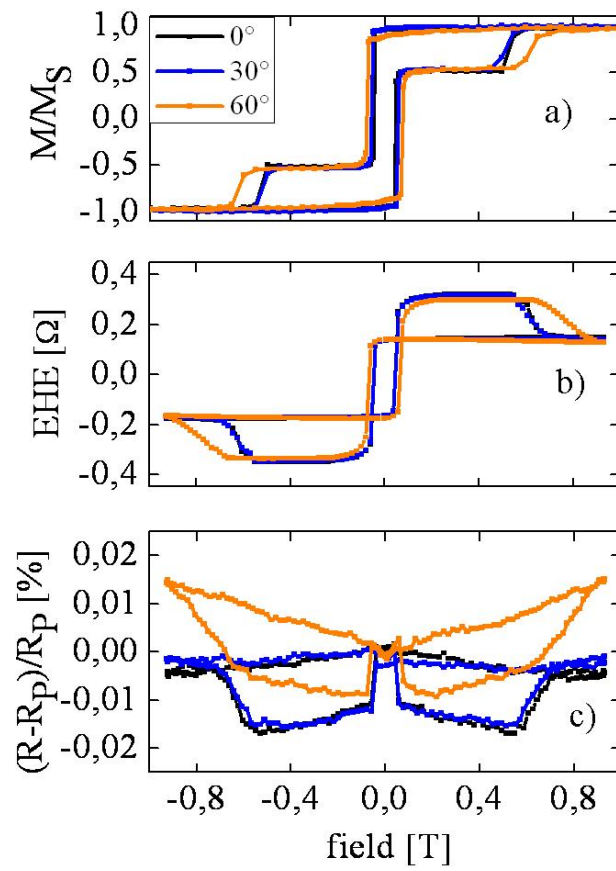


Figure 2.41: Angular dependence of magnetoresistance for a $Co_{74}Tb_{26}/Cu/Co_{88}Tb_{12}$ spin valve. a) VSM results. b) Hall resistance. c) GMR.

2.5 All-Optical magnetization switching in $Co_{1-x}Tb_x$ alloys

In this section we give a short overview of results which were recently obtained on all-optical magnetization reversal in cooperation with M. Aeschlimann's group at the University of Kaiserslautern. The obtained results open new perspectives for $Co_{1-x}Tb_x$ alloys apart from the intended spin torque experiments.

2.5.1 Mechanisms of all-optical magnetization switching

In the introduction of this script (sec.(1.3) and (1.4)) we discussed the reversal of magnetization under magnetic fields and spin-polarized electric currents. Recently it has been reported that the perpendicular magnetization of thin film GdCoFe alloys can be reversibly switched using circularly polarized laser light [112]. The mechanisms behind this phenomenon (e.g. the role of the temperature increase when the material is exposed to the laser beam [113]) are not understood yet. New materials would allow to get further insight in the involved processes. For more information on optical manipulation of magnetization one should consider e.g. [114].

2.5.2 First results obtained for $Co_{1-x}Tb_x$ alloys

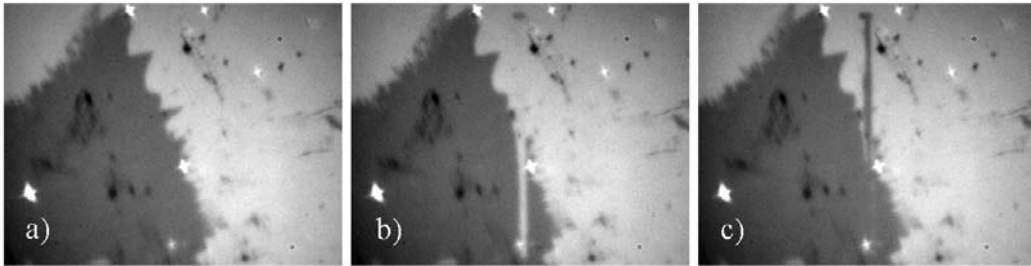


Figure 2.42: Demonstration of all-optical switching in for a 20nm thick $Co_{74}Tb_{26}$ film. Intensity of the laser beam is of the order of $10mJ/cm^2$. a) Faraday image of the magnetic domainstructure created in the sample using a permanent magnet before exposure to a circular-polarized laser beam. b) After exposure to a circular-polarized laser beam. c) After exposure to a circular-polarized laser beam with opposite helicity. The width of the written line-shaped domain is of the order of $20\mu m$.

A series of eight 20nm thick $Co_{1-x}Tb_x$ samples was grown on glass substrates. The composition x was varied in a large range ($x \in [0.12; 0.32]$). Glass substrate was chosen in order to allow to analyze the domain structure using Faraday effect. Optical experiments were done by M. Aeschlimann's group. The magnetic properties of the samples were measured using VSM and SQUID magnetometry in our lab.

A demonstration of the all-optical switching process is shown in fig.(2.42). The sample is first saturated and then a domain wall is created in the part of the sample inside the field of view of the experiment (fig.(2.42)a). In a next step a circularly polarized laser spot is moved over the sample. The used laser beam is pulsed with a pulse width of the order of several tenth of femto seconds. Pulses are repeated at a kHz

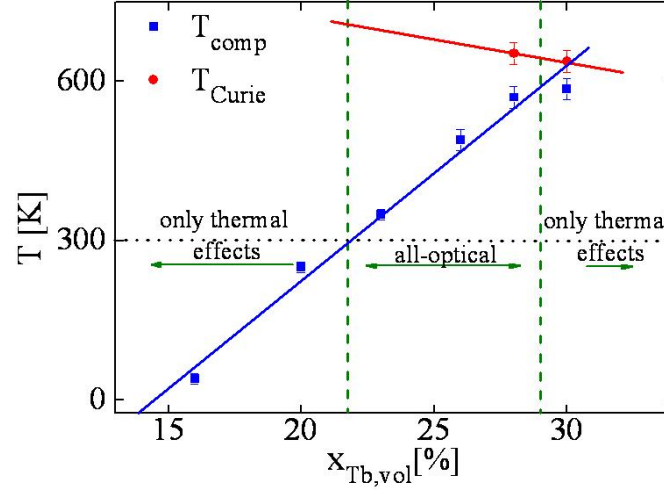


Figure 2.43: All-optical switching as a function of the sample composition for 20nm thick Co_xTb_{1-x} films. All-optical switching at room temperature is observed for three compositions: $Co_{77}Tb_{23}$, $Co_{74}Tb_{26}$ and $Co_{72}Tb_{28}$. For other samples only demagnetization due to heating by the laser spot could be observed.

frequency. A line-shaped reversed domain of a width of about $20\mu m$ is created inside the darker domain of (fig.(2.42)b) inside the zone which was exposed to the laser. The brighter domain remains unaffected. Then the helicity of the laser beam is reversed and the same area of the sample is exposed to the beam. As we see from fig.(2.42c) the previously created line-shaped domain in the darker domain disappears and a new line-shaped reversed domain is created inside the brighter domain. This proves, that the magnetization can be reversibly switched between the two antiparallel orientations of the perpendicular magnetization by using the helicity of the laser beam.

The above described all-optical switching was only observed in a certain range of sample compositions (see fig.(2.43)). All sample compositions for which all-optical switching was observed were samples with compensation temperatures T_{comp} above room temperature ($x_{vol,Tb} > 0.2$). Necessary intensities of the laser beam were of the order of $10mJ/cm^2$. Significant dependency on the sample composition was not found. However for samples with $x_{vol,Tb} > 0.28$ that all-optical switching phenomenon could not be observed any longer. For samples containing more than 28% of Tb the compensation temperature T_{comp} and the Curie temperature T_{Curie} are quite close. For samples containing more than 30% of Tb a compensation temperature does not exist anymore. The question, whether the crossing of the compensation point due to heating during the application of the laser pulses plays a role for the all-optical switching process is subject of current research.

2.5.3 Conclusion and new perspectives

All-optical magnetization reversal could be demonstrated for 20nm thick $Co_{1-x}Tb_x$ films if $x \in]0.2; 0.3[$. The concentration dependency of the all-optical switching phenomenon

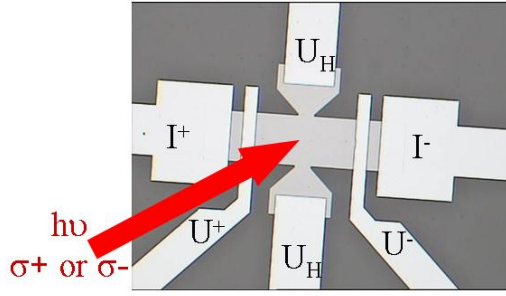


Figure 2.44: Sketch of demonstration experiment in progress: the circular polarized laser beam is supposed to reverse the magnetization by all-optical switching inside the Hall cross of the optically patterned sample. The width of the magnetic part of the sample is $200 \times 800 \mu m^2$.
(compare to fig.(2.32))

might lead to better insight into the physical processes involved in all-optical switching.

At present demonstration experiments which are supposed to show a change of magnetoresistance due to the writing of domains by all-optical switching are in progress. A sketch of the experiment is shown in fig.(2.44). The use of circular polarized light for the reversible manipulation of magnetoresistance might give rise to new magnetic data storage applications.

2.6 Conclusion and perspectives for CoTb alloys

$Co_{1-x}Tb_x$ alloys grown by co-sputtering in a large range of compositions are amorphous. Nevertheless they possess a perpendicular magnetic anisotropy (PMA). This perpendicular magnetic anisotropy as well as the netmagnetization of this ferrimagnet can be tuned in a large range. On the one side, one can choose a sample composition x in a large range (at least $x \in [0.08; 0.34]$) and maintain PMA. On the other side, one can tune the PMA and the magnetization of a chosen composition by sweeping the temperature. Of special interest might be the fact that it is possible to work with very small netmagnetizations as several models of spin transfer torque predict singularities of the dynamics for zero magnetization.

The reversal process of $Co_{1-x}Tb_x$ alloys was studied. Magnetization reversal in perpendicular applied fields happens by the nucleation of few reversed domains, which then grow by domain wall propagation. The limited number of nucleation events makes the system suitable for domain wall propagation experiments in nanowires. Studying the reversal process in spin valve structures by magnetometry and magnetic force microscopy we showed, that the propagation of domain walls can be tuned by using dipolar interactions between the two magnetic layers. This opens an interesting option for the control of artificial pinning sites in nanowires.

Several magnetoresistive effects have been analyzed for $Co_{1-x}Tb_x$ alloys. A large extraordinary Hall effect was found, which can be used for the observation of magnetic domain wall motion in nanowires. Spin valves based on CoTb alloys show a small ($GMR \approx 0.015\%$) GMR effect. This proves that a spin-polarized current can be injected in the spacer layer of the structure. The GMR was shown to be due to the relative sublattice orientation of the Co and Tb sublattice and not to the orientation of the magnetic netmoments of the layers. This allows also to observe GMR, when one of the magnetic layers is compensated and has no magnetization.

We conclude, that $Co_{1-x}Tb_x$ alloys are a model system for spin transfer torque experiments in the sense, that their magnetic properties can be tuned. The analysis of magnetization reversal showed, that they are suitable for current induced domain wall propagation experiments. Transport measurements showed that $Co_{1-x}Tb_x$ alloys can spin-polarize a current. These results are encouraging for future spin transfer torque experiments.

First basic experiments with nanowires could be done, however single domain wall propagation in a CoTb nanowire could not be shown yet. The necessary samples exist, microscopy with a Kerr microscope allowing to apply sufficiently high fields are in progress. The observation of single domain wall motion under field would be the next key point on the way to current induced domain wall motion in the CoTb system.

The elaboration of nanopillars from spin valve structures is in progress by collaborating labs.

Finally all-optical switching for several $Co_{1-x}Tb_x$ alloys was shown. This opens a new field for the use of this material apart from spin torque. The found range of sample compositions allowing all-optical switching leads to the assumption, that the crossing of the ferrimagnetic compensation point might play an important role for the still not understood mechanism of this effect. Experiments combining magnetoresistance measurements with all-optical switching are in progress in collaboration with M. Aeschlimann's group in Kaiserslautern. This might have interesting applications like

new types of magnetic memories.

Chapitre 3

Les super-réseaux $[Co/Ni](111)$ épitaxiés

Nous avons élaboré des super-réseaux $[Co/Ni](111)$ de structure fcc par épitaxie par jets moléculaire (MBE). Ils montrent une forte anisotropie magnétique perpendiculaire. Cette anisotropie est liée à une augmentation du moment orbital aux interfaces Co/Ni . Le paramètre d'amortissement de Gilbert (α) intrinsèque est obtenu ($\alpha \approx 0.01$). La polarisation en spin au niveau de Fermi est forte. Ce matériau est donc un bon candidat pour réaliser des mémoires magnétiques basées sur l'effet de transfert de spin. Des vannes de spin épitaxiées ont pu être élaborées et analysées.

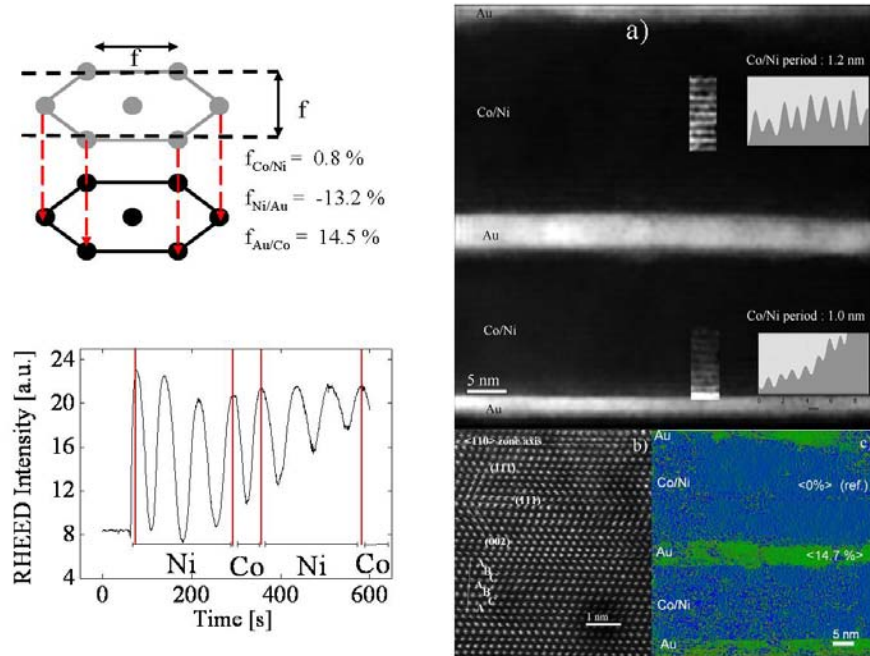


Fig. 3.1: Croissance et structures des super-réseaux $[Co/Ni](111)$. Relations d'épitaxie entre Au, Ni et Co. Oscillations de RHEED observées pendant la croissance du super-réseaux. Analyse détaillée de la structure à l'échelle atomique par des techniques de microscopie électronique en transmission (TEM).

Chapter 3

Epitaxial $[Co/Ni](111)$ superlattices

3.1 Growth and structure of epitaxial $[Co/Ni]$ films

Epitaxial $[Co/Ni]$ films were grown by molecular beam epitaxy (MBE). The goal was to have epitaxial growth of a $[Co/Ni]$ superlattice along the $[111]$ axis considering face-centered cubic structure of Co and Ni. The reason is that the $[111]$ direction corresponds to the easy axis of fcc Co. Hence this helps to get perpendicular magnetic anisotropy (PMA). Furthermore it has already been shown by previous work [26], that a $Co/Ni[111]$ interface gives a strong contribution to PMA.

We decided to grow our samples on $[11\bar{2}0]$ αAl_2O_3 substrates. In literature the epitaxial growth of $[Co/Ni](111)$ superlattices directly on the $[11\bar{2}0]$ αAl_2O_3 substrates is described [115]. However in this case a buffer of 50-80 Å of Co is necessary. This layer with its large demagnetizing field would make samples with PMA nearly impossible. Hence we use nonmagnetic buffer layers. From previous work done in our laboratory we know, that it is possible to grow a buffer of $V[110]$ and $Au[111]$ on $[11\bar{2}0]$ Al_2O_3 substrates. It is then possible to deposit the Co and Ni $[111]$ layers on this buffer.

In the following we describe the sample-preparation and structural analysis. During the growth, the crystalline structure of the samples was observed by reflexion high energy electron diffraction (RHEED). In the second part we describe the ex situ analysis of the sample structure by transmission electron microscopy and by X-ray diffraction.

3.1.1 Growth of $[Co/Ni](111)$ superlattices

The growth process with all its parameters (substrate temperature, annealing etc.) was done as by [116], which was a Master's thesis preliminarily to this PhD. The author thanks S. Girod for the large and helpful collection of provided data on this subject.

3.1.1.1 Al_2O_3 ($11\bar{2}0$) substrate

$\alpha-Al_2O_3$ is a rhombohedral structure of the $R\bar{3}c$ symmetry group.

The structure of a $\alpha-Al_2O_3$ ($11\bar{2}0$) plane, which we used as substrate, is shown in fig.(3.1). The lattice parameters that can be defined for this plane are $a\sqrt{3} = 0.8249nm$ (with $a = 0.476nm$ a lattice parameter of the hexagonal description of the $\alpha-Al_2O_3$ crystal) The detailed analysis of the sapphire structure is complicated. We limit ourselves to two diffraction patterns. One in the $[1\bar{1}00]$ and one in the $[0001]$ direction,

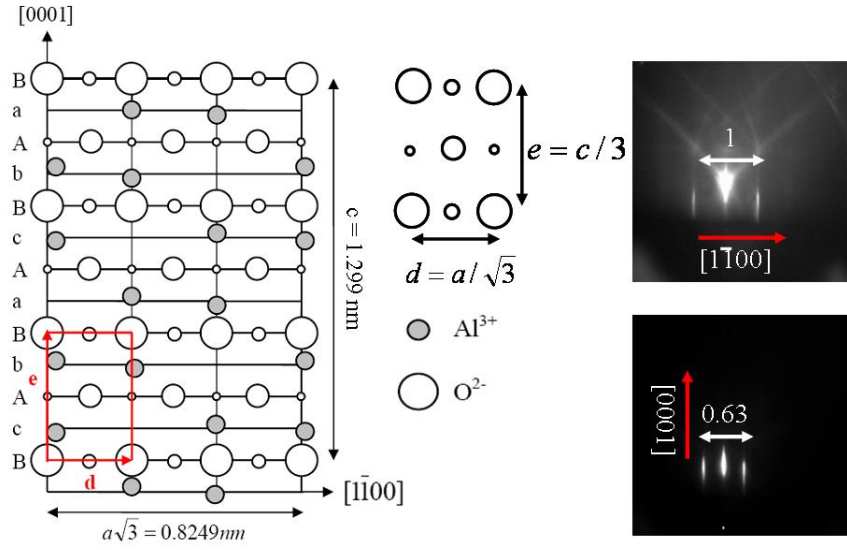


Figure 3.1: $\alpha\text{-Al}_2\text{O}_3$ (11 $\bar{2}$ 0) substrate. On the left: structure of the $\alpha\text{-Al}_2\text{O}_3$ (11 $\bar{2}$ 0) layer from [116]. On the right: Images showing electron diffraction pattern (RHEED) for two directions perpendicular to each other.

which are perpendicular to each other. The RHEED shows in these two directions the diffraction due to the rectangular lattice formed by the oxygen atoms corresponding to 1/3 of the size of the full lattice.

In order to clean the surface of the substrate the sapphire was annealed in the analysis chamber of the MBE system at 950°C during 10 to 15 minutes (compare to sec.(MBE growth)). Then it was introduced in the MBE chamber for the sample deposition.

3.1.1.2 Growth of V(110) on Al_2O_3 (11 $\bar{2}$ 0)

The vanadium was evaporated using an electron gun. The deposition rate was controlled using quartz micro balances. The typical velocity was of the order of $1 - 2 \text{ \AA/s}$.

The growth of V(110) on Al_2O_3 (11 $\bar{2}$ 0) is well known in literature ([117] and [118]). The bcc-V(110) lattice is rectangular. When grown on sapphire, the diagonal of this rectangle is oriented parallel to the short edge of the rectangle formed by the O atoms of Al_2O_3 (11 $\bar{2}$ 0) (direct space) (compare to fig.(3.2)). We have two equivalent orientations:

$$\begin{aligned} V[\bar{1}11] &\parallel \alpha - \text{Al}_2\text{O}_3[0001] \\ V[\bar{1}1\bar{2}] &\parallel \alpha - \text{Al}_2\text{O}_3[1\bar{1}00] \end{aligned} \quad (3.1)$$

or

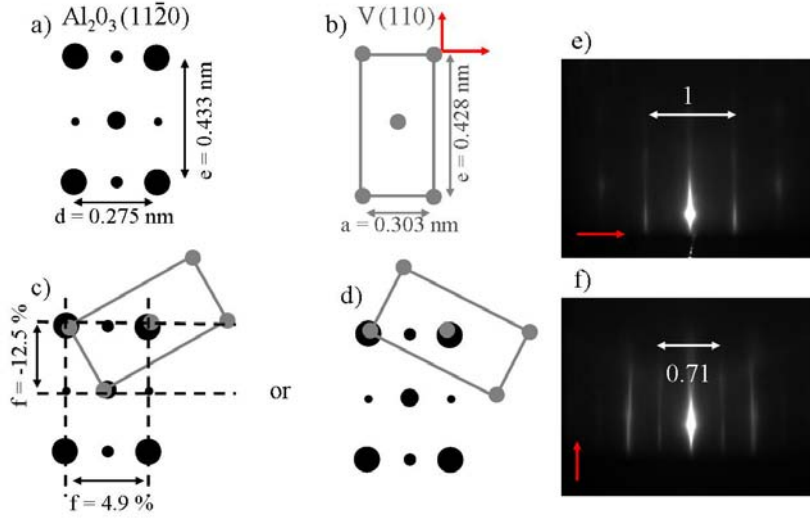


Figure 3.2: Growth of V(110) on sapphire substrate. a) sapphire lattice. b) bcc-V(110) lattice. c) and d) possible epitaxial relations. e) and f) results from RHEED for two direction perpendicular to each other of V.

$$\begin{aligned} V[\bar{1}1\bar{1}] &\parallel \alpha - Al_2O_3[0001] \\ V[\bar{1}12] &\parallel \alpha - Al_2O_3[1\bar{1}00] \end{aligned} \quad (3.2)$$

We observed that at high substrate temperatures during deposition ($T > 800^\circ C$) only one of the two possible domains remains. The chosen substrate temperature during deposition between $800^\circ C$ and $850^\circ C$ is a compromise. High temperature favors single domain growth. However if the temperature is too high, the V does no longer adhere to the substrate. At the beginning of the deposition process the RHEED pattern is spotty. This indicates as reported in literature, that the growth starts following the Volmer-Weber model. For thicknesses of more than 3-5 nm the RHEED pattern changes to lines proofing a 2D V(110) surface. This pattern can be seen in fig.(3.2 e,f).

3.1.1.3 Growth of Au(111) on V(110)

The next buffer layer was a fcc Au(111) layer deposited on V(110). Gold is evaporated in Knudsen cells at $1250^\circ C$. Between the deposition of the Au and the vanadium layer we wait until the substrate cooled down to room temperature. The observed epitaxial relation of the hexagonal Au(111) on the rectangular V(110) is of Nishiyama/Wassermann type (see fig.(3.3)). A detailed model of the growth of fcc (111) layers on a bcc(110) substrate is given in [119]. The growth mode for Au on V in this case is 2D (layer by layer) as the RHEED oscillations [120] confirm. The RHEED oscillations also allow the determination of the growth velocity, which is determined of the order of 70 s for the deposition of an atomic monolayer. After deposition of the Au buffer the substrate is annealed at approximately $300^\circ C$ during 15 minutes. This leads to a very flat Au surface, what can be seen from the very thin lines of the diffraction image.

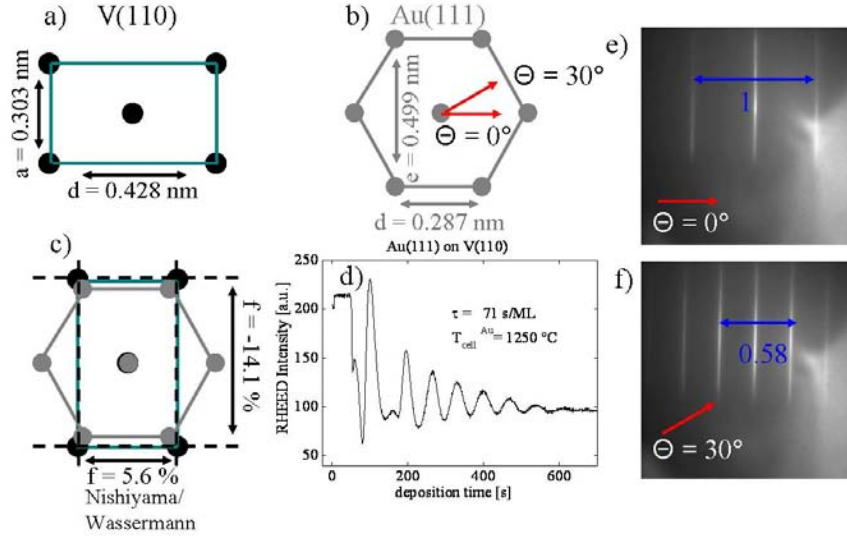


Figure 3.3: Growth of Au(111) on V(110). a) bcc V(110) lattice. b) fcc Au(111) lattice. c) Nishiyama/Wassermann epitaxial relation for Au on V. d) RHEED oscillations observed for growth of Au(111) on V(110). e) and f) RHEED diffraction patterns of Au(111) after annealing at 300°C during 15 minutes.

3.1.1.4 Growth of $[Co/Ni](111)$ superlattices on Au(111)

The $[Co/Ni]$ superlattice is grown on the Au(111) buffer once it has cooled down to room temperature after the annealing process. Co and Ni are deposited with Knudsen cells. Co, Ni and Au are fcc crystals. Consequently the (111) planes correspond to hexagons with atoms on all edges of the hexagon and one in the center of the hexagon (see fig.(3.4a-c)). The misfit between Co and Ni lattice is smaller than 1%. However the missfit between Ni and Au is of the order of 13% (see fig.(3.4d)). We start the deposition of the superlattice with Ni as Co does not show layer by layer growth when deposited on Au. When starting the growth with Ni the layer by layer growth of the $[Co/Ni]$ superlattice is confirmed by RHEED oscillations, which also allow to control the deposition rate (see fig.(3.4e)). The good crystalline structure of the deposited Co and Ni layers is confirmed by their RHEED pattern (see fig.(3.4f and g)). Finally 2nm of Au were deposited on the sample in order to prevent it from oxidation once exposed to air. More details on epitaxial growth of $[Co/Ni](111)$ superlattices can be found in [115].

3.1.1.5 Conclusion on the growth of $[Co/Ni](111)$ superlattices by molecular beam epitaxy

We conclude, that we can grow fully epitaxial $[Co/Ni](111)$ superlattices. The growth mode is two-dimensional. With the help of the RHEED oscillations the deposited thicknesses can be controlled very precisely. Consequently we have well controlled crystalline interfaces between the Co and the Ni layers. This allows to adjust the ratio between Co/Ni interfaces and the volume of the magnetic layers, and hence to tune the magnetic anisotropy of the samples (see sec.(3.2)).

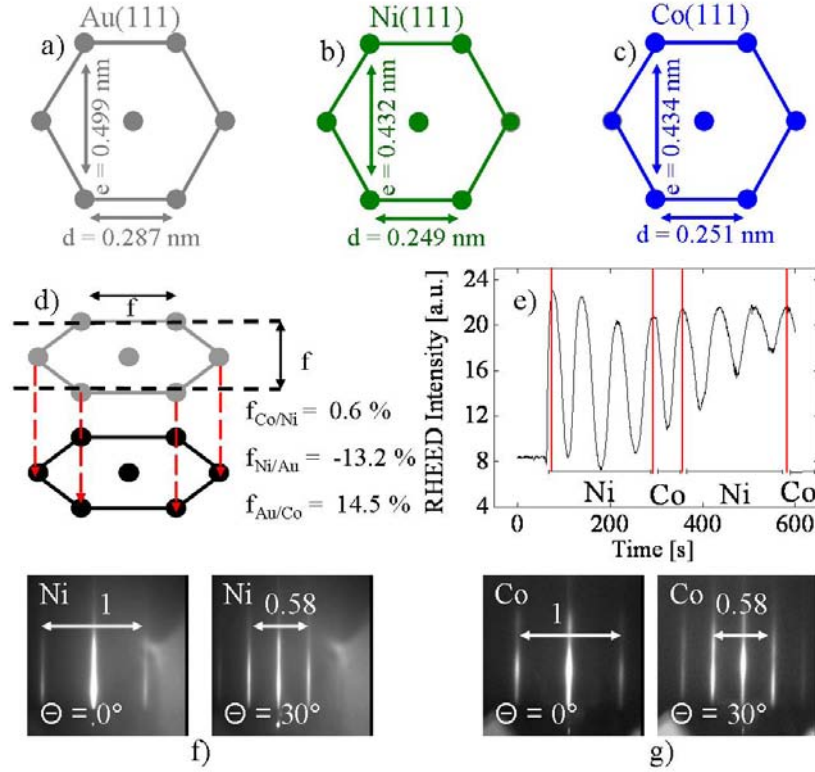


Figure 3.4: Growth of [Co/Ni](111) superlattices on Au(111). a) Au(111) -lattice. b) Ni(111)-lattice. c) Co(111)-lattice. d) lattice mismatches. e) RHEED oscillations during growth of a [Co/Ni](111) superlattice. f) RHEED diffraction pattern of Ni (111). g) RHEED diffraction pattern of Co(111).

3.1.2 Ex-situ analysis of the sample structure

The aim of our work on epitaxial [Co/Ni] superlattices is to have a magnetic model system for spin transfer torque experiments. RHEED analysis during sample growth confirmed the good epitaxial structure of the samples. However, in order to be able to compare experimental results on anisotropy, spin polarization, density of electronic states etc. with simulations based on current models, a very accurate knowledge of the sample structure is needed. Such detailed structural analysis is done in the following:

3.1.2.1 Verification of the atomic stacking by transmission electron microscopy (TEM)

Two crystalline structures of Co are possible: face centered cubic (fcc) or hexagonal closest packing (hcp). The (111) planes of fcc Co as well as the (0001) planes of hcp Co have a hexagonal symmetry and nearly identical lattice parameters. Consequently it is impossible doing RHEED analysis of the samples to distinguish whether Co is fcc or hcp. This distinction can be done by electron microscopy.

The electron microscopy experiments were done by E. Snoeck's group at CEMES Toulouse. We only give a short summary of the obtained results here.

A fully epitaxial spin valve with the following stack was grown: $Al_2O_3/V(50nm)/Au(10ML)/$ for the buffer, then $Ni(3ML)/[Co(1ML)/Ni(3ML)] \times 20$ for the first magnetic

layer, 20 atomic monolayers (ML) of Au for the non-magnetic spacer, $Ni(3ML)/[Co(2.5ML)/Ni(3ML)] \times 20$ for the second magnetic layer and finally 25 ML of Au for the capping.

A low magnification STEM HAADF image of the spin valve stacking is shown in the inset of fig.(3.5a). The contrast of the different elements depends strongly on their atomic number Z . The bright zones correspond to the gold layers with $Z = 79$. The darker zones correspond to the [Co/Ni] layers. As the atomic numbers of Co ($Z_{Co} = 27$) and Ni ($Z_{Ni} = 28$) are very close, the contrast between the two elements is quite weak. Anyhow, by optimizing the set-up parameters, a sharp interface between Co and Ni layers could be imaged (fig.(3.5a)). This proves that the growth mode is two-dimensional and that Co and Ni do not intermix. Furthermore the periodicity of the Co/Ni stack can be determined. For the first magnetic layer ($Ni(3ML)/[Co(1ML)/Ni(3ML)] \times 20$) a periodicity of $1.0nm$ was found, compared to an expected periodicity of $0.8nm$ as $d_{111} \approx 0.2nm$ for Co and Ni. For the second magnetic layer ($Ni(3ML)/[Co(2.5ML)/Ni(3ML)] \times 20$) a periodicity of $1.2nm$ was measured compared to $1.1nm$ expected from Co and Ni lattice parameters.

In a next step high resolution TEM images were taken. Fig.(3.5b) displays the crystalline structure of the Co/Ni stack of the spin valve sample observed along the $< 110 >$ zone axis. The fcc structure of the Co/Ni layer is evidenced over the entire multilayer with the A-B-C-A-B-C stacking of the (111) planes. This clearly demonstrates the coherent growth of the Co/Ni multilayer. The cobalt (nickel) atomic planes continue the stacking layer of nickel (cobalt) on which they are deposited. We have used geometric phase analysis (GPA) to analyze the deformation state of the Co/Ni stacking. The measurement of the deformation of the (111) stacking of the Co/Ni in the growth direction relative to the (111) planes of the Au layer is reported in fig.(3.5c). The (111) Au interplanar distance is found to be about 15% larger than the Co/Ni one. The lattice mismatch between fcc Ni (Co) and Au is of that magnitude, thus confirming the totally relaxed growth of Au on Ni/Co and viceversa. Meanwhile, no variation is observed within the Co/Ni stacking (within the spatial resolution of the GPA method used here). This is consistent with the similar (111) lattice spacing of bulk fcc Ni and Co lattice spacing - respectively equal to $0.2034nm$ and $0.2046nm$, and with the (111) spacing observed in high-resolution transmission electron microscopy (HRTEM) images of $\approx 0.20nm$.

3.1.2.2 Exact determination of lattice parameters

Co and Ni lattice parameters are very close for bulk material. In the epitaxial superlattice with thicknesses of few atomic monolayers, one can expect, that Co and Ni have the same in-plane lattice parameters (pseudomorphic growth) and consequently they are exposed to strain. This in-plane strain then deforms the structure also in the out-of-plane direction. We first measured the in-plane lattice parameters of our samples using Cu $K\alpha$ X-Ray diffraction. Then we calculated the out of plane lattice parameters using theory of elastic strain.

Determination of the lattice parameter in the (111) plane The used Cu $K\alpha$ radiation has a wavelength of $\lambda = 1.54056\text{\AA}$. In order to have a good signal a thick stack of Co/Ni was deposited on the usual sapphire, V, Au buffer. The chosen stack is

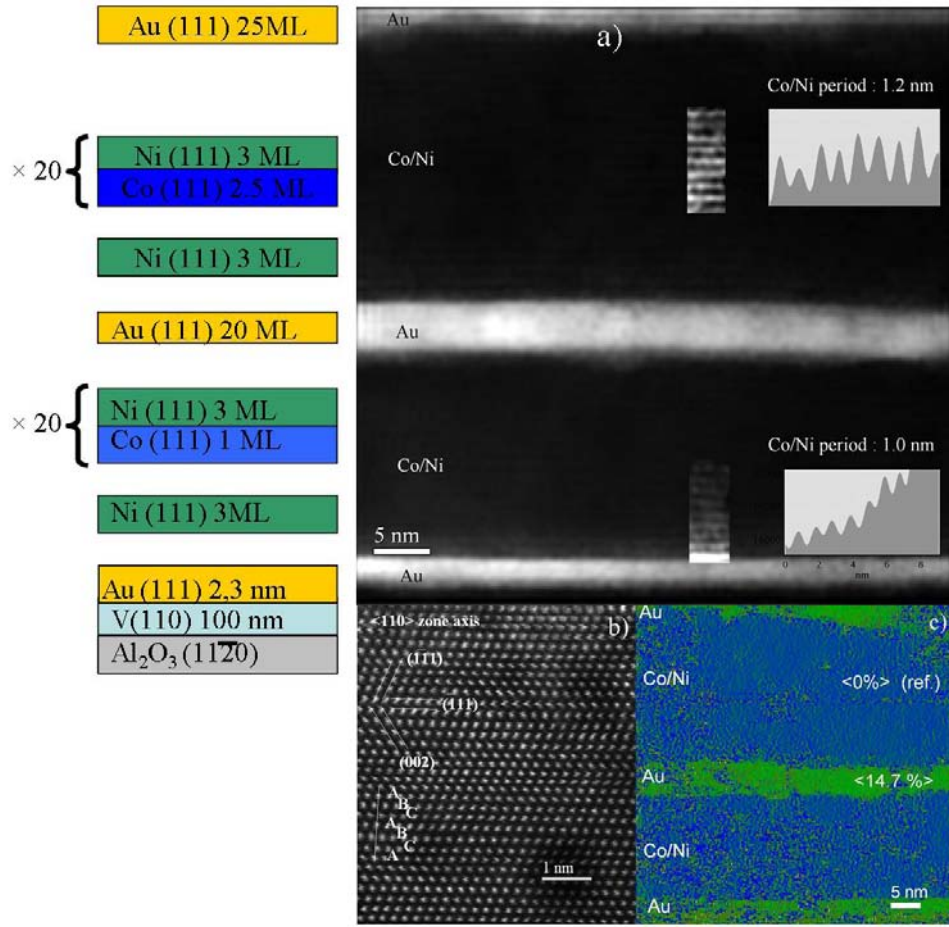


Figure 3.5: Analysis of the crystalline structure of a fully epitaxial [Co/Ni]-based spin-valve. a) Scheme showing the deposited sample stack and the TEM image of a cross sectional sample prepared from the spin valve. b) HRTEM image of the [Co/Ni] layers showing the atomic stacking. c) GPA measurement of the relative out-of-plane deformation of the Co/Ni and Au (111) planes. The lattice parameter of Co/Ni is used as a reference. Blue color indicates a lattice parameter close to the Co/Ni parameter. Green color indicates a lattice parameter, which is larger than the Co/Ni lattice parameter.

$[Ni(3ML)/Co(3ML)] \times 75$ and capped with 5 nm of Au. We start with a measurement of the lattice parameters in the direction perpendicular to the surface. This was done using a 2θ scan in the direction perpendicular to the sample surface (see fig.(3.7a)). In a single-crystalline superlattice, the most intense peak corresponds to an average of the distances between Co and Ni layers:

$$\langle d_{111} \rangle = \frac{n_{Co}d_{Co}(111) + n_{Ni}d_{Ni}(111)}{n_{Co} + n_{Ni}} \quad (3.3)$$

assuming that the distance at the Co/Ni interface is an average of both Ni and Co distances. In order to have access to the lattice parameters we have to measure the in-plane lattice parameter. The out-of-plane lattice parameter describing the distance between the (111) layers can then be determined by the application of the theory of elasticity.

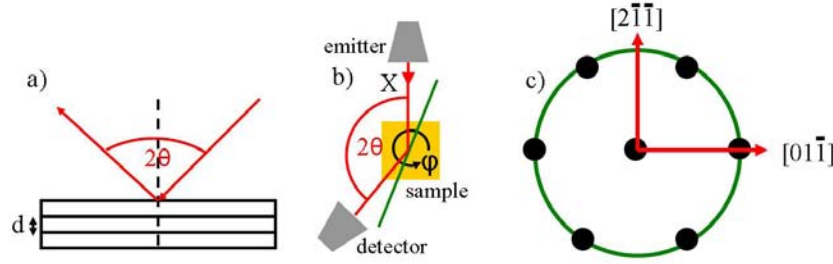


Figure 3.6: a) Diffraction experiment for the determination of the out-of-plane lattice parameter. b) Definition of the angles 2θ and ϕ for in-plane X-ray diffraction. c) (111) plane of the fcc structure and the crystallographic directions lying in this plane.

Doing diffraction on fcc-crystals only planes with all Miller indices odd or all Miller indices even lead to diffraction peaks. Consequently in the (111) plane the peak with the smallest 2θ is in the $2\bar{2}0$ direction. A sketch of the (111) plane is presented in fig.(3.6c).

The experimental problem is, that we have two unknown parameters for our experiment as we do not know the orientation of the $2\bar{2}0$ direction relative to the substrate. With

$$d_{hkl} = \frac{a}{\sqrt{h^2 + k^2 + l^2}} \quad (3.4)$$

and

$$2 \cdot \sin(\theta) d_{hkl} = \lambda \quad (3.5)$$

we find $2\theta_{CoNi[220]} \approx 76^\circ$ ($a_{[Co/Ni]} \approx 3.534\text{\AA}$). The angle between X-ray source and detector was set to this value. The sample was rotated around an axis perpendicular to the sample surface with an angle ϕ between 0 and 180° . Peaks appear, when the $[Co/Ni](2\bar{2}0)$ planes are oriented in a direction where they are close to the Bragg condition. We then optimize the sample orientation around this position by adjusting the angle between the sample surface and the plane defined by the X-ray emitter and the detector. A 2θ scan was then done (fig.(3.7b)).

We find $2\theta = 76,023 \pm 0,002^\circ$ for the $Co/Ni[220]$ planes. Using the Bragg condition this leads to $d_{220}(Co/Ni) = 1.250\text{\AA}$ and an in-plane lattice constant $a_{IP}(Co/Ni)$ of 3.537\AA . The in-plane deformation ϵ_{IP} can then be calculated by:

$$\epsilon_{IP} = \frac{a_{mes,IP} - a_{bulk}}{a_{bulk}} \quad (3.6)$$

with $a_{mes,IP}$, the measured in-plane parameter and a_{bulk} the bulk lattice constant. With $a_{Co,bulk} = 3,5447\text{\AA}$ [121] we find $\epsilon_{IP,Co} = -0.0022$ and using $a_{Ni,bulk} = 3,5236\text{\AA}$ [122] $\epsilon_{IP,Ni} = 0.0038$.

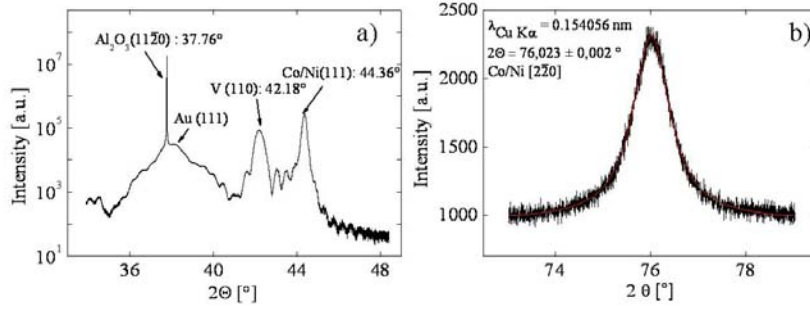


Figure 3.7: X-ray diffraction on a $[Ni(3ML)/Co(3ML)] \times 75$ super-lattice: a) out-of-plane 2θ -scan b) 2θ -scan in the $Co/Ni [2\bar{2}0]$ -direction of the (111) planes.

Determination of the lattice parameter perpendicular to the (111) plane
 In the following we are now calculating the lattice deformation perpendicular to the (111) planes in order to find the out of plane lattice parameters for Co and Ni using the theory of elastic deformation considering an isotropic crystal. We use as convention, that in the case of an isotropic crystal:

$$C_{44} = C_{11} - C_{12} \quad (3.7)$$

with $C_{i,j}$ the elastic constants.

In this case the Poisson coefficient ν is given by:

$$\nu = \frac{C_{12}}{C_{11} + C_{12}} \quad (3.8)$$

and we have

$$\epsilon_{\perp} = -\frac{2\nu}{1 - \nu}\epsilon_{\parallel} \quad (3.9)$$

Elastic constants of Ni(fcc) can be found in [123]:

$$C_{11} = 261.2 GPa, C_{12} = 150.8 GPa \text{ and } C_{44} = 131.7 GPa$$

The elastic constants of Co(fcc) are given in [124] as:

$$C_{11} = 225 \pm 25 GPa, C_{12} = 160 \pm 20 GPa \text{ and } C_{44} = 92 \pm 15 GPa.$$

Using this parameters we find for the elastic deformation of Co $\epsilon_{\perp,Co}$ and Ni $\epsilon_{\perp,Ni}$ perpendicular to the (111) plane :

$$\begin{aligned} \epsilon_{\perp,Ni} &= -0.0045 \\ \epsilon_{\perp,Co} &= +0.0032 \end{aligned} \quad (3.10)$$

Hence the lattice parameters perpendicular to the (111) plane are given by:

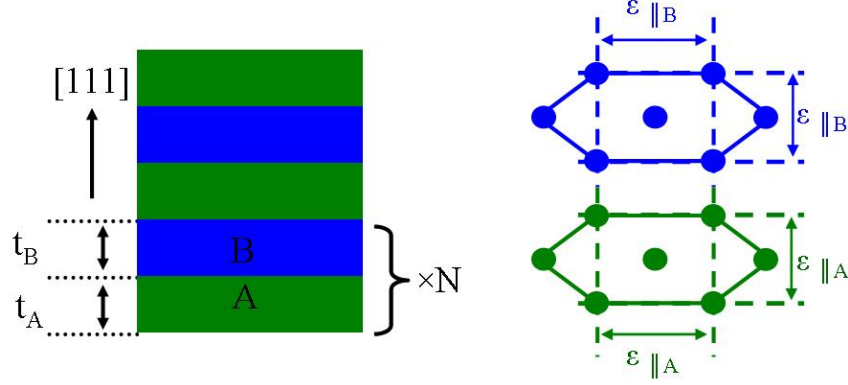


Figure 3.8: Epitaxial multilayer of two fcc crystals grown in the [111]-direction.

$$a_{\perp, Ni} = (1 + \epsilon_{\perp, Ni}) a_{Ni, bulk} = 3.508 \text{ \AA} \quad (3.11)$$

$$a_{\perp, Co} = (1 + \epsilon_{\perp, Co}) a_{Co, bulk} = 3.556 \text{ \AA}$$

Theoretical calculation of the lattice deformation In this part we are going to compare the measured in-plane lattice parameter with the result of a calculation minimizing the elastic energy of the superlattice. For an elastic deformation ϵ of an isotropic material the elastic energy density \tilde{E} is expressed as:

$$\tilde{E} = \frac{1}{2} E \epsilon^2 \quad (3.12)$$

with the Young modulus E given by:

$$E = \frac{(C_{11} - C_{12})(C_{11} + 2C_{12})}{(C_{11} + C_{12})} \quad (3.13)$$

This leads to an elastic energy per surface E_S for the [Co/Ni] superlattice with N repetitions given by:

$$E_S = \frac{1}{2} N (E_{Ni} \epsilon_{\parallel, Ni}^2 \cdot t_{Ni} + E_{Co} \epsilon_{\parallel, Co}^2 \cdot t_{Co}) \quad (3.14)$$

with t_{Co} and t_{Ni} the thicknesses of the Co and Ni layers.

$$\begin{aligned} E_S &= \frac{1}{2} N E_{Co} \epsilon_{\parallel, Co}^2 t_{Co} + \frac{1}{2} N E_{Ni} \epsilon_{\parallel, Ni}^2 t_{Ni} \\ &= \frac{1}{2} N \left(E_{Co} t_{Co} \left(\frac{a_{IP} - a_{Co, bulk}}{a_{Co, bulk}} \right)^2 + E_{Ni} t_{Ni} \left(\frac{a_{IP} - a_{Ni, bulk}}{a_{Ni, bulk}} \right)^2 \right) \end{aligned} \quad (3.15)$$

with $a_{Ni, bulk}$ and $a_{Co, bulk}$ the bulk lattice constants. The in plane lattice constant a_{IP} of Co and Ni is then found by calculating the derivative of E_S with respect to a_{IP} :

Lattice parameter	$a_{IP}(111)$	$d_{\perp}^{Ni}(111) [\text{\AA}]$	$d_{\perp}^{Co}(111) [\text{\AA}]$	$< d_{111} > [\text{\AA}]$
measured	3.537	2.025	2.053	2.039
calculated (isotropic)	3.532	2.029	2.057	2.043

Table 3.1: Lattice distances measured by X-ray diffraction of a $[Co3/Ni3] \times 75$ superlattice compared to values obtained from elastic theory. The calculations were performed assuming an isotropic material ($C_{11} - C_{12} = C_{44}$)

which leads to an expression for a_{IP} as a function of the layer thicknesses t_{Ni} and t_{Co} :

$$\Rightarrow a_{IP} = \frac{E_{Co}t_{Co} + E_{Ni}t_{Ni}}{\frac{E_{Co}t_{Co}}{a_{Co,bulk}} + \frac{E_{Ni}t_{Ni}}{a_{Ni,bulk}}} \quad (3.16)$$

We can calculate the Young modulus E for Co and Ni using the elastic constants given above. We find:

$$\begin{aligned} E_{Co} &= 92 GPa \\ E_{Ni} &= 150 GPa \end{aligned} \quad (3.17)$$

Using this data we find for a $[Ni3/Co3]$ multilayer:

$$\begin{aligned} a_{IP}(111) &= 3.532 \text{\AA} \\ d_{\perp}^{Ni}(111) &= 2.029 \text{\AA} \\ d_{\perp}^{Co}(111) &= 2.057 \text{\AA} \\ < d_{111} > &= 2.043 \text{\AA} \end{aligned} \quad (3.18)$$

Conclusion on the determination of lattice parameters of the $[Co/Ni]$ superlattices Comparing the values calculated assuming an isotropic material to the measure values obtained above (see tab.(3.1)) confirms that the Co and Ni layers constrain each other. In contrast they are not constrained by the buffer and capping layers as already observed by electron microscopy.

3.1.3 Conclusion on growth and structure of epitaxial $[Co/Ni]$ films

Epitaxial $[Co/Ni](111)$ superlattices can be grown on $Al_2O_3(11\bar{2}0)$ substrates. RHEED oscillations proof the layer by layer growth of our samples and allow to control the layer thicknesses down to 0.1 atomic monolayers. The fcc structure of the $[Co/Ni]$ layers was confirmed by electron microscopy experiments. The lattice parameters of Co and Ni layers of the superlattice could be determined by X-ray diffraction. The result proofs, that Co and Ni constrain each other, but are not constrained by Au. We hence have a very detailed knowledge of the structural properties of our $[Co/Ni](111)$ superlattices, allowing the application of models on electronic band structure etc.

3.2 Magnetic properties of epitaxial [Co/Ni] superlattices

As already mentioned [Co/Ni] multilayers potentially have a high perpendicular magnetic anisotropy (PMA) [26]. This anisotropy of our samples is measured using SQUID and VSM magnetometry. The results are then compared to a simple phenomenological model. In a second step, this anisotropy is studied on the atomic scale using X-Ray Magnetic Circular Dichroism (XMCD). Finally some samples are analyzed using ferromagnetic resonance spectroscopy (FMR). This experimental method gives access to the dynamic magnetic properties of our [Co/Ni] superlattices, the Gilbert damping parameter α is determined. Furthermore it is a second method, that can be used to determine the magnetic anisotropy, and to verify magnetometry results.

3.2.1 Part 1: Macroscopic magnetic properties

3.2.1.1 Hysteresis loops

A series of $Ni(3ML)/[Co(tML)/Ni(3ML)] \times 10$ samples was grown with $t_{Co} \in [0; 4]$, the thickness of the Co layers. Hysteresis-loops with the magnetic field applied parallel to the sample plane (IP) and perpendicular to the sample plane (OOP) were measured. Examples are represented in fig.(3.9). For $t_{Co} = 0$ (pure Ni sample) the magnetization is preferentially oriented in the plane of the sample (see fig.(3.9a)). For the smallest Co thickness experimentally realized of $t_{Co} = 0.13$, the magnetization is preferentially orientated out of plane (see fig.(3.9b)). We have an effective perpendicular magnetic anisotropy. When the Co thickness t_{Co} is further increased the effective anisotropy remains perpendicular until a Co thickness of 3.5 atomic monolayers. For a $Ni(3ML)/[Co(4ML)/Ni(3ML)] \times 10$ sample the magnetization is found to be preferentially in-plane. We thus have a large range of Co thicknesses ($t_{Co} \in [0.13; 3.5]$), for which the studied samples have an effective perpendicular magnetic anisotropy.

3.2.1.2 Magnetization

The determination of the sample area allows to calculate the magnetic saturation moment m_S per area m_S/S . The result is plotted in fig.(3.11b). The obtained values are compared with calculated values considering magnetic bulk moments for Co and Ni atoms. Therefore one has to calculate the number of atoms per surface and per atomic monolayer for fcc(111) planes. The (111) planes can be composed of rectangles $a \times b$, containing 2 atoms (see fig.(3.10)). From X-ray diffraction we know (see sec.(refsec:Xray)) the in-plane lattice parameter of Co and Ni $a = 3.534\text{\AA}$. This leads to $c = 2.50\text{\AA}$ and $b = 4.33\text{\AA}$ and hence to $185 \cdot 10^{17}$ atoms per m^2 and per atomic monolayer. The magnetic moment per Co atom for bulk Co is given as $1.7\mu_B$ and for Ni as $0.58\mu_B$ [69], with μ_B the Bohr magneton of $9.274 \cdot 10^{-24} J/T$. With this data theoretical values for m_S/S can be calculated. They are also plotted in fig.(3.11b). Within the error bars the agreement between calculated and experimental data is correct. We conclude that the Co and Ni moments might be slightly different from the bulk values but the precision of the measurements does not allow an unambiguous statement.

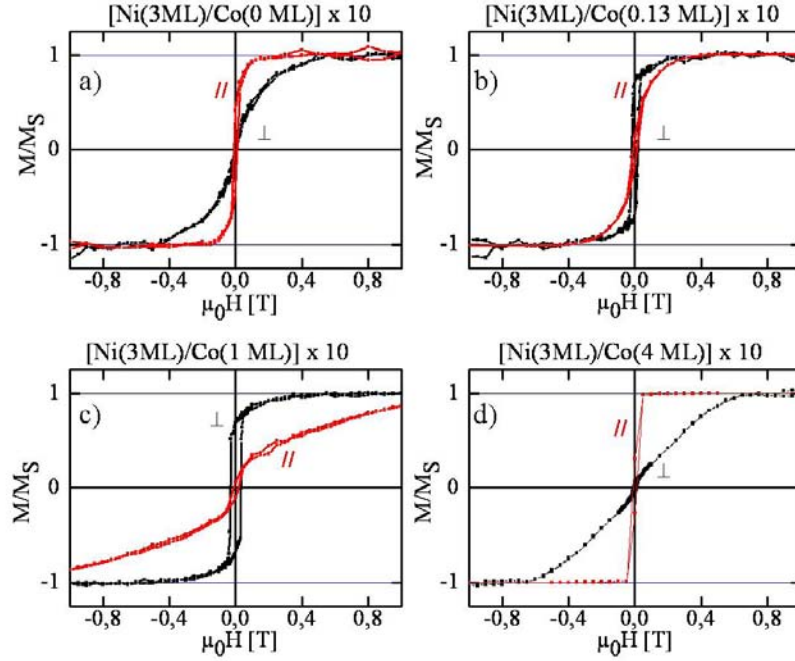


Figure 3.9: In-plane (IP) and out-of-plane (OOP) hysteresis loops for [Co/Ni] multilayers with different Co amounts.

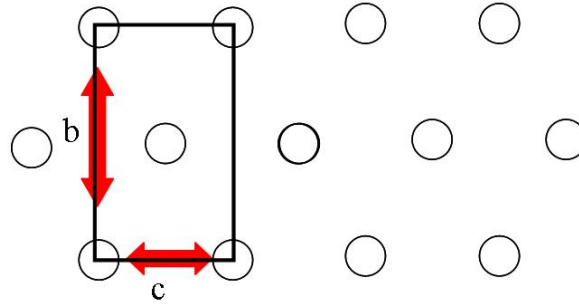


Figure 3.10: Sketch of the fcc (111) plane for the calculation of the atomic surface density.

3.2.1.3 Coercivity and saturation fields

The coercivity as a function of the Co thickness t_{Co} is plotted in fig.(3.11c). The coercivity is highest for Co thicknesses t_{Co} between 0.5 and 1 atomic monolayer. Coercivity depends on many parameters like anisotropy, magnetization, defects etc. (see sec.(1.3.2)) it is difficult to unambiguously conclude on this result. Furthermore the IP saturation field H_S (saturation higher than 97%) of the samples was determined and plotted in fig.(3.11d). H_S increases for $t \in [0; 1]$ and decreases for higher values. For $t_{Co} = 1$ a maximum of $\mu_0 H_S = 2T$ is reached indicating a strong PMA.

We can now determine the magnetic anisotropy of our samples making the assumption for the anisotropy field, that $H_A \approx H_S$. The effective anisotropy is then given by (compare to sec.(1.3.1)):

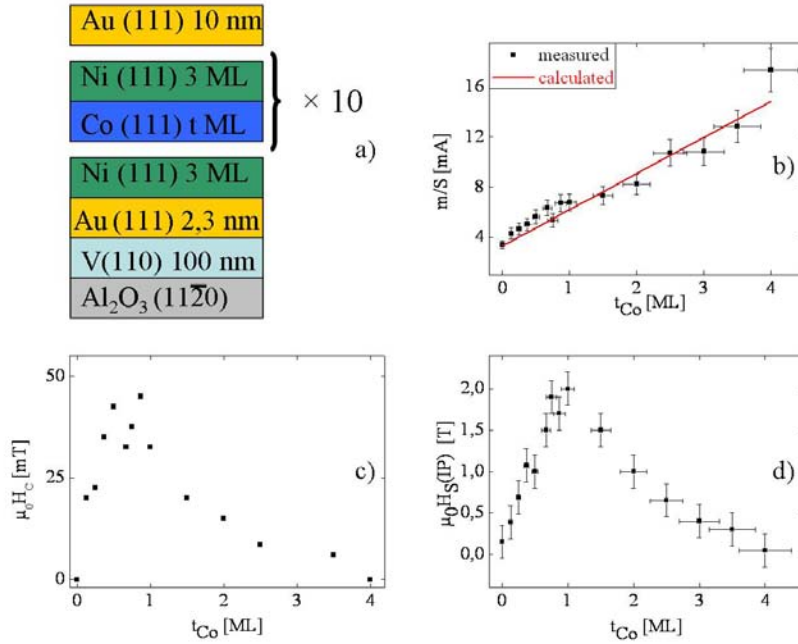


Figure 3.11: Magnetometry results for a series of multilayers: $[Ni(3ML)/Co(tML)] \times 10 / Ni(3ML)$ with $t \in [0; 4]$. a) Used sample stack b) Magnetic moment m per sample surface as a function of the Co amount t_{Co} (black), in red values calculated using bulk magnetic momenta of Co($1.7\mu_B$) and Ni($0.58\mu_B$). c) Coercivity $\mu_0 H_C$ as a function of the Co amount t_{Co} , d) In-plane saturation field $\mu_0 H_S$ as a function of the Co amount t_{Co} .

$$K_{eff} = \frac{1}{2}\mu_0 M_S H_S \quad (3.19)$$

where M_S is the saturation magnetization of the sample. These values are plotted in fig.(3.12a). Furthermore we can calculate the shape anisotropy K_{shape} using the measured magnetizations M_S :

$$K_{shape} = -\frac{1}{2}\mu_0 M_S^2 \quad (3.20)$$

which decreases with increasing Co thickness t_{Co} . The minus indicates that this contribution leads to an in-plane magnetization. The difference between effective and shape anisotropy leads to the magnetocrystalline anisotropy K_u :

$$K_u = K_{eff} - K_{shape} = \frac{1}{2}\mu_0 M_S H_S + \frac{1}{2}\mu_0 M_S^2 \quad (3.21)$$

The results are also plotted in fig.(3.12a). The magnetocrystalline anisotropy is positive for all Co thicknesses t_{Co} , hence it favors an out of plane magnetization for all samples. A maximum is reached for $t_{Co} = 1$. In addition we calculated the product $D \cdot K_{eff}$, where D is the sum of all thicknesses of all magnetic layers, and plotted it as a function of t_{Co} (see fig.(3.12a)). Two linear regimes can be observed: a linear increase of $D \cdot K_{eff}$ with t_{Co} for $t_{Co} \in [0; 1]$ and a linear decrease with t_{Co} for $t_{Co} > 1$.

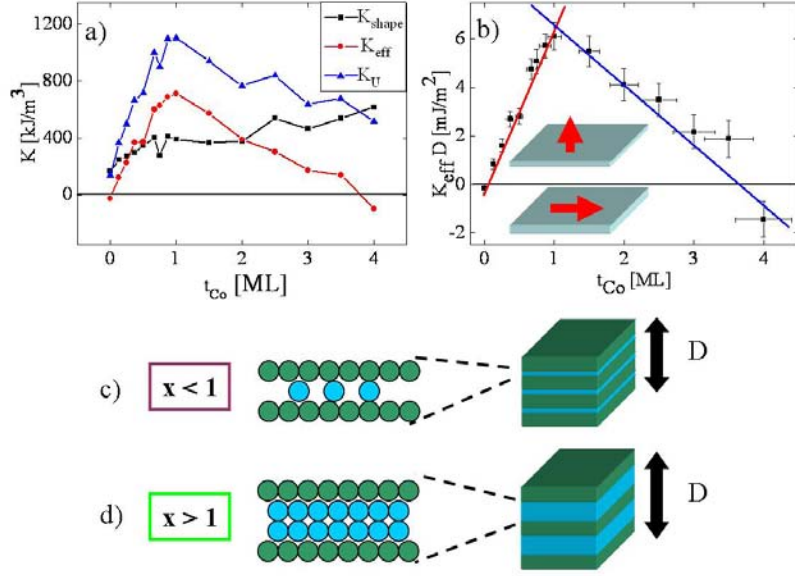


Figure 3.12: Anisotropy of $[Ni(3ML)/Co(tML)] \times 10 / Ni(3ML)$ multilayers with $t \in [0; 4]$. a) Effective anisotropy K_{eff} , uniaxial anisotropy constant K_u and the absolute value of the shape anisotropy K_{shape} as a function of t_{Co} . b) $K_{eff} \cdot D$ with D the sum of the thicknesses of all Co and Ni layers as a function of t_{Co} . Lines are guides to the eye. c) Sketch of the Co/Ni interface when $t_{Co} < 1$. d) Sketch of the Co/Ni interface when $t_{Co} > 1$.

This fits to the explanation, that the PMA is due to the Co/Ni interfaces and to the magnetocrystalline (111) contribution of Co. A detailed analysis is done in the following.

3.2.1.4 Simple model explaining the perpendicular anisotropy of $[Co/Ni]$ superlattices

The PMA of $[Co/Ni]$ superlattices is explained as the sum of the contributions from the Co/Ni interfaces leading to a perpendicular anisotropy $K_S^{Co/Ni}$ and the contribution to magnetocrystalline anisotropy of the [111] direction K_V^{Co} [26]. A phenomenological approach similar to [125] is done in the following. For this approach we calculate $D \cdot K_{eff}$ from interface contributions, contributions from the [111] axis and the shape anisotropy K_{shape} :

$$K_{eff} \cdot D = \sum (K_{interfaces} + K_V \cdot t_{layer} + K_{shape} \cdot t_{layer}) \quad (3.22)$$

In our case we have a series of samples deposited on a V/Au buffer consisting of $Ni(3)/[Co(t_{Co})/Ni(3)] \times 10$ layers. We distinguish two cases: one for $t_{Co} \in [0; 1]$ and one for $t_{Co} > 1$. We now first discuss the case $t_{Co} > 1$ (see fig.(3.12d)). In this case we have two complete Co/Ni interfaces for every Co layer independent of t_{Co} . Furthermore we take the anisotropy constant K_V^{Co} into account. In addition we have 2 Ni/Au interfaces of unknown anisotropy and the magnetocrystalline volume anisotropy

of Ni K_V^{Ni} . Taking the shape anisotropy into account we find for $K_{eff} \cdot D$ as a function of $t_{Co} > 1$:

$$DK_{eff} = 20K_S^{Co/Ni} + 2K_S^{Ni/Au} + 33d_{111}^{Ni}[K_V^{Ni} - \frac{1}{2}\mu_0 M_{Ni}^2] + 10d_{111}^{Co}t_{Co}[K_V^{Co} - \frac{1}{2}\mu_0 M_{Co}^2] \quad (3.23)$$

with d_{111}^{Co} and d_{111}^{Ni} the distance between (111)-planes. Consequently we can express DK_{eff} as

$$DK_{eff} = a + b \cdot t_{Co} \quad (3.24)$$

with

$$a = 20K_S^{Co/Ni} + 2K_S^{Ni/Au} + 33d_{111}^{Ni}[K_V^{Ni} - \frac{1}{2}\mu_0 M_{Ni}^2] \quad (3.25)$$

and

$$b = 10d_{111}^{Co}[K_V^{Co} - \frac{1}{2}\mu_0 M_{Co}^2] = 10d_{111}^{Co}K_{eff}^{Co} \quad (3.26)$$

where K_{eff}^{Co} is the effective anisotropy of a thin Co(111) film. Accordingly we find K_{eff}^{Co} when we make a linear fit of DK_{eff} as a function of $t_{Co} > 1$. We find $b = (-2.27 \pm 0.28)mJ/m^2$ and $a = (8.80 \pm 0.76)mJ/m^2$. With $d_{111}^{Co} = 0.206\text{\AA}$ (sec.3.1.2.2) this leads to $K_{eff}^{Co} = -(1.10 \pm 0.15)MJ/m^3$, and $K_V^{Co} = 0.13 \pm 0.15MJ/m^3$ for a Co (111) film. This values are of the same order of magnitude as the $K_{eff}^{Co} = -0.8MJ/m^3$ found by [125].

We now discuss the case of $t_{Co} \in [0; 1]$ (see fig.(3.12c)). As we observed a 2D growth for Co on Ni (see sec.(3.1.1.4)) we suppose, that for $t_{Co} \in [0; 1]$ we have $2 \times t_{Co}$ Co/Ni interfaces per Co layer. Consequently the interface contribution to PMA is $2 \cdot K_S^{Co/Ni} \cdot t_{Co}$. We consider a K_V^{Co} contribution as all Co atoms even though one can argue about this point as we are talking about layer thicknesses smaller than one atomic monolayer. For the shape anisotropies of Co and Ni as well as for the magnetocrystalline anisotropy of Ni we use the same expressions as in the previous case:

$$DK_{eff} = 20K_S^{Co/Ni}t_{Co} + 2K_S^{Ni/Au} + 33d_{111}^{Ni}[K_V^{Ni} - \frac{1}{2}\mu_0 M_{Ni}^2] + 10d_{111}^{Co}t_{Co}[K_V^{Co} - \frac{1}{2}\mu_0 M_{Co}^2] \quad (3.27)$$

Again we have a linear expression $DK_{eff} = a + b \cdot t_{Co}$. This time with

$$a = 2K_S^{Ni/Au} + 33d_{111}^{Ni}[K_V^{Ni} - \frac{1}{2}\mu_0 M_{Ni}^2] \quad (3.28)$$

and

$$b = 20K_S^{Co/Ni} + 10d_{111}^{Co}[K_V^{Co} - \frac{1}{2}\mu_0 M_{Co}^2] \quad (3.29)$$

A linear fit leads to $b = (6.50 \pm 0.32)mJ/m^2$ and $a = (-0.08 \pm 0.20)mJ/m^2$. The difference between the two slopes determined for $t_{Co} < 1$ and $t_{Co} > 1$ equals $20 \cdot K_S$. This leads to $K_S^{Co/Ni} = (0.44 \pm 0.04)mJ/m^2$. [125] finds with $K_S^{Co/Ni} = 0.42mJ/m^2$

t_{Co}	M_S [kA/m]	$\mu_0 H_C$ [mT]	$\mu_0 H_S$ [T]	K_{eff} [kJ/m ³]	K_u [kJ/m ³]
0	513	IP	-0.1	-26	27
0,13	625	20	0.39	121	271
0,25	657	22.5	0.69	226	380
0,37	684	35	1.1	368	522
0.5	741	42.5	1	371	536
0.67	798	32.5	1.5	599	741
0.75	659	37.5	1.9	627	897
0.87	808	45	1.7	687	868
1	788	32.5	1.8	710	1011
1.5	763	20	1.5	573	960
2	776	15	1	388	856
2.5	925	8.5	0.65	301	779
3	859	---	0.4	172	724
3.5	925	6	0.3	139	725
4	988	IP	-0.2	-99	640

Figure 3.13: Overview over the data obtained by magnetometry.

the same value as we do. This value is about 2 times larger than the value found for sputtered [Co/Ni] multilayers as reported for example by [126] who finds $K_S^{Co/Ni} = (0.23 \pm 0.03) mJ/m^2$. The higher interface anisotropy of the MBE grown samples is explained as due to the sharper interfaces compared to sputtered samples. Higher interface anisotropies K_S can be obtained when nonmagnetic layers like Pd are used instead of Ni. [127] finds $K_S^{Co/Pd} = (0.63 \pm 0.05) mJ/m^2$ for MBE grown [Co/Pd] samples. The higher anisotropy of the Co/Pd interface compared to the Co/Ni interface can be explained by the stronger L-S coupling of the heavier Pd atom. However, for spin torque experiments this larger L-S coupling is a disadvantage as it tends to increase the Gilbert damping term α and to decrease the polarization p [15].

Remarks on K_S

Finally we want to make a few remarks on the interface anisotropy K_S , which we introduced as a phenomenological term. In general a perpendicular contribution to the magneto crystalline anisotropy from an interface is explained as due to the reduced symmetry experienced by magnetic atoms at the interface. Such a reduction of symmetry can be due to hybridization of the electronic states at the interface or due to strain. Thus, as found by [128] we have to consider five sources of anisotropy, when we want to take the strain of the [Co/Ni] superlattice into account:

- Shape anisotropy $-\frac{1}{2}\mu_0 M_S^2$
- Magneto crystalline anisotropy of the [111] direction $K_{[111]}$
- Interface anisotropy due to the hybridization of the electronic states at the interface K_{int}

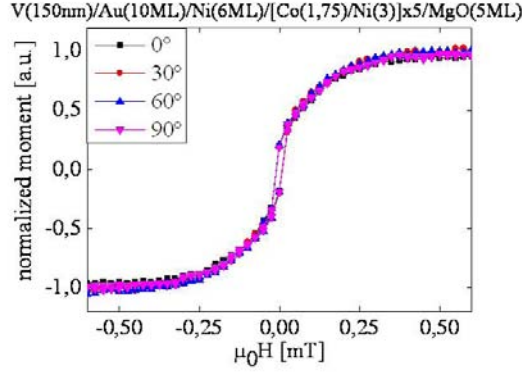


Figure 3.14: IP hysteresis loops for different IP angles between field and an arbitrarily chosen IP direction of the sample.

- Anisotropy due to the magnetoelastic coupling $B \cdot \epsilon$, where ϵ represents the appropriate components of the strain tensor
- Anisotropy due to the magnetoelastic coupling of the interface $B_{int} \cdot \epsilon/h$, where h is the layer thickness

It is known that strain can lead to perpendicular anisotropy as for example described by [129]. The problem that we have if we want to determine the contribution of strain to the magnetic anisotropy is, that we have no idea about the interface magnetoelastic coupling B_{int} . However, for the bulk magnetoelastic coupling, calculations exist as for example done by [130]. For the [Co3/Ni3] superlattice the in-plane strain was found to be $\epsilon_{Co} = -0.22\%$ for Co and $\epsilon_{Ni} = 0.38\%$. For a fcc Co with $\epsilon_{Co} = -0.22\%$ for the (111) plane [130] finds an out-of-plane contribution $K_{out,Co} \approx -25 kJ/m^3$. For a fcc Ni with $\epsilon_{Ni} = 0.38\%$ we have $K_{out,Ni} \approx 250 kJ/m^3$, which is ten times bigger than the value for Co. We can compare this to the measured uniaxial anisotropy K_U , which is about $724 kJ/m^3$ by:

$$\frac{K_U}{t_{Ni} + t_{Co}} \approx 5.8 \times K_{out,Ni} \cdot t_{Ni} \quad (3.30)$$

This means, that the magnetoelastic coupling can be responsible for at most less than one fifth of the magnetic anisotropy. The anisotropy must hence be mainly due to other sources than magnetoelastic coupling, except the case, that an important interface magnetoelastic coupling exists. Simulations to clear this point are in progress.

3.2.1.5 In-plane anisotropy of [Co/Ni] superlattices

In the previous section, we discussed the perpendicular magnetic anisotropy of our [Co/Ni] superlattices ignoring possible in-plane contributions to anisotropy. Such an approach seems to be justified as no dependence of the in-plane angle on the IP hysteresis loops could be observed as long as the samples had an effective perpendicular anisotropy (see fig.(3.14)).

However, a [Co(4ML)/Ni(3ML)] \times 10 sample with effective IP anisotropy due to its large shape anisotropy, is not isotropic when measured under different angles Φ . It

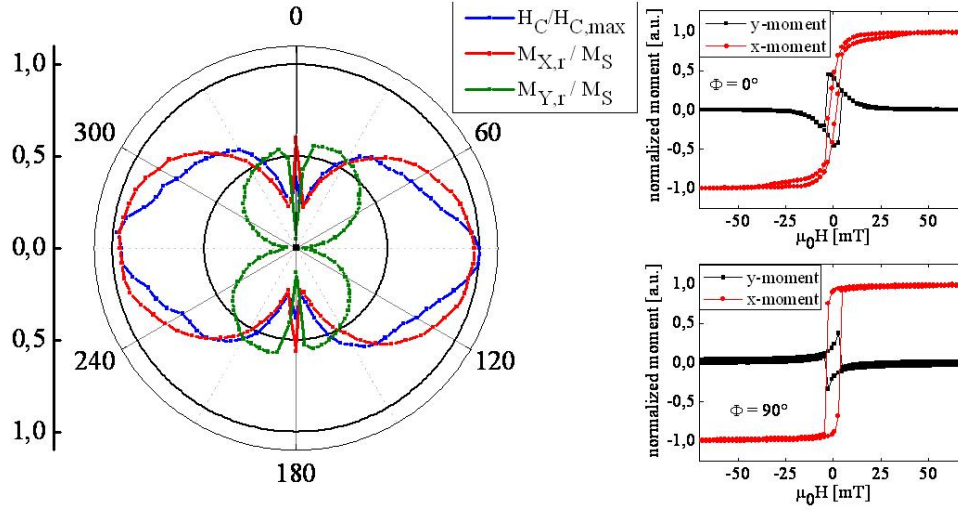


Figure 3.15: Normalized coercivity $H_C/H_{C,max}$, normalized remanent magnetization in the direction of the applied field $M_{X,r}/M_S$ and normalized remanent magnetization $M_{Y,r}/M_S$ in the direction perpendicular to the applied field as a function of the angle Φ between the applied field and an arbitrarily chosen in-plane axis of the sample.

is not possible to identify outstanding crystallographic axes of the substrate without using X-ray diffraction experiments. Hence the angle Φ is relative to an arbitrarily chosen IP-axis. IP hysteresis loops were measured in steps of 5° . At some angle the IP loop becomes nearly a square loop with a remanence of 95% and a coercivity of $\mu_0 H_{C,max} = 5 \text{ mT}$ (see fig.(3.15) $\Phi = 90^\circ$). Such square loop reappears only when the sample is turned by 180° .

In fig.(3.15) we see the development of the normalized coercivity $H_C/H_{C,max}$, the normalized remanent magnetization in the direction of the applied field $M_{X,r}/M_S$ and normalized remanent magnetization $M_{Y,r}/M_S$ in the direction perpendicular to the applied field as a function of the angle Φ between the applied field and the arbitrarily chosen in-plane axis of the sample. These data clearly show, that a preferential direction for the IP-magnetization exists. From the hexagonal symmetry of the (111) planes, we expected to find a periodicity of 60° degree for the IP loops. As this is not the case we tried to check if a lattice distortion of the (111) planes could be observed. Therefore we measured the angle 2θ of the $(\bar{2}\bar{2}0)$, $(\bar{2}20)$ and the $(0\bar{2}\bar{2})$ planes which are perpendicular to the (111) plane for the sample described in sec.(3.1.2.2). The result is:

Φ	2θ	$d_{220}[\text{\AA}]$
60°	$(76.019 \pm 0.005)^\circ$	1.261 ± 0.015
120°	$(76.017 \pm 0.008)^\circ$	1.265 ± 0.010
180°	$(76.018 \pm 0.004)^\circ$	1.263 ± 0.008

Thus, a significant variation of 2θ could not be measured.

A possible explanation for the outstanding magnetic axis might be to the morphology of the buffer. Scanning tunneling microscopy done in earlier studies in our lab shows

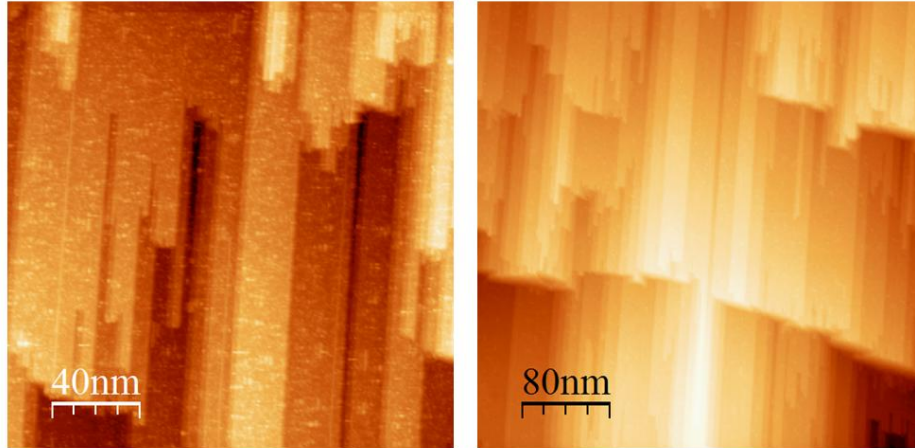


Figure 3.16: STM-images of V(110) grown on a sapphire ($11\bar{2}0$) substrate.

some stripe-shaped morphology of V(110) when growing on a sapphire buffer (see fig.(3.16)). Further analysis to find the origin of the IP contribution to anisotropy of the $[Co/Ni]$ superlattices was not done. However the existence of this IP anisotropy should be kept in mind for possible future simulations of magnetization reversal dynamics as such in-plane contribution can have important consequences for spin transfer torque phase diagrams as reported by [61].

3.2.2 Part 2: Microscopic magnetic properties

In the previous section the magnetism of $[Co/Ni]$ -superlattices at the macroscopic scale was analyzed. A strong perpendicular magnetic anisotropy was found and phenomenologically explained as due to the (111)-orientation, which represents the easy axis of fcc-cobalt, and particularly due to the Co/Ni-interfaces. In this section we are going to discuss the microscopic origin of this interface anisotropy.

3.2.2.1 Details on the experiment and the treatment of XMCD data

As indicated in sec.(1.1.3.4) interface anisotropy is microscopically due to an increase of the atomic orbital magnetic moment at the interface between a magnetic material and another material, which can be magnetic or not. An experimental technique allowing the element specific determination of spin and orbital moments at the atomic scale is the X-Ray Magnetic Circular Dichroism (XMCD) and its interpretation using sum rules as done by [39].

Two kinds of samples were prepared by MBE. First, $[Co(x)/Ni(y)] \times N$ superlattices were grown varying x from 0.1 to 4 atomic monolayers (ML), y from 1 to 4 ML, while keeping $N = 5$. Second, two wedges were prepared with the architecture $Ni_3/Co(x)/Ni_3$ with $x = 0.25, 0.5, 0.75, 1, 1.5, 2$ MLs for the first wedge and $x = 2, 3, 4, 5, 7, 10$ MLs for the second one. All the samples were capped with MgO to prevent them from oxidation on air. MgO was chosen because of its low X-ray absorption behavior compared to Au for instance. A sketch of the used wedges can be found in fig.(3.19a)

The XMCD measurements were performed at the Advanced Light Source in Berkeley at the B04 beamline. Co and Ni 2p edges were recorded using 100% circularly polarized

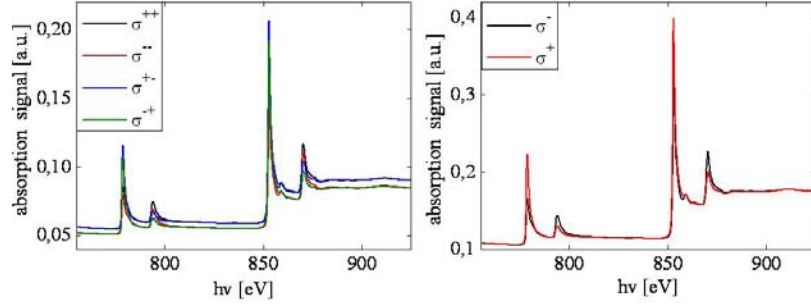


Figure 3.17: XMCD absorption spectra for a $[Ni3/Co1] \times 5$ superlattice. σ^{ij} ($i = +, -$ light polarization; $j = +, -$ magnetic field direction) and $\sigma^{+} = \sigma^{++} + \sigma^{--}$ and $\sigma^{-} = \sigma^{+-} + \sigma^{-+}$

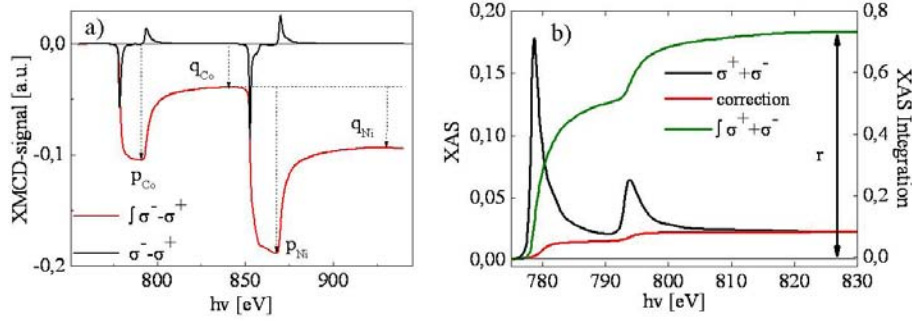


Figure 3.18: a) XMCD signal $\sigma^{-} - \sigma^{+}$ and integrated XMCD signal $\int \sigma^{-} - \sigma^{+}$ for a $[Ni3/Co1] \times 5$ superlattice. Definition of the parameters p and q as done by [39]. b) XAS signal $\sigma^{-} + \sigma^{+}$ and integrated XAS signal $\int \sigma^{-} + \sigma^{+}$ and determination of the parameter r on the Co $L_{2,3}$ edge of a $[Ni3/Co1] \times 5$ superlattice.

light. A perpendicular field was applied to the samples and varied in a range of -50 mT to +50 mT. The measurements were performed in total yield¹ for both circular left and right polarization along the normal of the surface, leading to 4 absorption curves σ^{ij} ($i = +, -$ light polarization; $j = +, -$ magnetic field direction). Such measurements allow us to eliminate the experimental asymmetry by calculating the absorption using $\sigma^{+} = \sigma^{++} + \sigma^{--}$ and $\sigma^{-} = \sigma^{+-} + \sigma^{-+}$.

An example of such spectra for a $[Ni3/Co1] \times 5$ lattice is given in fig.(3.17)

Following the treatment of this data as described by [39] we then calculate the XMCD signal $\sigma^{-} - \sigma^{+}$ and the XAS signal $\sigma^{+} - \sigma^{-}$.

Using sum rules on the XMCD and the XAS data, and the definitions of q , p and r as explained in fig.(3.18) and by [39] we find for the z -component of the orbital momentum L_z and the z -component of the spin momentum S_z :

¹This means all photoelectrons are measured.

$$\frac{\langle L_z \rangle}{n_h} = \frac{2q}{3r} \quad (3.31)$$

and

$$\frac{2 \langle S_z \rangle}{n_h} \left(1 + \frac{7 \langle T_z \rangle}{2 \langle S_z \rangle} \right) = \frac{2 \langle S_z \rangle_{eff}}{n_h} = \frac{3p - 2q}{r} \quad (3.32)$$

n_h is the number of holes of the valence band and $\langle T_z \rangle$ the expectation value of the magnetic dipole operator. The number of holes n_h was determined using ab initio calculations by L. Calmels' group in Toulouse. However $\langle T_z \rangle$ remains unknown. Usually $\langle T_z \rangle$ is neglected for bulk 3d metals, but it is well known that $\langle T_z \rangle$ can be strongly enhanced for Co and Ni at the interfaces [131].

In the following we are first going to discuss the XAS measurements allowing the determination of the number of holes in the valence band n_h for Ni and for Co.

3.2.2.2 XAS results

Absorption measurements using linear polarization have first been performed on the two wedges. The variation of the Co and Ni edges as a function of the thickness of Co is reported in fig.(3.19b). It should be noted, that the Ni edge slightly decreases for increasing Co thickness. This result is quite understandable because as the Co thickness increases, the XAS signal is less sensitive to the Ni layer which lies underneath. Moreover, we notice a discrepancy between the Ni edge and Co edge intensity variation with the Co thickness when comparing the two wedges. This discrepancy comes from a small difference of the thickness of the MgO capping layer for the two wedges (around 0.5 ML). After correction, we can plot the edge variation as a function of the Co thickness and consequently determine the electron escape length λ using the expression:

$$I_{Co} = K_{MgO+Ni} I_{Co}^{\infty} (1 - K_{Co}^n) \quad (3.33)$$

with $K_{Co} = e^{-\frac{1}{\lambda}}$, the attenuation factor due to the MgO capping and the Ni layer on top of the Co layer K_{MgO+Ni} , and K_{Co} the attenuation factor of a Co atomic plane.

We find $\lambda = 12 \pm 0.5 \text{ ML}$ (see fig.(3.19c)), in agreement with published values [132]. Finally, it is also possible to plot the Co on Ni edges intensity ratio which this time no longer depends on the thickness of the capping. This variation can be calculated by writing the edge intensity dependent on the attenuation factor K_{Ni} and K_{Co} . For the stacking of our wedges this ratio is equal to:

$$\frac{I_{Co}}{I_{Ni}} = \frac{I_{Co}^{\infty}}{I_{Ni}^{\infty}} \left\{ \frac{K_{Ni}^2 (1 - K_{Co}^n)}{(1 - K_{Ni}^2) + K_{Ni}^2 K_{Co}^n (1 - K_{Ni}^3)} \right\} \quad (3.34)$$

We consider that $K_{Co} \cong K_{Ni} = e^{-\frac{1}{\lambda}}$ which is actually the case as shown experimentally by [132]. Hence, the edge intensity ratio can be calculated without adjustable parameters and be compared to the measurements. The agreement between experiment and calculation is excellent as shown in fig.(3.19d). Moreover, the edge intensities of transition metals are proportional to the number of holes n_h [133]. If we assume, as a first approximation, that this number of holes does not strongly vary with the Co thickness in the superlattices, this later can be determined by comparing the Co and

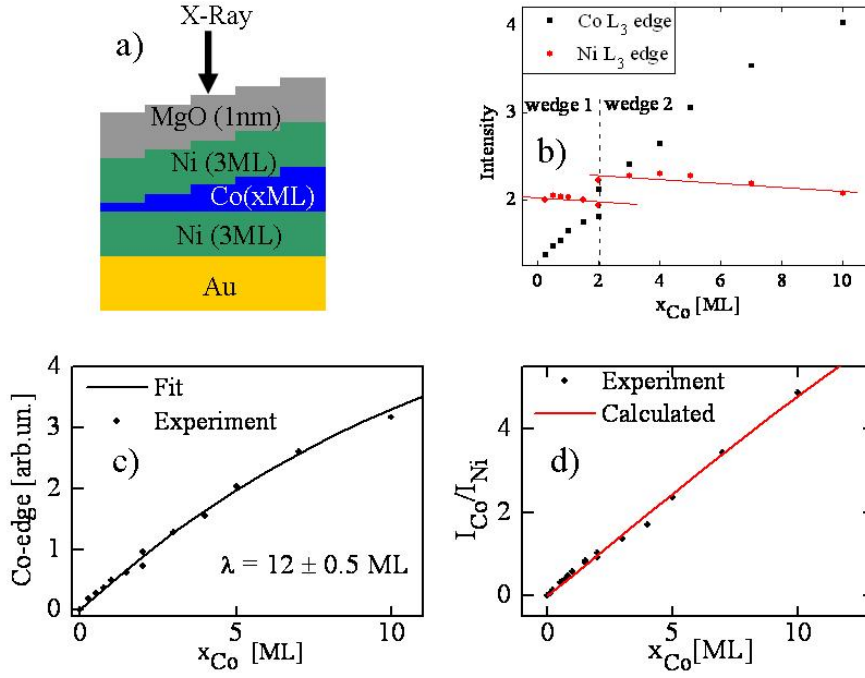


Figure 3.19: a) Structure of the used $Ni3/Co(x)/Ni3$ wedges grown by MBE. b) Variation of the L_3 edge for Co and for Ni as a function of the Co thickness. c) Corrected variation of the Co L_3 edge and fit for the determination of the escape depth λ . d) Ratio of the intensity of the Co and Ni L_3 edge and calculation using eqn.(3.34).

Ni bulk moments with XMCD measurements performed on thick epitaxial Co and Ni layers. We find $n_h^{Co} = 2.5 \pm 0.1$ and $n_h^{Ni} = 1.0 \pm 0.1$. The fact, that the experimental data fits well with the calculations confirms the good sample quality and allows a direct measurement of the Co and Ni number of holes ratio.

3.2.2.3 Determination of the magnetic moment by XMCD

For the two wedges, we measured hysteresis loops at the Co L_3 edge with the field applied along the normal of the samples in a range from -50 to +50 mT using a field increment of 2 mT (see fig.(3.20)). A perpendicular magnetization is found for Co-thicknesses between 0.25 and 4 ML. These results confirm the data shown in sec.(3.2.1).

XMCD measurements were performed on the wedges and on a series of superlattices. An example for the determination of p and q is shown above in fig.(3.18). From the sum rules as shown above (eqn.(3.31) and eqn.(3.32)) we find:

$$2q = \frac{\langle L_z \rangle}{2 \langle S_z \rangle_{eff}} (9p - 6q) \quad (3.35)$$

In fig.(3.21) we plotted $2q$ as a function of $(9p-6q)$ for all samples.

Surprisingly we find a linear variation passing through the origin (as appropri-

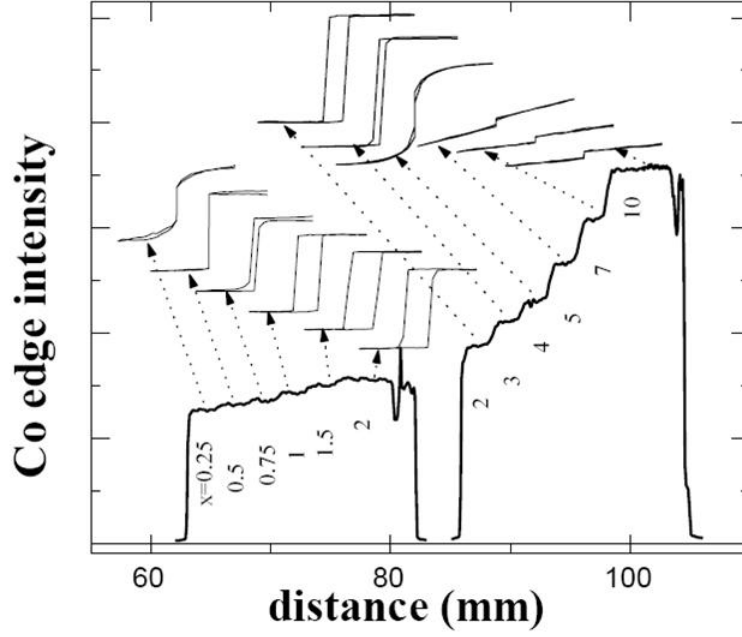


Figure 3.20: For each Co thickness of the two wedges, hysteresis loops at the Co L_3 edge were performed with the field applied along the normal of the samples.

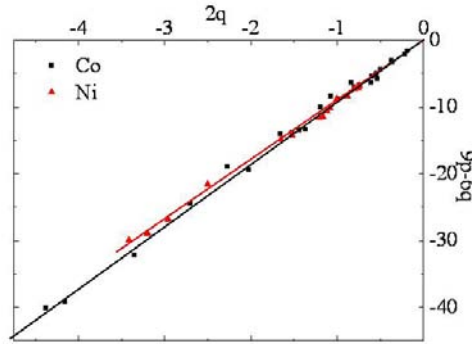


Figure 3.21: $2q$ as a function of $9p - 6q$ obtained from XMCD spectra for Co and Ni.

ate), showing that the ratio of the effective spin moment and the orbital moment $\langle L_z \rangle / 2 \langle S_z \rangle_{eff}$ is constant for Co and Ni and is independent of the Co thickness. In addition we also find that $\langle L_z \rangle / 2 \langle S_z \rangle_{eff}$ is the same for Co and Ni.

Furthermore the application of the sum rules to the XMCD data allows us to determine the dependency of the orbital magnetic moment and the effective spin magnetic moment as defined above. The results for Co are shown in fig.(3.22a). We notice, that for small Co thicknesses the orbital moment reaches $0.22 \pm 0.02 \mu_B/atom$. This is an increase of approximately 1/3 compared to the measures bulk value of $0.16 \pm 0.02 \mu_B/atom$. In addition, we also observe an increase of the effective spin

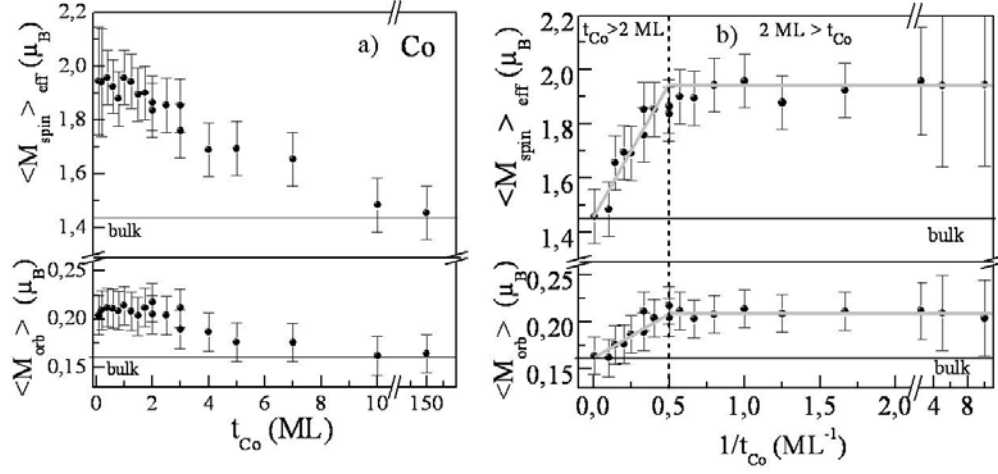


Figure 3.22: a) Effective spin moment and orbital moment of Co versus the Co thickness t_{Co} for a series of superlattices and wedges. b) Same data as in a), but plotted against $1/t_{\text{Co}}$.

moment. This result is not surprising since we found, that the ratio of these two quantities is constant. At this stage it is instructive to plot the magnetic moments according to the inverse of the thickness (fig.(3.22b)). Two regimes are then clearly identifiable. In a first regime between 0 and 2 atomic monolayers the average Co moments are constant. Beyond 2 ML a linear regime occurs. This result leads us to assume, that the moments of Co atoms in contact with a Ni layer are not the same as the Co bulk moment.

The moments of Ni are shown in fig.(3.23). It should be noted here, that only the superlattices are exploitable. Indeed, the moments of Ni obtained on the wedges are smaller. This is probably due to the fact that the top Ni layer is in contact with MgO. Hybridization with MgO might be the cause of the Ni moment decrease. However this hypothesis remains unchecked. In the superlattices, we also observe an increase of the effective spin moment when the Co thickness increases. Using these results it is very difficult to argue, that the Ni orbital moment increases, given the low moments and the error bars of the measurement. Nevertheless, given the fact, that the ratio between the effective spin moment and the effective orbital moment is constant as for Co (see fig.(3.21)), if the effective spin moment increases, the orbital moment should increase, too.

In superlattices, Co atoms are sometimes surrounded by only Co atoms (for thick Co layers), and sometimes by both Co and Ni atoms (at the interfaces). If we consider m_1 the Co moment at the Co/Ni interface and m_2 the Co moment for Co atoms in between 2 Co layers, the average atomic moment can be written as:

$$\text{For } 0 \leq t_{\text{Co}} \leq 2ML: \quad \langle m \rangle = m_1$$

$$\text{For } 2ML \leq t_{\text{Co}}: \quad \langle m \rangle = \frac{2(m_1 - m_2)}{t_{\text{Co}}} + m_2$$

Two linear regimes are actually obtained depending on the inverse of the Co thickness.

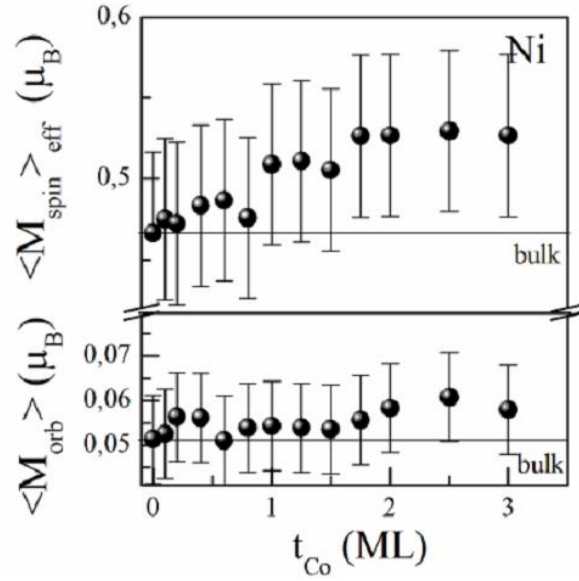


Figure 3.23: Effective spin moment and orbital moment of Ni versus the Co thickness t_{Co} for a series of superlattices.

A linear fit leads to the following Co moments:

$$m_1^{spin-eff} = 1.95 \pm 0.1 \mu_B \quad \text{and} \quad m_1^{orb} = 0.21 \pm 0.02 \mu_B$$

$$m_2^{spin-eff} = 1.5 \pm 0.1 \mu_B \quad \text{and} \quad m_2^{orb} = 0.16 \pm 0.02 \mu_B$$

We now come back to the fact that we measured a linear relation between orbital and effective spin moments (see fig.(3.21)). According to the determination of the spin and orbital moments determined above, we consider two regimes: one where all Co atoms are in contact with a Ni layer ($t_{Co} \leq 2$):

$$\langle L_z \rangle = \langle L_z \rangle_B + \langle \Delta L_{z,int} \rangle \quad (3.36)$$

and

$$\langle S_z \rangle_{eff} = \langle S_z \rangle_B + \langle \Delta S_{z,int} \rangle_{eff} \quad (3.37)$$

and we consider a second regime for thick Co layers ($t_{Co} \geq 2$):

$$\langle L_z \rangle = \langle L_z \rangle_B + \frac{2 \langle \Delta L_{z,int} \rangle}{t_{Co}} \quad (3.38)$$

and

$$\langle S_z \rangle_{eff} = \langle S_z \rangle_B + \frac{2 \langle \Delta S_{z,int} \rangle_{eff}}{t_{Co}} \quad (3.39)$$

For $t_{Co} \leq 2$ we can hence write for the ratio of orbital and effective spin moment:

$$\frac{\langle L_z \rangle}{\langle S_z \rangle_{eff}} = \frac{\langle L_z \rangle_B + \langle \Delta L_{z,int} \rangle}{\langle S_z \rangle_B + \langle \Delta S_{z,int} \rangle_{eff}} \approx \frac{\langle L_z \rangle_B}{\langle S_z \rangle_B} \left[1 + \left(\frac{\langle \Delta L_{z,int} \rangle}{\langle L_z \rangle_B} - \frac{\langle \Delta S_{z,int} \rangle_{eff}}{\langle S_z \rangle_B} \right) \right] \quad (3.40)$$

For $t_{Co} \geq 2$ we can write:

$$\frac{\langle L_z \rangle}{\langle S_z \rangle_{eff}} = \frac{\langle L_z \rangle_B}{\langle S_z \rangle_B} \cdot \frac{t_{Co} + \frac{2\langle \Delta L_{z,int} \rangle}{\langle L_z \rangle_B}}{t_{Co} + \frac{2\langle \Delta S_{z,int} \rangle_{eff}}{\langle S_z \rangle_B}} \quad (3.41)$$

A limited development of the above expression leads to:

$$\frac{\langle L_z \rangle}{\langle S_z \rangle_{eff}} \approx \frac{\langle L_z \rangle_B}{\langle S_z \rangle_B} \left[1 + \frac{2}{t_{Co}} \left(\frac{\langle \Delta L_{z,int} \rangle}{\langle L_z \rangle_B} - \frac{\langle \Delta S_{z,int} \rangle_{eff}}{\langle S_z \rangle_B} \right) \right] \quad (3.42)$$

From the experimental data on the spin and orbital moment we know that the term $\left(\frac{\langle \Delta L_{z,int} \rangle}{\langle L_z \rangle_B} - \frac{\langle \Delta S_{z,int} \rangle_{eff}}{\langle S_z \rangle_B} \right)$ is small. This explains the observed linear relation between $\langle L_z \rangle$ and $\langle S_z \rangle_{eff}$ for the [Co/Ni] system.

3.2.2.4 Conclusion on XMCD

A strong increase of the effective spin and orbital Co moments is observed at the interface. Moreover, below the interfacial atomic plane Co atoms bulk values have been found. The same assumption may be done for Ni moments, despite the fact that the moments are much lower and thus less accurate. Indeed, we observe in fig.(3.23), that the effective spin moment actually increases when increasing the Co thickness. Such a conclusion is however not obvious for the Ni orbital moment regarding the results in fig.(3.23), but one should keep in mind that the effective spin moment to orbital moment ratio is constant (fig.(3.21)). Consequently the orbital moment is also increasing. All these results allow us to conclude that at the Co/Ni interface, both Co and Ni effective spin and orbital momentum increase. The increase of Co and Ni orbital moments at the Co/Ni interface is around 1/3 compared to the bulk, and may explain the strong interface anisotropy of this system. This strong enhancement of the orbital moment is not confirmed by simulations [134].

However, the situation is not so clear concerning the effective spin moments. The strong enhancements of these effective spin moments at the interface do not mean, that the true spin moments follow the same variation. This increase of the effective spin moment can be also due to an increase of the T_z contribution at the interfaces, as predicted e.g. by [131]. Ab initio calculations, which are in progress, should allow to distinguish an increase of the effective spin moment due to an increase of the T_z contribution or to a increase of the spin moment.

3.2.3 Part 3: Dynamic magnetic properties

Ferromagnetic resonance spectroscopy (FMR) was done with [Co/Ni] superlattices by A. Kent's group at New York University. The measurements were done using a so-called

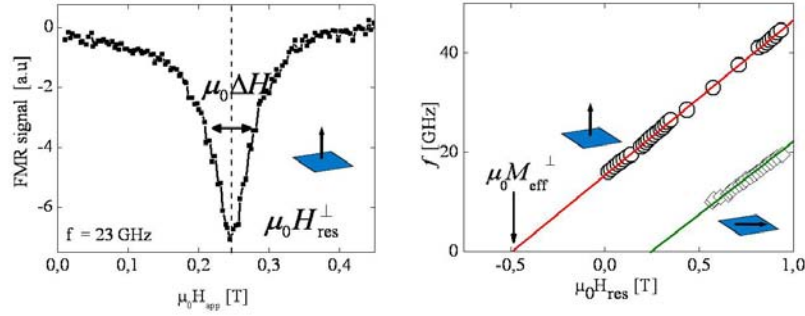


Figure 3.24: FMR spectroscopy of a $[Co(2.5ML)/Ni(3ML)] \times 20$ superlattice: a) FMR absorption signal at 23 GHz, field applied perpendicular to the sample surface. $\mu_0 \Delta H$ is the full width at half maximum of the absorption peak. $\mu_0 H_{res}$ the resonance field. b) Resonance frequency as a function of the applied field perpendicular (circles) to the sample surface and in plane (rectangles). The red line is a linear fit to the perpendicular data, the green line is a linear fit to the in-plane data.

flip chip method. For the FMR experiments superlattices with 20 instead of the usual 10 [Co/Ni] repetitions were used in order to get higher absorption signals.

The absorption signal of a $[Co(2.5ML)/Ni(3ML)] \times 20$ superlattice as a function of a perpendicularly applied field $\mu_0 H_{app}$ for a fixed frequency of 23 GHz is plotted in fig.(3.24a). The resonance peak has a full width at half maximum of about $\mu_0 \Delta H = 60mT$. The resonance field $\mu_0 H_{res}$ is around $0.25T$.

When the field H_{app} is applied perpendicular to the sample surface we have the following resonance condition [135]:

$$\frac{2\pi f}{g\mu_B/\hbar} = (\mu_0 H_{res} - \mu_0 M_{eff}^\perp) \quad (3.43)$$

with

$$\mu_0 M_{eff}^\perp = \mu_0 M - \frac{2K_u}{M_S} = \frac{-K_{eff}}{M_S} \quad (3.44)$$

the effective demagnetizing field, where K_u is the perpendicular magnetocrystalline anisotropy, K_{eff} the effective perpendicular anisotropy and M_S the saturation magnetization of the sample. Consequently the resonance frequency f is a linear function of the applied field $\mu_0 H_{res}$. A linear fit of the data is done. For the interception with the $\mu_0 H_{res}$ axis, we have the condition:

$$\mu_0 H_{res} = \mu_0 M_{eff}^\perp = \frac{-K_{eff}}{M_S} \quad (3.45)$$

which allows the determination of K_{eff} as the magnetization M_S is known from magnetometry. A comparison of the results obtained for some samples by FMR and the magnetometry results can be found in fig.(3.25a).

The FMR data confirms the results for PMA found by magnetometry. However the main issue for the FMR experiments with [Co/Ni] superlattices, was the determination

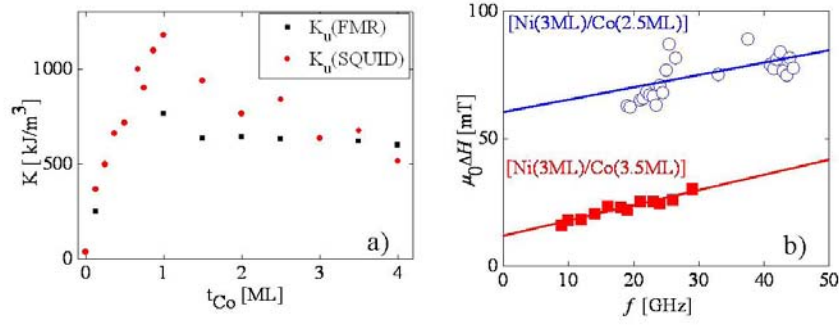


Figure 3.25: Results from FMR spectroscopy: a) Comparison between the uniaxial anisotropy K_u found by FMR and by magnetometry. b) Frequency dependence of the full width at half maximum $\mu_0 \Delta H$ of the resonance peak for $[\text{Co}(2.5)/\text{Ni}(3)] \times 20$ and for $[\text{Co}(3.5)/\text{Ni}(3)] \times 20$ superlattices.

of the Gilbert damping term α . Therefore the frequency dependence of the full width at half maximum $\mu_0 \Delta H$ of the resonance peak has to be measured. The results for two samples are plotted in fig.(3.25b). A linear fit with $\mu_0 \Delta H = a + b \cdot f$ leads to $a = (52 \pm 2)\text{mT}$ and $b = (0.63 \pm 0.06)\text{mT/GHz}$ for $[\text{Co}(2.5)/\text{Ni}(3)]$ and to $a = (11.6 \pm 1.1)\text{mT}$ and $b = (0.60 \pm 0.06)\text{mT/GHz}$ for the $[\text{Co}(3.5)/\text{Ni}(3)]$ sample. [136] gives a linear relation between $\mu_0 \Delta H$ and the applied frequency:

$$\mu_0 \Delta H = \mu_0 \Delta H_0 + \frac{4\pi\alpha}{g\mu_B/\hbar} f \quad (3.46)$$

Thus we have two contributions to $\mu_0 \Delta H$: one contribution which varies linearly with the frequency f and which is proportional to the damping term α , and one constant contribution $\mu_0 \Delta H_0$. Assuming that $g \approx 2$, we find $\alpha = 0.009 \pm 0.001$ for both samples. α hence seems to only have a small dependence on the Co thickness. However, the constant term $\mu_0 \Delta H_0$ seems to be very sensitive to the layer thicknesses. We find $\mu_0 \Delta H_0 = (52 \pm 2)\text{mT}$ for $[\text{Co}(2.5)/\text{Ni}(3)]$ and a 4 times smaller value of $\mu_0 \Delta H_0 = (11.6 \pm 1.1)\text{mT}$ for $[\text{Co}(3.5)/\text{Ni}(3)]$. The constant contribution is in general explained as caused by disorder [136]. The disorder is due to fluctuations of the anisotropy in the sample with macroscopic surface (several mm^2). Consequently, different parts of the sample are in resonance for different applied fields. Furthermore it is explained, that the disorder leads to relaxation via so-called two magnon scattering (also [136] and references there in).

We conclude, that the Gilbert damping parameter α of the order of 0.01 is of reasonable size in order to allow high spin transfer torque efficiency. Similar values were reported for the in-plane system permalloy ($\alpha = 0.0082 \pm 0.0002$ [137]), and for sputtered $[\text{Co}/\text{Ni}]$ multilayers with PMA ($\alpha \in [0.015; 0.035]$ [135]).

3.2.4 Conclusion on the magnetic properties of $[Co/Ni]$ superlattices

MBE-grown $[Co/Ni](111)$ superlattices have magnetic properties which make them a good candidate for a spin torque model system. Their magnetization and anisotropy can be easily tuned by varying the Co layer thicknesses. Within the experimental accuracy bulk values for the Co and Ni momenta fit to the measured magnetization. The strong PMA of the sharp Co/Ni interfaces allows to maintain perpendicular magnetization in a large range of sample compositions compared to sputtered $[Co/Ni]$ layers (see e.g. [126]). A simple phenomenological model, explaining anisotropy of the superlattice as the sum of interface anisotropy, bulk anisotropy of the $[111]$ direction and shape anisotropy, fits well to the experimental data.

XMCD measurements show that the orbital moment of Co and Ni increases for about 1/3 of the bulk values at the interfaces. This might explain the strong interface anisotropy of the superlattices found by magnetometry.

Ferromagnetic resonance spectroscopy confirms the expected low Gilbert damping parameter α of 0.01, indicating that a high spin transfer efficiency is possible.

3.3 Fully epitaxial spin valves based on [Co/Ni](111) superlattices

In this section we discuss the elaboration and analysis of fully epitaxial spin valves based on [Co/Ni](111) superlattices. The goal of this study is to have a system which can be patterned to nanopillars for spin torque experiments. We first discuss the elaboration of a sample which allows independent switching of soft and hard layer. In a next step spin resolved photoemission is done in order to measure the spin polarization of the [Co/Ni](111) superlattices at the Fermi level. In a last step magnetoresistance of a spin valve in the current in-plane configuration is studied.

3.3.1 Growth and magnetic properties

The growth of fully epitaxial spin valves based on [Co/Ni](111) superlattices can be easily done when Au is used as a nonmagnetic spacer. The challenge is to find a configuration of layers, where both magnetic layers can be switched independently and the nonmagnetic spacer layer is thin compared to the electron spin diffusion length.

Coupling effects, inhibiting independent reversal, can be due to exchange coupling via the RKKY interaction and due to dipolar stray fields. The range of the RKKY exchange is of the order of a few nanometer (see [138] and [139]) what makes a nonmagnetic spacer of the order of several nanometer necessary.

A more difficult problem is the dipolar coupling. Mainly two effects can lead to dipolar coupling between thin films with perpendicular magnetization: an orange peel coupling due to roughness of the sample [140] or domain walls created during the reversal process. A further difficulty is, that the influence of dipolar fields changes when the layers are nano structured as the coupling is no longer due to domain walls but due to the stray field at the border of the pillar. Hence, it is possible, that a sample that is decoupled as long as it is a full film, becomes coupled after nanostructuration.

In literature one can find, that the hard layer is often made more hard by coupling it to hard magnetic materials (e.g. Co/Pt in [15]) or to block its magnetization with an antiferromagnet. Such an artifice allows to be able to reverse the soft layer(SL), without reversing the hard layer(HL) of the spin valve. However, for our epitaxial growth by MBE, we were limited in the choice of materials. Thus the idea is to use a layer with high perpendicular anisotropy ([Co(1ML)/Ni(3ML)]) as hard layer and a layer with a smaller perpendicular anisotropy ([Co(2.5ML)/Ni(3ML)]) as soft layer. The choice of the [Co(2.5ML)/Ni(3ML)] layer is a compromise between a sample with a relatively low perpendicular anisotropy and the risk of losing a too small perpendicular anisotropy during nano structuration. The effective anisotropy field $\mu_0 H_A$ of the [Co(1ML)/Ni(3ML)] layer is 1.8T and it is 0.65T for the [Co(2.5ML)/Ni(3ML)] layer. The coercivity of a [Co(1ML)/Ni(3ML)] layer is 32.5mT and it is 8.5mT for the [Co(2.5ML)/Ni(3ML)] layer (compare table fig.(3.13)). In the following we are going to check if this differences are high enough to make the elaboration of a spin valve possible, which is based on these two layers and for which the SL can be reversed without affecting the HL.

From Kerr microscopy we know, that the reversal of a thin film of [Co(1ML)/Ni(3ML)] \times N with $N < 10$ happens in two steps: the creation of few reversed domains, and then their growth by domain wall propagation. We suppose, that this is similar for

$[Co(2.5ML)/Ni(3ML)] \times N$ layers, at least, when N is small enough. We can calculate the dipolar field due to a domain wall in the SL using the simple model described in sec.(2.3.2.3). As parameters we use $K_{eff} \approx 300kA/m$ as measured by magnetometry and $A_{Co/Ni} \approx 1.5 \cdot 10^{-11} J/m$. The value for the exchange constant A is an assumption based on the values given for Co and Ni in [141]. This leads to a domain wall width w of the order of 20nm. The magnetization of $[Co(2.5ML)/Ni(3ML)]$ is $900kA/m$. In fig.(3.26a) one can see the dipolar field $\mu_0 H_Z$ emitted by a DW as a function of the distance to the DW-center for different distances z to the surface of a $[Co(2.5ML)/Ni(3ML)] \times 3$ layer. From the inset in fig.(3.26a) we obtain, that using a 10 nm thick spacer can reduce the dipolar field for approximately one third compared to the hypothetical case where no spacer is used. In fig.(3.26b) one can see the dipolar field $\mu_0 H_Z$ emitted by a DW as a function of the distance to the DW center for different numbers N of repetition of the $[Co(2.5ML)/Ni(3ML)]$ stack at a fixed distance $z = 4nm$ to the surface of a $[Co(2.5ML)/Ni(3ML)] \times N$ layer. From the inset in fig.(3.26b) we obtain, that reducing the number of repetitions from 10 to 3 can reduce the dipolar field for approximately a factor of three, or in absolute values from a maximum amplitude of $0.79T$ down to a maximum amplitude of $0.27T$.

These considerations lead us to the elaboration of a sample using $[Ni(3ML)/Co(1ML)] \times 5$ as HL and $[Ni(3ML)/Co(2.5ML)] \times 3$ as SL and to separate them with a Au wedge as a spacer layer. The thickness of the wedge is increased from $1 - 7nm$ in steps of $1nm$ (see fig.(3.26)). The size of every step is $5mm$. The hysteresis loops for the different steps were measured by a setup using polar magneto-optical Kerr effect at the Institut d'Electronique Fondamentale in Paris. The measured region of the wedge is well defined by a laser-spot of the diameter of about 1 mm. This allows to have access to the thickness of the Au-spacer, which corresponds to the Kerr-measurement. Measuring the major hysteresis loops at different steps of the wedge one can see, that the reversal of the magnetization becomes a two-step reversal for Au thicknesses of 4 or more nanometer (see fig.(3.27a)). Minor loops for the SL were measured for Au-thicknesses of $4nm$ or more (see fig.(3.27b)). One can see, that the minor loops are not completely symmetric. The bias of the coercive fields is quite small (see fig.(3.27d)) compared to the precision of the measurement. However, it seems that the switching is less sharp when the SL is reversed from the direction antiparallel to the HL to the direction parallel to the HL compared to the inverse reversal process (fig.(3.27c)).

We conclude, that for a spin valve full film sample using $[Ni(3ML)/Co(1ML)] \times 5$ as HL and $[Ni(3ML)/Co(2.5ML)] \times 3$ as SL, the SL can be reversed without affecting the HL, when a Au spacer thicker than $4nm$ is used. SL and HL are not completely decoupled. It has to be checked if such independent reversal of the SL is also possible, when the structure is patterned to nanopillars.

3.3.2 Spin-resolved photoemission

For spin torque experiments high spin polarization of the current is needed in order to obtain a high spin torque efficiency (see sec.(1.4.2)). Therefore it is necessary, that the electronic bands, which are contributing to transport are strongly polarized. For a spin valve system, we assume that all states close to the Fermi level contribute to electronic transport. Consequently, for the creation of an optimum spin polarizing layer, we have to check, the polarization of the different $[Co/Ni]$ stackings at their surface and if this

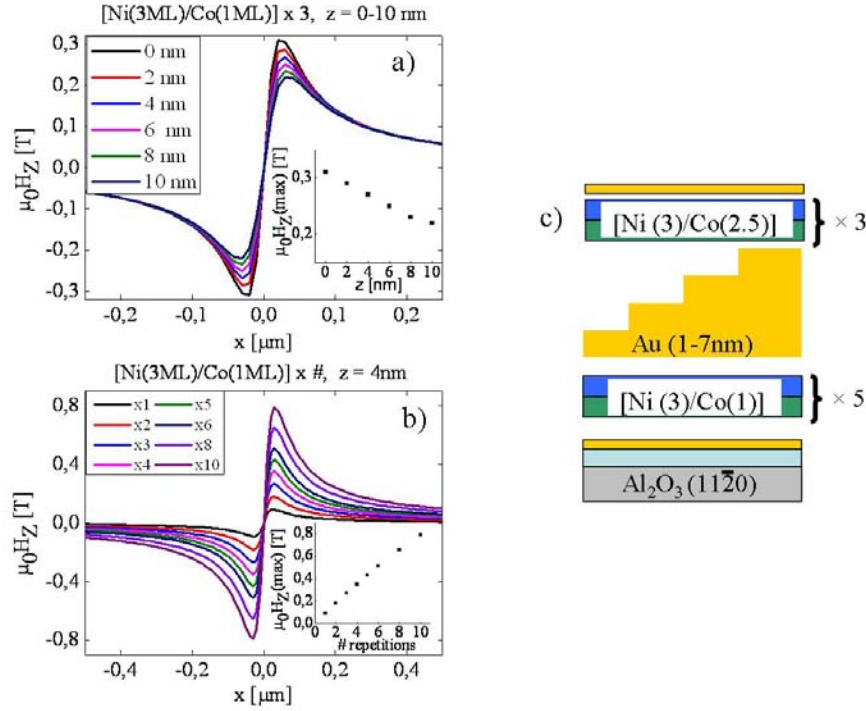


Figure 3.26: Choice of the sample-stacking for a fully epitaxial spin valve: a) Dipolar field $\mu_0 H_Z$ emitted by a DW as a function of the distance to the DW center for different distances z to the surface of a $[\text{Co}(2.5\text{ML})/\text{Ni}(3\text{ML})] \times 3$ layer. In the inset: maximum amplitude of the dipolar field $\mu_0 H_Z(\text{max})$ as a function of the distance z to the surface of a $[\text{Co}(2.5\text{ML})/\text{Ni}(3\text{ML})] \times 3$ layer. b) Dipolar field $\mu_0 H_Z$ emitted by a DW as a function of the distance to the DW center for different numbers N of repetition of the $[\text{Co}(2.5\text{ML})/\text{Ni}(3\text{ML})]$ stack at a fixed distance $z = 4\text{nm}$ to the surface of a $[\text{Co}(2.5\text{ML})/\text{Ni}(3\text{ML})] \times N$ layer. In the inset: maximum amplitude of the dipolar field $\mu_0 H_Z(\text{max})$ as a function of the number of repetitions N for $z = 4\text{nm}$. c) Stacking of a spin valve with a wedge shaped Au spacer between the two magnetic layers grown to find the minimum thickness of Au allowing to decouple the two magnetic layers.

polarization is maintained when the surface is covered by Au, which we have chosen as nonmagnetic spacer material for our spin valves. The electronic structure of bulk Co and Ni is known (e.g. [142]), however for our superlattices the electronic properties are expected to differ from bulk results (a large number of examples of changes in the electronic structure due to interfaces is given in [143] p.1269-1280). Hence we did spin-resolved photoemission in order to have access to the spin polarization close to the Fermi level at the surface of our superlattices.

Spin-resolved photoemission experiments were done at the beamline CASSIOPEE of the SOLEIL synchrotron in Paris, which is dedicated to angular resolved photo emission spectroscopy (ARPES) and spin-resolved photoemission. The line is equipped with undulators allowing to produce linear polarized beam of photons in a range between 8 and 1500 eV. Selection of energy is done using a high resolution PGM (Plane Grating Monochromator) with VLS (Variable Line Spacing) and VGD (Variable Groove Depth)

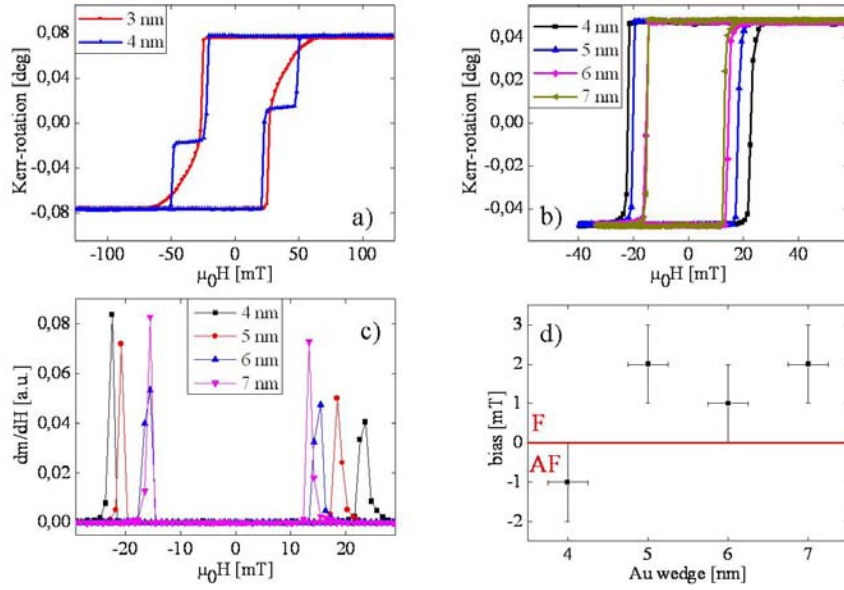


Figure 3.27: Hysteresis loops measured by Kerr effect: a) Major loop for a Au thickness of 3nm and a Au thickness of 4nm. b) Minor loops of the soft layer for different thicknesses of the Au spacer. c) Derivative of the magnetic moment m with respect to the applied field $\mu_0 H$ in arbitrary units for the minor loops. Step width of the minor loop is $1mT$. d) Bias of the SL relative to the HL as a function of the Au thickness.

gratings. Spin polarization of the photo electrons is measured using a so-called Mott detector. A Molecular Beam Epitaxy chamber for sample growth and characterization is connected to the photoemission chambers.

3.3.2.1 Basics of spin-resolved photoemission

The theory of spin-resolved photoemission is explained in several reviews e.g. [143] or [144]. We are only going to repeat some basic facts.

Two energies must be overcome to transform an electron of a solid metal in a free electron: The energy E_B which is the distance of the electron at the energy E to the Fermi level E_F :

$$E_B = E - E_F \quad (3.47)$$

and the material work function ϕ which is necessary to bring the electron from the Fermi level E_F to the vacuum E_{vac} :

$$\phi = E_{vac} - E_F \quad (3.48)$$

When a photon of the energy $h\nu$ is absorbed which brings an electron from its state with energy E into the vacuum, the conservation of energy imposes for the kinetic energy of this photoelectron, that:

$$E_{kin} = h\nu + E_B - \phi \quad (3.49)$$

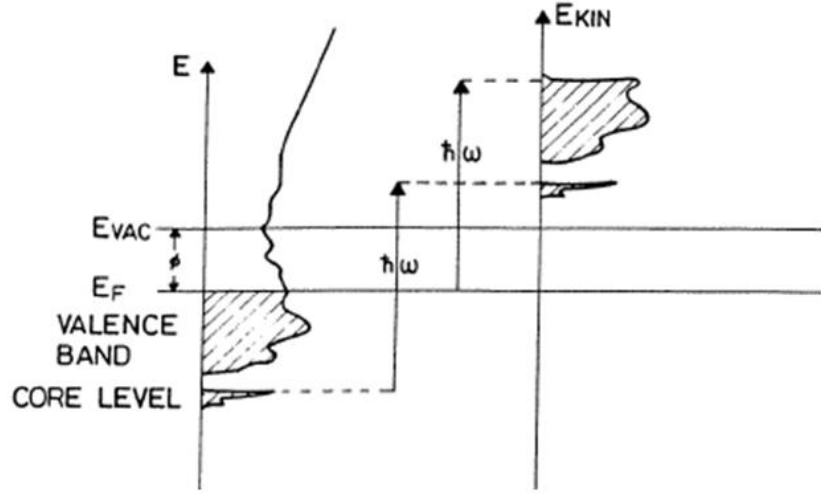


Figure 3.28: Photoemission process: The incident photon with energy $\hbar\omega$ excites an electron from an initial state below the Fermi level E_F to some final state above the vacuum level E_{vac} . The left panel shows the electron originating either from the valence band or the more localized core level. The right panel displays the excited electron energy distribution in the final state. (taken from [143])

Consequently, if we measure the kinetic energy of a photoelectron we can deduce E_B . The creation of photoelectrons mostly is spin-conservative for photon energies in the range of UV and soft X-ray [145]. This means, that the spin polarization of the photoelectron with a certain kinetic energy E_{kin} corresponds to the spin polarization of the electrons in the solid at the corresponding energy level $E = E_{kin} + \phi - \hbar\nu + E_F$.

The last point, we want to mention about photoemission is that it is a surface sensitive effect. For the typical photoemission experiment, the kinetic energy of the electron is about 10-100 eV. In this range the electron mean free path is limited to less than one nanometer as we can see from fig.(3.29). Thus only electrons from the sample surface can escape into the vacuum.

The spin polarization of the photoelectrons as a function of their energy is done with a so-called Mott detector. Electron optics allow the selection of electrons with a certain kinetic energy. Resolution in spin is obtained using spin-dependent scattering of the electrons on a Au target. As described in fig.(3.30), the spin-orbit coupling of the electron in the potential of a gold atom leads to an asymmetry in the scattering, dependent on the spin of the electron [143]. Two symmetrically opposite channeltrons can then measure the intensities I_L and I_R of the split beam. For the spin polarization of the incident electron beam we then get:

$$P = \frac{1}{S} \frac{I_L - I_R}{I_L + I_R} \quad (3.50)$$

where S is the so-called Sherman function of the Mott detector. The Sherman function describes the ability of the set-up to distinguish spin up and spin down states.

However, as we cannot be sure to have channeltrons with identical properties, two

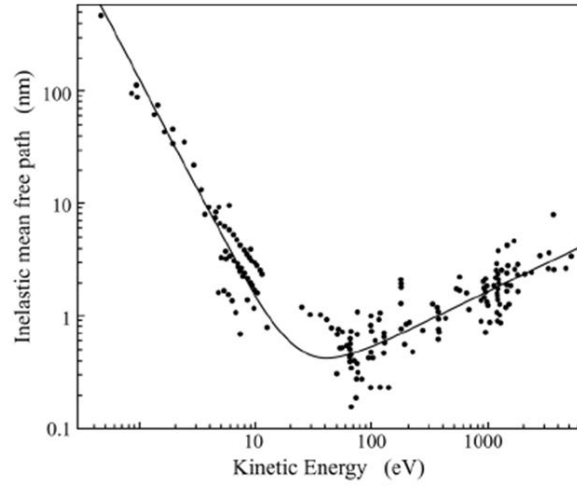


Figure 3.29: Kinetic energy dependence of the "universal" mean free path for excited electrons in solids. (taken from [146])

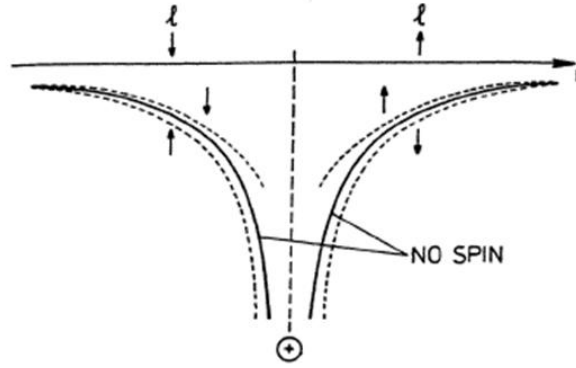


Figure 3.30: The potential curves experienced by an electron with spin up or spin down in the vicinity of a gold scattering atom both with and without spinorbit coupling. (taken from [143])

measurements with opposite magnetizations (designed as "+" and "-") have to be done to eliminate this possible asymmetry. We then obtain four sets of data (I_L^+, I_R^+ , and I_L^-, I_R^-) leading to the true spin polarization P given by [143]:

$$P = \frac{1}{S} \frac{\sqrt{I_L^+ I_R^-} - \sqrt{I_L^- I_R^+}}{\sqrt{I_L^+ I_R^-} + \sqrt{I_L^- I_R^+}} \quad (3.51)$$

With the definition

$$\langle I \rangle \equiv \frac{I_L^+ + I_R^- + I_L^- + I_R^+}{4} \quad (3.52)$$

we can then also calculate the individual majority (I^\uparrow) and minority (I^\downarrow) spectra by:

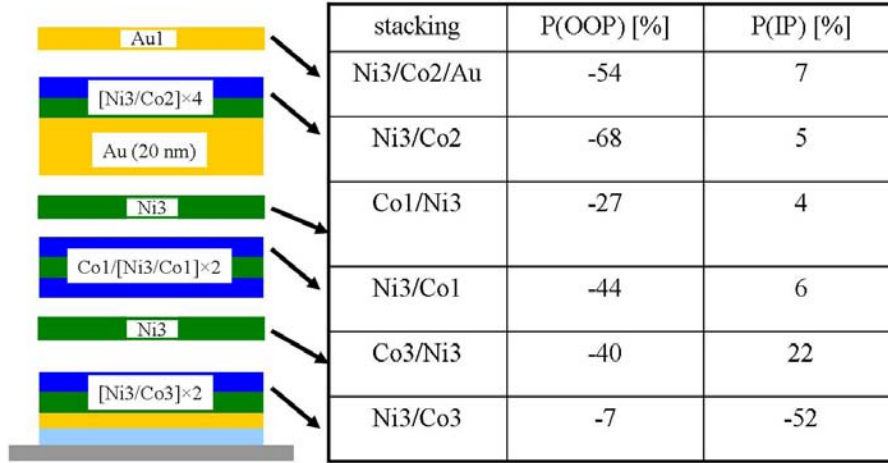


Figure 3.31: In-plane (IP) and out-of-plane (OOP) spin-polarization at the Fermi level for different stackings of $[Co/Ni]$.

$$I^\uparrow = (1 + P) \langle I \rangle \quad I^\downarrow = (1 - P) \langle I \rangle \quad (3.53)$$

3.3.2.2 Experimental results for $[Co/Ni]$ superlattices

The $[Co/Ni]$ superlattices were grown in the MBE chamber of the CASSIOPEE beam-line which is connected to the photoemission chamber. This allows to keep the samples permanently under ultra high vacuum ($p < 10^{-8}$ mbar), what guaranties clean sample surfaces. The evaporation of the metals was done by electron guns. The growth velocity was controlled by a quartz microbalance for the V buffer, and by RHEED oscillations for the other metals.

Once the V/Au buffer was deposited, a first $[Ni/Co]$ stack was grown on this buffer. The sample was then introduced in the photoemission chamber, it was measured, transferred back to the MBE chamber and the next Co and Ni layers were deposited on the same substrate. The development of the sample stack is drafted in fig.(3.31).

The photoemission experiment was done using photons of the energy of $h\nu = 30\text{eV}$.

The Mott detector has 4 channeltrons: 2 to measure the in-plane spin polarization and 2 to measure the out-of-plane spin polarization. The sample was saturated perpendicular to its surface and then the number of photoelectrons was measured in each channeltron as a function of the energy of the photoelectrons. About 100 spectra were measured for each channeltron and averaged in order to be minimize statistical fluctuations. The sample was then saturated in the opposite direction and again the number of photoelectrons was measured in each channeltron as a function of their energy.

In fig.(3.32) we show an example for the treatment of the recorded data for a $[Ni(3)/Co(2)] \times 4$ superlattice. In fig.(3.32a) we see the data for the two channeltrons measuring spin-dependent intensities for a spin orientation perpendicular to the sample surface for the two antiparallel magnetization orientations. This allows to obtain the spin-resolved spectra in fig.(3.32b) as well as the polarization fig.(3.32c) using the relations eq.(3.51) and eq.(3.53). One can see a clear asymmetry between the majority

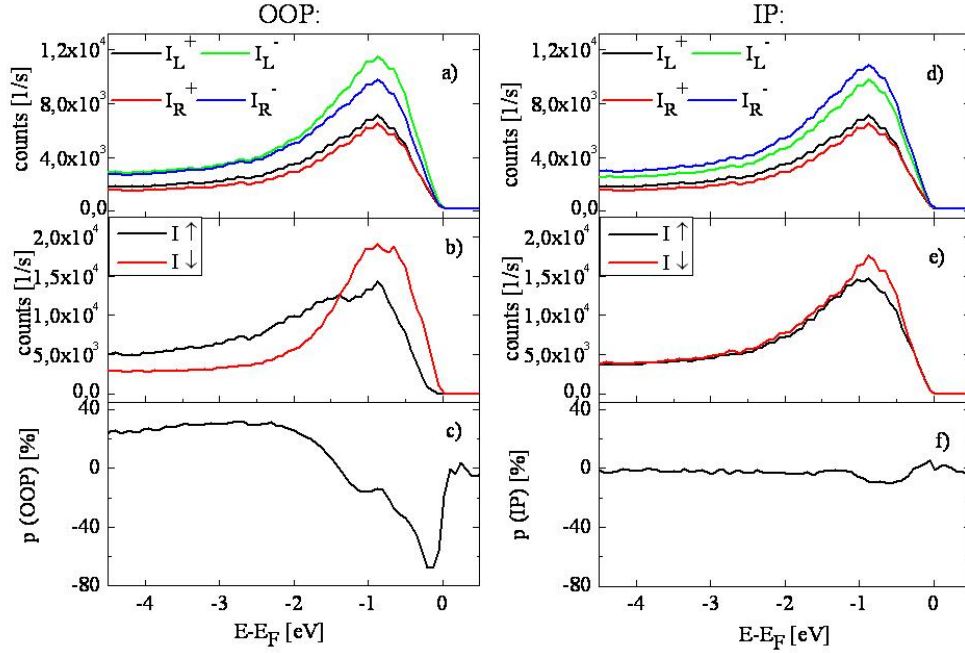


Figure 3.32: Spin-resolved photoemission experiment for a $[Ni(3)/Co(2)] \times 4$ superlattice (Co is at the surface of the sample): a) Spectra of the channeltrons for the perpendicular magnetization direction after saturation in the two antiparallel directions designated as + and -. b) Spectra for the two spin orientations up (I^\uparrow) and down (I^\downarrow) c) Perpendicular spin polarization. d)-f) as a)-c) but for the in-plane component of the magnetization.

(I^\uparrow) and the minority (I^\downarrow) spectrum. A maximum of the polarization close to the Fermi level of -68% is obtained. The same procedure is done for the measured in-plane data and shown in fig.(3.32d-f). In this case a maximum in-plane polarization of 5% is measured. The results for the other measured superlattices are shown in fig.(3.31). All samples except the $[Ni(3)/Co(3)]$ stack show a large perpendicular spin polarization close to the Fermi level compared to the in-plane polarization. It seems, that finishing the Ni/Co stacking with a Co layer increases the polarization significantly (e.g. -27% for $[Co(1)/Ni(3)]$ compared to -44% for $[Ni(3)/Co(1)]$). The fact, that the $[Ni(3)/Co(3)] \times 2$ stack has an in-plane magnetization, what is not the case for the before analyzed $[Ni(3)/Co(3)] \times 10 / Ni(3)$ can be understood by comparing the Co/Ni interface contribution: for $[Ni(3)/Co(3)] \times 2$ we only have 1.5 Co/Ni interfaces per Co layer. For $[Ni(3)/Co(3)] \times 10 / Ni(3)$ we have 2 Co/Ni interfaces per Co layer which are the main source of the perpendicular magnetic anisotropy. Furthermore we can assume the $Co/vacuum$ interface to give raise to an in-plane anisotropy, as found for the $Co(hcp)(0001)/vacuum$ interface [147]. Before doing the photoemission experiment, the sample was exposed to a $58mT$ OOP field as it was done for the other samples. Thus we can not be sure if the in-plane magnetization was saturated after the application of this field pulse. The polarization of -52% is hence a lower limit.

In a next step we studied the influence of a Co/Au interface on the polarization. It is important to check that the observed polarization is maintained at this interface. Indeed,

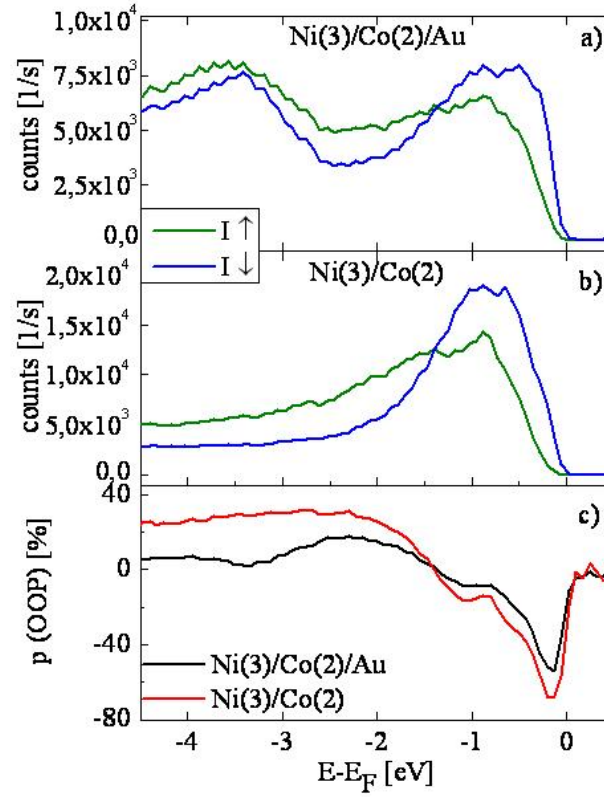


Figure 3.33: Spin-resolved photoemission for a $[Ni(3)/Co(2)] \times 4/Au(1)$ stack compared to a $[Ni(3)/Co(2)] \times 4$ -stacking: a) Spectra for the two spin-orientations up (I^\uparrow) and down (I^\downarrow) for $[Ni(3)/Co(2)] \times 4/Au(1)$ b) Spectra for the two spin-orientations majority (I^\uparrow) and minority (I^\downarrow) for $[Ni(3)/Co(2)] \times 4/Au(1)$. c) Polarization of both samples.

it was already shown for the interface between NiMnSb and MgO [148], or calculated for Ni/Cu [149], that the polarization disappears due to hybridization. For our experiment, a Au monolayer was deposited on the $[Ni(3)/Co(2)] \times 4$ stack. The result is shown in fig.(3.33) and compared to the result obtained for the $[Ni(3)/Co(2)] \times 4$ stack without the Au layer. The addition of Au slightly changes the shape of the majority (I^\uparrow) and the minority (I^\downarrow) spectrum, especially for $E - E_F < 2eV$. This can be explained by the addition of the Au states and a decrease of the Co contribution to the spectrum as the Co is now covered by Au. Besides we see a decrease of the absolute polarization of the photoelectrons at the Fermi level from -68% to -54% . This is explained by the addition of the nonpolarized Au states and a decrease of the Co contribution, too. Thus we conclude that the spin polarization is maintained in the case of a Co/Au interface.

At the end of the photoemission experiments the sample was measured by VSM magnetometry to check the remanence and the saturation field of the sample stacking. Remanence was found to be larger than 95% of the saturation moment. The saturation field is about $65mT$, hence the applied field for the photoemission experiments of $58mT$ was eventually not sufficient to saturate the sample for the last measurements. From

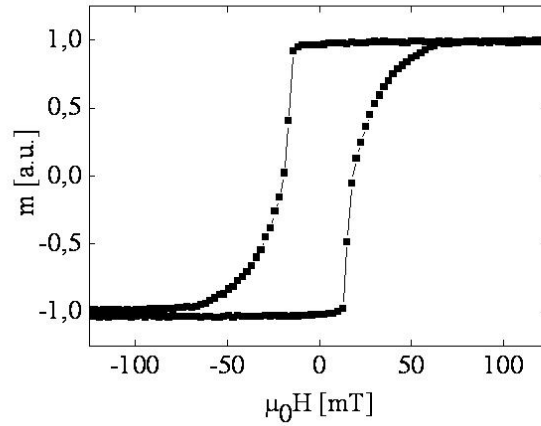


Figure 3.34: Hysteresis loop of the [Co/Ni] sample stacking for the photoemission experiments as described in fig.(3.31). Remanence is higher than 95% of the saturation moment. The saturation field $\mu_0 H_S$ is about 65 mT.

the hysteresis loop we can deduce that the sample had at least 90% of its saturation moment for the photoemission experiment.

In summary we found the OOP polarization of perpendicular magnetized [Co/Ni] superlattices near the Fermi level between -27% and -68% . The highest spin polarization at the surface for [Co/Ni]-superlattices is obtained when the stacking is finished by a Co layer. Furthermore it was shown that this polarization is maintained, when the final Co layer has an interface with Au, as it is the case in our spin valve system. [Co/Ni](111) superlattices have hence the potential of injecting highly spin-polarized currents in a Au(111)-layer, what is a necessary condition for high spin torque efficiency in the [Co/Ni]/Au/[Co/Ni] system.

3.3.3 Transport properties of [Co/Ni]/Au/[Co/Ni] spin valves

A $[Ni(3)/Co(1)] \times 5 / Au(4nm) / [Ni(3)/Co(2.5)] \times 3$ spin valve was grown in order to measure its current in-plane (CIP) transport properties. This was done, because the structuration of CIP devices is technically much easier than the elaboration of nanopillar structures for current perpendicular to plane measurements. In order to optimize the CIP measurement the thickness of buffer and capping layers was reduced to a minimum. The minimum thickness of V(110) allowing a continuous coverage of the substrate is around 5nm. We hence chose a buffer consisting of 5nm of vanadium and 3 atomic monolayers of Au. The Au capping layer was also reduced to a thickness of 3ML. The VSM hysteresis loop of the sample is shown in fig.(3.35a). It shows a two step reversal, proofing, that the SL can be reversed without affecting the HL. This layer was patterned by optical lithography in a geometric configuration as shown in fig.(3.35b). This configuration allows to measure the Hall resistance R_H and the resistance R as a function of the applied field $\mu_0 H$. We observe a GMR effect of the order of 1.5% at room temperature. Furthermore an Extraordinary Hall Effect (EHE) is observed for the Hall measurement fig.(3.35f). We observe, that the $[Ni(3)/Co(1)] \times 5$ has a negative

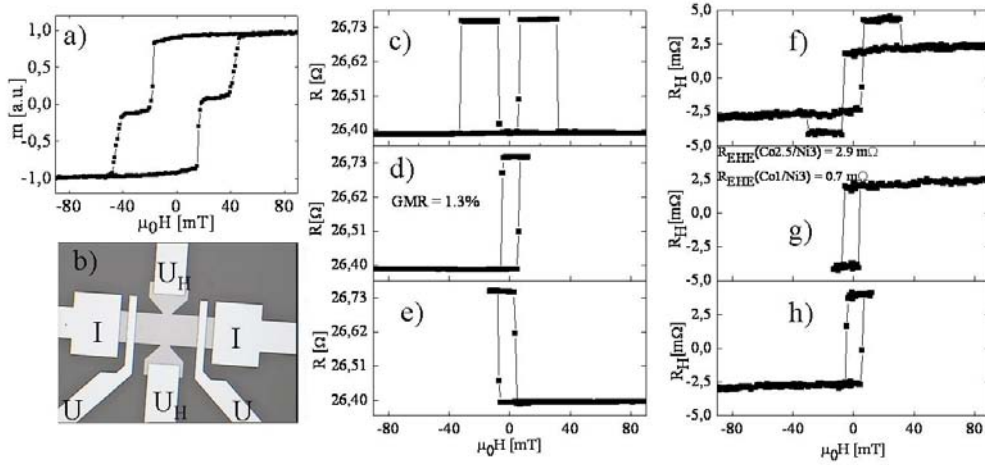


Figure 3.35: Transport properties of a $[Ni(3)/Co(1)] \times 5/Au(4nm)/[Ni(3)/Co(2.5)] \times 3$ spin valve. a) VSM hysteresis loop b) Geometry of the transport measurement. Length of the sample: $800\mu m$, width: $200\mu m$, distance between Au contacts: $400\mu m$ c)-e) Resistance R vs applied field $\mu_0 H$. f)-h) Hall resistance R_H vs applied field $\mu_0 H$

EHE coefficient, whereas $[Ni(3)/Co(2.5)] \times 3$ has a positive EHE coefficient. This can be explained, as the EHE coefficient of Ni was observed to be negative [150], in contrast to Co with a positive EHE coefficient. One can thus imagine that in a sample with a relatively small Co contribution the EHE is dominated by the Ni contribution and hence negative. At a certain critical thickness of Co, the sign of the EHE coefficient of the whole sample changes and becomes positive. A quantitative analysis of the EHE coefficients is not possible as the $[Co/Ni]$ -layers are "short-circuited" by the vanadium buffer and the Au spacer layer.

Minor loops for the resistance (fig.(3.35c and d)) and the Hall resistance (fig.(3.35g and h)) were measured. They show, as in the case of full layers, that the soft layer can be reversed without affecting the hard layer, as the amplitude of the resistance jumps for the minor loop is equal to the amplitude of the resistance jumps of the major loop.

Finally the GMR was measured using a cryostat as a function of temperature between 30 and 300 K (fig.(3.36)). We observe a linear increase of the GMR from 1.5% at room temperature to 3.5% at 30 K.

The 1.5% of GMR show, that there is an important polarization of the electrons passing through the Au spacer layer. Replacing the Au by Cu of the same thickness would probably allow to increase the GMR, as Cu has a smaller L-S coupling and is hence less depolarizing [151]. This would also lead to a potentially higher spin torque efficiency. First tests with Cu spacers have been done in the meantime. However a layer configuration allowing independent reversal of the SL was not found yet.

A linear decrease of GMR with increasing temperature was already observed in several other systems (see for example [152] or [153]). Models describing GMR as a function of temperature can be found in [154] or [155].

Further investigations on the GMR of $[Co/Ni]$ -based spin valves were not done for the moment.

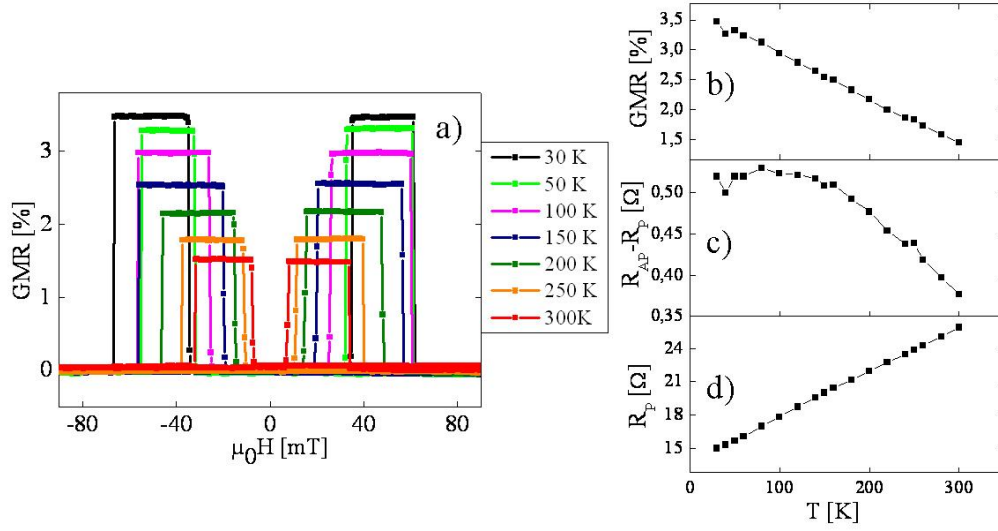


Figure 3.36: Temperature dependence of the GMR effect: a) GMR measurement for temperatures between 30K and 300K. b) GMR vs temperature c) Difference $R_{AP} - R_P$ of the resistance between antiparallel and parallel alignment of the magnetic layers vs temperature. d) Resistance of the spin valve for parallel alignment vs temperature.

3.3.4 Conclusion on $[Co/Ni]$ -based spin valve systems

In this section we showed, that it is possible to grow fully epitaxial spin valves based on $[Co/Ni]$ superlattices, if Au is used as nonmagnetic spacer layer. It remains to check, if it is still possible to reverse the SL independently from the HL, when the layers are patterned to nanopillars. Photoemission experiments showed that the highest spin polarization of the electronic states close to the Fermi level is obtained, when the stacking is finished with a Co layer. Values up to 68% of spin polarization could be measured. In addition we could show that the high spin polarization of the electrons close to the Fermi level is maintained, when the final Co layer is covered with Au. Finally, the transport properties of $[Co/Ni]$ based spin valves were analyzed. A GMR effect of 1.5% at room temperature was measured proving the spin polarization of the electrons flowing through the Au spacer layer. Patterning of these layers into nanopillars in order to do first spin torque experiments is in progress.

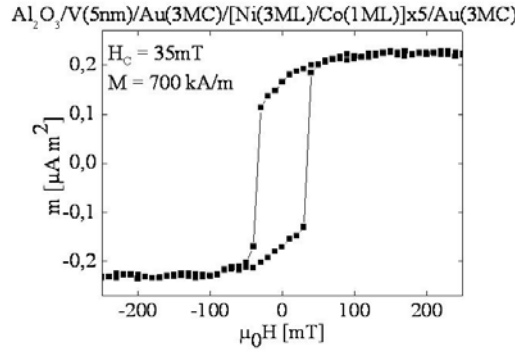


Figure 3.37: VSM hysteresis loop for a $V(5nm)/Au(3ML)[Ni(3ML)/Co(1ML)] \times 5Au(3ML)$ film.

3.4 Magnetization reversal of [Co/Ni] nanowires

In this section we show the propagation of a single domain wall inside a 500 nm large [Co/Ni] nanowire by Kerr Microscopy. The nanowires were patterned by E-beam lithography in "CC-MiNaLor" (the platform for micro and nano structuration of the IJL). Kerr Microscopy was performed at the Institut d'Electronique Fondamentale of the Université Paris Sud. The chosen sample stacking of the MBE grown sample is: $V(5nm)/Au(3ML)[Ni(3ML)/Co(1ML)] \times 5Au(3ML)$. The hysteresis loop measured for a full film by VSM can be seen in fig.(3.37)

The patterned structure consists of 24 pads of $120 \times 200 \mu m^2$ size with 9 nanowires on each pad. The nanowires are 500nm wide and about 50μm long. Two Hall crosses are located at a distance of 25μm from the pad for each wire. Moreover a constriction was added between the two Hall crosses as a supplementary artificial pinning site for domain walls. Furthermore a square of the dimension $200 \times 200 \mu m^2$, 5 $100 \times 25 \mu m^2$ rectangles and 400 $10 \times 10 \mu m^2$ squares were patterned in order to analyze the nucleation and propagation behavior of a [Co1/Ni3] structure. An overview of the patterned structures is given in fig.(3.38).

In order to find an optimum artificial pinning site several kinds of constrictions were tested. Their geometrical details can be found in fig.(3.39).

3.4.1 Magnetization reversal in patterned [Co/Ni] layers

The magnetization reversal in the patterned [Co/Ni] layer is studied by Kerr Microscopy. The images are taken at low resolution for a large field of view of $2 \times 3 mm^2$. The sample is saturated in a magnetic field of about $-160 mT$. A Kerr Microscopy image is taken and used as reference. Then 10 second long antiparallel field pulses were applied. The field amplitude is increased by 1mT for every step and a Kerr Microscopy image of the remanent state is taken. The reference image is subtracted in order to increase the magnetic contrast. Several of the resulting images are shown in fig.(3.40). For applied fields lower than 40mT, the pad is possible to observe pads that are partially reversed. However for applied fields higher than 40mT the observed pads are always either unreversed or totally reversed. At these fields the domain walls move fast enough to reverse the whole pad at a time scale, which is short compared to the 10 second long

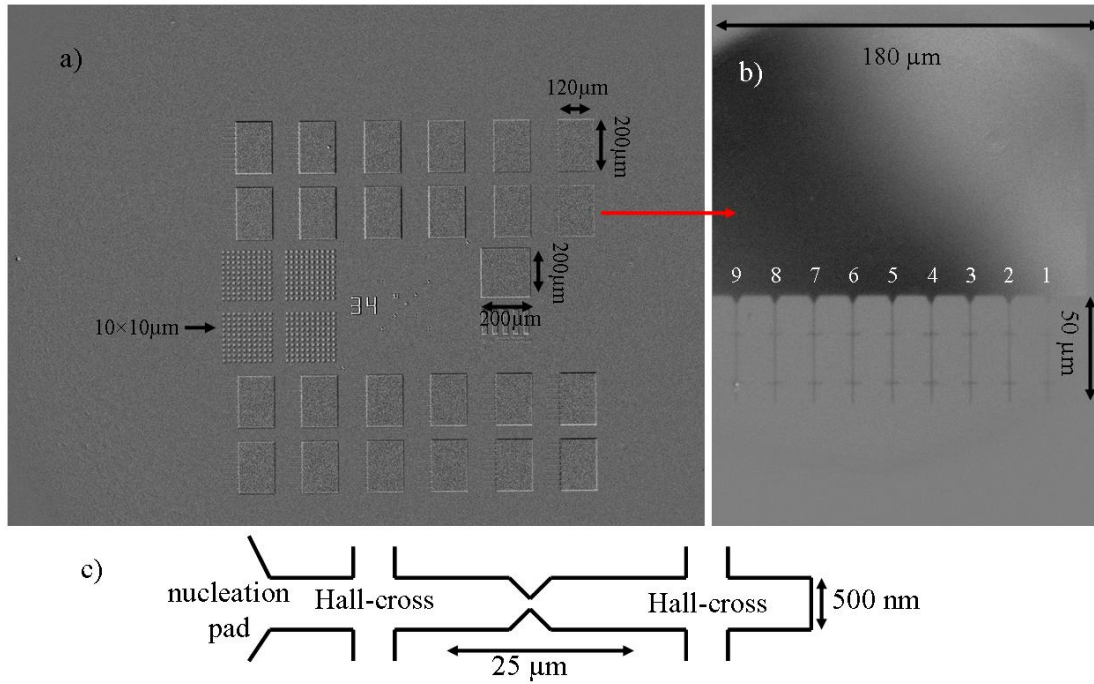


Figure 3.38: E-beam patterned samples from a $[Co1/Ni3] \times 5$ film. a) Overview over the whole patterned structure. b) Zoom on a nucleation pad with 9 $50 \mu m$ long and $500 nm$ wide wires. c) Sketch of the structure of the wire. The size of the Hall crosses is $500 \times 500 nm^2$. A constriction can be found in the center between the two Hall crosses.

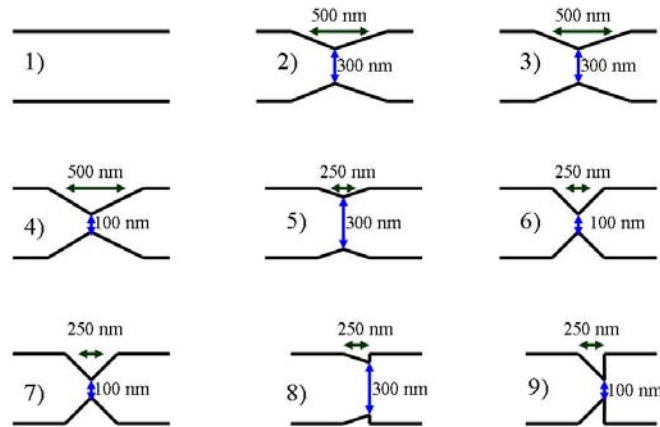


Figure 3.39: Different kinds of constrictions for the wires 1-9 of a nucleation pad.

field pulse. The last pad is reversed at a field of $78 mT$. The percentage of pads with a nucleated domain as a function of the amplitude of the applied field pulse is plotted in fig.(3.41).

In order to do successful domain wall propagation experiments the nucleation field of the pad must be lower than the propagation and pinning fields inside the wire. The approach which was chosen here, was to use large nucleation pads. However, the nucleation fields for most of the pads are found to be higher than the propagation field

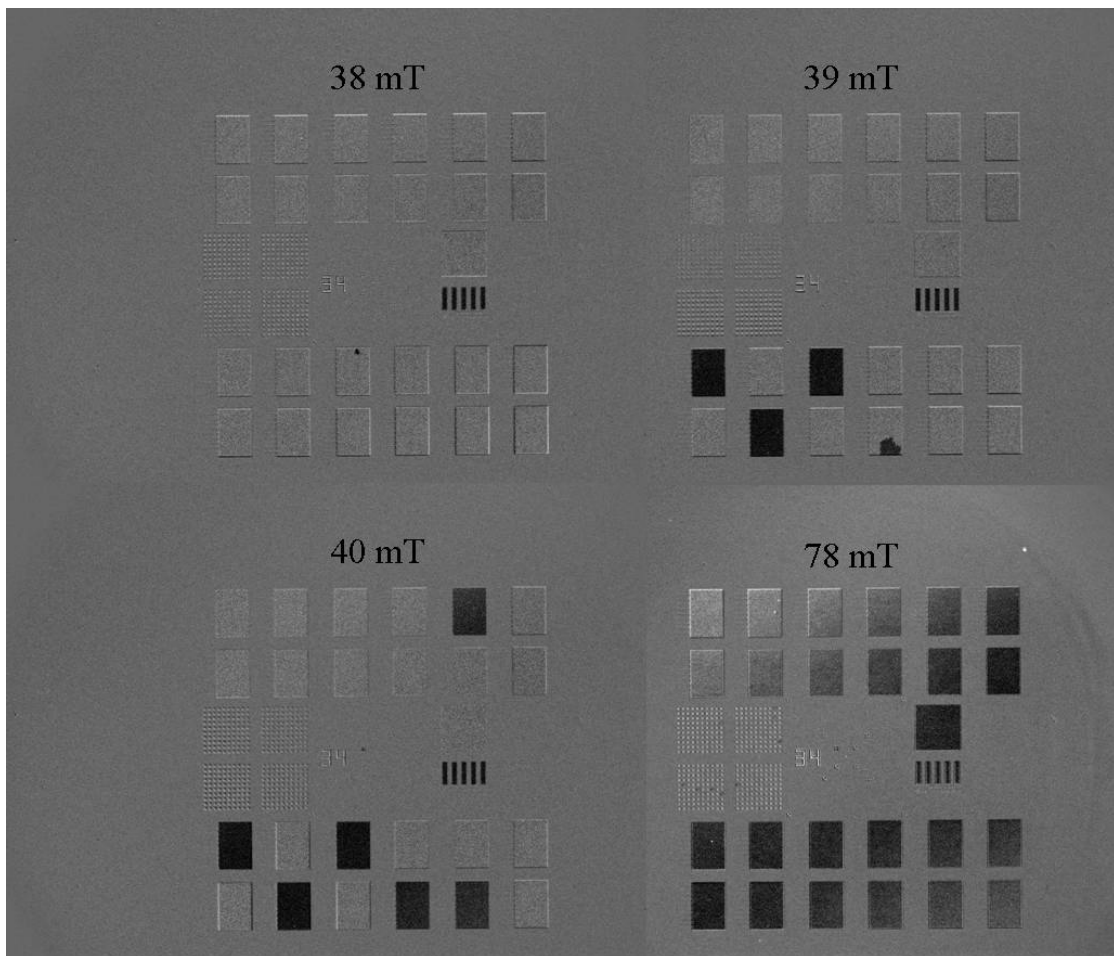


Figure 3.40: Difference of Kerr Microscopy images with a reference image at saturation for low resolution showing the reversal of the nucleation pads. The magnetic contrast is small and inverted for the region which is at the upper side on the left of the images due to an artifact of the microscope.

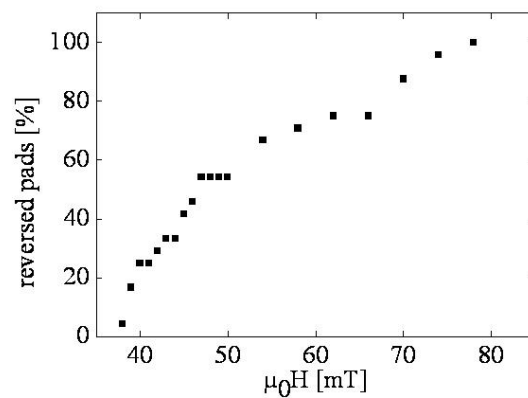


Figure 3.41: Percentage of reversed pads as a function of the amplitude $\mu_0 H$ of a 10 second field pulse.

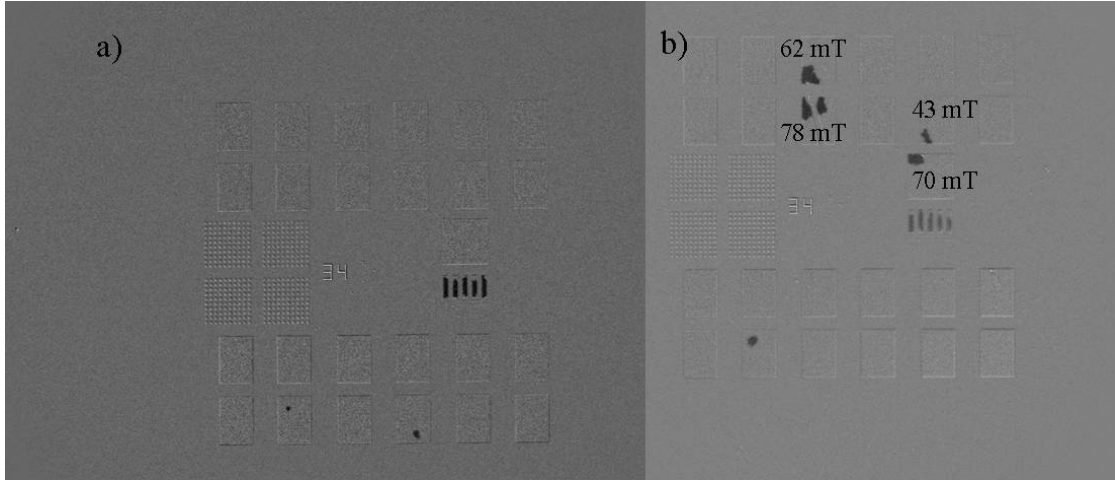


Figure 3.42: Kerr Microscopy images after a field pulse of 37 mT during 10 seconds: a) Sample as patterned b) After scratching with a bonding needle on some nucleation pads. The field amplitudes marked on the pads correspond to their nucleation fields before scratching with a bonding needle.

of the full film sample which is of the order of 35-40 mT (see fig.(3.37) and fig.(3.40)). These nucleation fields can be decreased using a simple method: making scratches with the needle of the bonding machine. The result is shown in fig.(3.42). One can see, that domains can be nucleated in the pads with a 10 second pulse at a field amplitude of the order of 37mT after scratching their surface.

3.4.2 Propagation of domain walls in [Co/Ni] nanowires

We now focus on the reversal of the magnetization in the nanowires. Therefore Kerr Microscopy images with high resolution were taken for a field of view of about $200 \times 240 \mu m^2$. As in the above experiment all images are taken at remanence. The sample is saturated in a high negative field and a reference pictures is taken again. For a 10 second long 36mT field pulse nucleation is observed in the nucleation pad (see fig.(3.43a)). Repeated application of 36 mT pulses allows to completely reverse the pad. Then a series of 10 second long pulses with an amplitude increased by 1mT at every step is applied. One can clearly see the propagation of a single domain wall inside the wires with increasing field. Pinning of domain walls was observed inside the hall crosses, at the constriction and in some wires at pinning sites only due to intrinsic defects.

Three series of Kerr Microscopy images of the domain wall propagation were taken and compared (see fig. (3.44)). The different possible pinning sites were marked with numbers from 0-7 as described in fig.(3.45). We can then compare the propagation of the DW under field between different wires and different measurement series.

From the Kerr Microscopy images, we obtain the DW position as a function of the applied field amplitude for the nanowires. The result is plotted in fig.(3.45).

As seen in sec.(1.3.5.1) for straight domain walls the following relation between the pinning fields and the geometry of the constriction can be found :

$$\mu_0 H_{dep,geo} \propto \frac{\partial L}{\partial S} \quad (3.54)$$

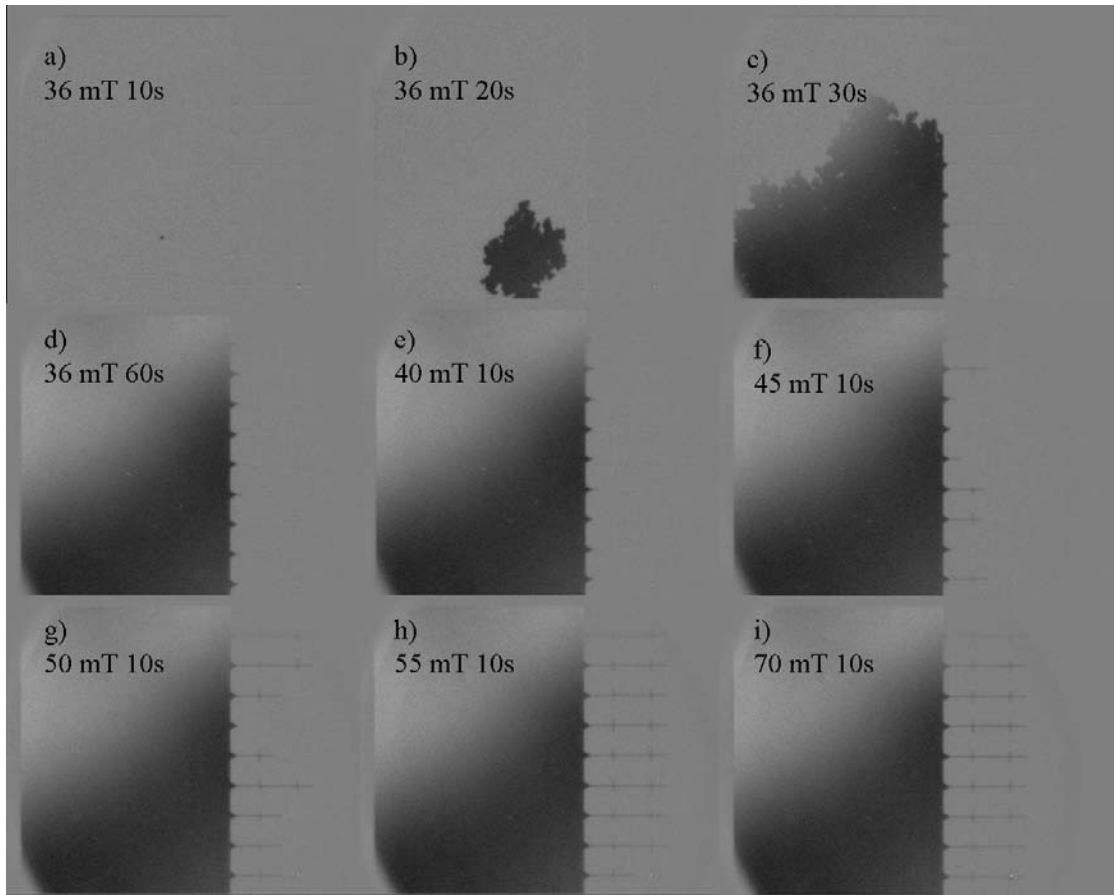


Figure 3.43: Nucleation of a domain in the nucleation pad and propagation of domain walls through the nanowires. The first of the nine wires of this sample is in the region, where the Kerr Microscope is not sensitive to magnetization.

where L is the length of the domain wall and S the area of the wire reversed by domain wall propagation. Consequently the strongest pinning can be expected for the Hall crosses and the constrictions of wire 8 and 9.

However we nearly do not observe the DW stopping in the first Hall cross (4 out of 24 measurements) which is equivalent for all wires. For the wire 8 the DW remains in the first Hall cross for field pulses up to 58 mT. For all other wires the DW had already passed the first Hall cross at this field. This might indicate, that an intrinsic defect increases the pinning potential of the first Hall cross of the wire 8. Wire 2 and 3 have identical constrictions. Despite this the DW stops in the constriction of wire 2 but not in the constriction of wire 3, what also indicates that the pinning might be influenced by intrinsic pinning sites. More data would be necessary to complete the analysis of the pinning sites, as pinning is a stochastic effect. This was not done by now.

3.4.3 Conclusion on the DW propagation in [Co/Ni] nanowires

Wires with a width of 500nm were patterned by E-beam lithography. $200 \times 120\mu\text{m}^2$ rectangular pads are used as nucleation pads. The nucleation field for magnetic domains

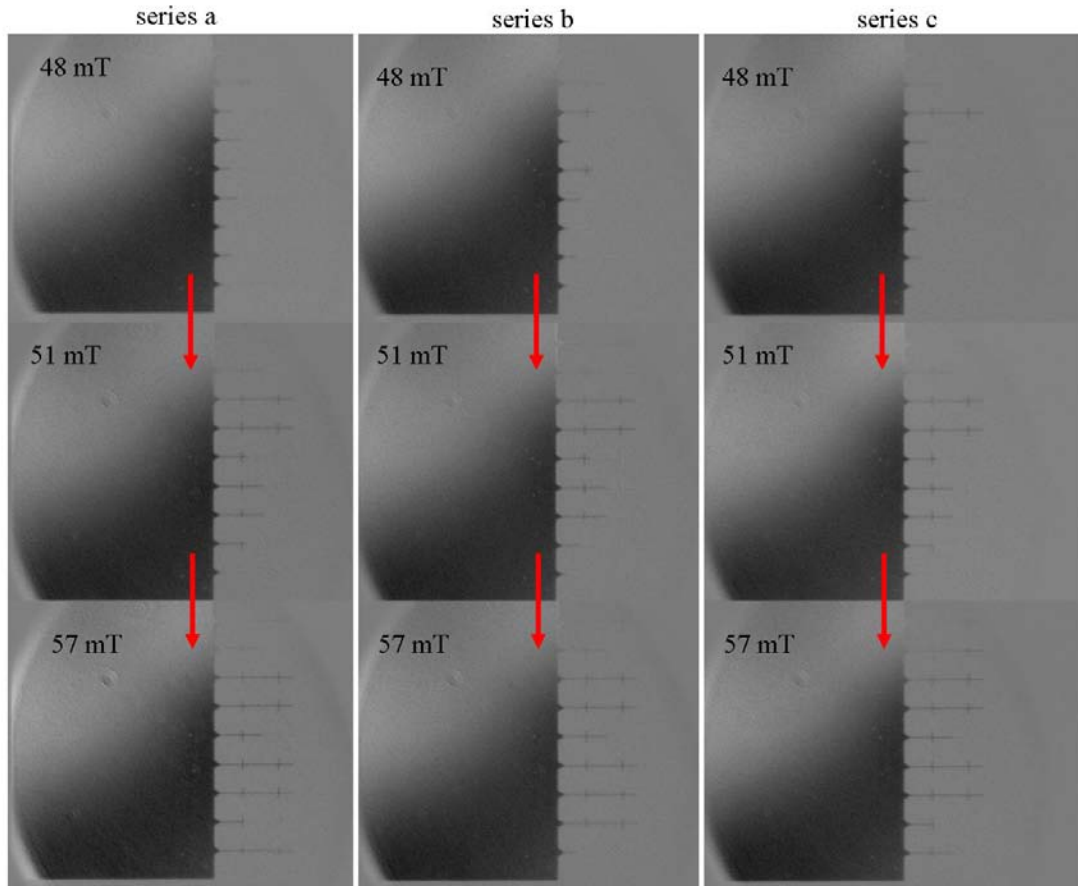


Figure 3.44: Comparison of the domain wall propagation between different hysteresis loops. For every loop the sample is saturated in one direction. Field pulses of 10 seconds with increasing amplitude are applied afterwards.

in the pads can be reproducibly limited to a value inferior to the propagation fields inside the wire by scratching mechanically on the surface of the pads.

The nucleation of reversed domains in the nucleation pad and the propagation of single domain walls through the wire was imaged by Kerr microscopy. Hall crosses and different constrictions were placed on the wire. Pinning fields can not be controlled by the geometry of artificial pinning sites. This is certainly due to randomly distributed intrinsic pinning sites.

In a next step one should add electrical contacts in order to do first studies on domain wall propagation under current for this material.

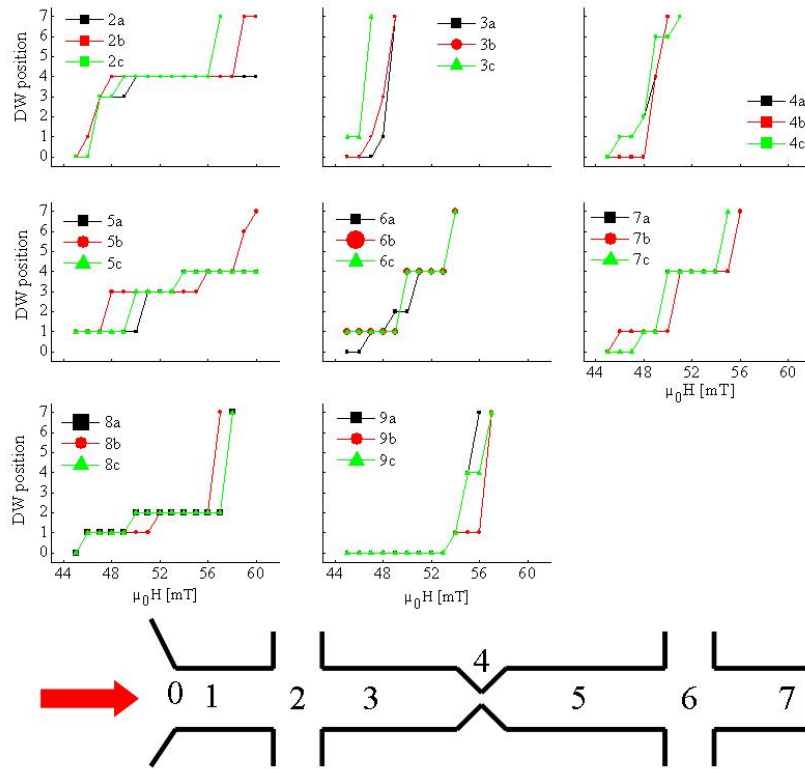


Figure 3.45: Comparison of the DW propagation as a function of field for the different wires. The letters a, b and c correspond to the measurement series, the numbers from 2-9 are the number of the wire as indicated in fig.(3.38). The sketch below the result explains the eight different possible positions of a DW in the wire: 0) pinning at the entrance of the wire, 1) pinning between entrance and first Hall cross, 2) first Hall cross, 3) between first Hall cross and constriction, 4) constriction, 5) between constriction and second Hall cross, 6) second Hall cross, 7) completely reversed

3.5 Conclusions and perspectives for epitaxial $[Co/Ni]$ superlattices

The growth of epitaxial $[Co/Ni](111)$ superlattices on $Al_2O_3(11\bar{2}0)$ substrates is well understood. RHEED oscillations during the growth of the Co and Ni layers proof a layer by layer 2D growth and they allow the control of the deposited layer thickness down to the tenth of an atomic monolayer. The supposed fcc structure of the superlattice was confirmed by transmission electron microscopy experiments. Exact lattice constants were obtained from X-ray diffraction experiments and the application of elastic theory. This detailed structural knowledge allows to simulate magnetic and electric properties of the material with standard methods and to compare them to the experimental results.

The magnetic properties were analyzed from different points of view. Macroscopic measurements using magnetometry showed, that the magnetization and the perpendicular magnetic anisotropy (PMA) of epitaxial $[Co/Ni](111)$ superlattices can be easily tuned by varying the Co layer thicknesses in a large range. A simple phenomenological model, explaining the anisotropy of the superlattice as the sum of interface anisotropy, bulk anisotropy of the $[111]$ direction and shape anisotropy, fits well to the experimental data. A more detailed understanding of the PMA was obtained from XMCD measurements, which gave insight into magnetism on the atomic scale. An increase of the orbital contribution to magnetism at the Co/Ni interface could be observed. The dynamical properties were studied using ferromagnetic resonance spectroscopy. We confirmed the expected low Gilbert damping parameter α of 0.01, a necessary key point for high spin transfer torque efficiency.

In a next step we showed, that it is possible to grow fully epitaxial spin valves based on $[Co/Ni]$ superlattices, if Au is used as nonmagnetic spacer layer. Soft and hard layer could be decoupled. We furthermore checked by doing photoemission experiments if $[Co/Ni](111)$ superlattices have the potential to inject highly spin-polarized currents in the Au spacer layer. Values up to 68% of spin polarization for the electrons close to the Fermi level could be measured when finishing the stack with a Co layer. In addition we could show that the high spin polarization of the electrons close to the Fermi level is maintained, when the final Co layer is covered with Au. CIP transport measurements showed a GMR effect of 1.5% at room temperature which could be increased up to 3.5% at 30K. This proves that the electrons flowing through the Au spacer are spin polarized.

The structuration of nanopillars from Co/Ni -based spin valves is in progress.

Furthermore nanowires were fabricated from $[Co/Ni](111)$ superlattices. Single domain wall motion could be shown inside these wires. Samples allowing to inject currents inside the wires in order to do current induced domain wall propagation experiments are in preparation.

Chapitre 4

Conclusion

Dans cette thèse nous avons étudié l'aptitude de deux systèmes magnétiques pour former des systèmes modèles pour l'étude du transfert de spin. Dans ce chapitre nous résumons les résultats les plus importants obtenus.

Critère	Alliages de $\text{Co}_{1-x}\text{Tb}_x$	Super-réseaux de $[\text{Co/Ni}](111)$
AMP	Dans une large gamme de compositions $x \in [0.08; 0.34]$	Dans des super-réseaux $[\text{Ni}(3\text{MC})/\text{Co}(x\text{MC})] \times 10$ pour $x \in [0.15; 3.5]$
Variabilité des paramètres magnétiques	Aimantation perpendiculaire: $M_s \in [0; 650 \text{ kA/m}]$ en choisissant une concentration x et une température T adaptée AMP: Constante d'anisotropie: $K_{\text{eff}} \in [0; 1600 \text{ kJ/m}^3]$ en choisissant une concentration x et une température T adaptée $K_{\text{eff}} \in [0; 1500 \text{ kJ/m}^3]$ en choisissant une concentration x et une température T adaptée	Aimantation perpendiculaire: $M_s \in [500 \text{ kA/m}; 900 \text{ kA/m}]$ en choisissant une épaisseur de Co adaptée AMP: Constante d'anisotropie: $K_{\text{eff}} \in [25 \text{ kJ/m}^3; 1000 \text{ kJ/m}^3]$ en choisissant une épaisseur de Co x adaptée $K_{\text{eff}} \in [0; 700 \text{ kJ/m}^3]$ en choisissant une épaisseur de Co x adaptée
Homogénéité	Très peu de points de nucléation de domaines renversés dans des couches pleines, renversement dû à la propagation de parois, par contre beaucoup de centres de piégeage intrinsèque	Échantillons fortement homogènes du à la croissance par épitaxie; très peu de points de nucléation de domaines renversés dans des couches pleines, renversement dû à la propagation de parois,
Efficacité du transfert de spin attendue	Grand paramètre d'amortissement de Gilbert supposé ($\alpha > 0.1$) à cause du fort couplage L-S et des résultats décrits dans la littérature Très faible GMR, ce qui pourrait indiquer une faible capacité de polariser des courants en spin. Cependant des résultats encourageantes pour la propagation de parois sous courant dans des matériaux similaires décrits dans la littérature	paramètre d'amortissement de Gilbert faible mesuré ($\alpha = 0.01$), GMR importante, forte polarisation en spin pour les électrons au niveau de Fermi, ce qui indique une forte capacité pour polariser des courants électriques en spin
Autres applications	All-optical switching	Modification de l'anisotropie par application d'un champ électrique

Fig. 4.1: Récapitulatif des résultats obtenus pour les alliages de $\text{Co}_{1-x}\text{Tb}_x$ et les super-réseaux de $[\text{Co/Ni}](111)$.

Chapter 4

Conclusion

The aim of this PhD thesis was to study magnetic systems for their suitability for spin torque experiments exploring basic models of material properties and spin transfer phenomena. Two systems were analyzed: $[Co/Ni]$ superlattices grown by molecular beam epitaxy and sputtered amorphous $CoTb$ alloys. Both materials possess tunable perpendicular magnetic anisotropy (PMA) and magnetization over a large range. The origin of this anisotropy was well understood for the $[Co/Ni]$ superlattices, whereas it remains unclear for the $Co_{1-x}Tb_x$ alloys. The work done on the magnetization reversal process in both systems showed that the $[Co/Ni]$ superlattices as well as the $Co_{1-x}Tb_x$ alloys are suitable for domain wall propagation experiments as reversal is mainly due to the propagation of a few nucleated domain walls. For high spin transfer torque efficiency it is helpful, to have a material with small Gilbert damping parameter α and a high potential to spin-polarize an electric current. Epitaxial $[Co/Ni](111)$ superlattices fulfill these conditions. The intrinsic Gilbert damping parameter α is found to be of the order of 0.01. The high potential to spin-polarize currents was shown by spin resolved photoemission spectroscopy and an important GMR effect. For $Co_{1-x}Tb_x$ alloys a small GMR effect was measured proving, that electric currents can be spin-polarized by this material. The Gilbert damping parameter α was not measured. In literature high values ($\alpha > 0.1$) are reported specially around the compensation point of the angular momentum [29] for rare earth - transition metal alloys. On the other hand the annihilation of the angular momentum should increase the spin transfer torque (STT) efficiency at this point. For the moment we can not give a reasonable estimation for the potential of the STT efficiency of this material. However, for the field of current induced domain wall motion encouraging results have been obtained recently for the similar TbCoFe system [30].

Unfortunately no spin torque experiments could be realized for $[Co/Ni]$ superlattices and $Co_{1-x}Tb_x$ alloys until now. The elaboration of the necessary nanostructured samples is under development.

A part from STT, other experimental applications for the two studied materials should be considered. For the $Co_{1-x}Tb_x$ alloys this is the field of all-optical magnetization switching as discussed in this manuscript. For $[Co/Ni]$ superlattices some work has been started on the Electric Field-Induced Modification of Magnetism [31] as they possess a well controllable anisotropy.

critereon	$\text{Co}_{1-x}\text{Tb}_x$ -alloys	$[\text{Co/Ni}](111)$ superlattices
PMA	in a large range of compositions $x \in [0.08; 0.34]$	In $[\text{Ni}(3\text{ML})/\text{Co}(x\text{ML})] \times 10$ superlattices for $x \in [0.15; 3.5]$
Variability of magnetic properties	Perpendicular magnetization: $M_S \in [0; 650 \text{ kA/m}]$ by chosing an adapted concentration x and temperature T PMA: Uniaxial anisotropy constant: $K_U \in [0; 1600 \text{ kJ/m}^3]$ by chosing an adapted concentration x and temperature T $K_{\text{eff}} \in [0; 1500 \text{ kJ/m}^3]$ by chosing an adapted concentration x and temperature T	Perpendicular magnetization: $M_S \in [500 \text{ kA/m}; 900 \text{ kA/m}]$ by chosing an adapted Co-layer thickness PMA: Uniaxial anisotropy constant: $K_U \in [25 \text{ kJ/m}^3; 1000 \text{ kJ/m}^3]$ by chosing an adapted Co-layer thickness $K_{\text{eff}} \in [<0; 700 \text{ kJ/m}^3]$ by chosing an adapted Co- layer thickness
Homogeneity	few weak nucleation points in films, reversal due to DW propagation, however high number of pinning defects for DWs	highly homogenous samples due to their epitaxial growth, few weak nucleation points in films, reversal due to DW propagation
STT efficiency	High Gilbert-damping parameter ($\alpha > 0.1$) expected due to important LS-coupling and results for similar systems in literature Very small GMR, which might indicate a very small potential for the spin- polarization of currents However encouraging results in literature for current induced domain wall motion experiments with similar materials.	Small Gilbert-damping parameter ($\alpha = 0.01$) measured, Important GMR, and high spin-polarization of the electrons at the Fermi-level indicating a high potential for the spin-polarization of currents
Further applications	All-optical switching	Electric Field-Induced Modification of Magnetism

Figure 4.1: Overview about the suitability of $[\text{Co/Ni}]$ superlattices and amorphous $\text{Co}_{1-x}\text{Tb}_x$ -alloys for spin transfer torque experiments. See also sec.(1.6)

References

- [1] G. Binasch, P. Grünberg, F. Saurenbach, and W. Zinn. Enhanced magnetoresistance in layered magnetic structures with antiferromagnetic interlayer exchange. *Phys. Rev. B*, 39:4828–4830, 1989.
- [2] M. N. Baibich, J. M. Broto, A. Fert, F. Nguyen Van Dau, F. Petroff, P. Etienne, G. Creuzet, A. Friederich, and J. Chazelas. Giant Magnetoresistance of (001)Fe/(001)Cr Magnetic Superlattices. *Phys. Rev. Lett.*, 61:2472–2475, 1988.
- [3] N. F. Mott. The Resistance and Thermoelectric Properties of the Transition Metals. *Proc. R. Soc.*, 156:368–382, 1936.
- [4] L. Berger. Emission of spin waves by a magnetic multilayer traversed by a current. *Phys. Rev. B*, 54(13):9353–9358, 1996.
- [5] J. C. Slonczewski. Current-driven excitation of magnetic multilayers. *Jour. Magn. Magn. Mat.*, 159:L1–L7, 1996.
- [6] M. Tsoi, A. G. M. Jansen, J. Bass, W.-C. Chiang, M. Seck, V. Tsoi, , and P. Wyder. Excitation of a Magnetic Multilayer by an Electric Current. *Phys. Rev. Lett.*, 80:4281–4284, 1998.
- [7] E. B. Myers, D. C. Ralph, J. A. Katine, R. N. Louie, and R. A. Buhrman. Current-Induced Switching of Domains in Magnetic Multilayer Devices. *Science*, 285(5429):867–870, 1999.
- [8] S. I. Kiselev, J. C. Sankey, I. N. Krivorotov, N. C. Emley, R. J. Schoelkopf, R. A. Buhrman, and D. C. Ralph. Microwave oscillations of a nanomagnet driven by a spin-polarized current. *Nature*, 425:380–383, 2003.
- [9] Y. Huai, F. Albert, P. Nguyen, M. Pakala, and T. Valet. Observation of spin-transfer switching in deep submicron-sized and low-resistance magnetic tunnel junctions. *Appl. Phys. Lett.*, 84(16):3118–3120, 2004.
- [10] L. Berger. Exchange interaction between ferromagnetic domain wall and electric current in very thin metallic films. *Jour. Appl. Phys.*, 55(6):1954–1956, 1984.
- [11] S. S. P. Parkin, M. Hayashi, and L. Thomas. Magnetic Domain-Wall Racetrack Memory. *Science*, 320:190–194, 2008.
- [12] J.A. Katine, F.J. Albert, R.A. Buhrman, E.B. Myers, and D.C. Ralph. Current-Driven Magnetization Reversal and Spin-Wave Excitations in Co/Cu/Co Pillars. *Phys. Rev. Lett.*, 84(14):3149–3152, 2000.

- [13] N. Vernier, D.A. Allwood, D. Atkinson, M. D. Cooke, and R. P. Cowburn. Domain wall propagation in magnetic nanowires by spin-polarized current injection. *Europhys. Lett.*, 65(4):526–532, 2004.
- [14] P.P. Freitas and L. Berger. Observation of s-d exchange force between domain walls and electric current in very thin Permalloy films. *Jour. Appl. Phys.*, 57(4):1266–1269, 1985.
- [15] S. Mangin, D. Ravelosona, J.A. Katine, M.J. Carey, B.D. Terris, and E.E. Fullerton. Current-induced magnetization reversal in nanopillars with perpendicular anisotropy. *Nat. Mat.*, 5:210–215, 2006.
- [16] D. Ravelosona, S. Mangin, J. A. Katine, E.E. Fullerton, and B.D. Terris. Threshold currents to move domain walls in films with perpendicular anisotropy. *Appl. Phys. Lett.*, 90(072508):1–3, 2007.
- [17] S. Mangin, Y. Henri, D. Ravelosona, J.A. Katine, and E.E. Fullerton. Reducing the critical current for spin-transfer switching of perpendicularly magnetized nanomagnets. *Appl. Phys. Lett.*, 94(012502):1–3, 2009.
- [18] Y. Henry, J. Cuchiarra, S. Mangin, J. A. Katine, and E. E. Fullerton. Distortion of the Stoner-Wohlfarth astroid by a spin-polarized current. *Phys. Rev. B*, 79(214422):1–7, 2009.
- [19] J. Cuchiarra, Y. Henry, D. Ravelosona, D. Lacour, E. E. Fullerton, J. A. Katine, and S. Mangin. Telegraph noise due to domain wall motion driven by spin current in perpendicular magnetized nanopillars. *Appl. Phys. Lett.*, 94(102503):1–3, 2009.
- [20] D. Bedau, H. Liu, J. Z. Sun, J. A. Katine, E. E. Fullerton, S. Mangin, and A. D. Kent. Spin-transfer pulse switching: From the dynamic to the thermally activated regime. *Appl. Phys. Lett.*, 97(262502):1–3, 2010.
- [21] C. Burrowes, D. Ravelosona, C. Chappert, S. Mangin, Eric E. Fullerton, J. A. Katine, and B. D. Terris. Role of pinning in current driven domain wall motion in wires with perpendicular anisotropy. *Appl. Phys. Lett.*, 93(172513):1–3, 2008.
- [22] C. Burrowes, A. P. Mihai, D. Ravelosona, J.-V. Kim, C. Chappert, L. Vila, A. Marty, Y. Samson, F. Garcia-Sanchez, L. D. Buda-Prejbeanu, I. Tudosa, E. E. Fullerton, and J.-P. Attané. Non-adiabatic spin-torques in narrow magnetic domain walls. *Nature Physics*, 6):17–21, 2010.
- [23] S. Zhang and Z. Li. Roles of nonequilibrium Conduction Electrons on the magnetization Dynamics of Ferromagnets. *Phys. Rev. Lett*, 93(12):127204–1–4, 2004.
- [24] J.C. Slonczewski. Currents and torques in metallic magnetic multilayers. *Jour. Mag. Mag. Mater.*, 247:324–338, 2002.
- [25] A. Yamaguchi, S. Nasu, H. Tanigawa, T. Ono, K. Miyake, K. Mibu, and T. Shinjo. Effect of Joule heating in current-driven domain wall motion. *Appl. Phys. Lett.*, 86(012511):1–3, 2005.

- [26] G. H. O. Daalderop, P. J. Kelly, and F. J. A. den Broeder. Prediction and Confirmation of Perpendicular Magnetic Anisotropy in Co/Ni Multilayers. *Phys. Rev. Lett.*, 68(3):682–685, 1992.
- [27] P. Hansen, C. Clausen, G. Much, M. Rosenkranz, and K. Witter. Magnetic and magneto-optical properties of rare-earth transition-metal alloys containing Gd, Tb, Fe, Co. *Jour. Appl. Phys.*, 66(2):756–767, 1989.
- [28] C. Kaiser, A.F. Panchula, and S.P. Parkin. Finite tunneling Spin Polarization at the Compensation Point of Rare-Earth-Metal-Transition-Metal Alloys. *Phys. Rev. Lett.*, 95(047202):1–4, 2005.
- [29] T. Kato, K. Nakazawa, R. Komiya, N. Nishizawa, S. Tsunashima, and S. Iwata. Compositional Dependence of g-Factor and Damping Constant of GdFeCo Amorphous Alloy Films. *IEEE Trans. Magn.*, 44(11):3380–3383, 2008.
- [30] H. Nakamura, S. Li, Xiaoxi Liu, and A. Morisako. Current-Induced Domain Wall Motion in TbFeCo micro wire. *Jour. Phys.:Conference Series*, 266(012082):1–4, 2011.
- [31] M. Weisheit, S. Fähler, A. Marty, Y. Souche, C. Poinsignon, and D. Givord. Electric Field-Induced Modification of Magnetism in Thin-Film Ferromagnets. *Science*, 315(5810):349–351, 2007.
- [32] S. S. Chabysheva and J. R. Hiller. Nonperturbative calculation of the electrons magnetic moment with truncation extended to two photons. *Phys. Rev. D*, 81(074030):1–18, 2010.
- [33] Albert Messiah. *Quantum Mechanics*. Dover Publications, inc. Mineola, New York, 1999.
- [34] Étienne du Trémolet de Lacheisserie. *Magnétisme, I - Fondements*. EDP Sciences, 2000.
- [35] E. C. Stoner. Collective Electron Specific Heat and Spin Paramagnetism in Metals . *Proc. R. Soc.*, 154:656–678, 1936.
- [36] T. Lewowski and K. Wozniak. Measurement of Curie temperature for gadolinium: a laboratory experiment for students. *Eur. J. Phys.*, 18:453–455, 1997.
- [37] H. Brooks. Ferromagnetic Anisotropy and the Itinerant Electron Model. *Phys. Rev.*, 58:909–918, 1940.
- [38] J. H. van Vleck. On the Anisotropy of Cubic Ferromagnetic Crystals. *Phys. Rev.*, 52:1178–1198, 1937.
- [39] C. T. Chen, Y. U. Idzerda, H.-J. Lin, N. V. Smith, G. Meigs, E. Chaban, G. H. Ho, E. Pellegrin, and F. Sette. Experimental Confirmation of the X-Ray Magnetic Circular Dichroism Sum Rules for Iron and Cobalt. *Phys. Rev. Lett.*, 75 (1):152–155, 1995.

- [40] L. Néel. Anisotropie magnétique superficielle et surstructures d'orientation. *J. Phys. Radium*, 15:225–239, 1954.
- [41] P. F. Carcia, A. D. Meinhaldt, and A. Suna. Perpendicular magnetic anisotropy in Pd/Co thin film layered structures. *Appl. Phys. Lett.*, 47(2):178–180, 1985.
- [42] K. Yakushiji, S. Yuasa, T. Nagahama, A. Fukushima, H. Kubota, T. Katayama, and K. Ando. Spin-Transfer Switching and Thermal Stability in an FePt/Au/FePt Nanopillar Prepared by Alternate Monatomic Layer Deposition. *Appl. Phys. Exp.*, 1(041302):1–3, 2008.
- [43] T.R. McGuire and R.I. Potter. Role of pinning in current driven domain wall motion in wires with perpendicular anisotropy. *Magnetics, IEEE*, 11(4):1018–1038, 1975.
- [44] C. Vouille, A. Barthélémy, F. Elokani Mpondo, A. Fert, P.A. Schroeder, S.Y. Hsu, A. Reilly, and R. Loloee. Microscopic mechanisms of giant magnetoresistance. *Phys. Rev. B*, 60:6710–6722, 1999.
- [45] J. M. Luttinger. Theory of the Hall Effect in Ferromagnetic Substances. *Phys. Rev.*, 112:739–751, 1958.
- [46] L. Berger. Side-Jump Mechanism for the Hall Effect of Ferromagnets. *Phys. Rev. B*, 2(11):4559–4566, 1970.
- [47] J. Moritz, B. Rodmacq, S. Auffret, and B. Dieny. Extraordinary Hall effect in thin magnetic films and its potential for sensors, memories and magnetic logic applications. *Jour. Phys. D: Appl. Phys.*, 41(135001):1–8, 2008.
- [48] E.C. Stoner and E.P. Wohlfarth. A Mechanism of Magnetic Hysteresis in Heterogeneous Alloys. *Phil. Trans. R. Soc. Lond*, 240(826):599–642, 1948.
- [49] A. Kirilyuk, J. Ferré, V. Grolier, J. P. Jamet, and D. Renard. Magnetization reversal in ultrathin ferromagnetic films with perpendicular anisotropy. *Jour. Magn. Magn. Mat.*, 171:45–63, 1997.
- [50] S. Lemerle. *Etude de la dynamique de renversement de l'aimantation dans les couches ultra-minces à anisotropie perpendiculaire: rôle de la nanostructure.* . PhD thesis, Université Paris XI Orsay, 1998.
- [51] S. Lemerle, J. Ferré, C. Chappert, V. Mathet, T. Giamarchi, and P. Le Doussal. Domain Wall Creep in an Ising Ultrathin Magnetic Film. *Phys. Rev. Lett.*, 80(4):849–852, 1998.
- [52] C. Burrowes. *Dynamique stochastique des parois de domaine dans les couches minces magnétiques à anisotropie perpendiculaire sous courant polarisé en spin.* PhD thesis, Université Paris-Sud XI, 2009.
- [53] P. J. Metaxas, J. P. Jamet, A. Mougin, M. Cormier, J. Ferré, V. Baltz, B. Rodmacq, B. Dieny, and R. L. Stamps. Creep and Flow Regimes of Magnetic Domain-Wall Motion in Ultrathin Pt/Co/Pt Films with Perpendicular Anisotropy. *Phys. Rev. Lett.*, 99 (21708):1–4, 2007.

- [54] N. L. Schryer and L. R. Walker. Motion of 180° domain walls in uniform DC magnetic fields . *Jour. Appl. Phys.*, 45(12):5406–5421, 1974.
- [55] A. Mougin, M. Cormier, J.P. Adam, P.J. Metaxas, and J. Ferré. Domain wall mobility, stability and Walker breakdown in magnetic nanowires. *Eur. Phys. Lett.*, 159(57007):1–6, 2007.
- [56] D. Ravelosona, D. Lacour, J. A. Katine, B.D. Terris, and C. Chappert. Nanometer Scale Observation of High Efficiency Thermally Assisted Current-Driven Domain Wall Depinning. *Phys. Rev. Lett.*, 95(117203):1–4, 2005.
- [57] J. P. Attané, D. Ravelosona, A. Marty, Y. Samson, and C. Chappert. Thermally Activated Depinning of a Narrow Domain Wall from a Single Defect. *Phys. Rev. Lett.*, 96 (147204):1–4, 2006.
- [58] J. Xiao, A. Zangwill, and M. D. Stiles. Macrospin models of spin transfer dynamics. *Phys. Rev. B*, 72(014446):1–13, 2005.
- [59] W. Wernsdorfer, E. Bonet Orozco, K. Hasselbach, A. Benoit, B. Barbara, N. Demoncy, A. Loiseau, H. Pascard, and D. Mailly. Experimental Evidence of the Néel-Brown Model of Magnetization Reversal. *Phys. Rev. Lett.*, 78(9):1791–1794, 1997.
- [60] L. Mei, D. Wachenschwanz, B. Bian, G. Bertero, L. He, and C. Chen. The relationship between thermal decayrate, thermal stability factor $K_u V / K_B T$ and grain size distribution in thin film magnetic recording media. *Jour. Magn. Magn. Mat.*, 239:385–389, 2002.
- [61] J. Cuchiarra, E. E. Fullerton, A. D. Kent, J. Z. Sun, Y. Henry, and S. Mangin. Current-induced magnetization reversal in terms of power dissipation . *submitted to PRB*, 2011.
- [62] T. Seki, S. Mitani, K. Yakushiji, and K. Takanashi. Spin-polarized current-induced magnetization reversal in perpendicularly magnetized $L1_0 - FePt$ layers. *Appl. Phys. Lett.*, 88(172504):1–3, 2006.
- [63] H. Meng and J.P. Wang. Spin transfer in nanomagnetic devices with perpendicular anisotropy. *Appl. Phys. Lett.*, 88(172506):1–3, 2006.
- [64] J. H. Park, M.T. Moneck, C. Park, and J. G. Zhu. Spin-transfer induced switching in nanomagneto-resistive devices composed of Co/Pt multilayers with perpendicular magnetic anisotropy. *Jour. Appl. Phys.*, 105(07D129):1–3, 2009.
- [65] K. Aoshima, N. Funabashi, K. Machida, Y. Miyamoto, N. Kawamura, K. Kuga, N. Shimidzu, T. Kimura Y. Otani, and F. Sato. Magneto-Optical and Spin-Transfer Switching Properties of Current-Perpendicular-to Plane Spin Valves with Perpendicular Magnetic Anisotropy. *IEEE Trans. Magn.*, 44(11):2491–2495, 2008.
- [66] W. B. Zeper, F. J. A. M. Greidanus, P. F. Carcia, and C. R. Fincher. Perpendicular magnetic anisotropy and magneto-optical Kerr effect of vapor-deposited Co/Pt-layered structures. *Jour. Appl. Phys.*, 65:4971–4975, 1989.

- [67] B. Yao and K. R. Coffey. Thickness dependence of structure and magnetic properties of annealed $[Fe/Pt]_n$ multilayer films. *Jour. Appl. Phys.*, 105(07A726:1–3, 2009.
- [68] M. Yamanouchi, J. Ieda, F. Matsukura, S. Barnes, S. Maekawa, and H. Ohno. Universality Classes for Domain Wall Motion in the Ferromagnetic Semiconductor (Ga,Mn)As. *Science*, 317(5845):1726–1729, 2007.
- [69] Charles Kittel. *Einführung in die Festkörperphysik*. R. Oldenbourg Verlag München Wien, 2000.
- [70] Z.G. Li, D. J. Smith, E.E. Marinero, and J.A. Willett. Investigations of microstructure of thin TbFeCo films by high-resolution electron microscopy. *Jour. Appl. Phys.*, 69(9):6590–6594, 1991.
- [71] T. Mizoguchi and G. S. Cargill. Magnetic anisotropy from dipolar interactions in amorphous ferrimagnetic alloys. *Jour. Appl. Phys.*, 50(5):3570–3582, 1979.
- [72] K. Moorjani and J.M.D. Coey. *Magnetic Glasses*. Elsevier, Amsterdam, 1984.
- [73] I. A. Campbell. Indirect exchange for rare earths in metals. *Journal of Physics F: Metal Physics*, 2 L47:1234567, 1972.
- [74] A. Grenier. *Etude à l'échelle atomique de multicouches magnétostrictives TbFe/Co et TbFeCo/Fe: structure, propriétés magnétiques et effet de l'irradiation aux ions lourds*. PhD thesis, Université de Rouen, 2008.
- [75] W.C. Thoburn, S. Legvold, and F.H. Spedding. Magnetic properties of Terbium metal. *Phys. Rev.*, 112(1):56–58, 1958.
- [76] C. Zener. Classical Theory of the Temperature Dependence of Magnetic Anisotropy Energy. *Phys. Rev.*, 96:1335–1337, 1954.
- [77] Y. Mimura, N. Imamura, T. Kobayashi, A. Okada, and Y. Kushiuro. Magnetic properties of amorphous alloy films of Fe with Gd, Tb, Dy, Ho, or Er. *Jour. Appl. Phys.*, 49(3):1208–1214, 1978.
- [78] F. Hellman. Measurement of magnetic anisotropy of ferrimagnets near compensation. *Appl. Phys. Lett.*, 59(21):2757–2759, 1991.
- [79] Y. J. Wang and Q. W. Leng. Thermal stability and the origin of perpendicular anisotropy in amorphous Tb-Fe-Co films. *Phys. Rev. B*, 41(1):651–657, 1990.
- [80] P. Chaudhari, J.J. Cuomo, and R. J. Gambino. Amorphous metallic films for magneto-optic applications. *Appl. Phys. Lett.*, 22:337–339, 1973.
- [81] F. Hellman and E. M. Gyorgy. Growth-Induced Magnetic Anisotropy in Amorphous Tb-Fe. *Phys. Rev. Lett.*, 68(9):1391–1394, 1992.
- [82] F. Hellman. Surface-induced ordering: A vapor-deposition growth of amorphous materials. *Appl. Phys. Lett.*, 64(5):1947–1949, 1994.

- [83] H. Takagi, S. Tsunashima, S. Uchiyama, and T. Fujii. Stress induced anisotropy in amorphous Gd-Fe and Tb-Fe . *Jour. Appl. Phys.*, 50(3):1642–1644, 1979.
- [84] Hong Fu, Masud Mansuripur, and Pierre Meystre. Generic Source of Perpendicular Anisotropy in Amorphous Rare-Earth-Transition-Metal Films. *Phys. Rev. Lett.*, 66 (8):1086–1089, 1991.
- [85] M. Hirscher, T. Egami, and E. E. Marinero. Atomistic study of magneto-optical amorphous thin films using synchrotron radiation. *Jour. Appl. Phys.*, 67(9):4932–4934, 1990.
- [86] X. Yan, M. Hirscher, T. Egami, and E. E. Marinero. Direct observation of anelastic bond-orientational anisotropy in amorphous $Tb_{26}Fe_{62}Co_{12}$ thin films by x-ray diffraction. *Phys. Rev. B*, 43(11):9300–9303, 1991.
- [87] R. J. Gambino and J. J. Cuomo. Selective resputtering-induced anisotropy in amorphous films. *J. Vac. Sci. Technol.*, 15:296–301, 1978.
- [88] V. G. Harris, K. D. Aylesworth, B. N. Das, W. T. Elam, and N. C. Koon. Structural origins of magnetic anisotropy in sputtered amorphous Tb-Fe films. *Phys. Rev. Lett.*, 69(13):1939–1942, 1992.
- [89] A. Hubert and R. Schäfer. *Magnetic Domains - The Analysis of Magnetic microstructures* . Springer, 1998.
- [90] A. Hubert and R. Schäfer. *Magnetic Domains - The Analysis of Magnetic microstructures* . Springer, 1998.
- [91] J. Stöhr and H. C. Siegmann. *Magnetism - From Fundamentals to Nanoscale Dynamics* . Springer, 2006.
- [92] R. C. Woodward, A. M. Lance, R. Street, and R. L. Stamps. Variation of the magnetic domain structure with reversal field. *Jour. Appl. Phys.*, 93(10):6567–6571, 2003.
- [93] A. Kirilyuk, J. Giergiel, J. Shen, and J. Kirschner. On the Barkhausen volume in ultrathin magnetic films with perpendicular magnetic anisotropy. *Jour. Magn. Magn. Mat.*, 159:27–32, 1995.
- [94] C. Burrowes E. E. Fullerton C. Chappert L. Prejebeanu F. Garcia-Sanchez S. Park, N. M. Nguyen and D. Ravelosona. Asymmetric domain wall depinning under current in spin valves with perpendicular anisotropy. *Appl. Phys. Lett.*, 98(232512):1–3, 2011.
- [95] L. Thomas, M. G. Samant, and S. S. P. Parkin. Domain-Wall Induced Coupling between Ferromagnetic Layers. *Phys. Rev. Lett.*, 84(8):1816–1819, 2000.
- [96] B. Rodmacq, V. Baltz, and B. Dieny. Macroscopic probing of domain configurations in interacting bilayers with perpendicular magnetic anisotropy. *Phys. Rev. B*, 73(092405):1–4, 2006.

- [97] V. Baltz, A. Marty, B. Rodmacq, and B. Dieny. Magnetic domain replication in interacting bilayers with out-of-plane anisotropy: Application to Co/Pt multilayers. *Phys. Rev. B*, 75(014406):1–6, 2007.
- [98] P. J. Metaxas, P. J. Zermatten, J.-P. Jamet, J. Ferré, G. Gaudin, B. Rodmacq, A. Schuhl, and R. L. Stamps. Periodic magnetic domain wall pinning in an ultrathin film with perpendicular anisotropy generated by the stray magnetic field of a ferromagnetic nanodot array. *Appl. Phys. Lett.*, 94(132504):1–3, 2009.
- [99] D. Rugar, H. J. Mamin, P. Guethner, S. E. Lambert, J. E. Stern, I. McFadyen, and T. Yogi. Magnetic force microscopy: General principles and application to longitudinal recording media. *Appl. Phys. Lett.*, 68:1169–1183, 1990.
- [100] Z. Q. Zou, H. Wang, and C. Yu. A computational method of temperature characteristics of magneto-optical Kerr effect in amorphous TbFeCo films with a multilayered structure. *Jour. Appl. Phys.*, 93(9):5268–5273, 2003.
- [101] R. Hasegawa. Static bubbles in amorphous Gd-Co. *Jour. Appl. Phys.*, 45(7):3109–3112, 1974.
- [102] T. R. McGuire, R. J. Gambino, and R. C. Taylor. Hall effect in amorphous thin-film magnetic alloys. *Jour. Appl. Phys.*, 48(7):2965–2970, 1977.
- [103] T. W. Kim and R. J. Gambino. Composition dependence of the Hall effect in amorphous Tb_xCo_{1-x} thin films. *Jour. Appl. Phys.*, 87(4):1869–1873, 2000.
- [104] R. Malmhäll. Extraordinary Hall resistivity in amorphous terbium-iron thin films and its temperature dependence. *Jour. Appl. Phys.*, 54(9):5128–5131, 1983.
- [105] R. A. Hajjar, M. Mansuripur, and H.-P. D. Shieh. Measurements of magnetoresistance in magneto-optical recording media. *Jour. Appl. Phys.*, 69(10):7067–7080, 1991.
- [106] J. J. Rhyne. *Amorphous magnetic rare earth alloys*. North-Holland Publishing Company, 1979.
- [107] C. Bellouard, H. D. Rapp, B. George, S. Mangin, G. Marchal, and J.C. Ousset. Negative spin-valve effect in $Co_{65}Fe_{35}/Ag/(Co_{65}Fe_{35})_{50}Gd_{50}$ trilayers. *Phys. Rev. B*, 53(9):5082–5084, 1996.
- [108] C.-H. Lai, C.-C. Lin, B. M. Chen, H.-P. D. Shieh, and C.-R. Chang. Positive giant magnetoresistance in ferrimagnetic/Cu/ferrimagnetic films. *Jour. Appl. Phys.*, 89(11):7124–7126, 2001.
- [109] P. J. Cote and L. V. Meisel. Resistivity in Amorphous and Disordered Crystalline Alloys. *Phys. Rev. Lett.*, 39:102–105, 1977.
- [110] A. K. Sinha. Electrical Resistivity, Thermoelectric Power, and X-Ray Interference Function of Amorphous Ni-Pt-P Alloys. *Phys. Rev. B*, 1:4541–4546, 1970.

- [111] B. Raquet, M. Viret, E. Sondergard, O. Cespedes, and R. Mamy. Electron-magnon scattering and magnetic resistivity in 3d ferromagnets. *Phys. Rev. B*, 66(024433):1–11, 2002.
- [112] C.D. Stanciu, F. Hansteen, A.V. Kimel, A. Kirilyuk, A. Tsukamoto, A. Itoh, and Th. Rasing. All-Optical Magnetic Recording with Circularly Polarized Light. *Phys. Rev. Lett.*, 99 (047601):1–3, 2007.
- [113] J. Hohlfeld, C. D. Stanciu, and A. Rebei. Athermal all-optical femtosecond magnetization reversal in GdFeCo. *Appl. Phys. Lett.*, 94 (152504):1–3, 2009.
- [114] A. Kirilyuk, A. V. Kimel, and Theo Rasing. Ultrafast optical manipulation of magnetic order. *Rev. Mod. Phys.*, 82:2731–2784, 2010.
- [115] J. M. Gallego, S. Kim, T. J. Moran, D. Lederman, and I. K. Schuller. Growth and structural characterization of Ni/Co superlattices. *Phys. Rev. B*, 51:25502555, 1995.
- [116] S. Girod. Croissance par épitaxie par jets moléculaires de multicouches *Co/Ni* à anisotropie perpendiculaire, 2008.
- [117] B. Kierren, T. Gourieux, F. Bertran, and G. Krill. Oxygen adsorption observed during the epitaxy of V(110) on the $11\bar{2}0$ α - Al_2O_3 surface. *Appl. Surf. Sci.*, 68:341–345, 1993.
- [118] H. Homma, K.-Y. Yang, and I. K. Schuller. Role of lattice matching in epitaxy: Novel Ce phase and new fcc-bcc epitaxial relationship. *Phys. Rev. B*, 36:94359438, 1987.
- [119] E. Bauer and Jan H. van der Merwe. Structure and growth of crystalline superlattices: From monolayer to superlattice. *Phys. Rev. B*, 33:36573671, 1985.
- [120] G. Lehmppfuhl, A. Ichimiya, and H. Nakahara. Interpretation of RHEED oscillations during MBE growth. *Surf. sci. lett.*, 245:L159–L162, 1991.
- [121] David R. Lide. *CRC Handbook of Chemistry and Physics*. CRC Press LLC, 2004.
- [122] J.C.A. Huang, T.E. Wang, C.C. Yu, Y.M. Hu, P.B. Lee, and M.S. Yang. Epitaxial growth and characterization of (100) and (110) permalloy films. *Journal of Crystal growth*, 171:442–446, 1997.
- [123] Yue-Lin Liu, Ying Zhang, Hong-Bo Zhou, Guang-Hong Lu, and Masanori Kohyama. Theoretical strength and charge redistribution of fcc Ni in tension and shear. *J. Phys.: Condens. Matter*, 20(335216):1–8, 2008.
- [124] J. Gump, Hua Xia, M. Chirita, R. Sooryakumar, M. A. Tomaz, and G. R. Harp. Elastic constants of face-centered-cubic cobalt. *Jour. Appl. Phys.*, 86(11):6005–6009, 1999.
- [125] M. T. Johnson, J. J. de Vries, N. W. E. McGee, J. aan de Stegge, and F. J. A. den Broeder. Orientational Dependence of the Interface Magnetic Anisotropy in Epitaxial *Ni/Co/Ni* Sandwiches. *Phys. Rev. Lett.*, 69(24):3575–3578, 1992.

- [126] Y. B. Zhang, J. A. Woollam, Z. S. Shan, J. X. Shen, and D. J. Sellmyer. Anisotropy and magneto-optical properties of sputtered *Co/Ni* multilayer thin films. *IEEE Trans. Magn.*, 30(6):4440–4442, 1994.
- [127] B. N. Engel, C. D. England, R. A. Van Leeuwen, M. H. Wiedmann, and C. M. Falco. Interface Magnetic Anisotropy in Epitaxial Superlattices. *Phys. Rev. Lett.*, 67(14):1910–1913, 1991.
- [128] G. Bochi, O. Song, and R. C. O’Handley. Surface magnetoelastic coupling coefficients of single-crystal fcc Co thin films. *Phys. Rev. B*, 50(3):2043–2046, 1994.
- [129] G. Bochi, H. E. Inglefield C. A. Ballentine, C. V. Thompson, and R. C. O’Handley. Perpendicular magnetization and surface magnetoelastic anisotropy in epitaxial Cu/Ni/Cu (001). *J. Appl. Phys.*, 79(8):5845–5847, 1996.
- [130] G. Y. Guo. Orientation dependence of the magnetoelastic coupling constants in strained FCC Co and Ni: an ab initio study. *Jour. Magn. Magn. Mat.*, 209:33–36, 2000.
- [131] R. Wu and A. J. Freeman. Limitation of the Magnetic-Circular-Dichroism Spin Sum Rule for Transition Metals and Importance of the Magnetic Dipole Term. *Phys. Rev. Lett.*, 73 (14):1994–1997, 1994.
- [132] R. Nakajima, J. Stöhr, and Y. U. Idzerda. Electron-yield saturation effects in L-edge x-ray magnetic circular dichroism spectra of Fe, Co, and Ni. *Phys. Rev. B*, 59(9):6421–6429, 1999.
- [133] J. Stöhr and H. C. Siegmann. *Magnetism - From Fundamentals to Nanoscale Dynamics*. Springer, 2006.
- [134] F. Gimberta and L. Calmels. Electron states and magnetic moments in Co/Ni(111) multilayers and overlayers. *Jour. Appl. Phys.*, 109(07C109):1–3, 2011.
- [135] J.-M. L. Beaujour, W. Chen, K. Krycka, C.-C. Kao, J. Z. Sun, and A. D. Kent. Ferromagnetic resonance study of sputtered Co/Ni multilayers. *Eur. Phys. J. B*, 59:475–483, 2007.
- [136] J.-M. L. Beaujour, D. Ravelosona, I. Tudosa, E. E. Fullerton, and A. D. Kent. Ferromagnetic resonance linewidth in ultrathin films with perpendicular magnetic anisotropy. *Phys. Rev. B*, 80(180415):1–4, 2009.
- [137] D. J. Twisselmann and R. D. McMichael. Intrinsic damping and intentional ferromagnetic resonance broadening in thin Permalloy films. *Jour. Appl. Phys.*, 93(10):6903–6905, 2003.
- [138] S. S. P. Parkin, N. More, and K. P. Roche. Oscillations in Exchange Coupling and Magnetoresistance in Metallic Superlattice Structures: Co/Ru, Co/Cr, and Fe/Cr. *Phys. Rev. Lett.*, 64 (19):2304–2307, 1990.

- [139] P. Bruno and C. Chappert. Oscillatory Coupling between Ferromagnetic Layers Separated by a Nonmagnetic Metal Spacer. *Phys. Rev. Lett.*, 67 (12):1602–1605, 1991.
- [140] J. Moritz, F. Garcia, J. C. Toussaint, B. Dieny, and J. P. Nozières. Orange peel coupling in multilayers with perpendicular magnetic anisotropy: Application to (Co/Pt)-based exchange-biased spin-valves. *Europhys. Lett.*, 65 (1):123–129, 2004.
- [141] C. A. F. Vaz, J. A. C. Bland, and G. Lauhoff. Magnetism in ultrathin film structures. *Rep. Prog. Phys.*, 71(056501):1–78, 2008.
- [142] A. K. See and L. E. Klebanoff. Spin-resolved density of states of 3d magnets. *Jour. Appl. Phys.*, 79:4796–4798, 1996.
- [143] P. D. Johnson. Spin-polarized photoemission. *Rep. Prog. Phys.*, 60:1217–1304, 1997.
- [144] J. Osterwalder. *Spin-Polarized Photoemission*. Springer-Verlag Berlin Heidelberg, 2006.
- [145] T. Feuchtwang, P.H. Cutler, and D. Nagy. A review of the theoretical and experimental analyses of electron spin polarization in ferromagnetic transition metals. *Surface Sci.*, 75:490–528, 1978.
- [146] M. P. Seah and W. A. Dench. Quantitative Electron Spectroscopy of Surfaces. *Surf. Interface Anal.*, 1:2–11, 1979.
- [147] J. Kohlhepp and U. Gradmann. Magnetic surface anisotropies of Co(0001)-based interfaces from in situ magnetometry of Co films on Pd(111), covered with ultrathin films of Pd and Ag. *Jour. Mag. Mag. Mater.*, 139:347–354, 1995.
- [148] M. Sicot, P. Turban, S. Andrieu, A. Tagliaferri, C. De Nadai, N.B. Brookes, F. Bertran, and F. Fortuna. Spin polarization at the NiMnSb/MgO(1 0 0) interface. *Jour. Mag. Mag. Mater.*, 303(1):54–59, 2006.
- [149] P. Krüger, M. Taguchi, and S. Meza-Aguilar. Magnetism of 3d transition-metal monolayers on Cu(111) and Ag(111). *Phys. Rev. B*, 61:15277–15283, 2000.
- [150] J.M. Lavine. Extraordinary Hall-Effect Measurements on Ni, Some Ni Alloys, and Ferrites. *Phys. Rev.*, 123:12731277, 1961.
- [151] B. Dieny, V. S. Speriosu, S. Metin, S. S. P. Parkin, B. A. Gurney, P. Baumgart, and D. R. Wilhoit. Magnetotransport properties of magnetically soft spin-valve structures. *Jour. Appl. Phys.*, 69(8):4774–4779, 1991.
- [152] M. A. M. Gijs and M. Okada. Magnetoresistance study of Fe/Cr magnetic multilayers: Interpretation with the quantum model of giant magnetoresistance. *Phys. Rev. B*, 46:2908–2911, 1992.
- [153] J. E. Mattson, M. E. Brubaker, C. H. Sowers, M. Conover, Z. Qiu, and S. D. Bader. Temperature dependence of the magnetoresistance of sputtered Fe/Cr superlattices. *Phys. Rev. B*, 44(17):9378–9384, 1991.

- [154] H. Hasegawa. Theory of the temperature-dependent giant magnetoresistance in magnetic multilayers. *Phys. Rev. B*, 47(22):15080–15085, 1993.
- [155] T. Fujimoto, M. Patel, E. Gu, C. Daboo, and J. A. C. Bland. Origin of the temperature dependence of the giant magnetoresistance in magnetic multilayers. *Phys. Rev. B*, 51:6719–6722, 1995.
- [156] D. Chiba, Y. Sato, T. Kita, F. Matsukura, and H. Ohno. Current-Driven Magnetization Reversal in a Ferromagnetic Semiconductor (Ga,Mn)As/GaAs/(Ga,Mn)As Tunnel Junction. *Phys. Rev. Lett.*, 93(216602):1–4, 2004.
- [157] P. M. Braganca, I. N. Krivorotov, O. Ozatay, A. G. F. Garcia, N. C. Emley, D. C. Ralph J. C. Sankey, and R. A. Buhrman. Reducing the critical current for short-pulse spin-transfer switching of nanomagnets. *Appl. Phys. Lett.*, 87(112507):1–3, 2005.
- [158] X. Jiang, L. Gao, J.Z. Sun, and S. S. P. Parkin. Temperature Dependence of Current-Induced Magnetization Switching in Spin Valves with a Ferrimagnetic CoGd Free Layer. *Phys. Rev. Lett.*, 97(217202):1–4, 2006.
- [159] H. Sukegawa, S. Kasai, T. Furubayashi, S. Mitani, and K. Inomata. Spin-transfer switching in an epitaxial spin-valve nanopillar with a full-Heusler $Co_2FeAl_{0.5}Si_{0.5}$ alloy. *Appl. Phys. Lett.*, 96(042508):1–3, 2010.

Résumé

Les effets de transfert de spin sont devenus un sujet de recherche majeur ces quinze dernières années. Cependant, nous avons constaté un manque de vérifications expérimentales pour beaucoup de modèles décrivant les effets de transfert de spin. Ceci est surtout lié à un manque de systèmes magnétiques modèles permettant un contrôle précis des paramètres pertinents utilisés dans les modèles théoriques. Dans ce travail nous avons analysé deux systèmes magnétiques à aimantation perpendiculaire : les alliages amorphes de $Co_{1-x}Tb_x$ élaborés par pulvérisation cathodique et les super-réseaux $[Co/Ni](111)$ élaborés par épitaxie par jets moléculaires. L'anisotropie et l'aimantation, qui sont des paramètres pertinents dans beaucoup de modèles sur le transfert de spin, sont variables dans une large gamme. L'origine de cette anisotropie est discutée. La structure des domaines magnétiques est analysée et les résultats des mesures de transport sont interprétés. Pour les super-réseaux $[Co/Ni](111)$ nous démontrons une forte polarisation en spin au niveau de Fermi grâce à des expériences de photoémission résolue en spin et un coefficient d'amortissement intrinsèque α très faible. Nous concluons que les alliages amorphes de $Co_{1-x}Tb_x$ et les super-réseaux $[Co/Ni](111)$ sont des systèmes modèles pour le transfert de spin.

Mots clés : Electronique de spin ; Matériaux magnétiques ; Anisotropie magnétique perpendiculaire

Summary

Spin transfer torque effects have become a research subject of high interest during the last 15 years. However, in order to probe the fundamental physics of spin transfer torque model systems are needed. For a model system it must be as simple as possible to tune the significant parameters (magnetic and structural). In this work we analyze the suitability of two materials for this need. The studied materials are amorphous $Co_{1-x}Tb_x$ alloys elaborated by sputtering and MBE grown $[Co/Ni](111)$ superlattices. Both systems show perpendicular magnetic anisotropy (PMA), which provides a uniaxial anisotropy to the system. This anisotropy and the magnetization, which are significant parameters for many models on spin transfer torque, can be tuned in a large range of values. The origin of this PMA is discussed. The domain structure is analyzed and transport measurements are interpreted. In addition we show a strong spin polarization of the electrons close to the Fermi level by doing photoemission experiments. A small intrinsic Gilbert damping parameter α is found by FMR spectroscopy. We conclude that both materials are good candidates to be used as model systems for spin transfer torque.

Keywords: Spintronics; Magnetic materials; Perpendicular magnetic anisotropy